Nonlinear Control Design for Neuromorphic Smart Sensing System for Sound Perception

Zur Erlangung des akademischen Grades eines

Doktors der Ingenieurwissenschaften (Dr.-Ing.)

von der KIT-Fakultät für Chemieingenieurwesen und Verfahrenstechnik
des Karlsruher Instituts für Technologie (KIT)

genehmigte

Dissertation

von

M. Sc. Hermann Folke Johann Rolf

aus Kiel

Tag der mündlichen Prüfung: 11. Februar 2026
Erstgutachter: Prof. Dr.-Ing. habil. Thomas Meurer
Zweitgutachter: Prof. Dr.-Ing. habil. Alexander Schaum

Abstract

Technological speech processing lacks behind the mammalian hearing perception with respect to energy efficiency and processing time. This comes from the fact that conventional speech processing is based on a feedforward structure, while the hearing perception is done by a feedback loop between the cochlea and the brain. With this feedback loop, the latter is able to react adaptively and quickly towards a changing environment in an energy efficient way. In this work, analysis and design of controllers employed on arrays of bio-inspired oscillators are showcased to mimic the feedback loop of this biological system and thus the functionality of the hearing perception. For this, results from theoretical biology are used that model the physiology of the cochlea by oscillators exhibiting Andronov-Hopf bifurcations. This comes from the fact that, if the bifurcation parameter of these oscillators is in the neighborhood of its critical point, the oscillators and the cochlea react frequency-selective and compressive to external stimuli. For this, a benchmark oscillator model based on the Hopf-Theorem is introduced to analyze the inherent properties, which have to be satisfied by a neuromorphic acoustic sensor. Hence, the Normal Form Theorem implies that any oscillator exhibiting at least an Andronov-Hopf bifurcations can be represented by this benchmark oscillator model. With these considerations, controllers based on coupling and a delayed feedback are employed on this oscillator model and their effects are analyzed. It is demonstrated that the characteristic frequency can be adjusted by controlling the coupling strengths or the time delay, while preserving the Andronov-Hopf bifurcations of the system. To verify the results on the benchmark oscillator, an experimental realization of the bio-inspired oscillator is discussed. This realization is a thermally actuated cantilevered or clamped-clamped microelectromechanical system (MEMS), whose deflection can be measured. The MEMS is operated in a feedback loop to enable the control of its dynamic properties. To analyze the dynamics of the MEMS, a mathematical model based on two coupled partial differential equations (PDEs) is derived. This model is approximated by applying the Rayleigh-Ritz method and the Galerkin method, so that a system of ordinary differential equations (ODEs) of order 3 is derived. The system is then analyzed in terms of its characteristic frequency and the emerging Andronov-Hopf bifurcations. In particular, two controllable Andronov-Hopf bifurcations can be induced by designing the feedback loop accordingly. Hence, the controller design based on the benchmark oscillator model can be verified by coupling the MEMS and by introducing a delayed feedback loop. For injective coupling, it is demonstrated that in comparison to two injectively coupled benchmark oscillators an additional bifurcation emerges. In contrast to this, the number of critical points induced by diffusive coupling and a delayed feedback have been predicted correctly by the analysis of the benchmark oscillator. This comes from the fact that diffusive coupling and the delayed feedback steer the MEMS to the original critical points with their control parameters implying that the

Normal Form Theorem is satisfied. In addition, the frequency tunability of the proposed controller is verified with this analysis. Finally, the results on the frequency tunability are exploited to enable in-sensor signal processing. The processing is employed by sampling the frequency response of a external signal with an array of benchmark oscillator models. For this, it is shown that the response of a frequency-selective oscillator is unique after transients have decayed. Thus, the spectrum of the external input can be reconstructed by an array of oscillators, whose bifurcation parameter is in a neighborhood on their critical point. With these considerations different algorithms, such as sequential sampling or machine learning-based approaches, are discussed.

Zusammenfassung

Die technische Sprachverarbeitung ist dem Hörsinn bezüglich der Energieeffizienz und der Verarbeitunggeschwindigkeit unterlegen. Dies liegt daran, dass die Sprachverarbeitung kaskadiert aufgebaut ist, wohingegen beim Hörsinn eine Rückkopplungsschleife zwischen der Hörschnecke und den Gehirn vorliegt. Daher kann letztere adaptiv und schnell auf Veränderungen in der Umgebung reagieren. In der vorliegenden Arbeit wird untersucht inwiefern man den Hörsinn nachahmen kann, indem man einen Regler für biologisch inspirierte Oszillatoren entwirft und deren nichtlineare Dynamik analysiert. Dafür werden Ergebnisse aus der theoretischen Biologie verwendet, die die Physiologie der Hörschnecke durch ein System mit steuerbaren Andronov-Hopf-Bifurkation modulieren. Solche Systeme können, wie die Hörschnecke, kompressiv und frequenzselektiv auf externe Anregungen reagieren. Für den Entwurf der Regler wird zunächst basierend auf den Hopf-Theorem und den Normalform Theorem ein Benchmark-Oszillatormodell definiert. Mit diesem Modell werden dann die Eigenschaften von verschiedenen Reglern, wie Kopplung zwischen Oszillatoren oder eine steuerbare Totzeit, analysiert. Neben der steuerbaren Andronov-Hopf-Bifurkation, wird bei der Analyse die charakteristische Frequenz der Systeme analysiert. Es wird dabei gezeigt, dass man die charakteristische Frequenz steuern kann, indem man die Regler anpasst. Um die Resultate der Reglerentwürfe mit Hilfe der Benchmark-Oszillatoren zu verifizieren, wird eine technische Realisierung eines biologisch inspirierten Oszillators untersucht. Diese Realisierung besteht aus einem thermisch aktuierten mikro-elektromechanischen System (MEMS), dessen Auslenkung gemesen werden kann. Die Dynamik des MEMS kann daher gesteuern, indem der MEMS mit der gemessene Auslenkung aktuiert wird. Um die Dynamik zu analysieren, wird zunächst ein mathematisches Modell des MEMS hergeleitet, das aus zwei gekoppelten partiellen Differentialgleichungen (PDEs) besteht. Diese PDEs werden approximiert, indem man die Rayleigh-Ritz-Methode und die Galerkin-Methode anwendet. Damit kann man das Modell des MEMS auf ein 3-dimensionales System bestehend aus gewöhnlichen Differentialgleichungen (ODEs) reduzieren. Dieses System aus ODEs wird bezüglich der charakteristischen Frequenz und der Entstehung von steuerbaren Andronov-Hopf Bifurkationen untersucht. Hierbei wird gezeigt, dass die charakteristische Frequenz des MEMS aufgrund dessen Geometrie steuerbar ist, und dass man zwei steuerbare Andronov-Hopf Bifurkationen erzeugen kann, wenn man die Rückkopplung richtig auslegt. Daher kann das MEMS-Modell im Rückkopplungsmodus genutzt werden, um die auf den Benchmark-Oszillator basierenden Regler zu validieren. Es stellt sich heraus, dass die Anzahl der Bifurkationen bei diffusiver Kopplung steuerbare Totzeit vorhergesagt werden können. In Gegensatz dazu, entsteht eine zusätzliche Bifurkation bei zwei injektiv gekoppelten MEMS. Dieser Unterschied wird dadurch hervorgerufen, dass der Bifurkationsparamter des einzelnen MEMS auch durch die diffusive Kopplung und die steuerbare Totzeit in die

Umgebung seines kritischen Punktes getrieben wird. Des Weiteren kann die charaketeristische Frequenz durch die drei Regler verstellt werden. Abschließend wird basierend auf der Frequenzverstellbarkeit die in-Sensor-Signalverarbeitung diskutiert. Dabei werden mehrere Benchmark-Oszillatoren benutzt, um die Frequenzantwort eines Signals abzutasten. Es wird gezeigt, dass die Antwort eines Benchmark-Oszillators eindeutig ist, nachdem die Transienten verschwunden sind, sodass man den Frequenzbereich mit diesen Oszillatoren rekonstruieren kann. Die Abtastung des Frequenzbereichs wird dann mit verschieden Algorithmen, wie sequentielles Abtasten und Abtastung basierend auf Reinforcement Learning, diskutiert.

Preface

Diese Arbeit begann im Jahr 2021 im Rahmen des Sonderforschungsbereichs (SFB) 1461 Neurotronics am Lehrstuhl für Regelungstechnik an der Christian-Albrechts-Universität zu Kiel und fand ihr Ende im Jahr 2025 bei der Arbeitsgruppe Digital Process Engineering am Karlsruher Institut für Technologie.

Mein ausdrüchlichen Dank richtet sich vor allem an Prof. Dr.-Ing. habil. Thomas Meurer, da mir die Möglichkeit zur Promotion gegeben hat. Vor allem das entspannte und inspirierende Arbeitsklima ermöglichte mir frei zu diesen Thema zu arbeiten, sodass außergewöhliche Ergebnisse zustande gekommen sind.

Diese angenehme Arbeitsklima wurde zusätzlich durch meine Lehrstuhlkollegen, vor allem durch Lukas Richter, Kai Bauer, Sönke Bartels, Jan-Niklas Busse, Dr. Marta Mandis und Dr.-Ing Pascal Jerono, erzeugt. Ich bin daher dankbar für euer Unterstützung und die schönen Abende, die wir hatten.

Des weiteren bin ich sehr dankbar für das interessante Themengebiet des SFBs 1461 und die überaus großzügige Finanzierung des integrieten Graduiertenkollegs und für dessen vielfältige Angebote, wodurch sich äußerest erfolgreiche Kollaborationen ergaben. Zum Beispiel erhielt ich dadurch eine finanizielle Möglichkeit Prof. Dr. Petro Feketa an der Queen Victoria University in Wellington, Neuseeland zu besuchen und an zahlreichen internationalen Konferenzen teilnehmen. Darüber hinaus haben ich die Sommerschule des SFBs und die schönen Abende mit den Doktoranden bei den Retreats genossen, wodurch sich Freundschaften entwickelt haben.

Ferner danke ich Kalpan Ved, Prof. Dr. rer. nat. Claudia Lenk und Prof. Dr. rer. nat. habil. Martin Ziegler für die Validierung meiner theoretischen Ergebnisse, wodurch meine Ergebnisse ein breiten Publikum eröffert wurde.

Ich bin außerdem dankbar für die Betreuung und Unterstützung von Dr.-Ing. Pascal Jerono, Dr.-Ing. Jonas Koch, Prof. Dr.-Ing. Stefan Pachnicke, Prof. Dr.-Ing. habil. Alexander Schaum und Prof. Dr. Petro Feketa während meines Bachelor- und Master-Studiums. Während des Studiums habe ich mich gerne mit meine Kommilitonen auf die Klausuren vorbereitet. Durch eure Fragen habe ich einen anderen Blickwinkel auf die unterschiedlichen Themen des Studiums erlagen könnte.

Nicht zuletzt danke ich meinen Freunden, die mich zum Teil schon seit meiner Kindheit bzw. Schulzeit begletien, und natürlich meiner Familie, die mich während der Promotion unterstützt haben.

Contents

Abbreviations and Symbols

Abbreviations

CP	Critical Point
DFT	Discrete Fourier Transform
FPGA	Field programmable gate array
IDFT	Inverse Discrete Fourier Transform
MEMS	Microelectromechanical system
ODE	Ordinary differential equations
PDE	Partial differential equations

Sets

$\mathbb{N}$	Natural numbers $\mathbb{N} = \{1, 2, \ldots\}$
$\mathbb{Z}$	Integer numbers $\mathbb{Z} = \{\ldots, 2, -1, 0, 1, 2, \ldots\}$
$\mathbb{Q}$	Rational numbers
$\mathbb{R}$	Real numbers
$\mathbb{C}$	Complex numbers
$\sigma(A)$	Spectrum of a matrix A

Operators and Mathematical Symbols

General Parameters

Γ, K	Adjacency matrix
μ, υ	Bifurcation parameter
s	Complex-valued frequency
$\boldsymbol{z}$	Complex-valued state vector
D	Discriminant
$\boldsymbol{f}(\cdot)$	Drift vector field
λ	Eigenvalue
k	Feedback strength
$\boldsymbol{\phi}_t(\boldsymbol{x}_0)$	Flow of an vector field
Λ	Jordan matrix
n, m, l	Length of a series or magnitude of a set
V	Lyapunov function candidate
$\boldsymbol{h}(\cdot)$	Measurement map
$\boldsymbol{y}$	Measurement vector
C	Output matrix
a, b, c, d, e	Parameters of a polynomial or matrix
P	Polynomial
$\boldsymbol{x}, \boldsymbol{\chi}$	Real-valued state vector
i, j, k, l	Running indices for series and etc.
d	Sensitivity
$\boldsymbol{q}$	State vector of the envelope
A	System matrix
ϕ	Test function
$g(s)$	Transfer function
$G(s), H(s)$	Transfer matrix
V, W	Transformation matrix
t	Time
τ	Time delay

General Subscripts

act	Actuation
H	Andronov-Hopf bifurcation
eq	Equilibrium
C	Characteristic
cpl	Complete topology
conv	Convergence
crit	Critical point
o	Cycle topology
DC	Direct current
G	Galerkin method
HH	Hopf-Hopf bifurcation
kin	Kinetic
pot	Potential
I	Line topology
M	Mechanical
NC	Non-conservative
RF	Reinforcement learning
R	Rayleigh-Ritz method
seq	Sequential sampling
T	Thermal

Oscillator Parameters

ρ, r, F	Amplitudes
γ, ξ	Coupling strength
μ, η	Damping coefficient
ω, ν, Ω	(Angular) Frequency
f	(Normalized) Frequency
φ, ϕ	Phase
Q	Q-factor
R	Resistance
c	Spring constant
β, T	Time constants
α, κ, ζ	Transfer factor

Geometric and Material Parameters

A	Area
f	Body force
$z = [z_1, z_2, z_2]^{\mathrm{T}}$	Spacial coordinates
λ	Hear conductivity
w	Deflection
ρ	Density
s	Entropy
F	Force
I	First moment of area
q	Heat flow
h	Height
a, b, l	Length
μ	Linear friction coefficient
α	Linear heat expansion coefficient
ν	Poisson ration
P	Power
S	Second moment of area
c_e	Specific heat at constant strain
c	Spring constant
ϵ	Nonlinear strain
e	Linear strain
σ	Stress
T, θ	Temperature
J	Variational of work
v	Velocity
$V, \mathcal{V}$	Volume
d	Width
W	Work
E	Young's modulus

Part I.

Introduction and Preliminaries

1. Introduction

In technology, speech is typically processed using a feedforward architecture consisting of three steps – measuring the external stimuli, (nonlinear) pre-processing of the measured signal, and recognizing the patterns of the processed signal by, e.g., a neural network or a hidden Markov model [55]. These steps are illustrated in Figure 1.1. In recent years, this approach has become extremely efficient by mimicking pre-processing schemes similar to biology. For instance, it is shown in [2] that the word success rate can be up to 80% without additional recognition, if there is a compressive nonlinearity in pre-processing. A compressive nonlinearity is characterized by its reaction to external stimuli. In particular, small amplitudes are amplified and large amplitudes are attenuated by this nonlinearity, so that redundancies are introduced to the spectrum of the measured signal [70]. For instance, this nonlinearity can be found in the pre-processing of the hearing perception of mammals [26, 27, 40, 41] and amphibians [92, 103]. Additionally, the pre-processing in the cochlea is also frequency-selective and active [26, 27, 40, 41, 92, 103]. To compare both approaches in more detail, the measuring of the signal and the technological pre-processing are summarized subsequently.

In the first step, the external, mechanical stimuli is transformed into an electrical signal by a microphone. For instance, a sketch of a MEMS microphone is shown in Figure 1.1a. In principle, the movable diaphragm of this microphone-type is excited by the external stimuli and this movement is transduced by a piezo-electric layer into an electric signal. The frequency response of this mechanism is usually designed to capture the complete frequency range of the human ear [144], which is in a range from 20 Hz to 20 kHz [50, 121]. After that the signal is discretized in time to be able to process it digitally [90].

In the second step, the digital signal is usually transformed into the frequency domain and then processed by a nonlinear filter to increase the word success rate [1, 2, 28, 137]. These steps can be distinguished into fixed signal transformations, such as the linear spectrogram [2], the wavelet-transform [1], the cochleagram [2, 86, 87], the Mel-frequency cepstral

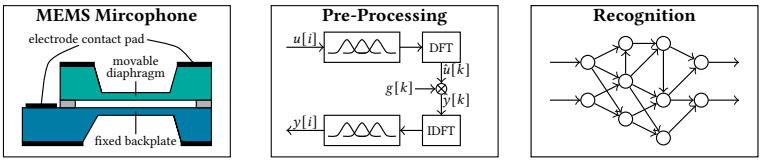

(a) Sketch of an MEMS microphone.

(b) Block diagram of a filter bank.

(c) Sketch of an artificial neural network.

Figure 1.1.: Sketches of the three different stages in speech processing.

coefficient, or learning signal transformations, which are based on machine learning [1]. Furthermore, the cochleagram and the Mel-frequency cepstral coefficient are used in technology most often [2, 55], since these approaches are motivated by the functionality of the cochlea [2]. This is summarized in the following to motivate bio-inspired acoustic sensing and thus an alternative architecture for speech processing.

1.1. Bio-Inspired Methods

As elaborated before, the response of the cochlea can vary between linear response and compressive and frequency-selective response. For example, it has been observed that the hearing perception inside the cochlea is an active process, which can be compressive [26, 27, 40, 41]. Thus, the dynamical regime of the cochlea ranges from processing of faint sounds in almost noiseless environments to the reconstruction and separation of heavily jammed signals. The latter regime is described by the so-called cocktail party effect [14, 20]. To model these dynamics either filter banks, or coupled critical oscillators can be used. These approaches are discussed subsequently.

Filter banks are blackbox models, which estimate the input-output behavior of the cochlea. This is done by fitting suitable models on data based on psychoacoustical experiments [105] and animal experiments [112, 113, 119]. Subsequently, three methods to implement a filter bank are briefly discussed. In [63] a filter bank based on the so-called Gammatone filter is introduced. This filter is based on an inverse correlation of the response of the neurons to an external stimuli of the cochlea and can be implemented digitally by a linear filter with either a finite or infinite impulse response, respectively [56, 84, 125]. In particular, this filter bank consists of filters, whose frequency responses are distributed similarly to the Gamma distribution [56]. Compression is implemented by adding an additional branch, which consists of a cascade of Gammatone filters and a compressive nonlinearity [84]. Alternatively in [86, 87], filter banks consisting of a pole–zero filter cascade with a sophisticated automatic gain control are proposed. The poles and the zeros of the pole-zero filter are chosen to mimic the frequency-selectivity of the cochlea, while the automatic gain control enables the compression. Finally, the filter bank can be implemented by a cochlear amplifier. For this, the measured signal is processed by neuromorphic hardware [135, 146], a field programmable gate array (FPGA) [5], or a very-large-scale-integrated chip [142].

The cochlea can also be modeled by coupled oscillators. In contrast to the filter bank approach, this model is based on the physiology of the cochlea. For this, the cochlea is separated into sections and each section is modeled by an oscillator, which exhibits a controllable Andronov-Hopf bifurcation [8, 18, 31, 34, 43, 60, 61, 64, 69, 103, 131]. This comes from the fact that a system with an Andronov-Hopf bifurcation exhibits two remarkable properties. First, the response of the system to an external excitation varies under certain conditions from linear to frequency selective and compressive [8, 18, 31, 34]. Second, the system can start to oscillate under certain conditions [48, 91]. Interestingly,

the latter property can be also observed in the cochlea. This is called otoacoustic emission and it is assumed to enhance the dynamical range of the cochlea [16, 67, 68, 83].

To mimic the second cochlea model, two approaches can be employed: On the one hand, frequency-selectivity is enabled by combing sub-wavelength resonators with metamaterials [6, 120, 145] or mimicking the geometry of the cochlea [25]. Metamaterials are synthetic materials, whose properties drastically differ from natural materials [6]. With these materials, the frequency components of external stimuli are separated. To enable a controllable Andronov-Hopf bifurcation, these frequency components are locally fed back [120]. On the other hand, an array consisting of bio-inspired oscillators, which exhibit at least an Andronov-Hopf bifurcation, can be used to mimic the physiology of the cochlea [130, 129]. These oscillators can be implemented, e.g., by a thermally actuated, cantilevered, microelectromechanical system (MEMS), whose deflection can be deduced by a piezoelectric strain gauge placed at the base of the MEMS [47, 62, 81]. These MEMSs can exhibit Andronov-Hopf bifurcations by designing an appropriate feedback loop for operation [80, 82, 81, 136, 147, 149, 150, 153, 155].

1.2. Scope of the Work

The present work is based on the preliminary work of the author in [147, 148, 149, 152, 153, 154, 155, 156]. The main goal is to design nonlinear controllers to tune the response of bio-inspired oscillators enabling the realization of neuromorphic acoustic sensors. On the one hand, controllers based on coupling oscillators or controlling a delayed feedback are analyzed. It is shown that these controllers enable controllable Andronov-Hopf bifurcations and that the characteristic frequencies can be adapted in the neighborhood of the critical point. On the other hand, signal processing in neuromorphic acoustic sensors is discussed by implementing an in-sensor Fourier transform. For this, the design of the sensor is either based on an array of oscillators, whose characteristic frequencies are constant and cover the desired frequency domain of the Fourier transform, or a single oscillator with a tunable characteristic frequency. In particular, the latter approach enables the design of superordinate controllers, which assign the sampled frequency. These controllers can be, e.g., based on sequential sampling or reinforcement learning.

To derive methods to design a nonlinear controller for bio-inspired oscillators, Andronov-Hopf oscillators are considered. These oscillators are based on the super-critical normal form of the Andronov-Hopf bifurcation. Hence, the Normal Form Theorem implies that any oscillator exhibiting a super-critical Andronov-Hopf bifurcation converges to a submanifold, which can be transformed by an isomorphism to the Andronov-Hopf oscillator, if the bifurcation parameter of the oscillator is in a neighborhood of the critical point [49]. Thus, this oscillator model can be seen as a benchmark oscillator model for neuromorphic acoustic sensing. To enable frequency tunability, networks of injectively coupled oscillators [154], two diffusively coupled oscillators [156], and an oscillator with a controllable delay [152] are analyzed. In addition, the in-sensor Fourier transform is implemented for an array of Andronov-Hopf oscillators [148].

To validate the results of the controller design, an oscillator model based on a thermally actuated MEMS introduced and considered in [47, 62, 81] is investigated. For this, the MEMS is modeled by an approximation of a continuum model consisting of a mechanical subsystem and a thermodynamic subsystem. This oscillator model is derived by employing the Rayleigh-Ritz method on the mechanical subsystem and the Galerkin method on the thermal subsystem and truncating the approximation after the first mode [155]. It is demonstrated that this oscillator model can exhibit Andronov-Hopf bifurcations, which are induced by a controllable feedback loop [153, 155]. Hence, this oscillator model can be used to verify the proposed controllers by analyzing the dynamic properties of the coupled MEMS [149] and MEMS with a delayed feedback [147].

1.3. Structure of the Work

The work is structured into fours part and seven chapters. A summary of the content is given subsequently.

The preliminaries for this work are introduced in Chapter 2. For this, the anatomy and physiology of the cochlea are summarized. This covers how frequency-selectivity and the compressive nonlinearity are induced by a nonlinear feedback loop. In addition, the mathematical preliminaries to analyze the local bifurcations of ordinary differential equations are introduced. The chapter is concluded by summarizing the Normal Form Theorem and some results of local bifurcations. Particularly, the emergence of Andronov-Hopf bifurcations and their remarkable properties are discussed in detail.

Part II: Controller Design for a Benchmark Oscillator Model for Neuromorphic Acoustic Sensors

In Part II, the design of controllers for benchmark oscillator models for neuromorphic acoustic sensors is proposed. For this, methods to control multiple Andronov-Hopf bifurcations and to enable frequency tunability, i.e., the characteristic frequency of an oscillator can be adjusted by a controllable input, are discussed. In addition, a superordinate controller is designed to demonstrate an application of frequency tunability in neuromorphic acoustic sensing. These results are discussed in two consecutive chapters.

In Chapter 3, the notion of frequency tunability and the Andronov-Hopf oscillator is introduced. Two controllers to enable frequency tunability for the benchmark oscillator model are discussed by analyzing the emergence of Andronov-Hopf bifurcations. First, it is shown that frequency tunability can be induced by coupling oscillators. This is done by analyzing small networks of injectively coupled oscillators and two diffusively coupled oscillators. In addition, the maximum and minimum number of controllable Andronov-Hopf bifurcations in networks of injectively coupled oscillators are analyzed. Second, the effects of a delayed feedback on the characteristic frequency of an Andronov-Hopf bifurcation are investigated.

An application for frequency tunability in neuromorphic acoustic sensors is discussed in Chapter 4. For this, an in-sensor Fourier transform is implemented by sampling the frequency domain using Andronov-Hopf oscillators. This approach exploits the frequency-selectivity and it is demonstrated that the frequency domain can be uniquely reconstructed, if the oscillators are frequency-selective. This implies that an array of oscillators exhibiting at least one Andronov-Hopf bifurcation can be used to enable the in-sensor Fourier transform, if their bifurcation parameter is in a neighborhood of the critical point. Finally, an algorithm based on untunable oscillators and two algorithms based on tunable oscillators are proposed to enable sampling of the frequency domain. In particular, more sophisticated methods than sequential sampling can be implemented by using tunable oscillators. For the scope of this work, an approach based on reinforcement learning is discussed.

Part III: A Neuromorphic Smart Sensing System

In Part III, a possible neuromorphic smart sensing system, which is centered around a MEMS, is introduced. For this, the mathematical model of this MEMS is derived and its dynamics are analyzed.

In Chapter 5, the MEMS is introduced. The system consists of a clamped-clamped MEMS, which can be actuated thermally. The continuum model of the MEMS is derived by separating the system into a mechanical subsystem and a thermodynamic subsystem. After that, the continuum model is simplified to a system of ordinary differential equations (ODEs) by applying the Galerkin and the Rayleigh-Ritz method, respectively, on the continuum model of the MEMS. The considered MEMS model is then derived after truncating the series expansion after one mode as acoustic signals are band limited. In particular, it is demonstrated that the mathematical model of the mechanical subsystem is governed by the Duffing equation.

The properties of the MEMS model are analyzed in Chapter 6. In particular, the analysis focuses on investigating the emergence of controllable Andronov-Hopf bifurcations and on verifying the predicted frequency tunability of the controller, which are designed for the benchmark oscillator model. For this, it is shown that the model of the MEMS has two Andronov-Hopf bifurcations. In addition, the frequency tunability is demonstrated by coupling two MEMS and controlling the pre-deflection of the MEMS with a geometric nonlinearity and a delay in the feedback loop.

Part VI: Conclusions and Outlook

Finally, some remarks conclude this thesis. The results of the thesis are summarized and a detailed outlook is given based on the results of the work and the ongoing work.

2. Preliminaries

Subsequently, the essential preliminaries for the control design to adapt the response of a neuromorphic acoustic sensor are discussed. For this, first the anatomy, physiology and the properties of the mammalian cochlea are summarized, which inspire the development of neuromorphic acoustic sensors. Secondly, the mathematical preliminaries for this work are introduced. Third, bifurcation theory is briefly discussed. This is done by introducing the Normal Form Theorem and analyzing the properties of the normal form of the Andronov-Hopf bifurcation. Finally, the subsequent chapters are motivated by introducing the Hopf Theorem.

2.1. Mammalian Hearing Perception

To process an acoustic signal in the brain,s a feedback loop between the cochlea and the nervous system is exploited. With this, an acoustic signal can be transduced into an electric signal by an adaptive and nonlinear response, so that a large operation regime for signal processing is obtained. Subsequently, the functionality and the setup of this feedback loop are explained by summarizing the anatomy and physiology of the cochlea. This description is based on standard literature, e.g., [50, 121].

The cochlea is a snail shell-like structure consisting of three tubes. These tubes are called scala tympani, scala media and scala vestibuli, which can be visualized by the uncoiled and laid out straight cochlea (see Figure 2.1). The scala vestibuli and the scala tympani are connected at the apex of the cochlea the so-called heliocotrema. In addition, the scala tympani and scala media are separated by the basilar membrane and the scala vestibuli and the scala media are separated by Reissner's membrane, respectively. Both membranes have ion pumps transferring potassium ions K^+ from the scala tympani and scala vestibuli to the scala media. The scala tympani and the scala vestibuli are filled with the so-called perilymph, which has a low potassium concentration so that both tubes have an electric potential of $-40\,\mathrm{mV}$. In contrast to this, the scala media is filled with the potassium rich endolymph resulting in an electric potential of $80\,\mathrm{mV}$. Moreover, there are hair cells and an additional membrane, the so-called tectorial membrane, inside of the scala media. These can be visualized by considering the cross-section of the scala media (see Figure 2.2). The hair cells are located on the basilar membrane and they have extensions, which are called stereocilia and are organized in bundles. In addition, the hair cells can be categorized into two different types: the inner and the outer hair cells. Subsequently, the anatomy of these two different types of hair cells is briefly explained.

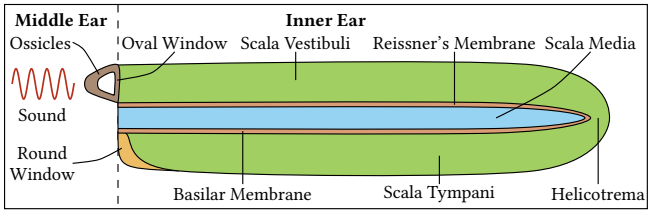

Figure 2.1.: Sketch of the laid out and uncoiled cochlea. (From Ref. [148], used under Creative Commons CC-BY license.)

The stereocilia of the inner hair cells have different lengths and the bundles of these stereocilla are arranged by increasing lengths, respectively. Additionally, the tip of the stereocilla is free and there is a mechanically gated K^+ channel at their tip. The gate of this channel is connected via the tip link to the larger neighbor of the stereocilia. If the stereocilla are not bent towards their larger neighbor, this channel is closed (see Figure 2.3a). The channel is opened by bending towards their larger neighbor. Then potassium ions K^+ are diffusing into the stereocilia resulting in a depolarization of the inner hair and thus an excitation of the cochlea nerve cells (see Figure 2.3b).

In comparison to the stereocilia of the inner hair cells, the bundles of stereocilia of the outer hair cells are arranged into a V-shape and their tip is connected to the tectorial membrane. Moreover, motor neurons are inside of these stereocilia enabling the nervous system to control the response of the cochlea. Hence, the response of the tectorial membrane and the sensitivity of the hair cells can be modulated, so that external stimuli are either attenuated or amplified.

The processing and transduction of an acoustic signal follows several steps: An acoustic signal is transferred by ossicles from the outer ear over the middle ear to the cochlea. As the flexibility and the width of the basilar membrane increases from the middle ear to the heliocotrema space, high frequency components of the external stimuli pass the basilar membrane close to the base of the cochlea, while low frequency components cross the basilar membrane close to the heliocotrema. This results in a frequency decomposition over space, which can be interpreted as a Fourier transform. These frequency components stimulate the hair cells by exciting the basilar membrane. In addition to the frequency decomposition, the feedback loop from the inner hair cells and tectorial membrane over

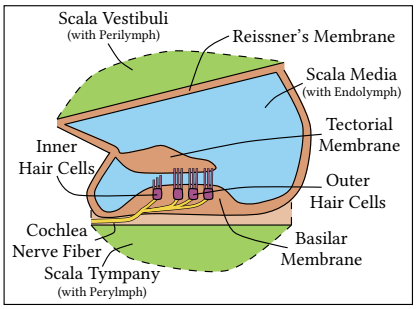

Figure 2.2.: Sketch of the cross-section of the cochlea. (From Ref. [148], used under Creative Commons CC-BY license.)

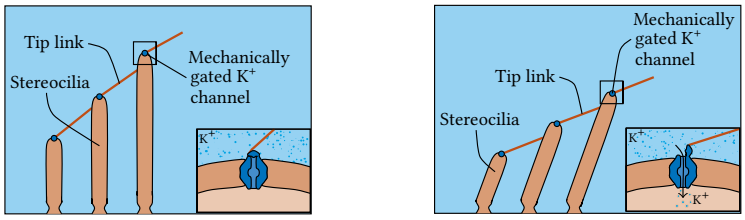

(a) Sketch of an unstimulated bundle of stereocilia with a magnification of a closed K^+ gate.

(b) Sketch of an stimulated bundle of stereocilia with a magnification of an open K^+ gate.

Figure 2.3.: Sketch of the depolarization mechanism of the inner hair cells-. Herein, the mechanically gated K^+ channel of the stereocilla is opened by bending towards their larger neighbor, resulting in a depolarization of the inner hair cells by the diffusion of potassium ions K^+. (From Ref. [148], used under Creative Commons CC-BY license.)

the neurons to outer hair cells enables high adaptability, so that the response can be tuned between a linear and nonlinear compressive regime, which can be utilized for two scenarios. On the one hand, a linear response can be exploited to process faint sound in (nearly) noiseless environments as the reconstruction of these signals can be directly deduced in this regime. On the other hand, a nonlinear, compressive response adds redundancy to the acoustic stimuli. This redundancy simplifies the separation of heavily distorted signals as multiple solutions support the reconstruction of the sound of one source [70].

2.2. Mathematical Preliminaries

In the following, the used notations and a summary of the local analysis of nonlinear ordinary differential equations (ODEs), together with an investigation of the normal form of the Andronov-Hopf bifurcation are provided. In particular, the latter model is the super-critical normal form of an Andronov-Hopf bifurcation.

2.2.1. Notation

The sets of numbers are given by the set of natural numbers without zero $\mathbb{N}$, the set of integers $\mathbb{Z}$, the set of rational numbers $\mathbb{Q}$, the set of real numbers $\mathbb{R}$, and the set of complex numbers $\mathbb{C}$. In addition, let $p, q \in \mathbb{Z}$ with $p < q$. Then an closed and open interval is denoted by $[p, q] = \{x \in \mathbb{R} \mid p \leq x \leq q\}$ and $(p, q) = \{x \in \mathbb{R} \mid p < x < q\}$, respectively. Restrictions on these sets of numbers are shown by a index. For instance, the set of natural numbers including zero is given by $\mathbb{N}_0 = \mathbb{N} \cup \{0\}$ and the set of real numbers larger than $a \in \mathbb{R}$ reads $\mathbb{R}_{\geq a} = [a, \infty)$. Furthermore, $\mathbb{K}^n$ and $\mathbb{K}^{n\times m}$ for any $n, m \in \mathbb{N}$ denote the space of vectors and matrices over the field of real and complex numbers $\mathbb{K} = \mathbb{R}, \mathbb{C}$. General variables are represented by lower case letters, e.g., $a \in \mathbb{K}$, vectors by boldface letters, e.g.,

$\boldsymbol{x} \in \mathbb{K}^n$, and matrices by capital letters, e.g., $A \in \mathbb{K}^{n\times m}$. Finally, vector-valued functions and polynomials are given by $f, g, h : \mathbb{R}^n \to \mathbb{R}^m$ and $P : \mathbb{R} \to \mathbb{R}$.

2.2.2. Local Analysis of Ordinary Differential Equations

As mentioned before, the local bifurcation can model the remarkable behavior of the cochlea. Henceforth, the local analysis of ODEs is briefly summarized. This introduction follows standard textbooks on nonlinear dynamics, e.g., [48, 76, 132].

In general, bifurcations describe a qualitative change of a trajectory of a system given by a differential equation or a system of coupled differential equations. Bifurcation theory is usually introduced for coupled, nonlinear ODEs. For this, let $n_1 \in \mathbb{N}$ $n_2 \in \mathbb{N}$ be the number of states, inputs and, outputs. Then a nonlinear system is in general given by

$$\dot{\boldsymbol{x}} = \boldsymbol{f}(\boldsymbol{x}; \mu), \qquad t > 0, \qquad \boldsymbol{x}(0) = \boldsymbol{x}_0, \tag{2.1a}$$

$$\boldsymbol{y} = \boldsymbol{h}(\boldsymbol{x}; \mu), \qquad t \geq 0 \tag{2.1b}$$

with the state vector $\boldsymbol{x}(t) \in \mathbb{R}^{n_1}$, the output vector $\boldsymbol{y}(t) \in \mathbb{R}^{n_2}$, the drift vector field $\boldsymbol{f}(\boldsymbol{x}; \mu) \in \mathbb{R}^{n_1}$, the measurement map $\boldsymbol{h}(\boldsymbol{x}; \mu) \in \mathbb{R}^{n_2}$, and the initial conditions $\boldsymbol{x}_0 \in \mathbb{R}^{n_1}$. The parameter $\mu \in \mathbb{R}$ takes the role of the so-called bifurcation parameter, whose values are subsequently used to express the resulting variations of the dynamical behavior of the nonlinear system. In addition, a solution of the system (2.1) is called the flow $\boldsymbol{x} = \boldsymbol{\phi}_t(\boldsymbol{x}_0)$.

Theorem 2.1 (Local Existence and Uniqueness [71]) *Let $\boldsymbol{f}(\boldsymbol{x})$ satisfy the Lipschitz condition*

$$\|\boldsymbol{f}(\boldsymbol{x}) - \boldsymbol{f}(\boldsymbol{y})\| \leq L\|\boldsymbol{x} - \boldsymbol{y}\| \tag{2.2}$$

for all $\boldsymbol{x}, \boldsymbol{y} \in \mathcal{U} = \{\boldsymbol{x} \in \mathbb{R}^{n_1} \mid \|\boldsymbol{x} - \boldsymbol{x}_0\|\}$ with a norm $\|\cdot\|$. Then, there exists some $\delta > 0$ such that the state equation $\dot{\boldsymbol{x}} = \boldsymbol{f}(\boldsymbol{x})$ with $\boldsymbol{x}(0) = \boldsymbol{x}_0$ has a unique solution for $t \in [0, \delta]$.

Remark 2.1 *By asserting that the drift vector field $\boldsymbol{f}(\boldsymbol{x}; \mu)$ is locally continuously differentiable, it is satisfied that the solution of* (2.1) *is locally unique and exists, since local continuous differentiability is a stronger condition than local Lipschitz continuity given by* (2.2)*. In particular, this property simplifies the analysis of local existence and uniqueness of* (2.1) *as it is easier to show that a vector field is continuously differentiable.*

To analyze local bifurcations, the local properties of a nonlinear system have to be analyzed. This analysis is usually structured in three steps: First, the equilibria of the system are derived. Second, the nonlinear system is linearized around the equilibria. Third, the stability of this equilibrium is analyzed. Thus, these notions starting with the notion of an equilibrium are introduced as follows.

Definition 2.1 (Equilibrium [48]) *Denote $\boldsymbol{x}_{\text{eq}} \in \mathbb{R}^{n_1}$ as the equilibrium of the state vector. The nonlinear system* (2.1) *is said to have an equilibrium $\boldsymbol{x}_{\text{eq}}$, if the rate of change $\dot{\boldsymbol{x}}$ vanishes at this point, i.e., $\dot{\boldsymbol{x}}_{\text{eq}} = 0$.*

As elaborated earlier, after deriving the equilibria the system can be linearized around it. This can be done by computing the Jacobian of the drift vector field and the measurement map with respect to the state vector $\boldsymbol{x}$ and the input vector $\boldsymbol{u}$.

Theorem 2.2 (Linearization [48]) *Let $\boldsymbol{x}_{\text{eq}} \in \mathbb{R}^{n_1}$ be an equilibrium of* (2.1)*. Then the nonlinear system* (2.1) *can be represented by the linear ODE system*

$$\Delta\dot{\boldsymbol{x}} = A\Delta\boldsymbol{x}, \tag{2.3a}$$

$$\Delta\boldsymbol{y} = C\Delta\boldsymbol{x} \tag{2.3b}$$

in a neighborhood of the equilibrium $\boldsymbol{x}_{\text{eq}}$ with the error state vector $\Delta\boldsymbol{x}(t) = \boldsymbol{x}(t) - \boldsymbol{x}_{\text{eq}} \in \mathbb{R}^{n_1}$ and the shifted output vector $\Delta\boldsymbol{y}(t) = \boldsymbol{y} - \boldsymbol{y}_{\text{eq}} \in \mathbb{R}^{n_2}$. Herein, the system matrix A and the output matrix C are given by

$$A = \frac{\partial \boldsymbol{f}}{\partial \boldsymbol{x}}(\boldsymbol{x}_{\text{eq}}) \in \mathbb{R}^{n_1 \times n_1}, \tag{2.4a}$$

$$C = \frac{\partial \boldsymbol{h}}{\partial \boldsymbol{x}}(\boldsymbol{x}_{\text{eq}}) \in \mathbb{R}^{n_2 \times n_1} \tag{2.4b}$$

Note that the flow of the linearization (2.3) is given by $\boldsymbol{\phi}_t(\boldsymbol{x}) = \mathrm{e}^{At}\boldsymbol{x}$, if the input matrix vanishes, i.e., $B = 0$, and it is usually derived by diagonalizing the system matrix A. This is done by computing the eigenvalues and (generalized) eigenvectors.

Definition 2.2 (Eigenvalue Problem [48]) *Assume $n \in \mathbb{N}$ and let $A \in \mathbb{R}^{n\times n}$ be a matrix, $\boldsymbol{w} \in \mathbb{C}_i^n \setminus \{0\}$ a non-negative vector and $\lambda_i \in \mathbb{C}$ a scalar for all $i = 1, \ldots, n$. Then the eigenvalue problem is given by*

$$A\boldsymbol{w}_i = \lambda_i \boldsymbol{w}_i. \tag{2.5}$$

Herein, $\boldsymbol{w}_i$ and λ_i are called eigenvector and eigenvalue of the matrix A. In addition, the space $\mathcal{E} = \operatorname{span}\{\boldsymbol{x}_1, \ldots, \boldsymbol{x}_n\}$ is called eigenspace.

In particular, the eigenvalue problem is solved by determining the zeros of the polynomial $P_A(\lambda)$

$$P_A(\lambda) = \det(A - \lambda I). \tag{2.6}$$

In addition, (2.5) implies that a diagonal element is given by multiplying an eigenvector to the system matrix. Thus, the flow is determined by

$$\boldsymbol{\phi}_t = W\mathrm{e}^{\Lambda t}W^{-1}\boldsymbol{x}_0$$

with the diagonal matrix $\Lambda = \operatorname{diag}(\lambda_1, \ldots, \lambda_n) = W^{-1}AW$, the transformation matrix $W = \begin{bmatrix}\boldsymbol{w}_1 & \ldots & \boldsymbol{w}_n\end{bmatrix}$, and the matrix exponential

$$\mathrm{e}^{\Lambda t} = \begin{bmatrix} \mathrm{e}^{\lambda_1 t} & 0 & \cdots & 0 \\ 0 & \mathrm{e}^{\lambda_2 t} & \cdots & 0 \\ \vdots & \vdots & \ddots & \vdots \\ 0 & 0 & \cdots & \mathrm{e}^{\lambda_n t} \end{bmatrix}. \tag{2.7}$$

Note that (2.7) implies that the eigenvalues of the systems matrix can be used to determine the stability of the linear system. Hence, the notion of asymptotic stability of a system governed by (2.1) is introduced in the following.

Definition 2.3 ([48]) *Let $\boldsymbol{x}(t) \in \mathbb{R}^n$ be the solution of* (2.1) *and denote the euclidean norm by $\|\cdot\|$. Then the system* (2.1) *is said to be asymptotically stable, if*

$$\lim_{t\to\infty} \|\boldsymbol{x}(t)\| = 0.$$

With these considerations, the (local) stability of an equilibrium $\boldsymbol{x}_{\text{eq}}$ can be characterized by the eigenvalues of the system matrix A as summarized subsequently.

Theorem 2.3 ([48]) *Let $\boldsymbol{x}_{\text{eq}} \in \mathbb{R}^{n_1}$ be an equilibrium of* (2.1). *In addition, denote the linearized system matrix of* (2.1) *at the equilibrium $\boldsymbol{x}_{\text{eq}}$ by $A \in \mathbb{R}^{n_1 \times n_1}$. Then the equilibrium $\boldsymbol{x}_{\text{eq}}$ is asymptotically stable, if all eigenvalues λ_i of the system matrix A have a negative real part, i.e.,* $\operatorname{Re} \lambda_i < 0$ *for all* $i = 1, \ldots, n_1$.

However, as the degree of the system increases, computing the eigenvalues directly becomes complicated numerically and analytically. For instance, following the Abel-Ruffini theorem, a general polynomial with a degree larger than 4 can not be solved analytically [10, 13]. Thus, other methods have to be applied to obtain this information. For example, the Routh-Hurwitz criterion can be used to obtain the number of eigenvalues on the left half and right half complex plane.

Theorem 2.4 (Routh-Hurwitz Criterion [85, 118]) *Let $n \in \mathbb{N}$ and consider the polynomial*

$$P(x) = a_n x^n + a_{n-1} x^{n-1} + a_{n-2} x^{n-2} + \cdots + a_1 x^1 + a_0$$

with the coefficients a_i for all $i = 0, 1, \ldots, n$. Denote by

$$\begin{array}{llll}
\Delta_{2,0} = \Delta_{0,0} - c_0 \Delta_{1,0}, & \Delta_{2,1} = \Delta_{0,1} - c_0 \Delta_{1,1}, & \cdots & \Delta_{2,k} = 0, \\
\Delta_{3,0} = \Delta_{1,0} - c_1 \Delta_{2,0}, & \Delta_{3,1} = \Delta_{1,1} - c_1 \Delta_{2,1}, & \cdots & \Delta_{3,k} = 0, \\
\vdots & \vdots & \ddots & \vdots \\
\Delta_{n,0} = \Delta_{n-2,0} - c_{n-1} \Delta_{n-1,0}, & \Delta_{n,1} = 0, & \cdots & \Delta_{n,k} = 0
\end{array}$$

with $\Delta_{0,i} = a_{n-2i}$, $\Delta_{1,i} = a_{n-2i-1}$, $c_j = \Delta_{j,0}/\Delta_{j+1,0}$, and $k = \lfloor n/2 + 1 \rfloor$ for[1] and $j = 0, 1, \ldots, n$ all $i = 0, 1, \ldots, \lfloor \frac{n}{2} \rfloor$. Then the number of zeros with positive real part are given by the number of sign changes of the series

$$\left(\Delta_{i,0}\right)_{i=0,1,\ldots n} = \left\{\Delta_{0,0}, \Delta_{1,0}, \ldots, \Delta_{n,0}\right\}.$$

[1] The floor function $\lfloor a \rfloor$ determines the greatest integer less than or equal to $a \in \mathbb{R}$.

It remains to be analyzed under which conditions the (local) behavior of (2.1) can be deduced from the properties its linearization given by (2.3). For this, assume that the system matrix A has an eigenvalue given by $\lambda = 0$ and that the remaining eigenvalues of A have a negative real-part. Then the linearization (2.3) is not asymptotically stable. However, it turns out that (2.1) can be asymptotically stable, if the nonlinear terms are stabilizing. Hence, the properties of the linearization cannot be used in general to deduce properties of the nonlinear system. This example is generalized by the Theorem of Hartman-Grobman.

Theorem 2.5 (Theorem of Hartman-Grobman [48]) *If the system matrix A has no eigenvalues located on the imaginary axis, then there is a homeomorphism h defined on some neighborhood $\mathcal{U}$ of the equilibrium $\boldsymbol{x}_{\mathrm{eq}} \in \mathbb{R}^{n_1}$ locally taking orbits of the nonlinear flow $\boldsymbol{\phi}_t(\boldsymbol{x})$ of* (2.1)*, to those of the linear flow $\mathrm{e}^{At}\boldsymbol{x}$ of* (2.3)*. The homeomorphism preserves the sense of orbits and can also be chosen to preserve parameterization by time.*

It follows from the Theorem of Hartman-Grobman (see Theorem 2.5) that the linearization of a system is only approximating the local dynamics of the nonlinear system if all eigenvalues have a non-vanishing real part, i.e., $\operatorname{Re} \lambda_i \neq 0$ for all $i = 1, \ldots, n$. Hence, the dynamics of a nonlinear system can be then divided into three different manifolds by using the results of Theorem 2.5, i.e., the manifolds are separated into a locally stable manifold $\mathcal{W}^{\mathrm{s}}$ for the eigenvalues with negative real-part, a locally unstable manifold $\mathcal{W}^{\mathrm{u}}$ for the eigenvalues with positive real-part and a center manifold $\mathcal{W}^{\mathrm{z}}$ for the eigenvalues with zero real-part. This separation is done by using the eigenvectors of the system matrix A as a state transformation of the nonlinear system (2.1). Then the linearization can be used to deduce the dynamic properties of the stable and the unstable manifolds. This claim is summarized by the Center Manifold Theorem as elaborated subsequently.

Theorem 2.6 (Center Manifold Theorem [48]) *Consider the system* (2.1) *with an equilibrium $\boldsymbol{x}_{\mathrm{eq}} \in \mathbb{R}^{n_1}$ and divide the spectrum of A into three parts, σ_{s}, σ_{z}, σ_{u} with*

$$\begin{aligned} \sigma_{\mathrm{s}} &= \{\lambda \in \sigma \mid \operatorname{Re} \lambda < 0\}, \\ \sigma_{\mathrm{z}} &= \{\lambda \in \sigma \mid \operatorname{Re} \lambda = 0\}, \\ \sigma_{\mathrm{u}} &= \{\lambda \in \sigma \mid \operatorname{Re} \lambda > 0\}. \end{aligned}$$

Let the eigenspaces of σ_{s}, σ_{z}, and σ_{u} be $\mathcal{E}^{\mathrm{s}}$, $\mathcal{E}^{\mathrm{z}}$ and $\mathcal{E}^{\mathrm{u}}$, respectively. Then there exists a stable and an unstable invariant manifold $\mathcal{W}^{\mathrm{s}}$ and $\mathcal{W}^{\mathrm{u}}$ tangent to $\mathcal{E}^{\mathrm{s}}$ and $\mathcal{E}^{\mathrm{u}}$ at $\boldsymbol{x}_{\mathrm{eq}}$ and a center manifold $\mathcal{W}^{\mathrm{z}}$ tangent to $\mathcal{E}^{\mathrm{z}}$. The manifolds $\mathcal{W}^{\mathrm{s}}$, $\mathcal{W}^{\mathrm{z}}$, and $\mathcal{W}^{\mathrm{u}}$ are all invariant for the flow of $\boldsymbol{f}$. The stable and unstable manifolds are unique, but $\mathcal{W}^{\mathrm{z}}$ may not be.

In comparison to the stable manifold $\mathcal{W}^{\mathrm{s}}$ and the unstable manifold $\mathcal{W}^{\mathrm{u}}$, the center manifold $\mathcal{W}^{\mathrm{z}}$ might represent a normal form of a bifurcation. For instance, the necessary condition of a Andronov-Hopf bifurcation are two complex conjugated eigenvalues with zeros real part, i.e., $\operatorname{Re} \lambda = \operatorname{Re} \lambda^* = 0$ [48]. Thus, it is necessary to analyze the properties of this manifold. For instance, the stability of a nonlinear system at this critical point has to be analyzed in the subsequent chapters. This can be done, e.g., by applying Lyapunov's direct method.

Theorem 2.7 (Lyapunov's Direct Method [71]) *Consider the system* (2.1) *and assume that the equilibrium of* (2.1) *is given by* $\boldsymbol{x}_{\mathrm{eq}} = \mathbf{0}$. *In addition, denote the Lyapunov function candidate by* $V(\boldsymbol{x}) \in \mathbb{R}$ *for* $x \in \mathcal{D} \subset \mathbb{R}^n$. *Let* $V(\boldsymbol{x})$ *be positive definite, i.e.,* $V(\boldsymbol{x}) > 0$ *for all* $\boldsymbol{x} \in \mathcal{D} \setminus \{\mathbf{0}\}$ *and* $V(\mathbf{0}) = 0$. *Then the system is asymptotically stable, if the rate of change of the Lyapunov function along the solution trajectory* $\boldsymbol{x}$ *is negative definite, i.e.,* $\frac{\mathrm{d}V}{\mathrm{d}t} < 0$ *for all* $\boldsymbol{x} \in \mathcal{D} \setminus \{\mathbf{0}\}$.

Note that the condition on the equilibrium, i.e., $\boldsymbol{x}_{\mathrm{eq}} = \mathbf{0}$, is easily satisfied by introducing a linear coordinate shift, e.g., $\Delta\boldsymbol{x} = \boldsymbol{x} - \boldsymbol{x}_{\mathrm{eq}}$ with the state vector $\boldsymbol{x} \in \mathbb{R}^n$, the equilibrium $\boldsymbol{x}_{\mathrm{eq}} \in \mathbb{R}^n$ and the shifted state vector $\Delta\boldsymbol{x} \in \mathbb{R}^n$.

2.2.3. Introduction into Local Bifurcations

Subsequently, the Andronov-Hopf bifurcation is introduced by analyzing the respective normal form and its properties. The main idea of bifurcation theory is to analyze simple nonlinear systems, which are called normal forms, and to determine conditions, so that a more complicated nonlinear system can be reduced to these normal forms. For this, the Center Manifold Theorem (see Theorem 2.6) has to be employed first to reduce the order of the nonlinear system. Then the so-called Normal Form Theorem can be exploited to transform the sub-manifold of the nonlinear system to the normal form.

Theorem 2.8 (Normal Form Theorem [49, 51]) *Assume that an equilibrium of* (2.1) *is given by* $\boldsymbol{x}_{\mathrm{eq}} = \mathbf{0}$. *Then there are polynomials* $U(\boldsymbol{x};\mu) \in \mathbb{R}^{n_1}$ *and* $g(\boldsymbol{x};\mu) \in \mathbb{R}^{n_1}$ *of degree* k *with* $U(\mathbf{0};0) = \frac{\partial U}{\partial \boldsymbol{x}}(\mathbf{0};0) = 0$ *such that by the change of variables* $\boldsymbol{x} \longrightarrow \boldsymbol{x} + U(\boldsymbol{x};\mu)$, (2.1) *becomes*

$$\dot{\boldsymbol{x}} = A\boldsymbol{x} + g(\boldsymbol{x};\mu) + O\left(\|[\boldsymbol{x}^{\mathrm{T}},\mu]\|^{k+1}\right)$$

with a norm $\|\cdot\|$. *In addition,* g *satisfies* $g(\boldsymbol{x};\boldsymbol{\mu}) = g(\mathrm{e}^{tA}\boldsymbol{x};\boldsymbol{\mu})$ *for all* $\boldsymbol{x} \in \mathbb{R}^{n_1}$, $\mu \in \mathbb{R}$, *and* $t > 0$.

As elaborated previously, the dynamics of the cochlea can be modeled by a system exhibiting an Andronov-Hopf bifurcation, since it is frequency-selective and compressive in the sub-critical regime. Thus, this bifurcation is briefly discussed. This is done as follows: First, the formal definition of an Andronov-Hopf bifurcation is provided by introducing its normal form. Then, the steady state of the harmonically excited normal form of the Andronov-Hopf bifurcation in the sub-critical regime is analyzed. Finally, the Hopf-Theorem in $\mathbb{R}^n$ is considered, which gives conditions to prove that a general nonlinear system exhibits an Andronov-Hopf bifurcation.

To visualize the properties of an Andronov-Hopf bifurcation, consider its (super-critical) normal form

$$\dot{z} = (\mu + \mathrm{i}\omega)z - |z|^2 z + u, \qquad z(0) = z_0, \qquad t > 0 \tag{2.8}$$

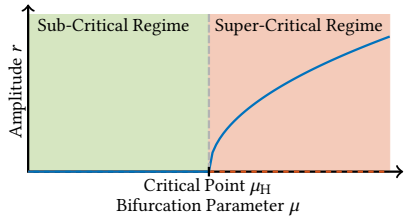

Figure 2.4.: Sketch of the bifurcation diagram of the normal form of the Andronov-Hopf bifurcation given by (2.8). Herein, the amplitude r of the emerging limit cycle is given as a function of the bifurcation parameter μ.

with the state $z(t) \in \mathbb{C}$, the external input $u(t) \in \mathbb{C}$ and the initial conditions $z_0 \in \mathbb{C}$. Additional parameters are given by the damping coefficient $\mu \in \mathbb{R}$ and the (angular) frequency $\omega > 0$. To induce a bifurcation, the damping coefficient μ is assumed to be the bifurcation parameter and the critical point is given by $\mu_H = 0$.

For now, assume that $u = 0$ holds true. Then the system (2.8) has a unique, asymptotically stable equilibrium z_{eq}, if $\mu \leq 0$. In contrast to this, if $\mu > 0$, a stable limit cycle emerges. After transients have decayed, the amplitude of this limit cycle is derived by inserting $z = re^{i(\omega t+\varphi)}$ with the amplitude $r > 0$ and the phase $\varphi \in [0, 2\pi)$ of the limit cycle into (2.8). This implies $r = \sqrt{\mu}$. To visualize this, bifurcation diagrams can be used. The bifurcation diagram of the Andronov-Hopf bifurcation is obtained by depicting the relationship between the amplitude r of the limit cycle and the bifurcation parameter μ (see Figure 2.4).

To show the frequency selective and compressive behavior of the Andronov-Hopf bifurcation, the harmonically excited normal form is considered, i.e., the input is given by $u = F_{ex}e^{i(\omega_{ex}t+\varphi_{ex})}$ with the amplitude $F_{ex} > 0$, the phase $\varphi_{ex} \in [0, 2\pi)$, and the frequency ω_{ex}. Assuming that the state z is given by $z = qe^{i\omega_{ex}t}$ with the envelope $q(t) \in \mathbb{C}$ and inserting this assumption into (2.8) yields

$$\dot{q} = (\mu + i\omega_\Delta)q - |q|^2 q + F_{ex}e^{i\varphi_{ex}} \tag{2.9}$$

with the frequency difference $\omega_\Delta = \omega - \omega_{ex}$. Note that the equilibrium of (2.9) yields the amplitude of the harmonically excited normal form. After inserting $\dot{q}_{eq} = 0$, and separating absolute value and phase, i.e., $q_{eq} = r_{eq}e^{i\varphi_{eq}}$ with the amplitude $r_{eq} \in \mathbb{R}$ and the phase $\varphi_{eq} \in [-\pi, \pi)$, the following conditions arise

$$0 = r_{eq}^6 - 2\mu r_{eq}^4 + [\mu^2 + \omega_\Delta^2]r_{eq}^2 - F_{ex}^2, \tag{2.10a}$$

$$\varphi_{eq} = \arctan\left[\frac{\sqrt{\mu^2 + \omega_\Delta^2}\sin(\varphi)}{r_{eq}^2 - \sqrt{\mu^2 + \omega_\Delta^2}\cos(\varphi)}\right] + \varphi_{ex} \tag{2.10b}$$

with the phase $\varphi = \arctan(\omega_\Delta/\mu)$. In particular, the two equations of (2.10) are cascaded, so that amplitude r_{eq} can be determined independent from the phase φ_{eq}. Eq. (2.10a) is analyzed by substituting $x_{eq} = r_{eq}^2$. Then a cubic polynomial arises, which is investigated using the subsequent proposition.

Proposition 2.1 ([100]) *Consider a cubic polynomial given by* $P = x^3 + a_2x^2 + a_1x + a_0$. *Then the number of real-valued zeros of* P *is determined by*

$$D_{P,x} \begin{cases} > 0, & P \text{ has 1 real root,} \\ = 0, & P \text{ has 3 real roots and 2 roots are equal,} \\ < 0, & P \text{ has 3 different, real roots.} \end{cases} \tag{2.11a}$$

with the polynomial discriminant

$$D_{P,x} = \left(\frac{p}{3}\right)^3 + \left(\frac{q}{2}\right)^2. \tag{2.11b}$$

and the coefficients

$$p = \frac{3a_1 - a_2^2}{3}, \tag{2.11c}$$

$$q = \frac{9a_2a_1 - 27a_0 - 2a_2^3}{27}. \tag{2.11d}$$

With this, the parameters for the polynomial discriminant are given by

$$p_{\mathrm{H}} = \frac{\omega_\Delta^2 - \mu^2}{3}, \qquad q_{\mathrm{H}} = \frac{2\mu^3 + 18\mu\omega_\Delta^2 - 27F_{\mathrm{ex}}}{27}.$$

Inserting these expressions into (2.11b), yields

$$D_{\mathrm{H},r_{\mathrm{eq}}} = \frac{F_{\mathrm{ex}}^2}{4} + \frac{\omega_\Delta^6 + 78\omega_\Delta^4\mu^2 + 21\omega_\Delta^2\mu^4 - 27\mu^3F_{\mathrm{ex}} - 243\omega_\Delta^2\mu F_{\mathrm{ex}}}{729}. \tag{2.12}$$

In particular, (2.12) is positive, i.e., $D_{\mathrm{H},r_{\mathrm{eq}}} > 0$, if the bifurcation parameter $\mu \leq 0$. This implies that the steady state of (2.8) with harmonic excitation is unique in the sub-critical regime. To visualize the linear and nonlinear response of (2.8), the amplitude r_{eq} and the phase φ_{eq} in terms of the frequency difference $\Delta\omega$ are depicted in Figure 2.5, respectively. Here, the natural frequency and the bifurcation parameter are assumed to be $\omega = 20\,\frac{1}{\mathrm{s}}$, $\mu = -5\,\frac{1}{\mathrm{s}}$ for the linear response, and $\mu = 0\,\frac{1}{\mathrm{s}}$ for the nonlinear response. In particular, this normal form has a drastic change from a linear response to a frequency-selective, compressive response.

This nonlinear response can also be interpreted in terms of the shift of the critical point μ_{H}. This is shown by inserting $\Delta q = q - q_{\mathrm{eq}}$ into (2.9) and simplifying the absolute value squared by $|x|^2 = x \cdot x^*$ with a complex number $x \in \mathbb{C}$ and its complex conjugate x^*. This results in the shifted system, which is governed by

$$\Delta\dot{q} = \left[\mu - 2|q_{\mathrm{eq}}|^2 + \mathrm{i}\Delta\omega\right]\Delta q - q_{\mathrm{eq}}^2\Delta q^* - 2q_{\mathrm{eq}}|\Delta q|^2 - q_{\mathrm{eq}}^*\Delta q^2 - |\Delta q|^2\Delta q. \tag{2.13}$$

After linearizing (2.13) around q_{eq}, the system matrix is given by $A = \mu - 2|q_{\mathrm{eq}}|^2 + \mathrm{i}\Delta\omega$, so that the critical point reads $\mu_{\mathrm{H}} = 2|q_{\mathrm{eq}}|^2$. This implies that the gain of (2.8) is attenuated more for a larger excitation amplitude resulting in a compressive response. In addition, if

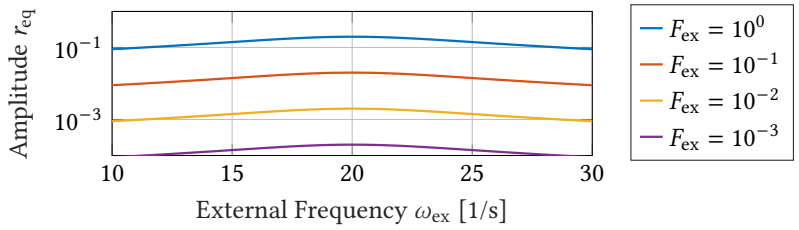

(a) Amplitude response of the normal form of the Andronov-Hopf bifurcation in linear regime.

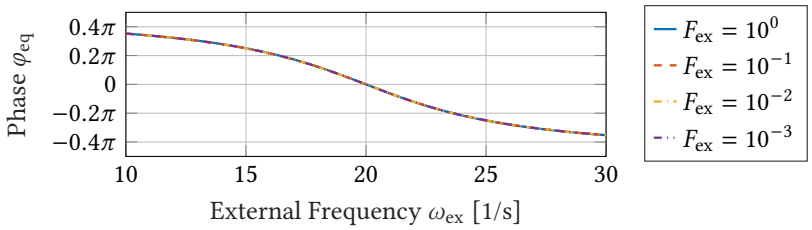

(b) Phase response of the normal form of the Andronov-Hopf bifurcation in linear regime.

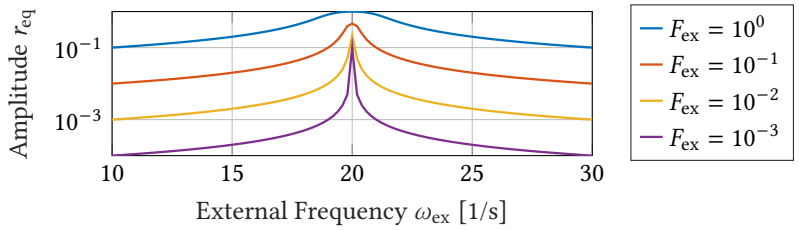

(c) Amplitude response of the normal form of the Andronov-Hopf bifurcation in nonlinear regime.

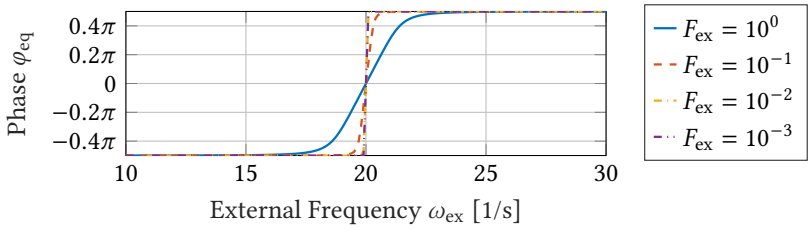

(d) Phase response of the normal form of the Andronov-Hopf bifurcation in nonlinear regime.

Figure 2.5.: Amplitude and phase of (2.8) in terms of the external frequency ω_{ex}.

the gain of (2.8) for large amplitude has to be increased, the system (2.8) has to be operated at a sufficiently large $\mu > 0$. This results in the emergence of a limit cycle, if the excitation decreases quickly and the emergence of otoacoustic emissions in the cochlea, i.e., acoustic stimuli induced by the stereocilla of the outer hair cells [72, 89, 138], can be explained in principle.

To conclude this chapter, the Hopf Theorem in $\mathbb{R}^n$ and the Normal Form Theorem are summarized. Following this theorem, it can be shown that nonlinear ODE posses an Andronov-Hopf bifurcation.

Theorem 2.9 (Hopf Theorem in $\mathbb{R}^n$ [48, 76, 91]) *Suppose that the system* (2.1) *has an unique equilibrium* $(\boldsymbol{x}_{\mathrm{eq}}, \mu_{\mathrm{H}})$ *fulfilling*

(H1) The system matrix $A(\mu_{\mathrm{H}})$ *has a simple pair of pure imaginary eigenvalues and no other eigenvalues with zero real part. This implies that there is a smooth curve of equilibria* $(\boldsymbol{x}_{\mathrm{eq}}(\mu), \mu)$ *with* $\boldsymbol{x}_{\mathrm{eq,H}} = \boldsymbol{x}_{\mathrm{eq}}(\mu_{\mathrm{H}})$*. The eigenvalues* $\lambda(\mu)$ *and* $\lambda(\mu)^*$ *of* $A(\mu)$ *which are imaginary at* $\mu = \mu_{\mathrm{H}}$ *vary smoothly with* μ*.*

(H2) If

$$\frac{\mathrm{d}}{\mathrm{d}\mu}\left(\mathrm{Re}\ \lambda(\mu)\right)|_{\mu=\mu_{\mathrm{H}}} = d \neq 0, \tag{2.14}$$

then there is a unique three-dimensional center manifold passing through $(\boldsymbol{x}_{\mathrm{eq}}(\mu), \mu)$ *in* $\mathbb{R}^{n_1} \times \mathbb{R}$ *and a smooth system of coordinates (preserving the planes* $\mu = \mathrm{const.}$*) for which the Taylor expansion of degree 3 on the center manifold is given by*

$$\dot{x} = [d\mu_\Delta + a(x^2 + y^2)]x - [\omega + c\mu_\Delta + b(x^2 + y^2)]y, \tag{2.15a}$$

$$\dot{y} = [\omega + c\mu_\Delta + b(x^2 + y^2)]x + [d\mu_\Delta + a(x^2 + y^2)]y \tag{2.15b}$$

with the characteristic frequency $\omega > 0$*, the difference* $\mu_\Delta = \mu - \mu_{\mathrm{H}}$ *and the parameters* $a, b, c \in \mathbb{R}$*.*

(H3) If $a \neq 0$*, there is a surface of periodic solutions in the center manifold, which has quadratic tangency with the eigenspace of* $\lambda(\mu_{\mathrm{H}})$*,* $\lambda(\mu_{\mathrm{H}})^*$ *agreeing to second order with the paraboloid* $\mu = -(a/d)(x^2 + y^2)$*. If* $a < 0$*, then these periodic solutions are stable limit cycles, while if* $a > 0$*, the periodic solutions are repelling.*

Remark 2.2 *The stability criterion (H3) is easily shown by analyzing the stability in the critical point: If the system at this point is asymptotically stable, the parameter a is negative , i.e.,* $a < 0$*. Otherwise, the parameter a is positive, i.e.,* $a > 0$ *[91]. For instance, this can be verified by applying the Center Manifold Theorem (see Theorem 2.6) or Lyapunov's Direct Method (see Theorem 2.7).*

Remark 2.3 *Note that a system satisfying Theorem 2.9 converges to a sub-manifold, which is described by* (2.8)*. Therefore, the normal form* (2.8) *can be used as a benchmark model for oscillators, which mimic the functionality of the cochlea.*

Remark 2.4 *Note that the center manifold* (2.15) *can be transformed into the polar coordinates using the amplitude* $r^2 = x^2 + y^2$ *and phase* $\tan(\phi) = y/x$*. The resulting expressions read*

$$\dot{r} = (d\mu + ar^2)r, \tag{2.16a}$$

$$\dot{\phi} = \omega + c\mu + br^2. \tag{2.16b}$$

In particular, the stability criterion (H3) directly follows by analyzing the slope of (2.16a) *at the critical point* $\mu_{\mathrm{H}} = 0$. *In addition, the center manifold* (2.15) *has the form* (2.8) *such that the results of the analysis of the normal form also hold locally for any system satisfying Theorem 2.15. Hence, the functionality of a cochlea can be mimicked by designing a system, which satisfies Theorem 2.15.*

Remark 2.5 *In principle, an Andronov-Hopf bifurcation will also emerge in partial differential equations (PDEs) and delayed differential equations (DDEs), if Theorem 2.9 is satisfied. However, as these equations are infinite dimensional, there can be additional conditions, so that a linearization exists and the spectrum of the linearized operator can be used to solve this equation. For instance, these conditions are elaborated for PDEs in [91] and for DDEs in [95, 126].*

Part II.

Controller Design for a Benchmark Oscillator Model for Neuromorphic Acoustic Sensors

3. Adapting the Response of Benchmark Oscillators

Subsequently, controllers are designed to enhance the tunability of the characteristic frequency of an oscillator, while preserving a controllable Andronov-Hopf bifurcation. For this, it is assumed that the characteristic frequency of the oscillator is constant and that the oscillator already exhibits a controllable Andronov-Hopf bifurcation. The tunability enhancements can be, e.g., utilized for oscillators in a neuromorphic acoustic sensing. These are used to measure a frequency band of an external stimuli, since the oscillators act as band pass filters. With this, the frequency response of the external stimuli can be reconstructed with an array of these oscillators. However, many oscillators are needed for this reconstruction, if the bandwidth of the oscillators is small. The number of oscillators in an array can be reduced by asserting that the characteristic frequency of the oscillator can be adjusted, since the oscillators can sample multiple frequency bands. This approach is further discussed in Chapter 4. The notion of frequency tunability is introduced in the following.

Definition 3.1 (Frequency Tunability [149, 152]) *An oscillator or a network of oscillators is called frequency tunable if its characteristic frequency (or synchronization frequency, i.e., the common frequency in an oscillator network at which the oscillators align, respectively) can be changed by a controllable input. In addition, the parameter controlling the frequency tunability of the oscillator or network of oscillators is called (frequency) tunability parameter.*

Remark 3.1 *In particular, the term frequency glides (or frequency modulation, respectively) refers to a similar observation in the cochlea [19, 29, 97, 109, 123]. It is defined as frequency variations in the impulse response of the basilar membrane [29, 109] and the auditory nerve cells [19]. It should be noted that frequency glides cannot be induced by the nonlinearities in the cochlea, since the frequency glides are invariant to intensity of the stimuli [19, 29, 97, 109]. Hence other mechanisms, e.g., traveling-wave dispersion [123], might cause this effect.*

With these considerations, two different types of parameters can be identified for an oscillator exhibiting an Andronov-Hopf bifurcation: First, the tunability parameters to tune the characteristic frequency of an oscillator and secondly the bifurcation parameters to control either the response and amplification of the oscillator in the sub-critical regime or the amplitude of the limit cycle in the super-critical regime. To analyze the principle of frequency tunability, the following assumptions are asserted on the oscillator of the neuromorphic sensor:

(A3.1) Let n be the number of oscillators. Then the oscillators are assumed to be Andronov-Hopf oscillators. The dynamics of the i-th oscillator can be described by either the complex-valued representation

$$\dot{z}_i = (\mu_i + \mathrm{i}\omega_i) z_i - |z_i|^2 z_i, \qquad z_i(0) = z_{i,0}, \qquad t > 0 \tag{3.1}$$

or their real-valued representation

$$\dot{\boldsymbol{x}}_i = \begin{bmatrix} \mu_i & -\omega_i \\ \omega_i & \mu_i \end{bmatrix} \boldsymbol{x}_i - \begin{bmatrix} (x_1^2 + x_2^2) x_{1,i} \\ (x_1^2 + x_2^2) x_{2,i} \end{bmatrix} \boldsymbol{x}_i, \quad \boldsymbol{x}_i(0) = \boldsymbol{x}_{i,0}, \quad t > 0 \tag{3.2}$$

with the states $z_i(t) \in \mathbb{C}$ or $\boldsymbol{x}_i(t) \in \mathbb{R}^2$ and the initial conditions $z_{i,0} \in \mathbb{C}$ or $\boldsymbol{x}_{i,0} \in \mathbb{R}^2$, respectively, for all $i = 1, \ldots, n$. The parameters are given by the damping coefficient $\mu_i \in \mathbb{R}$ and the natural frequency $\omega_i > 0$.

(A3.2) The natural frequency ω_i is constant and, hence, cannot be tuned directly.

In particular, following the Normal Form Theorem (see Theorem 2.8) and the Hopf Theorem (see Theorem 2.9) Assumption (A3.1) is valid for any system, whose bifurcation parameter is in the neighborhood of the critical point of its Andronov-Hopf bifurcation. Thus, the investigation of the frequency tunability can be simplified by analyzing controllers acting on the Andronov-Hopf oscillator (3.1) or (3.2). To validate the control design, the results are extended in a Chapter 6 to an oscillator model, which represents a candidate to enable neuromorphic acoustic sensing. In addition, the system representation of (3.1) and (3.2) are equivalent as (3.1) can be transformed into (3.2) by using $\boldsymbol{x} = [\mathrm{Re}\, z, \mathrm{Im}\, z]^{\mathrm{T}}$. The inverse of this transformation is given by $z = x_1 + \mathrm{i}x_2$. However, the analysis of (3.1) and (3.2) differ, such that the choice of the representation is crucial for the bifurcation and tunability analysis. In contrast to this, Assumption (A3.2) has to be asserted, since the frequency tunability of the individual oscillator could not be enhanced otherwise.

The tunability enhancements in this chapter can be divided into two different methods:

1. Multiple oscillators are coupled together. Then the tunability parameter is a function of the damping coefficient and the bifurcation parameter is a function of the coupling strengths.
2. A delayed feedback is introduced to the oscillators. With this, the tunability parameter is a function of the instantaneous damping, delayed damping coefficient, and the delayed frequency. In contrast, the bifurcation parameter is the time delay.

Finally, the proof of the frequency tunability can be done by determining the eigenvalues of the system. However, this cannot be done analytically for systems with an order greater than 4 since the Theorem of Abel-Ruffini is violated [10, 13]. The analysis of the frequency tunability is subsequently simplified by proving that the investigated system satisfies the Hopf Theorem (see Theorem 2.9). With this, the tunability is shown by analyzing the characteristic frequency at the critical point.

3.1. Coupled Oscillators

The idea to enable frequency tunability by coupling is motivated by the consensus and synchronization between non-identical oscillators. For instance, two coupled Kuramoto oscillators with different frequencies synchronize at a common frequency, if the coupling strength is strong enough. In particular, this common frequency is given as a function of the frequencies of these oscillators and the asymmetry between the coupling [132]. This is subsequently elaborated in more detail.

Example 3.1 ([149]) *Kuramoto oscillators are coupled phase models of an oscillator with constant frequency. Subsequently, tunability of two coupled Kuramoto oscillators is induced by varying the coupling. These two oscillators are governed by*

$$\dot{\phi}_1 = \omega_1 + \gamma_{12}\sin(\phi_2 - \phi_1), \qquad t>0, \qquad \phi_1(0) = \phi_{1,0}, \tag{3.3a}$$

$$\dot{\phi}_2 = \omega_2 + \gamma_{21}\sin(\phi_1 - \phi_2), \qquad t>0, \qquad \phi_2(0) = \phi_{2,0} \tag{3.3b}$$

with the phases $\phi_1(t), \phi_2(t) \in \mathbb{R}$ and the initial conditions $\phi_{1,0}, \phi_{2,0} \in \mathbb{R}$ [132]. The parameters are given by the coupling coefficients $\gamma_{12}, \gamma_{21} \in \mathbb{R}$ and the frequencies $\omega_1, \omega_2 > 0$. In addition, assume that the frequencies ω_1 and ω_2 are fixed, while the coupling coefficients γ_{12} and γ_{21} are assumed to be controllable and hence serve as the tunability parameters. Tunability of (3.3) *is investigated by analyzing the properties of the synchronized system, i.e., $\dot{\phi}_{\text{sync}} = \nu_{\text{sync}}(\gamma_{12}, \gamma_{21})$ with the synchronization frequency $\nu_{\text{sync}}(\gamma_{12}, \gamma_{21}) > 0$. In particular, the synchronized system is determined by computing the steady state of the phase error $\Delta\phi_{12} = \phi_1 - \phi_2$, which results in*

$$\Delta\dot{\phi}_{12} = \omega_1 - \omega_2 - (\gamma_{12} + \gamma_{21})\sin(\Delta\phi_{12}).$$

Asserting $\Delta\dot{\phi}_{12,\text{eq}} = 0$, yields the conditions for synchronization

$$\sin(\Delta\phi_{12,\text{eq}}) = \frac{\omega_1 - \omega_2}{\gamma_{12} + \gamma_{21}}. \tag{3.4}$$

Eq. (3.4) *implies that* (3.3) *only synchronizes, if $|\omega_1 - \omega_2|/|\gamma_{12} + \gamma_{21}| \leq 1$. Then inserting* (3.4) *into* (3.3) *and comparing the result with the synchronized system results in the dynamics in the synchronized state, whose synchronization frequency is given by*

$$\nu_{\text{sync}}(\gamma_{12}, \gamma_{21}) = \frac{\gamma_{21}\omega_1 + \gamma_{12}\omega_2}{\gamma_{12} + \gamma_{21}} = \frac{\omega_1 + \xi_{12}\omega_2}{1 + \xi_{12}}$$

with the relative coupling strength $\xi_{12} = \gamma_{12}/\gamma_{21}$. Note that the asymmetry of the coupling enables frequency tunability, since $\nu_{\text{sync}}(\gamma, \gamma) = (\omega_1 + \omega_2)/2$ with the symmetric coupling $\gamma \in \mathbb{R}$. In addition, the synchronization frequency ν_{sync} as a function of the relative coupling ξ is simulated numerically. For this, the frequencies of the Kuramoto oscillators are given by $\omega_1 = 10\ \frac{1}{\text{s}}$ and $\omega_2 = 20\ \frac{1}{\text{s}}$. The result is illustrated in Figure 3.1. In particular, the synchronization frequency ν_{sync} approaches the frequency ω_1 as $\xi_{12} \to \infty$, while ν_{sync} approaches ω_2 as $\xi_{12} \to 0$.

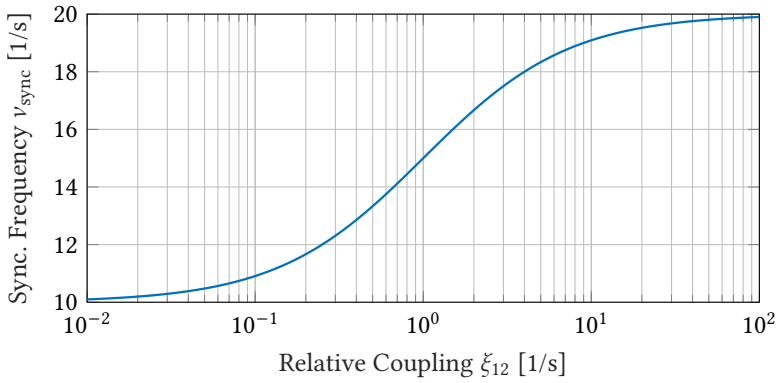

Figure 3.1.: Synchronization frequency ν_{sync} of the two coupled Kuromoto oscillators of Example 3.1 as a function of the relative coupling ξ_{12}.

From this example, it follows that the synchronization frequency of coupled oscillators can be adjusted by controlling the asymmetry between the oscillators in the network. In addition, it is implied that a frequency difference between the oscillators is necessary for tunability enhancements. Note that these conditions complicate the analysis of coupled oscillators. In contrast, the analysis can be simplified tremendously by assuming that the oscillators are identical or that the network is symmetric with respect to a Lie group, i.e., the topology and properties of the network are not changed by rearranging the oscillators with certain operations. Then the desynchronization and symmetry-breaking can be analyzed by applying the so-called Equivariant Hopf Theorem to these networks [42]. This can be, e.g., exploited to describe animal gaits and central pattern generators [23, 24, 122]. In addition to these simplifications, weak coupling can be asserted. This assumption allows to describe the oscillator in a lower dimensional state space, which is called phase model of the oscillator. For instance, the oscillator model in Example 3.1 can be obtained by assuming weak coupling. The phase model can be employed to analyze chemical reactions [74, 99] and neuronal networks [59]. More details for this method and its derivation are given, e.g., in [9, 35, 36, 93].

In contrast to these simplifications, the characteristic frequency and the corresponding tunability analysis is investigated for oscillators with strong coupling, asymmetric networks, and non-identical oscillators. The complete dynamics of this network hence has to be analyzed. It should be noted that Assumptions (A3.1) and (A3.2) are asserted for this analysis. For this, two different types of coupling are investigated. On the one hand, injective coupling is considered and it refers to coupling the oscillator with their outputs. On the other hand, the effects of diffusive coupling are analyzed. The coupling is said to be diffusive, if the oscillators are coupled by difference between their outputs. It should be noted that the qualitative behavior and bifurcations induced by injective and diffusive coupling for two Andronov-Hopf oscillators with identical coupling and damping coefficient are analyzed in [7]. However, the assumption on the coupling and damping coefficient restricts the tunability of these two coupled oscillators. Therefore, the scope of the subsequent analysis is to extent the analysis in [7] to two coupled Andronov-Hopf oscillators with arbitrary parameters. In addition to this, multi-clustering of injectively

coupled oscillators is investigated by analyzing the possibility of higher order degradation, such as Hopf-Hopf bifurcations. A Hopf-Hopf bifurcation occurs, if two complex conjugated eigenvalues are located on the imaginary axis [42, 48, 76]. The analysis is separated into two steps: First, bifurcations induced by injective coupling are analyzed for small and large networks of Andronov-Hopf oscillators. Secondly, the emergence of Andronov-Hopf bifurcations by coupling two Andronov-Hopf oscillators diffusively is investigated.

3.1.1. Networks of Injectively Coupled Oscillators

In the following, the emergence of controllable Andronov-Hopf bifurcations and the tunability of their characteristic frequency is investigated for networks of injectively coupled Andronov-Hopf oscillators. For this, let the number of Andronov-Hopf oscillators in the network be $n \in \mathbb{N}$ and denote a weighted, directed graph by $\mathbb{G}(\mathcal{V}, \mathcal{E})$ with the finite set of vertices $\mathcal{V} = \{1, 2, \ldots, n\}$ and the set of edges $\mathcal{E}$. An edge is a pair consisting of two vertices, i.e., (i, j) for all $i, j \in \mathcal{V}$. In addition, it is assumed that the interconnection of the graph $\mathbb{G}(\mathcal{V}, \mathcal{E})$ represents injective coupling between these oscillators and that in each vertex there is an Andronov-Hopf oscillator given in the complex-valued coordinates (3.1). The complex-valued coordinates simplify the bifurcation analysis by reducing the dimension of the network. The i-th Andronov-Hopf oscillator is governed by

$$\dot{z}_i = (\mu_i + \mathrm{i}\omega_i) z_i - |z_i|^2 z_i + \sum_{j=1}^{n} \gamma_{ij} z_j, \quad t > 0, \quad z_i(0) = z_{i,0} \tag{3.5}$$

with the state $z_i(t) \in \mathbb{C}$ and the initial conditions $z_{i,0} \in \mathbb{C}$ for all $i = 1, \ldots, n$. The parameters are given by the damping coefficient $\mu_i \in \mathbb{R}$, the natural frequency $\omega_i \in \mathbb{R}$, the coupling strength $\gamma_{ij} \in \mathbb{R}$, and the initial state $z_{i,0} \in \mathbb{C}$ for all $i, j \in \mathcal{V}$ and $(i, j) \in \mathcal{E}$.

The emergence of controllable Andronov-Hopf bifurcations and the enhancement of frequency tunability are analyzed as follows: The bifurcations and tunability enhancements of two small networks consisting of two and three oscillators, respectively, are analyzed with respect to their network topology by applying the Hopf Theorem (see Theorem 2.9). It turns out that the network topology and network size influence the number of controllable Andronov-Hopf bifurcations. These results are then generalized for large networks by analyzing the necessary condition (H1) of the Hopf Theorem (see Theorem 2.9). Finally, an approach based on clustering identical oscillators in a group is proposed to determine the critical points of a network of coupled Andronov-Hopf oscillators.

Two Injectively Coupled Oscillators

Subsequently, the emergence of controllable Andronov-Hopf bifurcation and the tunability enhancement by coupling two Andronov-Hopf oscillators injectively are discussed. These two Andronov-Hopf oscillators are governed by

$$\dot{z} = \begin{bmatrix} (\mu_1 + \mathrm{i}\omega_1) z_1 - |z_1|^2 z_1 + \gamma_{12} z_2 \\ (\mu_2 + \mathrm{i}\omega_2) z_2 - |z_2|^2 z_2 + \gamma_{21} z_1 \end{bmatrix}, \qquad t > 0, \qquad z(0) = z_0 \tag{3.6}$$

with the state vector $z(t) = [z_1(t), z_2(t)]^T \in \mathbb{C}^2$, the damping coefficients $\mu_1, \mu_2 \in \mathbb{R}$, the natural frequencies $\omega_1, \omega_2 \in \mathbb{R}$, the coupling strengths $\gamma_{12}, \gamma_{21} \in \mathbb{R}$, and the initial conditions $z_0 = [z_{1,0}, z_{2,0}]^T \in \mathbb{C}^2$. By introducing injective coupling the dynamics of the Andronov-Hopf oscillators change fundamentally, such that the coupling coefficients γ_{12}, γ_{21} and the frequencies ω_1, ω_2 also play a crucial role for the bifurcation in that system as elaborated subsequently.

Theorem 3.1 ([154]) *Let the product $v_2 = \gamma_{12}\gamma_{21}$ be the bifurcation parameter. Then the system* (3.6) *has Andronov-Hopf bifurcation. Its critical point and the characteristic frequency at the critical point are given by*

$$v_{2,\mathrm{H}} = \frac{\mu_1\mu_2}{(\mu_1+\mu_2)^2}\left[(\mu_1+\mu_2)^2 + (\omega_1-\omega_2)^2\right], \tag{3.7a}$$

$$\omega_{\mathrm{C}} = \frac{\omega_1+\omega_2}{2} - \frac{\mu_1-\mu_2}{\mu_1+\mu_2}\frac{\omega_1-\omega_2}{2}. \tag{3.7b}$$

If $v_2 < v_{2,\mathrm{H}}$, $\mu_1\mu_2 < 0$ and $\mu_1+\mu_2 > 0$ or $v_2 > v_{2,\mathrm{H}}$, $\mu_1\mu_2 > 0$ and $\mu_1+\mu_2 < 0$, a stable limit cycle emerges. In contrast to this, if $v_2 < v_{2,\mathrm{H}}$, $\mu_1\mu_2 < 0$ and $\mu_1+\mu_2 < 0$ or $v_2 > v_{2,\mathrm{H}}$, $\mu_1\mu_2 > 0$ and $\mu_1+\mu_2 > 0$, the oscillators synchronize.

Proof. The proof follows the outline of Hopf Theorem (see Theorem 2.9), such that it is divided into the parts (H1)-(H3).

(H1) To show the necessary condition (H1) of Theorem 2.9, the system (3.6) is linearized around its equilibrium $z_{\mathrm{eq}} = \mathbf{0}$. This yields

$$\Delta\dot{z} = A\Delta z = \begin{bmatrix} \mu_1 + \mathrm{i}\omega_1 & \gamma_{12} \\ \gamma_{21} & \mu_2 + \mathrm{i}\omega_2 \end{bmatrix} \begin{bmatrix} \Delta z_1 \\ \Delta z_2 \end{bmatrix}$$

with $\Delta z = z - z_{\mathrm{eq}}$. The characteristic polynomial is given by

$$P(\lambda) = \lambda^2 + [\mu_\Sigma + \mathrm{i}\omega_\Sigma]\lambda + v_2 + (\mu_1 + \mathrm{i}\omega_1)(\mu_2 + \mathrm{i}\omega_2) \tag{3.8}$$

and the corresponding eigenvalues read

$$\tilde{\lambda}_{1,2} = \frac{\mu_\Sigma + \mathrm{i}\omega_\Sigma \pm \sqrt{(\mu_\Delta + \mathrm{i}\omega_\Delta)^2 + 4\gamma_{12}\gamma_{21}}}{2} \tag{3.9}$$

with $\mu_\Sigma = \mu_1 + \mu_2$, $\omega_\Sigma = \omega_1 + \omega_2$, $\mu_\Delta = \mu_1 - \mu_2$, $\omega_\Delta = \omega_1 - \omega_2$, and $v_2 = \gamma_{12}\gamma_{21}$. To impose zero real part of (3.9), the real and imaginary part have to be derived. For this, consider a complex number $x = |x|\mathrm{e}^{\mathrm{i}\varphi_x} \in \mathbb{C}$ with the phase $\varphi_x \in (-\pi, \pi]$. The square root of x can be evaluated according to

$$\begin{aligned}
\sqrt{x} &= \sqrt{|x|}\left[\cos\left(\frac{\varphi_x}{2}\right) + \mathrm{i}\sin\left(\frac{\varphi_x}{2}\right)\right] \\
&= \sqrt{\frac{|x|}{2}}\left[\sqrt{1+\cos(\varphi_x)} + \mathrm{i}\sqrt{1-\cos(\varphi_x)}\right] \\
&= \sqrt{\frac{|x|}{2}}\left[\sqrt{1+\frac{\mathrm{Re}\,x}{|x|}} + \mathrm{i}\sqrt{1-\frac{\mathrm{Re}\,x}{|x|}}\right] \\
&= \sqrt{\frac{|x|+\mathrm{Re}\,x}{2}} + \mathrm{i}\sqrt{\frac{|x|-\mathrm{Re}\,x}{2}}.
\end{aligned}$$

Thus, by substituting $x = (\mu_\Delta + \mathrm{i}\omega_\Delta)^2 + 4\gamma_{12}\gamma_{21}$, the real and imaginary part of (3.9) are divided into

$$\operatorname{Re}\tilde{\lambda}_{1,2} = \frac{\mu_\Sigma}{2} \pm \sqrt{\frac{\sqrt{\left(4\upsilon_2 + \mu_\Delta^2 - \omega_\Delta^2\right)^2 + 4\mu_\Delta^2\omega_\Delta^2} + 4\upsilon_2 + \mu_\Delta^2 - \omega_\Delta^2}{8}},$$

$$\operatorname{Im}\tilde{\lambda}_{1,2} = \frac{\omega_\Sigma}{2} \pm \sqrt{\frac{\sqrt{\left(4\upsilon_2 + \mu_\Delta^2 - \omega_\Delta^2\right)^2 + 4\mu_\Delta^2\omega_\Delta^2} - 4\upsilon_2 - \mu_\Delta^2 + \omega_\Delta^2}{8}}.$$

With these considerations, the eigenvalues of coupled oscillators in real-valued representation are given by

$$\lambda_1 = \operatorname{Re}\tilde{\lambda}_1 + \mathrm{i}\operatorname{Im}\tilde{\lambda}_1, \quad \lambda_2 = \operatorname{Re}\tilde{\lambda}_1 + \mathrm{i}\operatorname{Im}\tilde{\lambda}_2,$$
$$\lambda_3 = \operatorname{Re}\tilde{\lambda}_2 + \mathrm{i}\operatorname{Im}\tilde{\lambda}_1, \quad \lambda_4 = \operatorname{Re}\tilde{\lambda}_2 + \mathrm{i}\operatorname{Im}\tilde{\lambda}_2.$$

By imposing zero real part for the eigenvalues λ_1 and λ_2, (3.7) follows.

(H2) To prove the crossing condition (2.14) consider the real part of the eigenvalues λ_i, $i = 1, 2, 3, 4$ and assume that the oscillators are not coupled, i.e., $\gamma_{12} = \gamma_{21} = 0$. As elaborated before, the eigenvalues are given by $\lambda_i = \mu_i + \mathrm{i}\omega_i$ for all $i = 1, 2$. The fact that $\operatorname{Re}\lambda_i = \mu_i$ can be exploited to locate the eigenvalues and their respective sensitivity with respect to the bifurcation parameter υ_2 in the coupled case. Thus, the location of the eigenvalues are determined by the damping coefficient μ_1 and μ_2, if

$$\upsilon_2 \leq \mu_1\mu_2 + \left(\frac{\omega_1 - \omega_2}{2}\right)^2 \tag{3.10}$$

is satisfied, since one pair of complex conjugated eigenvalues will cross the axis at the critical point (3.7a). In addition, the sensitivity (2.14) for eigenvalues, which cross the imaginary axis, must not reduce to zeros to satisfy the crossing condition, i.e.,

$$d = \frac{\mathrm{d}}{\mathrm{d}\mu}\left(\operatorname{Re}\lambda(\mu)\right)|_{\mu=\mu_\mathrm{H}} \neq 0.$$

Inserting the characteristic polynomial (3.8) and the critical point (3.7a) into (2.14), results in

$$d = \frac{\mathrm{d}}{\mathrm{d}\upsilon_2}(\operatorname{Re}\lambda)|_{\upsilon_2=\upsilon_{2,\mathrm{H}}} = -\frac{\mu_1 + \mu_2}{(\mu_1 + \mu_2)^2 + (\omega_1 + \omega_2 + 2\omega_\mathrm{C})^2}$$

so that its sign is given by

$$\operatorname{sign}(d)\begin{cases} > 0, & \text{if } \mu_1 + \mu_2 < 0, \\ = 0, & \text{if } \mu_1 + \mu_2 = 0, \\ < 0, & \text{if } \mu_1 + \mu_2 > 0. \end{cases} \tag{3.11}$$

This implies that the bifurcation is a super-critical Andronov-Hopf bifurcation, if $\mu_1\mu_2 < 0$ and $\mu_1 + \mu_2 < 0$ or $\mu_1\mu_2 > 0$ and $\mu_1 + \mu_2 > 0$.

(H3) Finally, it has to be shown that (3.6) is asymptotically stable at the critical point. For this consider the Lyapunov function candidate $V(\boldsymbol{z}) = \frac{1}{2}\boldsymbol{z}\cdot\boldsymbol{z}^* > 0$ with $\boldsymbol{z}^*$ the complex conjugate of $\boldsymbol{z}$ and note that

$$\dot{\boldsymbol{z}} = A\boldsymbol{z} - \begin{bmatrix} |z_1|^2 z_1 \\ |z_2|^2 z_2 \end{bmatrix}.$$

Hence, the rate of change of $V(\boldsymbol{z})$ along a solution of (3.6) at the critical point reads

$$\dot{V}(\boldsymbol{z}) = \frac{1}{2}\boldsymbol{z}^T\left(A^{\mathrm{T}} + A^*\right)\boldsymbol{z}^* - |z_1|^4 - |z_2|^4 \leq \mathrm{Re}(\lambda_{\max})|\boldsymbol{z}|^2 - \left(|z_1|^4 + |z_2|^4\right) < 0$$

with $\mathrm{Re}(\lambda_{\max}) = \mathrm{Re}(\max\sigma(A))$ and $\sigma(\cdot)$ denoting the spectrum for all $n \in \mathbb{N}$. If $\mu_1\mu_2 < 0$ and $\mu_1 + \mu_2 < 0$ or $\mu_1\mu_2 > 0$ and $\mu_1 + \mu_2 > 0$, it follows that $A^{\mathrm{T}} + A$ is negative semi-definite, such that $\mathrm{Re}\,\lambda_{\max} = 0$. In this case, it can be concluded, that (3.6) is asymptotically stable at the critical point. □

Following Theorem 3.1 two injectively coupled Andronov-Hopf oscillators exhibit a controllable Andronov-Hopf bifurcation, whose characteristic frequency ω_{C} at the critical point $v_{2,\mathrm{H}}$ is tunable in terms of the damping coefficients μ_1 and μ_2. The tunability enhancement is induced by the asymmetry between the two oscillators. Hence, the characteristic frequency ω_{C} is closer to the natural frequency of the oscillator with the smaller damping. This implies that the tunable characteristic frequency ω_{C} is bounded by the interval between the natural frequencies ω_1 and ω_2. In particular, these properties can be shown by inserting the relative damping $\eta_{12} = \mu_1/\mu_2$ into (3.7b), which yields

$$\omega_{\mathrm{C}} = \frac{\omega_1 + \omega_2}{2} - \frac{\eta_{12} - 1}{\eta_{12} + 1}\frac{\omega_1 - \omega_2}{2}. \tag{3.12}$$

Analyzing the limits $\lim_{\eta_{12}\to 0}\omega_{\mathrm{C}}$ and $\lim_{\eta_{12}\to\infty}\omega_{\mathrm{C}}$ implies the boundaries of the characteristic frequency ω_{C}. These are given by

$$\omega_{\mathrm{C}} = \begin{cases} \omega_1, & \text{if } \mu_1 = 0 \wedge \mu_2 < 0, \\ \omega_2, & \text{if } \mu_1 < 0 \wedge \mu_2 = 0. \end{cases}$$

Note that the bifurcation parameter vanishes for $\mu_1 = \mu_2 = 0$, i.e., $\gamma_{12}\gamma_{21} = 0$. In this case, both oscillators are decoupled, such that the characteristic frequencies of the system (3.6) are given by the natural frequencies of the individual oscillators. To conclude the discussion, the results on the tunability enhancement are verified numerically.

Example 3.2 *The characteristic frequency ω_{C} at the critical point as a function of the relative damping coefficient η_{12} and the characteristic frequency ω_{C} in the sub-critical regime as a function of the bifurcation parameter $\gamma_{12}\gamma_{21}$ and the damping μ_1 evaluated numerically. The parameters are assumed to be given by the damping coefficient $\mu_2 = -1\,\frac{1}{\mathrm{s}}$ and the natural frequencies $\omega_1 = 10\,\frac{1}{\mathrm{s}}$ and $\omega_2 = 20\,\frac{1}{\mathrm{s}}$. In particular, note that the sub-critical regime of the system* (3.6) *for the assumed parameters is bounded by $v_2 \leq v_{2,\mathrm{H}}$.*

The results of the numerical study are depicted in Figure 3.2. The characteristic frequency ω_{C} at the critical point is shown in Figure 3.2a. In this example, the characteristic frequency ω_{C} is

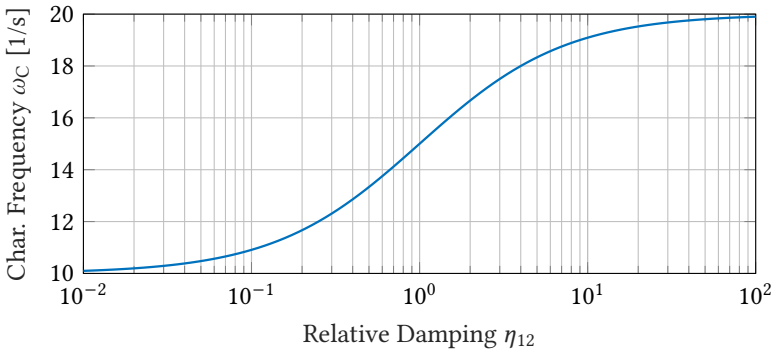

(a) Characteristic frequency ω_H of two coupled Andronov-Hopf oscillators at the critical point $v_{2,H}$ as a function of the relative damping coefficient η.

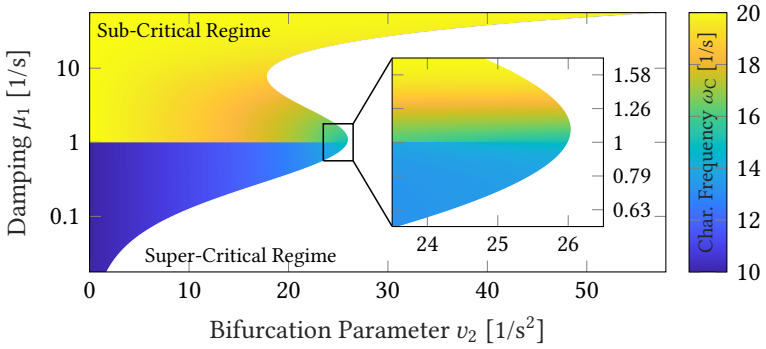

(b) Characteristic frequency ω_H of two coupled Andronov-Hopf oscillators in the sub-critical regime as a function of the damping coefficient μ_1 and the bifurcation parameter v_2.

Figure 3.2.: Characteristic frequency of two coupled Andronov-Hopf oscillators at the bifurcation point and in the sub-critical regime. The numerical values are given for the natural frequencies and the damping coefficient of the second oscillator are given by $\omega_1 = 10\,\frac{1}{s}$, $\omega_2 = 20\,\frac{1}{s}$ and $\mu_2 = -1\,\frac{1}{s}$.

tunable inside the interval (ω_1, ω_2)*. Moreover, the characteristic frequency* ω_C *in sub-critical regime is depicted in Figure 3.2b. Herein, a neighborhood around the critical point* $v_{2,H}$ *at* $\eta = 1$ *is magnified as the characteristic frequency* ω_H *is only tunable in this neighborhood. In contrast, if the bifurcation parameter* v_2 *is not in the neighborhood of the critical point* $v_{2,H}$*, the characteristic frequency* ω_C *can be localized in a neighborhood of either* ω_1 *or* ω_2*.*

Three Injectively Coupled Oscillators

Subsequently, the emergence of controllable Andronov-Hopf bifurcations of three injectively coupled oscillators are investigated. These coupled oscillators are governed by

$$\dot{z} = f_3(z), \qquad t > 0, \qquad z(0) = z_0 \tag{3.13a}$$

with

$$\boldsymbol{f}_3(\boldsymbol{z}) = \begin{bmatrix} (\mu_1 + \mathrm{i}\omega_1) z_1 - |z_1|^2 z_1 + \gamma_{12} z_2 + \gamma_{13} z_3 \\ (\mu_2 + \mathrm{i}\omega_2) z_2 - |z_2|^2 z_2 + \gamma_{21} z_1 + \gamma_{23} z_3 \\ (\mu_3 + \mathrm{i}\omega_3) z_3 - |z_3|^2 z_3 + \gamma_{31} z_1 + \gamma_{32} z_2 \end{bmatrix}. \tag{3.13b}$$

with the state vector $\boldsymbol{z}(t) = [z_1(t), z_2(t), z_3(t)]^{\mathrm{T}} \in \mathbb{C}^3$, the damping coefficients $\mu_1,\ \mu_2,\ \mu_3 \in \mathbb{R}$, the natural frequencies $\omega_1,\ \omega_2,\ \omega_3 > 0$, the adjacency matrix $\Gamma \in \mathbb{R}^{3\times3}$, and the initial conditions $\boldsymbol{z}_0 = [z_{1,0}, z_{2,0}, z_{3,0}]^{\mathrm{T}} \in \mathbb{C}^3$.

To analyze the necessary condition (H1) of the Hopf Theorem (see Theorem 2.9) for system (3.13), independent bifurcation parameters in terms of the adjacency matrix $\Gamma_3 \in \mathbb{R}^{3\times3}$ are identified. With this, a cubic polynomial is determined to compute the critical points of (3.13) in terms of these bifurcation parameters. Then, the number of critical point are investigated by analyzing the number of real-valued roots of the polynomial and by investigating the emergence of Hopf-Hopf bifurcations.

Preliminaries The bifurcation analysis of three coupled oscillators is prepared by evaluating the characteristic polynomial of the linearization of (3.13) around its equilibrium $\boldsymbol{z}_{\mathrm{eq},i} = \boldsymbol{0}$. With the resulting system matrix

$$A_3 = \begin{bmatrix} \mu_1 + \mathrm{i}\omega_1 & \gamma_{12} & \gamma_{13} \\ \gamma_{21} & \mu_2 + \mathrm{i}\omega_2 & \gamma_{23} \\ \gamma_{31} & \gamma_{32} & \mu_3 + \mathrm{i}\omega_3 \end{bmatrix}, \tag{3.14}$$

the characteristic polynomial reads

$$P_{A_3}(\lambda) = \lambda^3 + (a_2 + \mathrm{i}b_2)\lambda^2 - (\gamma_{12}\gamma_{21} + \gamma_{13}\gamma_{31} + \gamma_{23}\gamma_{32} - a_1 - \mathrm{i}b_1)\,\lambda + R_0 \tag{3.15}$$

with the coefficients

$$\begin{aligned} R_0 = -\,[&\gamma_{12}\gamma_{23}\gamma_{31} + \gamma_{13}\gamma_{21}\gamma_{32} - \gamma_{23}\gamma_{32}\mu_1 - \gamma_{13}\gamma_{31}\mu_2 \\ &-\gamma_{12}\gamma_{21}\mu_3 - a_0 - \mathrm{i}\,(\gamma_{23}\gamma_{32}\omega_1 + \gamma_{13}\gamma_{31}\omega_2 + \gamma_{12}\gamma_{21}\omega_3 + b_0)] \end{aligned}$$

and

$$a_0 = \mu_1\mu_2\mu_3 - \omega_2\omega_3\mu_1 - \omega_1\omega_3\mu_2 - \omega_1\omega_2\mu_3, \tag{3.16a}$$
$$a_1 = \mu_1\mu_2 + \mu_1\mu_3 + \mu_2\mu_3 - \omega_1\omega_2 - \omega_1\omega_3 - \omega_2\omega_3, \tag{3.16b}$$
$$a_2 = -\mu_1 - \mu_2 - \mu_3, \tag{3.16c}$$
$$b_0 = -\omega_1\omega_2\omega_3 + \mu_2\mu_3\omega_1 + \mu_1\mu_3\omega_2 + \mu_1\mu_2\omega_3, \tag{3.16d}$$
$$b_1 = \mu_1\,(\omega_2 + \omega_3) + \mu_2\,(\omega_1 + \omega_3) + \mu_3\,(\omega_1 + \omega_2)\,, \tag{3.16e}$$
$$b_2 = -\omega_1 - \omega_2 - \omega_3. \tag{3.16f}$$

To define suitable bifurcation parameters, three graphs are considered and are visualized

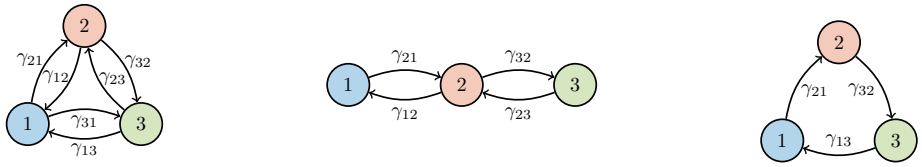

(a) Complete graph of 3 vertices. **(b)** Line graph of 3 vertices. **(c)** Cycle graph of 3 vertices.

Figure 3.3.: Investigated graphs for the bifurcation analysis of three coupled Andronov-Hopf oscillators. In particular, the different colors indicate different parameters of the oscillators.

in Figure 3.3: the complete graph, the line graph, and the cycle graph. These graph have the following characteristic polynomials

$$\det\left(\Gamma_{\text{cpl}} - \lambda I\right) = -\lambda^3 + \left(\gamma_{12}\gamma_{21} + \gamma_{23}\gamma_{32} + \gamma_{13}\gamma_{31}\right)\lambda + \gamma_{12}\gamma_{23}\gamma_{31} + \gamma_{13}\gamma_{21}\gamma_{32}, \tag{3.17a}$$

$$\det\left(\Gamma_{\text{I}} - \lambda I\right) = -\lambda^3 + \left(\gamma_{12}\gamma_{21} + \gamma_{23}\gamma_{32}\right)\lambda, \tag{3.17b}$$

$$\det\left(\Gamma_{\text{o}} - \lambda I\right) = -\lambda^3 + \gamma_{13}\gamma_{21}\gamma_{32}, \tag{3.17c}$$

with their adjacency matrices

$$\Gamma_{\text{cpl}} = \begin{bmatrix} -\lambda & \gamma_{12} & \gamma_{13} \\ \gamma_{21} & -\lambda & \gamma_{23} \\ \gamma_{31} & \gamma_{32} & -\lambda \end{bmatrix}, \qquad \Gamma_{\text{I}} = \begin{bmatrix} -\lambda & \gamma_{12} & 0 \\ \gamma_{21} & -\lambda & \gamma_{23} \\ 0 & \gamma_{32} & -\lambda \end{bmatrix}, \qquad \Gamma_{\text{o}} \begin{bmatrix} -\lambda & 0 & \gamma_{13} \\ \gamma_{21} & -\lambda & 0 \\ 0 & \gamma_{32} & -\lambda \end{bmatrix}.$$

Comparing the coefficients with the coefficients of the characteristic polynomial (3.15) implies that the characteristic polynomial of the cycle graph and the line graph have a fundamentally different influence on the characteristic polynomial (3.15). The coefficients R_1 and R_0 of (3.15) can be adjusted by assigning the line graph, while the cycle graph can only influence the coefficient R_0 of (3.15). Hence, two different bifurcation parameters based on the cycle graph and the line graph are considered

$$\upsilon_3 = \gamma_{12}\gamma_{23}\gamma_{31} + \gamma_{13}\gamma_{21}\gamma_{32}, \tag{3.18a}$$

$$\upsilon_2(\boldsymbol{x}) = \gamma_{23}\gamma_{32}x_1 + \gamma_{13}\gamma_{31}x_2 + \gamma_{12}\gamma_{21}x_3 = \xi_2 x_1 + \xi_3 x_2 + \xi_1 x_3. \tag{3.18b}$$

with the vector $\boldsymbol{x} = [x_1, x_2, x_3]^{\text{T}}$ and $\upsilon_2(\mathbf{1}) = \xi_1 + \xi_2 + \xi_3 (= \upsilon_2)$. It follows from the coefficients R_1 and R_0 of (3.15) that υ_3 is a one-parameter family of (3.13) and $\upsilon_2(\cdot)$ is a two-parameter family of (3.13). A one-parameter family (or two-parameter family, respectively) of (3.13) acts with one parameter (or two parameters, respectively) on the dynamic behavior of (3.13) [76]. In particular, the indices of the bifurcation parameters υ_3 and υ_2 are motivated by length of the products of the determinants (3.17b) and (3.17c).

To determine the critical point, impose $\lambda = \text{i}\omega_{\text{H}}$ with the characteristic frequency $\omega_{\text{H}} > 0$ at the critical point, so that the necessary condition (H1) is satisfied. Inserting $\lambda = \text{i}\omega_{\text{H}}$ and sorting terms, results in

$$0 = -a_2\omega_{\text{H}}^2 - b_1\omega_{\text{H}} - \gamma_{12}\gamma_{23}\gamma_{31} - \gamma_{13}\gamma_{21}\gamma_{32} + \gamma_{23}\gamma_{32}\mu_1 + \gamma_{13}\gamma_{31}\mu_2 + \gamma_{12}\gamma_{21}\mu_3 + a_0, \tag{3.19a}$$

$$0 = \gamma_{23}\gamma_{32}\omega_1 + \gamma_{13}\gamma_{31}\omega_2 + \gamma_{12}\gamma_{21}\omega_3 + b_0 - \left(\gamma_{12}\gamma_{21} + \gamma_{13}\gamma_{31} + \gamma_{23}\gamma_{32} - a_1\right)\omega_{\text{H}} - b_2\omega_{\text{H}}^2 - \omega_{\text{H}}^3. \tag{3.19b}$$

Solving (3.19a) for ω_{H}, yields

$$\omega_{\mathrm{H}}^{\pm} = -\frac{b_1 \pm \sqrt{b_1^2 - 4a_2a_0 - 4a_2\left(v_3 - v_2(\boldsymbol{\mu})\right)}}{2a_2}. \tag{3.20}$$

In particular, (3.20) is real-valued, if the discriminant $D_{\omega_{\mathrm{H}}}$ of (3.19a) satisfies

$$D_{\omega_{\mathrm{H}}} = b_1^2 - 4a_2a_0 - 4a_2\left(v_3 - v_2(\boldsymbol{\mu})\right) > 0. \tag{3.21}$$

Inserting (3.20) into (3.19b) and sorting terms, eq. (B.1) in Appendix B is obtained. This equation is a cubic polynomial in terms the bifurcation parameters v_3 and v_2. Hence, (B.1) can be solved analytically, as its degree is less than four [10, 13]. However, the number of real-valued roots can vary, which can imply the emergence of a Hopf-Hopf bifurcation or the collision of two critical point. This is subsequently analyzed.

Number of Critical Points The number of critical points of Andronov-Hopf bifurcations of the coupled oscillators (3.13) is investigated by analyzing the discriminant of (3.15). Following Proposition 2.1, the discriminant for a cubic polynomial $P_3(x) = x^3+c_2x^2+c_1x+c_0$ reads

$$D_{P_3,x} = 4c_1^3 - c_2^2c_1^2 - 18c_0c_2c_1 + 4c_0c_2^3 + 27c_0^2$$

and the number of real roots can be determined by evaluating the sign of the discriminant D_{P_3}, i.e.,

$$D_{P_3,x}\begin{cases} > 0, & P_3 \text{ has 1 real root} \\ = 0, & P_3 \text{ has 3 real roots and 2 roots are equal} \\ < 0, & P_3 \text{ has 3 different, real roots} \end{cases}.$$

With this, the number of critical points induced by the bifurcation parameters v_2 and v_3 is investigated.

Theorem 3.2 *Assume that v_3 is the bifurcation parameter. Additionally, denote the function*

$$\begin{aligned} g_{\mathrm{o}}(\xi_1,\xi_2,\xi_3) = {} & 27b_0^2 - 4a_1^3 + 4b_2^3\left[b_0 - (\xi_2\omega_1 + \xi_3\omega_2 + \xi_1\omega_3)\right] \\ & + 12a_1^2\left(\xi_1+\xi_2+\xi_3\right) - 54b_0\left(\xi_2\omega_1 + \xi_3\omega_2 + \xi_1\omega_3\right) \\ & + 18b_2\left[a_1 - (\xi_1+\xi_2+\xi_3)\right]\left[b_0 - (\xi_2\omega_1 + \xi_3\omega_2 + \xi_1\omega_3)\right] \\ & + 27\left(\xi_2\omega_1 + \xi_3\omega_2 + \xi_1\omega_3\right)^2 - b_2^2\left[a_1 - (\xi_1+\xi_2+\xi_3)\right]^2 \\ & - 12a_1\left(\xi_1+\xi_2+\xi_3\right)^2 + 4\left(\xi_1+\xi_2+\xi_3\right)^3. \end{aligned} \tag{3.22}$$

with $\xi_1 = \gamma_{12}\gamma_{21}$, $\xi_2 = \gamma_{32}\gamma_{32}$, and $\xi_3 = \gamma_{13}\gamma_{31}$ and denote the real-valued roots of (B.1) *with respect to ξ_1 by $\xi_{1,i}$ for all $i = 1, 2, 3$. These roots are sorted by the magnitude of their real part beginning with the smallest value. Then the number of critical points of* (3.13) *with respect to v_3 can be determined by*

$$m_{v_3,\xi_1} = \begin{cases} 1, & \text{if } \left(\xi_1 \in (\xi_{1,1},\infty) \wedge \xi_2 \notin \mathcal{I}_{\mathrm{o}}\right) \vee \left(\xi_1 \in (\xi_{1,1},\xi_{1,2}) \cup (\xi_{1,3},\infty) \wedge \xi_2 \in \mathcal{I}_{\mathrm{o}}\right) \\ 3, & \text{if } \left(\xi_1 \notin (\xi_{1,1},\infty) \wedge \xi_2 \notin \mathcal{I}_{\mathrm{o}}\right) \vee \left(\xi_1 \notin (\xi_{1,1},\xi_{1,2}) \cup (\xi_{1,3},\infty) \wedge \xi_2 \in \mathcal{I}_{\mathrm{o}}\right) \end{cases} \tag{3.23}$$

with the interval $\mathcal{I}_{\mathrm{o}} = [\min\{\xi_{\mathrm{o},2,1}, \xi_{\mathrm{o},2,2}\}, \max\{\xi_{\mathrm{o},2,1}, \xi_{\mathrm{o},2,2}\}]$ *and the constants*

$$\xi_{\mathrm{o},2,1} = \frac{b_0 - a_1\omega_3 + b_2\omega_3^2 + \omega_3^3 + \gamma_{13}\gamma_{31}\,(\omega_3 - \omega_2)}{\omega_1 - \omega_3}, \tag{3.24a}$$

$$\xi_{\mathrm{o},2,2} = \frac{-9b_2^2\omega_3 - b_2^3 - 27a_1\omega_3 + 27b_0 + 27\gamma_{13}\gamma_{31}\,(\omega_3 - \omega_2)}{27\,(\omega_1 - \omega_3)}. \tag{3.24b}$$

Remark 3.2 *The conditions in Theorem 3.2 are defined in terms of the product* $\xi_1 = \gamma_{12}\gamma_{21}$. *Similar conditions in terms of* $\xi_2 = \gamma_{23}\gamma_{32}$ *and* $\xi_3 = \gamma_{13}\gamma_{31}$ *can also be derived, since the bifurcations parameter* $v_2(\cdot)$ *is a weighted sum of* ξ_1, ξ_2 *and* ξ_3. *As the derivation follows the same route, these conditions are not further elaborated.*

Proof. Subsequently, the number of real-valued zeros of (B.1) in Appendix B is investigated by analyzing the sign of its discriminant. This is done by separating its discriminant into a positive function and a cubic polynomial. The sign of the discriminant is determined by the sign of this cubic polynomial, which is done by analyzing the behavior as its variables approach positive and negative infinity and deriving the number of its zeros.

As eq. (B.1) is a cubic polynomial with respect to the bifurcation parameter v_3, its discriminant reads

$$D_{P_{\mathrm{N}},v_3} = 256a_2^{12}f_{\mathrm{o}}^2(\xi_1,\xi_2,\xi_3)g_{\mathrm{o}}(\xi_1,\xi_2,\xi_3) \tag{3.25}$$

with $\xi_1 = \gamma_{12}\gamma_{21}$, $\xi_2 = \gamma_{32}\gamma_{32}$, $\xi_3 = \gamma_{13}$,

$$\begin{aligned} f_{\mathrm{o}}(\xi_1,\xi_2,\xi_3) = a_2^3\,[b_2\,[c_1 - (\xi_1+\xi_2+\xi_3)] + b_0 - (\xi_2\omega_1 + \xi_3\omega_2 + \xi_1\omega_3)] \\ + a_2^2 b_1\left[b_2^2 - a_1 + (\xi_1+\xi_2+\xi_3)\right] - 2a_2b_1^2b_2 + b_1^3, \end{aligned} \tag{3.26}$$

and $g_{\mathrm{o}}(\xi_1,\xi_2,\xi_3)$ is given by (3.22). Here, the function (3.26) and the constant a_2 cannot change the sign of (3.25), so that the number of roots of (B.1) is derived by analyzing the sign of (3.22).

Subsequently, the sign of (3.22), which is a function of ξ_1, ξ_2, or ξ_3, is determined in terms of its (real-valued) zeros and by combing these results with the behavior of (3.22) as ξ_1, ξ_2, or ξ_3 approach positive (or negative infinity, respectively). As the coefficients of the cubic terms are positive (3.22) satisfies

$$\lim_{\xi_i\to\infty} g_{\mathrm{o}}(\xi_1,\xi_2,\xi_3) = \infty, \qquad \lim_{\xi_i\to-\infty} g_{\mathrm{o}}(\xi_1,\xi_2,\xi_3) = -\infty \tag{3.27}$$

for all $i = 1, 2, 3$. Thus, the number of roots of (B.1) in terms of v_3 is given by

$$m_{v_3,\xi_1} = \begin{cases} 1, & \text{if } \left(\xi_1 \in (\xi_{1,1},\infty) \wedge D_{g_{\mathrm{o}},\xi_1} > 0\right) \\ & \qquad \vee \left(\xi_1 \in (\xi_{1,1},\xi_{1,2}) \cup (\xi_{1,3},\infty) \wedge D_{g_2,\xi_1} \le 0\right) \\ 3, & \text{if } \left(\xi_1 \notin (\xi_{1,1},\infty) \wedge D_{g_{\mathrm{o}},\xi_1} > 0\right) \\ & \qquad \vee \left(\xi_1 \notin (\xi_{1,1},\xi_{1,2}) \cup (\xi_{1,3},\infty) \wedge D_{g_2,\xi_1} \le 0\right) \end{cases} \tag{3.28}$$

with the real-valued zeros $\check{\xi}_{1,1}$, $\check{\xi}_{1,2}$, and $\check{\xi}_{1,3}$ of (3.22), and the discriminant $D_{g_o,\check{\xi}_1}$ of (3.22) with respect to $\check{\xi}_1$ reads

$$\begin{aligned} D_{g_o,\check{\xi}_1} = -16 \left[b_0 - a_1\omega_3 + b_2\omega_3^2 + \omega_3^3 - (\omega_1 - \omega_3)\,\check{\xi}_2 - (\omega_2 - \omega_3)\,\check{\xi}_3 \right] \\ \times \left\{ 9b_2^2\omega_3 + b_2^3 + 27\left[a_1\omega_3 - b_0 + (\omega_1 - \omega_3)\,\check{\xi}_2 + (\omega_2 - \omega_3)\,\check{\xi}_3 \right] \right\}^3 . \end{aligned} \tag{3.29}$$

To determine the number of zeros of (3.22), the sign of (3.29) has to be investigated. Here, eq. (3.29) is a quartic polynomial, which is given by four linear functions in terms of $\check{\xi}_2$ and $\check{\xi}_3$. Three of these linear functions are equivalent. Hence, the product between the two unique linear functions and -1 determines the sign of the discriminant (3.29). This product is given by

$$\begin{aligned} h_o(\check{\xi}_2, \check{\xi}_3) = 27\,(\omega_1 - \omega_3)^2\,\check{\xi}_2^2 + 54\,(\omega_1 - \omega_3)\,(\omega_2 - \omega_3)\,\check{\xi}_2\check{\xi}_3 \\ + (\omega_1 - \omega_3)\left(9b_2^2\omega_3 - 27b_2\omega_3^2 + b_2^3 - 27\left(2b_0 - 2a_1\omega_3 + \omega_3^3 \right) \right)\check{\xi}_2 \\ + (\omega_2 - \omega_3)\left(9b_2^2\omega_3 - 27b_2\omega_3^2 + b_2^3 - 27\left(2b_0 - 2a_1\omega_3 + \omega_3^3 \right) \right)\check{\xi}_3 \\ - \left(\left(9\omega_3\left(3a_1 + b_2^2 \right) + b_2^3 + 27b_0 \right)\left(\omega_3\left(\omega_3\left(b_2 + \omega_3 \right) - a_1 \right) - b_0 \right) \right) \end{aligned} \tag{3.30}$$

The coefficients of the quadratic term of (3.30) are positive, so that (3.29) diverges to (positive) infinity for $\check{\xi}_2, \check{\xi}_3 \to \pm\infty$, i.e., $\lim_{\check{\xi}_i \to \pm\infty} h_o(\check{\xi}_2, \check{\xi}_3) = \infty$ for all $i = 2, 3$. Thus, (3.30) has to be negative, if

$$\check{\xi}_2 \in \mathcal{I}_o = \left[\min\{\check{\xi}_{o,2,1}, \check{\xi}_{o,2,2}\}, \max\{\check{\xi}_{o,2,1}, \check{\xi}_{o,2,2}\} \right]$$

holds true. Combining (3.27) and the sign of (3.30) and denoting an interval starting by the (real-valued) minimum of (3.24) and ending at the (real-valued) maximum of (3.24), eq. (3.23) follows. This concludes the proof. □

Theorem 3.3 *Assume that $\check{\xi}_1 = \gamma_{12}\gamma_{21}$ is the bifurcation parameter. Additionally, introduce the function*

$$\begin{aligned} g_I(\upsilon_3, \check{\xi}_1, \check{\xi}_2, \check{\xi}_3) = d_{000} + d_{100}\upsilon_3 + d_{010}\check{\xi}_2 + d_{001}\check{\xi}_3 + d_{200}\upsilon_3^2 + d_{020}\check{\xi}_2^2 + d_{002}\check{\xi}_3^2 + d_{110}\upsilon_3\check{\xi}_2 + d_{101}\upsilon_3\check{\xi}_3 \\ + d_{011}\check{\xi}_2\check{\xi}_3 + d_{300}\upsilon_3^3 + d_{030}\check{\xi}_2^3 + d_{003}\check{\xi}_3^3 + d_{210}\upsilon_3^2\check{\xi}_2 + d_{120}\upsilon_3\check{\xi}_2^2 \\ + d_{201}\upsilon_3^2\check{\xi}_3 + d_{102}\upsilon_3\check{\xi}_3^2 + d_{021}\check{\xi}_2^2\check{\xi}_3 + d_{021}\check{\xi}_2\check{\xi}_3^2 + d_{111}\upsilon_3\check{\xi}_2\check{\xi}_3 \end{aligned} \tag{3.31}$$

with $\check{\xi}_2 = \gamma_{32}\gamma_{32}$ and $\check{\xi}_3 = \gamma_{13}\gamma_{31}$. The coefficients are given by (B.2) *in Appendix B. Let real-valued roots of* (B.2) *with respect to $\check{\xi}_1$ be given by $\check{\xi}_{1,i}$ for all $i = 1, 2, 3$. Then the number of critical points of* (3.13) *is given by*

$$m_{\check{\xi}_1,\upsilon_3} = \begin{cases} 1, & \text{if } \left(C_{\upsilon_3,1} \wedge \check{\xi}_2 \in \mathcal{I}_{I,1} \right) \vee \left(C_{\upsilon_3,2} \wedge \check{\xi}_2 \notin \mathcal{I}_{I,1} \right) \\ 3, & \text{if } \left(\neg C_{\upsilon_3,1} \wedge \check{\xi}_2 \in \mathcal{I}_{I,1} \right) \vee \left(\neg C_{\upsilon_3,2} \wedge \check{\xi}_2 \notin \mathcal{I}_{I,1} \right) \end{cases}, \tag{3.32a}$$

if (3.31) *is solved for υ_3, and*

$$m_{\check{\xi}_1,\check{\xi}_2} = \begin{cases} 1, \text{ if } \left(C_{\check{\xi}_2,1} \wedge \upsilon_3 \notin \mathcal{I}_{I,2} \right) \vee \left(C_{\check{\xi}_2,2} \wedge \upsilon_3 \in \mathcal{I}_{I,2} \right) \\ 3, \text{ if } \left(\neg C_{\check{\xi}_2,1} \wedge \upsilon_3 \notin \mathcal{I}_{I,2} \right) \vee \left(\neg C_{\check{\xi}_2,2} \wedge \upsilon_3 \in \mathcal{I}_{I,2} \right) \end{cases}, \tag{3.32b}$$

if (3.31) *is solved for* ξ_2*. The conditions*

$$C_{\upsilon_3,1} = \left(\upsilon_3 \in (\upsilon_{3,1}, \infty) \wedge \mu_1 + \mu_2 < 0\right) \vee \left(\upsilon_3 \in (-\infty, \upsilon_{3,1}) \wedge \mu_1 + \mu_2 > 0\right), \tag{3.33a}$$

$$C_{\upsilon_3,2} = \left(\upsilon_3 \in (\upsilon_{3,1}, \upsilon_{3,2}) \cup (\upsilon_{3,3}, \infty) \wedge \mu_1 + \mu_2 < 0\right) \vee \left(\upsilon_3 \in (-\infty, \upsilon_{3,1}) \cup (\upsilon_{3,2}, \upsilon_{3,3}) \wedge \mu_1 + \mu_2 > 0\right), \tag{3.33b}$$

$$C_{\xi_2,1} = \left[\xi_2 \in (\xi_{2,1}, \infty) \wedge (\mu_1 - \mu_3)(\mu_1 + \mu_2) > 0\right] \vee \left(\xi_2 \in (-\infty, \xi_{2,1}) \wedge (\mu_1 - \mu_3)(\mu_1 + \mu_2) < 0\right), \tag{3.33c}$$

$$C_{\xi_2,2} = \left[\xi_2 \in (\xi_{2,1}, \xi_{2,2}) \cup (\xi_{2,3}, \infty) \wedge (\mu_1 - \mu_3)(\mu_1 + \mu_2) > 0\right] \vee \left(\xi_2 \in (-\infty, \xi_{2,1}) \cup (\xi_{2,2}, \xi_{2,3}) \wedge (\mu_1 - \mu_3)(\mu_1 + \mu_2) < 0\right), \tag{3.33d}$$

the intervals

$$\mathcal{I}_{\mathrm{I},1} = \left(\min\left\{\xi_{\mathrm{I},2,1}, \xi_{\mathrm{I},2,2}\right\}, \max\left\{\xi_{\mathrm{I},2,1}, \xi_{\mathrm{I},2,2}\right\}\right), \tag{3.34a}$$

$$\mathcal{I}_{\mathrm{I},2} = \left(\min\left\{\upsilon_{\mathrm{I},3,1}, \upsilon_{\mathrm{I},3,2}\right\}, \max\left\{\upsilon_{\mathrm{I},3,1}, \upsilon_{\mathrm{I},3,2}\right\}\right), \tag{3.34b}$$

and the real-valued zeros $\upsilon_{3,1}$*,* $\upsilon_{3,2}$*,* $\upsilon_{3,3}$*,* $\xi_{2,1}$*,* $\xi_{2,2}$*, and* $\xi_{2,3}$ *of* (3.31)*. Here, the real-valued zeros are sorted by the magnitude of their real part beginning with the smallest value. In addition, the constants* $\xi_{\mathrm{I},2,1}$*,* $\xi_{\mathrm{I},2,2}$*,* $\upsilon_{\mathrm{I},2,1}$*, and* $\upsilon_{\mathrm{I},2,2}$ *read*

$$\xi_{\mathrm{I},2,2} = \frac{c_{\mathrm{I},\upsilon_3,1,00} + c_{\mathrm{I},\upsilon_3,1,01}\xi_3}{c_{\mathrm{I},\upsilon_3,1,10}}, \tag{3.35a}$$

$$\xi_{\mathrm{I},2,2} = \frac{c_{\mathrm{I},\upsilon_3,2,00} + c_{\mathrm{I},\upsilon_3,2,01}\xi_3}{c_{\mathrm{I},\upsilon_3,2,10}}, \tag{3.35b}$$

$$\upsilon_{\mathrm{I},2,1} = \frac{c_{\mathrm{I},\xi_2,1,00} + c_{\mathrm{I},\xi_2,1,01}\xi_3}{c_{\mathrm{I},\xi_2,1,10}}, \tag{3.35c}$$

$$\upsilon_{\mathrm{I},2,2} = \frac{c_{\mathrm{I},\xi_2,2,00} + c_{\mathrm{I},\xi_2,2,01}\xi_3}{c_{\mathrm{I},\xi_2,2,10}} \tag{3.35d}$$

with the coefficients given by (B.3)*.*

Proof. In the following, the number of real-valued zeros of (B.1) in Appendix B is investigated. For this, its discriminant with respect to ξ_1 is analyzed, since (B.1) is a cubic polynomial in terms of ξ_1. This is done by splitting this discriminant into a positive function and a cubic polynomial. The sign of the discriminant is determined by the sign of this cubic polynomial, which is done by analyzing the behavior as its variables approaches positive and negative infinity and deriving the number of its zeros.

The discriminant of (B.1) in terms of ξ_1 is given by

$$D_{P_{\mathrm{N}},\xi_1} = 256 a_2^{12} f_{\mathrm{I}}^2(\upsilon_3, \xi_2, \xi_3) g_{\mathrm{I}}(\upsilon_3, \xi_2, \xi_3) \tag{3.36}$$

with

$$\begin{aligned} f_{\mathrm{I}} = &-a_2^3 b_2 \left[a_0 - a_1\mu_3 + b_1\omega_3 - \xi_2(\mu_1 - \mu_3) - \xi_3(\mu_2 - \mu_3) + M_3\right] \\ &- a_2^3 \left[a_0\omega_3 - b_0\mu_3 + \xi_2(\mu_3\omega_1 - \mu_1\omega_3) + \xi_3(\mu_3\omega_2 - \mu_2\omega_3) + M_3\omega_3\right] \\ &+ a_2^2 b_1 \left[a_0 - a_1\mu_3 + b_2^2\mu_3 + b_1\omega_3 + \xi_2(\mu_1 - \mu_3) - \xi_3(\mu_2 + \mu_3) + M_3\right] \\ &+ a_2^4 \left[b_0 - a_1\omega_3 + \xi_3(\omega_3 - \omega_2) + \xi_2(\omega_3 - \omega_1)\right] + b_1^3\mu_3 - 2a_2 b_1^2 b_2\mu_3 \end{aligned} \tag{3.37}$$

and g_I introduced in (3.31). Only (3.31) is analyzed as the constant a_2 and the function (3.37) are positive for all parameters. Eq. (3.31) is a cubic polynomial with respect to v_3, ξ_2, and ξ_3. To determine the sign of (3.31), the signs of the coefficients of the cubic terms have to be derived. After evaluating the behavior of (3.31) as v_3, ξ_2, and ξ_3 approach infinity, the sign of (3.31) can be determined in terms of its zeros. For this, insert (3.16) into (B.2k)–(B.2m) in Appendix B, so that

$$d_{300} = -4\left(\mu_1+\mu_2\right), \tag{3.38a}$$
$$d_{030} = 4\left(\mu_1-\mu_3\right)^3\left(\mu_1+\mu_2\right), \tag{3.38b}$$
$$d_{003} = 4\left(\mu_2-\mu_3\right)^3\left(\mu_1+\mu_2\right) \tag{3.38c}$$

arise. Hence, the limit of (3.31) as v_3, ξ_2, or ξ_3 approaches positive infinity is given by

$$\lim_{v_3\to\infty} g_\mathrm{I} = \begin{cases} -\infty, & \text{if } \mu_1+\mu_2 > 0 \\ \infty, & \text{if } \mu_1+\mu_2 < 0 \end{cases}, \quad \lim_{\xi_i\to\infty} g_\mathrm{I} = \begin{cases} \infty, & \text{if } \left(\mu_1-\mu_3\right)\left(\mu_1+\mu_2\right) > 0 \\ -\infty, & \text{if } \left(\mu_1-\mu_3\right)\left(\mu_1+\mu_2\right) < 0 \end{cases},$$

and the limit of (3.31) as v_3, ξ_2, or ξ_3 approaches negative infinity reads

$$\lim_{v_3\to-\infty} g_\mathrm{I} = \begin{cases} \infty, & \text{if } \mu_1+\mu_2 > 0 \\ -\infty, & \text{if } \mu_1+\mu_2 < 0 \end{cases}, \lim_{\xi_i\to-\infty} g_\mathrm{I} = \begin{cases} -\infty, & \text{if } \left(\mu_1-\mu_3\right)\left(\mu_1+\mu_2\right) > 0 \\ \infty, & \text{if } \left(\mu_1-\mu_3\right)\left(\mu_1+\mu_2\right) < 0 \end{cases}$$

for all $i = 2, 3$. With this, the number of roots of (B.1) in terms of v_3 and ξ_1 is given by

$$m_{\xi_1,v_3} = \begin{cases} 1, & \text{if } \left(C_{v_3,1} \wedge D_{g_\mathrm{I},v_3} > 0\right) \vee \left(C_{v_3,2} \wedge D_{g_\mathrm{I},v_3} \leq 0\right) \\ 3, & \text{if } \left(\neg C_{v_3,1} \wedge D_{g_\mathrm{I},v_3} > 0\right) \vee \left(\neg C_{v_3,2} \wedge D_{g_\mathrm{I},v_3} \leq 0\right) \end{cases}, \tag{3.39a}$$

if (3.31) is solved for v_3, or

$$m_{\xi_1,\xi_2} = \begin{cases} 1, & \text{if } \left(C_{\xi_2,1} \wedge D_{g_\mathrm{I},\xi_2} > 0\right) \vee \left(C_{\xi_2,2} \wedge D_{g_\mathrm{I},\xi_2} \leq 0\right) \\ 3, & \text{if } \left(\neg C_{\xi_2,1} \wedge D_{g_\mathrm{I},\xi_2} > 0\right) \vee \left(\neg C_{\xi_2,2} \wedge D_{g_\mathrm{I},\xi_2} \leq 0\right) \end{cases}, \tag{3.39b}$$

if (3.31) is solved for ξ_2. The conditions $C_{v_3,1}$, $C_{v_3,2}$, $C_{\xi_2,1}$, and $C_{\xi_2,2}$ given by (3.33). In addition, the discriminants D_{g_I,v_2} and D_{g_I,ξ_2} read

$$D_{g_\mathrm{I},v_3} = 16\mu_3 h_{v_3,1} h_{v_3,2}^3 \tag{3.40a}$$
$$D_{g_\mathrm{I},\xi_2} = 16\mu_3 h_{\xi_2,1} h_{\xi_2,2}^3 \tag{3.40b}$$

with the linear functions

$$\begin{aligned} h_{v_3,1} &= c_{\mathrm{I},v_3,1,00} + c_{\mathrm{I},v_3,1,10}\xi_2 + c_{\mathrm{I},v_3,1,01}\xi_3, \\ h_{v_3,2} &= c_{\mathrm{I},v_3,2,00} + c_{\mathrm{I},v_3,2,10}\xi_2 + c_{\mathrm{I},v_3,2,01}\xi_3, \\ h_{\mathrm{I},\xi_2,1} &= c_{\mathrm{I},\xi_2,1,00} + c_{\mathrm{I},\xi_2,1,10}v_3 + c_{\mathrm{I},\xi_2,1,01}\xi_3, \\ h_{\mathrm{I},\xi_2,2} &= c_{\mathrm{I},\xi_2,2,00} + c_{\mathrm{I},\xi_2,2,10}v_3 + c_{\mathrm{I},\xi_2,2,01}\xi_3 \end{aligned}$$

and the coefficients given by (B.3). The functions $h_{v_3,1}$, $h_{v_3,2}$ are linear in terms of ξ_2 and ξ_3 and the functions $h_{\xi_2,1}$ and $h_{\xi_2,2}$ are linear in terms of v_3 and ξ_3.

To determine the signs of (3.40a) and (3.40b), the zeros of $h_{v_3,1}$, $h_{v_3,2}$, $h_{\xi_2,1}$, and $h_{\xi_2,2}$, the limit of the products between $h_{v_3,1}h_{v_3,2}$, and $h_{\xi_2,1}h_{\xi_2,2}$, and the sign of μ_3 have to be analyzed. First, the interval in which the sign of (3.40a) and (3.40b) stays constant is derived by determining the zeros of (B.3). Here, the zeros are given by (3.35). Thus, after sorting the solutions by their magnitude starting by their minimum, (3.34) is obtained. Second, the sign of the limit of the product $h_{v_3,1}h_{v_3,2}$ as ξ_2 and ξ_3 approach (negative or positive) infinity and the sign of the limit of the product $h_{\xi_2,1}h_{\xi_2,2}$ as v_3 and ξ_3 approach (negative or positive) infinity are determined by analyzing the sign of the coefficients of the quadratic term. This can be done since

$$\begin{aligned} h_{v_3,1}h_{v_3,2} &= d_{v_3,20,\xi_2}\xi_2^2 + d_{v_3,02,\xi_3}\xi_3^2 + r_{\mathrm{I},v_3}(\xi_2,\xi_3) \\ h_{\xi_2,1}h_{\xi_2,2} &= d_{\xi_2,20,v_3}v_3^2 + d_{\xi_2,02,\xi_3}\xi_3^2 + r_{\mathrm{I},\xi_2}(v_3,\xi_3) \end{aligned}$$

are polynomials of even order. Here, the coefficients read

$$\begin{aligned} d_{v_3,20,\xi_2} &= -27\mu_3\left(\omega_1-\omega_3\right)^2\left(a_2+\mu_3\right)^2, \\ d_{v_3,02,\xi_3} &= -27\mu_3\left(\omega_2-\omega_3\right)^2\left(a_2+\mu_3\right)^2, \\ d_{\xi_2,20,v_3} &= 27\mu_3\left(\mu_1-\mu_3\right)^2\left(\omega_1-\omega_3\right)^2\left(a_2+\mu_3\right)^2 \\ d_{\xi_2,02,\xi_3} &= 27\mu_3\left(\mu_1-\mu_3\right)^2\left(a_2+\mu_3\right)^2\left(\mu_3\left(\omega_1-\omega_2\right)+\mu_1\left(\omega_2-\omega_3\right)+\mu_2\left(\omega_3-\omega_1\right)\right)^2 \end{aligned}$$

and r_{v_3} and r_{ξ_2} denote (arbitrary) linear functions. As the coefficients also depend on μ_3, the sign of μ_3 is canceled, so that the sign of the limits of (3.40a) as ξ_2 and ξ_3 approach infinity and the sign of the limits of (3.40b) as v_3 and ξ_3 approach infinity reads

$$\begin{aligned} \operatorname{sign}\left(\lim_{\xi_1\to\pm\infty} D_{g_\mathrm{I},v_3}\right) &= -1, & \operatorname{sign}\left(\lim_{\xi_2\to\pm\infty} D_{g_\mathrm{I},v_3}\right) &= -1, \\ \operatorname{sign}\left(\lim_{v_3\to\pm\infty} D_{g_\mathrm{I},\xi_2}\right) &= 1, & \operatorname{sign}\left(\lim_{\xi_3\to\pm\infty} D_{g_\mathrm{I},\xi_2}\right) &= 1. \end{aligned}$$

Combing this with the zeros, (3.32) is derived. This concludes the proof. □

In comparison to the cycle graph, it is possible to control two critical points induced by the line graph by assigning the coupling strength in the line graph, since $v_2(\cdot)$ is a two-parameter family of (3.13). This is particularly interesting as a controllable Hopf-Hopf bifurcation can be induced, so that it is possible to control two Andronov-Hopf bifurcations by solely assigning the weights of the line graph correctly. In contrast to this, by only adapting the weights of the cycle graph this is not possible since v_3 is a one-parameter family of (3.13). To conclude the analysis of emerging Andronov-Hopf bifurcations in three coupled Andronov-Hopf oscillators, the number of critical points induced by the bifurcation parameter v_3 is investigated numerically.

Example 3.3 *Subsequently, the emergence of Andronov-Hopf bifurcations in three coupled Andronov-Hopf oscillators* (3.13) *is investigated by verifying the results on the number of critical points* $v_{3,\mathrm{H}}$. *For this, the oscillator parameters are given by the damping coefficients* $\mu_1 = -1\,\frac{1}{\mathrm{s}}$, $\mu_2 = -2\,\frac{1}{\mathrm{s}}$, *and* $\mu_3 = -3\,\frac{1}{\mathrm{s}}$ *and the natural frequencies* $\omega_1 = -4\,\frac{1}{\mathrm{s}}$, $\omega_2 = -5\,\frac{1}{\mathrm{s}}$,

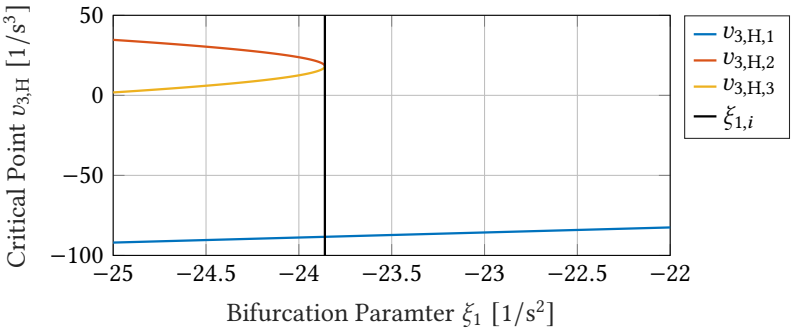

(a) Critical points $v_{3,\mathrm{H}}$ in terms of the parameter ξ_1. The parameter ξ_2 is assumed to be outside of $\mathcal{I}_0$.

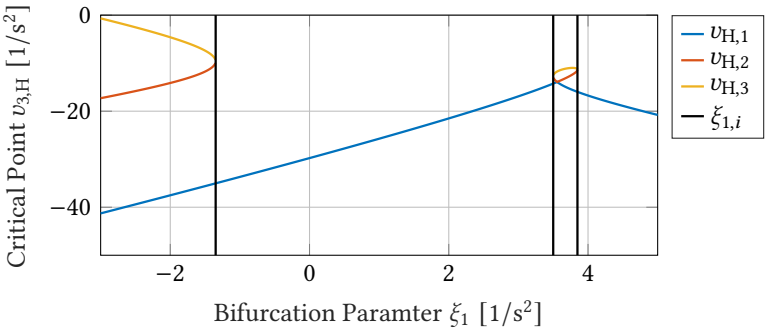

(b) Critical points $v_{3,\mathrm{H}}$ in terms of the parameter ξ_1. The parameter ξ_2 is assumed to be inside of $\mathcal{I}_0$.

Figure 3.4.: Critical points $v_{3,\mathrm{H}}$ of three coupled Andronov-Hopf oscillator as a function of the parameter ξ_1.

and $\omega_3 = -6\,\frac{1}{\mathrm{s}}$. *To induce the bifurcations, Theorem 3.2 is used and the adjacency matrix is assumed to be*

$$\Gamma = \begin{bmatrix} 0 & \hat{\gamma}_{12} & \hat{\gamma}_{13} \\ \hat{\gamma}_{21} & 0 & \hat{\gamma}_3 \\ 0 & \hat{\gamma}_3 & 0 \end{bmatrix}$$

with $\hat{\gamma}_{21} = 1$, *which implies that the bifurcation parameter reads* $v_3 = \hat{\gamma}_{21}\hat{\gamma}_{32}\hat{\gamma}_{13}$ *and the number of colliding, critical points can be controlled by adjusting* ξ_1 *and* ξ_2. *For this, the interval* $\mathcal{I}_0$ *to determine the number of colliding, critical points is given by* $\mathcal{I}_0 = [7.5, 8]$. *The critical points are evaluated by determining the real-valued solutions of* (B.1) *in Appendix B as a function of* ξ_1 *for* $\xi_2 \in \{2.7839, 3.9370\}$. *In addition, the roots* $\xi_{1,i}$ *of* (3.22) *are evaluated to compute the point where two critical points are colliding. The results are visualized in Figure 3.4. It is showcased that the number of critical points are determined by Theorem 3.2.*

Emerging Hopf-Hopf bifurcations Subsequently, the emergence of Hopf-Hopf bifurcations in the network (3.13) is investigated. By inducing this bifurcation type, it is implied that two Andronov-Hopf bifurcations with different characteristic frequencies can be controlled at the same time, so that two characteristic frequencies can be tuned and two clusters can emerge. To determine the conditions on the emergence of Hopf-Hopf bifurcations,

the discriminant of (B.1) has to be zero. Then two eigenvalues of (3.15) will lay on the imaginary axis. However, it has to be additionally imposed that this zero is a local maximum, since this condition implies that the eigenvalues on the imaginary axis are not equal, so that they are not colliding and the imaginary part of the two pairs of eigenvalues are different.

Theorem 3.4 *Assume that v_3 and ξ_1 are bifurcation parameters. Then two critical points of the Andronov-Hopf bifurcation of* (3.13) *determined by Theorem 3.2 are equivalent and their value define a critical point of a Hopf-Hopf bifurcation, if the bifurcation parameter ξ_1 is equal to the critical value*

$$\begin{aligned}\xi_{1,\mathrm{HH,o}} = \frac{1}{a_2^3\left(b_2+\omega_3\right)-a_2^2 b_1}\Big[&a_2^2 b_1\left(b_2^2-a_1+\gamma_{23}\gamma_{32}+\gamma_{13}\gamma_{31}\right)\\ &+a_2^3\left(b_2\left(c_1-\gamma_{23}\gamma_{32}-\gamma_{13}\gamma_{31}\right)+b_0-\omega_1\gamma_{23}\gamma_{32}-\omega_2\gamma_{13}\gamma_{31}\right)+b_1^3-2a_2 b_1^2 b_2\Big]\end{aligned} \tag{3.41}$$

and the condition

$$\begin{aligned}\Big\{\Big[&\left(\omega_1>\omega_3\wedge\xi_2<\xi_{2,\mathrm{HH,o}}\right)\vee\left(\omega_1<\omega_3\wedge\xi_2>\xi_{2,\mathrm{HH,o}}\right)\Big]\\ &\wedge\Big[\left(\omega_1>\omega_3\wedge\mu_1>\mu_{1,\mathrm{HH,o}}\right)\vee\left(\omega_1<\omega_3\wedge\mu_1<\mu_{1,\mathrm{HH,o}}\right)\Big]\Big\}\\ \vee\Big\{\Big[&\left(\omega_1>\omega_3\wedge\xi_2>\xi_{2,\mathrm{HH,o}}\right)\vee\left(\omega_1<\omega_3\wedge\xi_2<\xi_{2,\mathrm{HH,o}}\right)\Big]\\ &\wedge\Big[\left(\omega_1>\omega_3\wedge\mu_1<\mu_{1,\mathrm{HH,o}}\right)\vee\left(\omega_1<\omega_3\wedge\mu_1>\mu_{1,\mathrm{HH,o}}\right)\Big]\Big\}\end{aligned} \tag{3.42}$$

is satisfied. Here, the interval limits are denoted by

$$\begin{aligned}\xi_{2,\mathrm{HH,o}} = \frac{}{4a_2^3\left(\omega_1-\omega_3\right)}\Big\{&4a_2^3\left[b_0-a_1\omega_3+\xi_3\left(\omega_3-\omega_2\right)\right]\\ &-4a_2^2 b_1 b_2\omega_3-a_2 b_1^2\left(b_2-3\omega_3\right)+b_1^3\Big\},\end{aligned} \tag{3.43a}$$

$$\mu_{1,\mathrm{HH,o}} = -\frac{\omega_2-\omega_3}{\omega_1-\omega_3}\mu_2. \tag{3.43b}$$

Proof. To determine that the discriminant (3.25) has a local maximum, which is also a root of (3.25), its structure is exploited, as the discriminant (3.25) is composed of a product between the function (3.22) and (3.26), where (3.26) is squared. Hence, if the (squared) function (3.26) vanishes, (3.25) has a local extremum, which is a root. In addition, the sign of (3.22) at the extremum determines, if the extremum is a minimum or a maximum. If its sign is positive, the extremum is a minimum otherwise a maximum.

First, the roots of (3.26) in terms of ξ_1 are determined. As (3.26) is a linear function in ξ_1, ξ_2 and ξ_3, the critical point of the Hopf-Hopf bifurcation is unique and the critical point (3.41) is obtained by solving (3.26) for ξ_1.

Second, the sign of the discriminant (3.25) is investigated by analyzing (3.22) at the critical point (3.41) of the Hopf-Hopf bifurcation. Inserting (3.41) into (3.25), results in

$$g_{\mathrm{o}}(\xi_{1,\mathrm{HH,o}}) = \frac{f_{\mathrm{o,HH}}^2(\xi_2,\xi_3)\,g_{\mathrm{o,HH}}(\xi_2,\xi_3)}{h_{\mathrm{o,HH}}} \tag{3.44}$$

with

$$f_{\mathrm{o,HH}} = a_2^3 \left(b_2^2\omega_3 + b_2^3 - a_1\omega_3 + d_0 + \xi_2\left(\omega_3 - \omega_1\right) + \xi_3\left(\omega_3 - \omega_2\right)\right) - 4a_2^2 b_1 b_2\left(b_2 + \omega_3\right) + a_2 b_1^2\left(5b_2 + 3\omega_3\right) - 2b_1^3, \quad (3.45a)$$

$$g_{\mathrm{o,HH}} = b_1^3 - 4a_2^2 b_1 b_2\omega_3 - a_2 b_1^2\left(b_2 - 3\omega_3\right) + 4a_2^3\left[b_0 - a_1\omega_3 + \xi_3\left(\omega_3 - \omega_2\right) + \xi_2\left(\omega_3 - \omega_1\right)\right], \quad (3.45b)$$

$$h_{\mathrm{o,HH}} = a_2^6\left[a_2\left(b_2 + \omega_3\right) - b_1\right]^3. \quad (3.45c)$$

Here, (3.45a) cannot influence the sign of (3.44), since this function is squared. Hence, the sign of (3.44) is determined by

$$\operatorname{sign}\left(g_{\mathrm{o}}(\xi_{1,\mathrm{HH,o}})\right) = \begin{cases} 1, & \text{if } \left(g_{\mathrm{o,HH}} > 0 \wedge h_{\mathrm{o,HH}} > 0\right) \vee \left(g_{\mathrm{o,HH}} < 0 \wedge h_{\mathrm{o,HH}} < 0\right) \\ -1, & \text{if } \left(g_{\mathrm{o,HH}} > 0 \wedge h_{\mathrm{o,HH}} < 0\right) \vee \left(g_{\mathrm{o,HH}} < 0 \wedge h_{\mathrm{o,HH}} > 0\right) \end{cases}.$$

On the one hand, the sign of eq. (3.45b) is determined in terms of ξ_2 and (3.45b) is a linear function in ξ_2 and ξ_3. Thus, solving it for ξ_2, results in (3.43a). As the slope of (3.45b) is given by $\omega_3 - \omega_1$, its sign reads

$$g_{\mathrm{o,HH}} \begin{cases} < 0, & \text{if } \left(\omega_1 > \omega_3 \wedge \xi_2 < \xi_{2,\mathrm{HH,o}}\right)\left(\omega_1 < \omega_3 \wedge \xi_2 > \xi_{2,\mathrm{HH,o}}\right) \\ > 0, & \text{if } \left(\omega_1 > \omega_3 \wedge \xi_2 > \xi_{2,\mathrm{HH,o}}\right)\left(\omega_1 < \omega_3 \wedge \xi_2 < \xi_{2,\mathrm{HH,o}}\right) \end{cases}. \quad (3.46)$$

On the other hand, the sign of (3.45c) is evaluated in terms of μ_1. For this, (3.16) is inserted into (3.45c), which yields

$$h_{\mathrm{o,HH}} = \mu_1\left(\omega_1 - \omega_3\right) + \mu_2\left(\omega_2 - \omega_3\right). \quad (3.47)$$

Hence, (3.47) is a linear function in μ_1 and μ_2. Solving (3.47) for μ_1, results in (3.43b). Taking the slope of (3.45c) into account, the sign of (3.45c) is determined by

$$h_{\mathrm{o,HH}} \begin{cases} < 0, & \text{if } \left(\omega_1 > \omega_3 \wedge \mu_1 < \mu_{1,\mathrm{HH,o}}\right) \vee \left(\omega_1 < \omega_3 \wedge \mu_1 > \mu_{1,\mathrm{HH,o}}\right) \\ > 0, & \text{if } \left(\omega_1 > \omega_3 \wedge \mu_1 > \mu_{1,\mathrm{HH,o}}\right) \vee \left(\omega_1 < \omega_3 \wedge \mu_1 < \mu_{1,\mathrm{HH,o}}\right) \end{cases}. \quad (3.48)$$

The condition (3.42) is thus obtained by combing (3.46) and (3.48) and asserting

$$\operatorname{sign}(g_{\mathrm{o}}(\xi_{1,\mathrm{HH,o}})) = -1,$$

which concludes the proof. □

Theorem 3.5 *Assume that ξ_1 and ξ_2 are bifurcation parameters and let*

$$\begin{aligned} \xi_{3,\mathrm{HH,I}} = {} & \frac{1}{4a_2^3\left(\mu_3\left(\omega_2 - \omega_1\right) + \mu_2\left(\omega_1 - \omega_3\right) + \mu_1\left(\omega_3 - \omega_2\right)\right)} \\ & \times \left(4a_2^2 b_1 b_2\left(\mu_1\omega_3 - \mu_3\omega_1\right) + a_2 b_1^2\left(\omega_3\left(a_2 - 3\mu_1\right) - \omega_1\left(a_2 - 3\mu_3\right)\right.\right. \\ & \left.\left. + b_2\left(\mu_1 - \mu_3\right)\right) + 4a_2^3\left(a_1\left(\mu_1\omega_3 - \mu_3\omega_1\right) + \left(\omega_1 - \omega_3\right)\left(a_0 + M_3\right)\right. \right. \\ & \left.\left. + b_0\left(\mu_3 - \mu_1\right)\right) + b_1^3\left(\mu_3 - \mu_1\right)\right) \end{aligned} \quad (3.49a)$$

$$\mu_{1,\mathrm{HH,I}} = -\frac{\mu_2\left(\mu_3\left(\omega_1 + \omega_2 - 2\omega_3\right) + \mu_2\left(\omega_1 - \omega_3\right)\right)}{2\mu_3\left(\omega_1 - \omega_3\right) + \mu_2\left(2\omega_1 - \omega_2 - \omega_3\right)}, \quad (3.49b)$$

$$\mu_{2,\mathrm{HH,I}} = -\frac{2\mu_3\left(\omega_1 - \omega_3\right)}{2\omega_1 - \omega_2 - \omega_3}. \quad (3.49c)$$

Then two critical points of the Andronov-Hopf bifurcation of (3.13) *determined by Theorem 3.3 are equivalent and they define a critical point of a Hopf-Hopf bifurcation, if the bifurcation parameter ξ_2 is equal to the critical point*

$$\begin{aligned}\xi_{2,\mathrm{HH,I}} = &\frac{a_2^2 b_1 \left[\mu_3 \left(b_2^2 - c_1 + \xi_3\right) + b_1\omega_3 + a_0 - \mu_2\xi_3 + M_3\right]}{a_2^3 \left[\omega_1 \left(a_2 + \mu_3\right) - \omega_3 \left(a_2 + \mu_1\right) + b_2 \left(\mu_3 - \mu_1\right)\right] + a_2^2 b_1 \left(\mu_1 - \mu_3\right)} \\ &- \frac{a_2^3 b_2 \left[b_1\omega_3 + \mu_3 \left(\xi_3 - a_1\right) + a_0 - \mu_2\xi_3 + M_3\right]}{a_2^3 \left[\omega_1 \left(a_2 + \mu_3\right) - \omega_3 \left(a_2 + \mu_1\right) + b_2 \left(\mu_3 - \mu_1\right)\right] + a_2^2 b_1 \left(\mu_1 - \mu_3\right)} \\ &- \frac{a_2^3\omega_3 \left(a_0 - \mu_2\xi_3 + M_3\right) + \mu_3 \left(b_0 - \xi_3\omega_2\right)}{a_2^3 \left[\omega_1 \left(a_2 + \mu_3\right) - \omega_3 \left(a_2 + \mu_1\right) + b_2 \left(\mu_3 - \mu_1\right)\right] + a_2^2 b_1 \left(\mu_1 - \mu_3\right)} \\ &+ \frac{b_1^3\mu_3 - 2a_2 b_1^2 b_2\mu_3 + a_2^4 \left[\omega_3 \left(\xi_3 - a_1\right) + b_0 - \xi_3\omega_2\right]}{a_2^3 \left[\omega_1 \left(a_2 + \mu_3\right) - \omega_3 \left(a_2 + \mu_1\right) + b_2 \left(\mu_3 - \mu_1\right)\right] + a_2^2 b_1 \left(\mu_1 - \mu_3\right)}\end{aligned} \tag{3.50}$$

and

$$\begin{aligned}\Big[\big(\xi_3 > \xi_{3,\mathrm{HH,I}} \wedge C_{\mathrm{I,HH}}\big) \vee \big(\xi_3 < \xi_{3,\mathrm{HH,I}} \wedge \neg C_{\mathrm{I,HH}}\big) \\ \wedge(\mu_1 > \mu_{1,\mathrm{HH,I}} \wedge \mu_2 < \mu_{2,\mathrm{HH,I}}) \vee (\mu_1 < \mu_{1,\mathrm{HH,I}} \wedge \mu_2 > \mu_{2,\mathrm{HH,I}})\Big] \\ \vee \Big[\big(\xi_3 < \xi_{3,\mathrm{HH,I}} \wedge C_{\mathrm{I,HH}}\big) \vee \big(\xi_3 > \xi_{3,\mathrm{HH,I}} \wedge \neg C_{\mathrm{I,HH}}\big) \\ \wedge(\mu_1 > \mu_{1,\mathrm{HH,I}} \wedge \mu_2 > \mu_{2,\mathrm{HH,I}}) \vee (\mu_1 < \mu_{1,\mathrm{HH,I}} \wedge \mu_2 < \mu_{2,\mathrm{HH,I}})\Big]\end{aligned} \tag{3.51}$$

is satisfied with the condition

$$\begin{aligned}C_{\mathrm{I,HH}} = \Big[&\mu_1 \in \left(\min\{\mu_{1,\mathrm{H,I},1}, \mu_{1,\mathrm{H,I},2}\}, \max\{\mu_{1,\mathrm{H,I},1}, \mu_{1,\mathrm{H,I},2}\}\right) \wedge \omega_2 > \omega_3) \\ &\vee(\mu_1 \notin \left(\min\{\mu_{1,\mathrm{H,I},1}, \mu_{1,\mathrm{H,I},2}\}, \max\{\mu_{1,\mathrm{H,I},1}, \mu_{1,\mathrm{H,I},2}\}\right) \wedge \omega_2 > \omega_3\Big]\,.\end{aligned} \tag{3.52}$$

Here, $\neg C_{\mathrm{I,HH}}$ denotes the negation of the condition $C_{\mathrm{I,HH}}$, while the interval limits $\mu_{1,\mathrm{H,I},1}$ and $\mu_{1,\mathrm{H,I},2}$ of (3.52) *are given by*

$$\mu_{1,\mathrm{H,I},1} = -\mu_2 - \mu_3, \qquad \mu_{1,\mathrm{H,I},2} = \frac{\mu_3 \left(\omega_2 - \omega_1\right) + \mu_2 \left(\omega_1 - \omega_3\right)}{\omega_2 - \omega_3}.$$

Proof. The proof follows the route of the proof of Theorem 3.4. For this, the bifurcation parameters are assumed to be ξ_1 and ξ_2.

First, the roots of (3.37) in terms of ξ_2 are derived. As (3.37) is linear function in ξ_2 and ξ_3, it has a unique root, which is given by (3.50).

Second, the sign of (3.31) at the extremum values is investigated. Inserting (3.50) into (3.31) and sorting terms, yields

$$g_{\mathrm{I}}(\xi_{2,\mathrm{HH,I}}) = \frac{f_{\mathrm{I,HH}}^2(v_3, \xi_3) g_{\mathrm{I,HH}}(v_3, \xi_3)}{h_{\mathrm{I,HH}}} \tag{3.53}$$

with the linear function

$$
\begin{aligned}
f_{\mathrm{I,HH}} = {} & a_2^3\left(\omega_1-\omega_3\right)\left(a_2+\mu_3\right)^2 v_3 + a_2^3\left(a_2+\mu_3\right)^2\left(\mu_3\left(\omega_1-\omega_2\right)+\mu_1\left(\omega_2-\omega_3\right)\right. \\
& \left.+\mu_2\left(\omega_3-\omega_1\right)\right)\xi_3 - a_2^5\left(\omega_3\left(a_0-\omega_1\left(b_1-2b_2\mu_3\right)-a_1\mu_1\right)+\omega_3^2\left(b_2\left(\mu_1-3\mu_3\right)+b_1\right.\right. \\
& \left.\left.-\mu_3\omega_1\right)+\omega_1\left(a_1\mu_3-a_0\right)+b_0\left(\mu_1-\mu_3\right)+\mu_1\omega_3^3\right) + a_2^4\mu_3\left(\omega_3\left(b_2^2\left(2\mu_1-3\mu_3\right)\right.\right. \\
& \left.\left.-2b_2\mu_3\omega_1+2a_1\mu_1-2a_0\right)+\omega_1\left(\mu_3\left(b_2^2-2a_1\right)+2a_0\right)+2b_2\mu_1\omega_3^2+2b_1\left(\omega_3-\omega_1\right)\right. \\
& \left.\times\left(b_2-2\omega_3\right)+2b_0\left(\mu_3-\mu_1\right)\right) + a_2^3\mu_3\left(\mu_3\left(b_2^2\left(\mu_3\omega_1-\mu_1\omega_3\right)+b_2^3\left(\mu_3-\mu_1\right)\right.\right. \\
& \left.\left.+\omega_1\left(a_0-a_1\mu_3\right)+\omega_3\left(a_1\mu_1-a_0\right)+b_0\left(\mu_3-\mu_1\right)\right)+b_1\left(b_2^2\left(\mu_1-\mu_3\right)\right.\right. \\
& \left.\left.-2b_2\left(\mu_3\left(3\omega_1-4\omega_3\right)+\mu_1\omega_3\right)+3\omega_3\left(\mu_3\omega_1-\mu_1\omega_3\right)\right)+2b_1^2\left(\omega_1-\omega_3\right)\right) \\
& + a_2^2 b_1\mu_3\left(b_1\left(2b_2\left(\mu_3-\mu_1\right)+5\mu_3\left(\omega_1-\omega_3\right)\right)+4b_2\mu_3\left(b_2\left(\mu_1-\mu_3\right)-\mu_3\omega_1\right.\right. \\
& \left.\left.+\mu_1\omega_3\right)\right) + a_2 b_1^2\mu_3\left(\mu_3\left(5b_2\left(\mu_3-\mu_1\right)+3\mu_3\omega_1-3\mu_1\omega_3\right)+b_1\left(\mu_1-\mu_3\right)\right) \\
& + a_2^6\left(\omega_1-\omega_3\right)\omega_3^2 + 2b_1^3\left(\mu_1-\mu_3\right)\mu_3^2, \qquad (3.54a)
\end{aligned}
$$

$$
\begin{aligned}
g_{\mathrm{I,HH}} = {} & 4a_2^3\left(\mu_3\left(\omega_1-\omega_2\right)+\mu_1\left(\omega_2-\omega_3\right)+\mu_2\left(\omega_3-\omega_1\right)\right)\xi_3 + 4a_2^3\left(\omega_1-\omega_3\right)v_3 \\
& + 4a_2^2 b_1 b_2\left(\mu_1\omega_3-\mu_3\omega_1\right)+b_1^3\left(\mu_3-\mu_1\right)+a_2 b_1^2\left(\omega_3\left(a_2-3\mu_1\right)-\omega_1\left(a_2-3\mu_3\right)\right. \\
& \left.+b_2\left(\mu_1-\mu_3\right)\right)+4a_2^3\left(\omega_1\left(a_0-a_1\mu_3\right)+\omega_3\left(a_1\mu_1-a_0\right)+b_0\left(\mu_3-\mu_1\right)\right), \qquad (3.54b)
\end{aligned}
$$

$$
h_{\mathrm{I,HH}} = a_2^6\left(a_2\left(a_2\left(\omega_1-\omega_3\right)+b_2\left(\mu_3-\mu_1\right)+\mu_3\omega_1-\mu_1\omega_3\right)+b_1\left(\mu_1-\mu_3\right)\right)^3. \qquad (3.54c)
$$

In particular, only (3.54b) and (3.54c) influence the sign of (3.53), since (3.54a) is squared. Hence, the sign of (3.53) is given by

$$
\operatorname{sign}\left(g_{\mathrm{I}}(\xi_{2,\mathrm{HH,I}})\right) = \begin{cases} 1, & \text{if } \left(g_{\mathrm{I,HH}}>0 \wedge h_{\mathrm{I,HH}}>0\right) \vee \left(g_{\mathrm{I,HH}}<0 \wedge h_{\mathrm{I,HH}}<0\right) \\ -1, & \text{if } \left(g_{\mathrm{I,HH}}>0 \wedge h_{\mathrm{I,HH}}<0\right) \vee \left(g_{\mathrm{I,HH}}<0 \wedge h_{\mathrm{I,HH}}>0\right) \end{cases}.
$$

On the one hand, the sign of (3.54b) is determined in terms of ξ_3. Eq. (3.54b) is a linear function in v_3 and ξ_3. Thus, solving it for ξ_3, results in (3.49a). In addition, its slope in terms of ξ_3 is given by

$$
\frac{\mathrm{d}g_{\mathrm{I,HH}}}{\mathrm{d}\xi_3} = -4(\mu_1+\mu_2+\mu_3)^3\left(\mu_3\left(\omega_1-\omega_2\right)+\mu_1\left(\omega_2-\omega_3\right)+\mu_2\left(\omega_3-\omega_1\right)\right) \qquad (3.55)
$$

As $(\mu_1+\mu_2+\mu_3)^2$ does not influence the sign of (3.55), it can be viewed as a quadratic polynomial in terms of μ_1, μ_2, or μ_3. Then the sign of (3.55) in terms of μ_1 is determined by

$$
\operatorname{sign}\left(\frac{\mathrm{d}g_{\mathrm{I,HH}}}{\mathrm{d}\xi_3}\right) = \begin{cases} >0, & \text{if } C_{\mathrm{I,HH}} \\ <0, & \text{if } \neg C_{\mathrm{I,HH}} \end{cases}.
$$

with the condition $C_{\mathrm{I,HH}}$ given by (3.52) and $\neg C_{\mathrm{I,HH}}$ denoting the negation of $C_{\mathrm{I,HH}}$, since it is a quadratic term of (3.55) in terms μ_1 reads $-4(\omega_2-\omega_3)$. Hence, the sign of (3.53) is given by

$$
\operatorname{sign}\left(g_{\mathrm{I}}(\xi_{2,\mathrm{HH}})\right) = \begin{cases} 1, & \text{if } \left(\xi_3>\xi_{3,\mathrm{HH,I}} \wedge C_{\mathrm{I,HH}}\right) \vee \left(\xi_3<\xi_{3,\mathrm{HH,I}} \wedge \neg C_{\mathrm{I,HH}}\right) \\ -1, & \text{if } \left(\xi_3<\xi_{3,\mathrm{HH,I}} \wedge C_{\mathrm{I,HH}}\right) \vee \left(\xi_3>\xi_{3,\mathrm{HH,I}} \wedge \neg C_{\mathrm{I,HH}}\right) \end{cases}. \qquad (3.56)
$$

On the other hand, the sign of (3.45c) is evaluated in terms of μ_1. For this, (3.16) is inserted into (3.45c), which yields

$$h_{\mathrm{I,HH}} = \mu_2 \left(\mu_3 \left(\omega_1 + \omega_2 - 2\omega_3\right) + \mu_2 \left(\omega_1 - \omega_3\right)\right) + \mu_1 \left(2\mu_3 \left(\omega_1 - \omega_3\right) + \mu_2 \left(2\omega_1 - \omega_2 - \omega_3\right)\right). \quad (3.57)$$

Hence, eq. (3.57) is a linear function in μ_1 and μ_3 and a quadratic function in μ_2. After determining the root of (3.57) and its slope in terms of μ_1, it follows that

$$\operatorname{sign}\left(h_{\mathrm{I}}(\xi_{2,\mathrm{HH}})\right) = \begin{cases} 1, & \text{if } (\mu_1 > \mu_{1,\mathrm{HH,I}} \wedge \mu_2 > \mu_{2,\mathrm{HH,I}}) \\ & \quad \vee (\mu_1 < \mu_{1,\mathrm{HH,I}} \wedge \mu_2 < \mu_{2,\mathrm{HH,I}}) \\ -1, & \text{if } (\mu_1 > \mu_{1,\mathrm{HH,I}} \wedge \mu_2 < \mu_{2,\mathrm{HH,I}}) \\ & \quad \vee (\mu_1 < \mu_{1,\mathrm{HH,I}} \wedge \mu_2 > \mu_{2,\mathrm{HH,I}}) \end{cases} \quad (3.58)$$

with $\mu_{1,\mathrm{HH,I}}$ and $\mu_{2,\mathrm{HH,I}}$ given by (3.49b) and (3.49b). The condition (3.51) is thus obtained by combing (3.56) and (3.58) and asserting $\operatorname{sign}(g_{\mathrm{I}}(\xi_{2,\mathrm{HH,I}})) = -1$, which concludes the proof. □

To conclude the bifurcation analysis of three coupled Andronov-Hopf oscillators, the number of critical points and the tunability enhancement are visualized.

Example 3.4 *The emergence of the Hopf-Hopf bifurcation and the frequency tunability as a function of the damping coefficient μ_2 in a neighborhood of its critical point is computed numerically. The oscillator parameters are given by the damping coefficients $\mu_1 = -1\,\frac{1}{\mathrm{s}}$, $\mu_2 \in [-5, 0]\,\frac{1}{\mathrm{s}}$, and $\mu_3 = -3$ and the natural frequencies $\omega_1 = 3\,\frac{1}{\mathrm{s}}$, $\omega_2 = 4\,\frac{1}{\mathrm{s}}$, and $\omega_3 = 5\,\frac{1}{\mathrm{s}}$. The network topology is assumed to be described by the adjacency matrix*

$$\Gamma = \begin{bmatrix} 0 & \hat{\gamma}_{12} & \hat{\gamma}_{13} \\ \hat{\gamma}_{21} & 0 & \hat{\gamma}_{23} \\ 0 & \hat{\gamma}_{32} & 0 \end{bmatrix}$$

with the coupling coefficients $\hat{\gamma}_{13} = -12\,\frac{1}{\mathrm{s}}$, $\hat{\gamma}_{21} = 1\,\frac{1}{\mathrm{s}}$, and $\hat{\gamma}_{32} = 1\,\frac{1}{\mathrm{s}}$. The remaining coupling coefficients follow Theorem 3.5 implying

$$\hat{\gamma}_{12} = \frac{\xi_{1,\mathrm{HH}}}{\gamma_{21}}, \qquad \hat{\gamma}_{23} = \frac{\xi_{2,\mathrm{HH}}}{\gamma_{32}}.$$

The results are depicted in Figure 3.5. It is demonstrated that the characteristic frequencies at the critical points can be tuned by adjusting μ_2. In contrast to two coupled Andronov-Hopf oscillators, these characteristic frequencies are not constrained by the natural frequencies of the oscillator.

Influence of the network topology on higher order degradation

Subsequently, the influence of the network topology on the emergence of higher-order degradation and thus the controllability of multiple Andronov-Hopf bifurcations is analyzed in networks of injectively coupled Andronov-Hopf oscillators. In particular, the

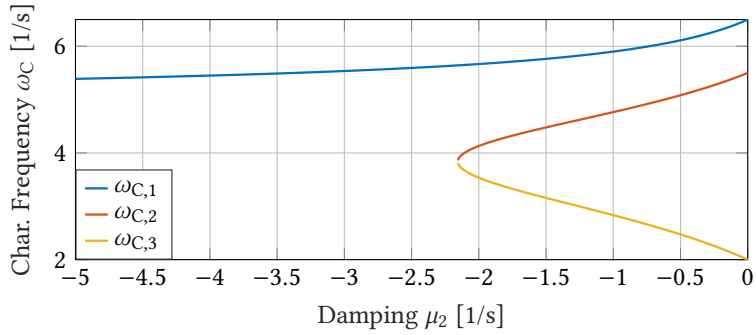

(a) Characteristic frequencies $\omega_{C,1}$ at the critical point of the Andronov-Hopf bifurcation, $\omega_{C,2}$ and $\omega_{C,3}$ at the critical point of the Hopf-Hopf bifurcation.

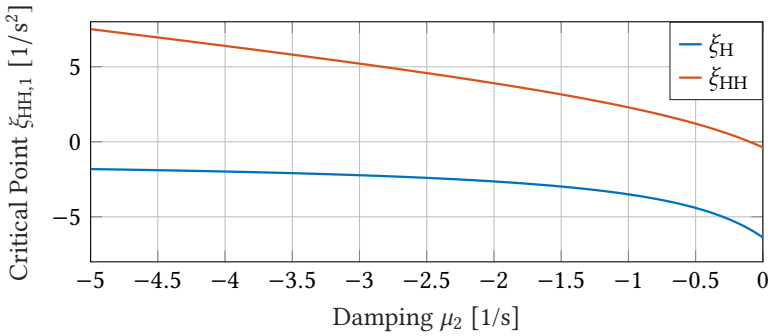

(b) Critical points ξ_H of the Andronov-Hopf bifurcation and ξ_{HH} of the Hopf-Hopf bifurcation.

Figure 3.5.: Characteristic frequencies $\omega_{C,1}$ at the critical point of the Andronov-Hopf bifurcation, $\omega_{C,2}$ and $\omega_{C,3}$ at the critical point of the Hopf-Hopf bifurcation and critical points ξ_H of the Andronov-Hopf bifurcation and ξ_{HH} of the Hopf-Hopf bifurcation as a function of the damping coefficient μ_2.

number of Andronov-Hopf bifurcations can be exploited to control multiple characteristic frequencies and the dynamics of the network (3.5). The i-th oscillator in the network is governed by

$$\dot{z}_i = (\mu_i + \mathrm{i}\omega_i)z_i - |z_i|^2 z_i + \sum_{j=1}^{n} \gamma_{ij} z_j, \qquad t > 0, \qquad z_i(0) = z_{i,0}.$$

Motivated by the bifurcation analysis of three coupled Andronov-Hopf oscillators, network graphs are identified, which are independent and induce N-parameter family of the network (3.5) with the size $N \in \mathbb{N}$, i.e., N parameters act on the dynamic behavior of the network (3.5) [76]. This is done by determining the number of coefficients of the characteristic polynomial of the system matrix of (3.5), which can be adjusted by the coupling strengths of the graphs. This number is equivalent to the size N of the N-

parameter family of the network (3.5). To obtain the system matrix, (3.5) is linearized around $z_{i,\mathrm{eq}} = 0$, which yields

$$A_n = \begin{bmatrix} \mu_1 + \mathrm{i}\omega_1 & \gamma_{12} & \gamma_{13} & \cdots & \gamma_{1n} \\ \gamma_{21} & \mu_2 + \mathrm{i}\omega_2 & \gamma_{23} & \cdots & \gamma_{2n} \\ \gamma_{31} & \gamma_{32} & \mu_3 + \mathrm{i}\omega_3 & \cdots & \gamma_{3n} \\ \vdots & \vdots & \vdots & \ddots & \vdots \\ \gamma_{n1} & \gamma_{n2} & \gamma_{n3} & \cdots & \mu_n + \mathrm{i}\omega_n \end{bmatrix}. \tag{3.59}$$

The analysis is subsequently done by first analyzing the maximum size of the N-parameter family of (3.5) that can be induced by a graph. Second, the size N of certain network graphs is derived.

Lemma 3.1 *Consider the network* (3.5) *of* $n \in \mathbb{N}$ *coupled oscillators and assume that the coupling coefficients* γ_{ij} *for all* $(i,j) \in \mathcal{E}$ *are the bifurcation parameters. Then the maximum size* $N_{\max}$ *of the* N*-parameter family of the network* (3.5) *induced by the coupling* γ_{ij} *is given by* $N_{\max} = n - 1$.

Proof. To verify the claim, it is shown that the characteristic polynomial of (3.5) does not satisfy the condition that there exists a parameter configuration of the bifurcation parameters γ_{ij} for all $i,j \in \mathcal{V}$, so that n complex conjugated eigenvalues have zero real part. This implies that at maximum $n-1$ complex conjugated eigenvalues with zero real part can be induced by the bifurcation parameters γ_{ij}.

The system matrix of (3.5) is given by (3.59), so that its characteristic polynomial reads

$$P_{A_n}(\lambda) = \sum_{i=0}^{n} a_i \lambda^i$$

with the coefficients $a_i \in \mathbb{C}$ for all $i = 0, 1, \ldots, n$. However, its coefficients a_i are rather difficult to compute in general. Only the $n-1$-th coefficient is easily determined. This coefficient is given by

$$a_{n-1} = \operatorname{tr}\left(\left. \frac{\mathrm{d}\boldsymbol{f}(\boldsymbol{z})}{\mathrm{d}\boldsymbol{z}} \right|_{z_{\mathrm{eq}}=0} \right) = \sum_{i=1}^{n} (\mu_i + \mathrm{i}\omega_i). \tag{3.60}$$

It follows that (3.60) cannot be adjusted by the coupling γ_{ij} for all $(i,j) \in \mathcal{E}$. Thus, amending that the characteristic polynomial of (3.59) has n complex eigenvalues on the imaginary axis, implies that $\mathrm{Re}(a_{n-1}) = 0$ has to be satisfied. However, this cannot be satisfied by assigning the bifurcation parameters γ_{ij} for all $(i,j) \in \mathcal{E}$, so that the claim follows. □

The results of Lemma 3.1 and their implications are further investigated by analyzing the N-parameter family of n-cycle graph and the tree graph. Examples for these graphs are sketched in Figure 3.6.

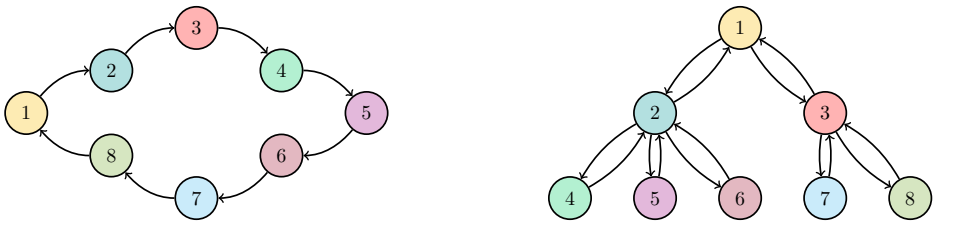

(a) Eight oscillators coupled in a 8-cycle graph. **(b)** Eight oscillators coupled in a tree graph.

Figure 3.6.: Exemplary sketches of the investigated graphs.

Proposition 3.1 *Consider the network* (3.5) *of* $n \in \mathbb{N}$ *coupled oscillators and assume that the oscillators are coupled in a n-cycle graph. In addition, let the bifurcation parameter be the coupling* γ_{ij} *for all* $(i,j) \in \mathcal{E}$*. Then the size* N_o *of the* N*-parameter family induced by the coupling* γ_{ij} *is given by* $N_o = 1$*.*

Proof. To verify the claim, the characteristic polynomial of the linearization of (3.5) is analyzed. The system matrix of Andronov-Hopf oscillators coupled in a n-cycle graph reads

$$A_o = \begin{bmatrix} \mu_1 + \mathrm{i}\omega_1 & 0 & 0 & \cdots & 0 & \gamma_{1n} \\ \gamma_{21} & \mu_2 + \mathrm{i}\omega_2 & 0 & \cdots & 0 & 0 \\ 0 & \gamma_{32} & \mu_3 + \mathrm{i}\omega_3 & \cdots & 0 & 0 \\ \vdots & \vdots & \vdots & \ddots & \vdots & \vdots \\ 0 & 0 & 0 & \cdots & \gamma_{(n-1)n} & \mu_n + \mathrm{i}\omega_n \end{bmatrix}. \tag{3.61}$$

Subsequently, the characteristic polynomial is determined by employing the Laplace expansion, see, e.g., [75], on the determinant of $A - \lambda I_n$ with the identity matrix $I_n \in \mathbb{R}^{n\times n}$. This results in

$$\det\left(A_o - \lambda I_n\right) = \left(\mu_1 + \mathrm{i}\omega_1 - \lambda\right) \det(A_{o,11} - \lambda I_{n-1}) - \gamma_{21} \det(A_{o,21} - \lambda I_{n-1})$$

with the determinants

$$\begin{aligned} \det(A_{o,11} - \lambda I_{n-1}) &= \det\left(\begin{bmatrix} \mu_2 + \mathrm{i}\omega_2 - \lambda & 0 & \cdots & 0 \\ \gamma_{32} & \mu_3 + \mathrm{i}\omega_3 - \lambda & \cdots & 0 \\ \vdots & \vdots & \ddots & \vdots \\ 0 & 0 & \cdots & \mu_n + \mathrm{i}\omega_n - \lambda \end{bmatrix}\right) \\ &= \prod_{i=2}^{n} \left(\mu_i + \mathrm{i}\omega_i - \lambda\right), \\ \det(A_{o,21} - \lambda I_{n-1}) &= \det\left(\begin{bmatrix} 0 & 0 & \cdots & \gamma_{1n} \\ \gamma_{32} & \mu_3 + \mathrm{i}\omega_3 - \lambda & \cdots & 0 \\ \vdots & \vdots & \ddots & \vdots \\ 0 & 0 & \cdots & \mu_n + \mathrm{i}\omega_n - \lambda \end{bmatrix}\right) \\ &= (-1)^{n-1} \gamma_{1n} \prod_{i=3}^{n} \left(\gamma_{i(i-1)}\right). \end{aligned}$$

Combining the results, yields

$$\det\left(A_{\mathrm{o}} - \lambda I_n\right) = \prod_{i=1}^{n} \left(\mu_i + \mathrm{i}\omega_i - \lambda\right) + (-1)^n \gamma_{1n} \prod_{i=2}^{n} \left(\gamma_{i(i-1)}\right). \tag{3.62}$$

Hence, only one coefficient of the characteristic polynomial of (3.61) can be controlled by assigning the coupling strength γ_{ij} for all $(i,j) \in \mathcal{E}$, if the Andronov-Hopf oscillators are coupled in a n-cycle graph. This concludes the proof. □

Proposition 3.2 *Consider the network* (3.5) *of $n \in \mathbb{N}$ coupled oscillators and assume that the network graph is coupled in a tree graph with $l < n$ leafs. In addition, let the bifurcation parameter be the coupling γ_{ij} for all $(i,j) \in \mathcal{E}$. Then the size of the N-parameter family induced by the coupling γ_{ij} is given by $N_{\mathrm{T}} = n - 1$.*

Proof. The claim is shown by analyzing the characteristic polynomial of a tree graph by employing the Laplace expansion, see, e.g., [75]. This is done by defining the network topology and then investigating the characteristic polynomial.

The characteristic polynomial of oscillators coupled in a tree graph with $l > 1$ leafs is investigated. The number of oscillators in this network are sorted in terms of the leafs, For this, denote the number of oscillators of the i-th leaf by m_i for all $i = 1, 2 \ldots, l$, so that the sum of the number of oscillators of each leaf reads $\sum_{j=1}^{l} = n - 1$. The oscillator in the root vertex is assumed to be "oscillator 1" and the m_1 oscillators of the first leaf are the next m_1 oscillators. This is repeated with the next leafs until every oscillator has been assigned. Sorting the oscillators in this way, results in

$$A_{\mathrm{T},l} = \begin{bmatrix} \eta_1 & \gamma_{12} & \gamma_{13} & \cdots & 0 & \cdots & 0 \\ \gamma_{21} & \eta_2 & 0 & \cdots & \gamma_{2(m_1+1)} & \cdots & 0 \\ \gamma_{31} & 0 & \eta_3 & \cdots & 0 & \cdots & 0 \\ \vdots & \vdots & \vdots & \ddots & \vdots & \ddots & \vdots \\ 0 & \gamma_{(m_1+1)2} & 0 & \cdots & \eta_{m_1+1} & \cdots & 0 \\ \vdots & \vdots & \vdots & \ddots & \vdots & \ddots & \vdots \\ 0 & 0 & \gamma_{(m_1+m_2+1)2} & \cdots & \eta_{m_1+m_2+1} & \cdots & 0 \\ \vdots & \vdots & \vdots & \ddots & \vdots & \ddots & \vdots \\ 0 & 0 & 0 & \cdots & 0 & \cdots & \eta_n \end{bmatrix} \tag{3.63}$$

with $\eta_i = \mu_i + \mathrm{i}\omega_i$. The characteristic polynomial of (3.63) is determined by employing the Laplace expansion, which yields

$$\det\left(A_{\mathrm{T},l} - \lambda I_n\right) = (\eta_1 - \lambda)\det(A_{\mathrm{T},l,11} - \lambda I_{n-1}) - \sum_{j=2}^{m_1} \left[(-1)^j \gamma_{j1} \det(A_{\mathrm{T},l,j1} - \lambda I_{n-1})\right] \tag{3.64}$$

with the sub-matrices

$$A_{\mathrm{T},l,11} = A_{\mathrm{T},l-1} = \begin{bmatrix} \eta_2 & 0 & \cdots & \gamma_{2(m_1+1)} & \cdots & 0 \\ 0 & \eta_3 & \cdots & 0 & \cdots & 0 \\ \vdots & \vdots & \ddots & \vdots & \ddots & \vdots \\ \gamma_{(m_1+1)2} & 0 & \cdots & \eta_{m_1+1} & \cdots & 0 \\ \vdots & \vdots & \ddots & \vdots & \ddots & \vdots \\ 0 & \gamma_{(m_1+m_2+1)2} & \cdots & 0 & \cdots & 0 \\ \vdots & \vdots & \ddots & \vdots & \ddots & \vdots \\ 0 & 0 & \cdots & 0 & \cdots & \eta_n \end{bmatrix}, \tag{3.65a}$$

$$A_{\mathrm{T},l,j_1 1} = \begin{bmatrix} \gamma_{12} & \gamma_{13} & \cdots & \gamma_{1(j_1-1)} & \gamma_{1j_1} & \gamma_{1(j_1+1)} & \cdots & 0 \\ \eta_2-\lambda & 0 & \cdots & 0 & 0 & 0 & \cdots & 0 \\ 0 & \eta_3-\lambda & \cdots & 0 & 0 & 0 & \cdots & 0 \\ \vdots & \vdots & \ddots & \vdots & \vdots & \vdots & \ddots & \vdots \\ 0 & 0 & \cdots & \eta_{j_1-1}-\lambda & 0 & 0 & \cdots & 0 \\ 0 & 0 & \cdots & 0 & 0 & \eta_{j_1+1}-\lambda & \cdots & 0 \\ \vdots & \vdots & \ddots & \vdots & \vdots & \vdots & \ddots & \vdots \\ 0 & 0 & \cdots & 0 & 0 & 0 & \cdots & \eta_n-\lambda \end{bmatrix} \tag{3.65b}$$

for all $j_1 = 2, 3, \ldots, m_1$. Investigating the coefficients of (3.64) implies that

$$(\eta_1 - \lambda)\det(A_{\mathrm{T},l,11} - \lambda I_{n-1})$$

results in a polynomial in λ of a degree of n, while the degree of $\gamma_{j1}\det(A_{\mathrm{T},l,j1} - \lambda I_{n-1})$ in λ is given by $n-1$. Hence, the products between the coupling of the leafs can only appear in the 0th to $n-2$th coefficients of the characteristic polynomial, so that the bifurcation parameters γ_{ij} in oscillators coupled in a tree graph span an $(n-1)$-parameter-family. This concludes the proof. □

It is implied by Proposition 3.1 and Proposition 3.2 that the number of coupled oscillators determine the size of controllable Andronov-Hopf bifurcation. Following Proposition 3.2, the maximum number of controllable Andronov-Hopf bifurcations in a network is induced by a tree network. In contrast, the minimal number of controllable Andronov-Hopf bifurcations is induced by an n-cycle graph.

Groups of oscillators

As discussed, the bifurcation analysis of oscillator networks becomes increasingly difficult for larger numbers of oscillators. To circumvent this issue, the notion groups of oscillators is introduced.

Definition 3.2 (Groups of oscillators [149]) *A group of oscillators is a network of identical oscillators. The coupling inside the group is called self-coupling, while the coupling*

between groups is referred as cross-coupling. The adjacency matrix of two coupled groups can be written by block matrix, e.g., for two groups the adjacency matrix Γ *is given by*

$$\Gamma = \begin{bmatrix} \Gamma_{11} & \Gamma_{12} \\ \Gamma_{21} & \Gamma_{22} \end{bmatrix} \tag{3.66}$$

with the self-coupling matrices Γ_{11}, Γ_{22} *and cross-coupling matrices* Γ_{12}, Γ_{21}.

To showcase the relevance of the notion on the bifurcation analysis of oscillator networks, two coupled groups of Andronov-Hopf oscillators are analyzed.

Theorem 3.6 *Consider the network* (3.5) *consisting of Andronov-Hopf oscillators and assume that this network can be sorted of two groups of oscillators. In addition, denote the adjacency matrix of this network by* Γ *introduced in* (3.66) *and let*

$$C_{2,1} = [\mu_1 + \mathrm{i}(\omega_1 - \omega_\mathrm{H})]\Gamma_{22} + [\mu_2 + \mathrm{i}(\omega_2 - \omega_\mathrm{H})]\Gamma_{11}^{(12)} + \Gamma_{22}\Gamma_{11}^{(12)} - \Gamma_{21}\Gamma_{12} \tag{3.67a}$$

$$C_{2,2} = [\mu_1 + \mathrm{i}(\omega_1 - \omega_\mathrm{H})]\Gamma_{22} + [\mu_2 + \mathrm{i}(\omega_2 - \omega_\mathrm{H})]\Gamma_{11}^{(21)} + \Gamma_{11}^{(21)}\Gamma_{22} - \Gamma_{21}\Gamma_{12} \tag{3.67b}$$

$$C_{2,3} = [\mu_1 + \mathrm{i}(\omega_1 - \omega_\mathrm{H})]\Gamma_{22}^{(12)} + [\mu_2 + \mathrm{i}(\omega_2 - \omega_\mathrm{H})]\Gamma_{11} + \Gamma_{22}^{(12)}\Gamma_{11} - \Gamma_{12}\Gamma_{21} \tag{3.67c}$$

$$C_{2,4} = [\mu_1 + \mathrm{i}(\omega_1 - \omega_\mathrm{H})]\Gamma_{22}^{(21)} + [\mu_2 + \mathrm{i}(\omega_2 - \omega_\mathrm{H})]\Gamma_{11} + \Gamma_{11}\Gamma_{22}^{(21)} - \Gamma_{12}\Gamma_{21} \tag{3.67d}$$

with the transformed self-coupling matrices

$$\Gamma_{11}^{(12)} = \Gamma_{12}^{-1}\Gamma_{11}\Gamma_{12}, \tag{3.68a}$$

$$\Gamma_{11}^{(21)} = \Gamma_{21}\Gamma_{11}\Gamma_{21}^{-1}, \tag{3.68b}$$

$$\Gamma_{22}^{(12)} = \Gamma_{12}\Gamma_{22}\Gamma_{12}^{-1}, \tag{3.68c}$$

$$\Gamma_{22}^{(21)} = \Gamma_{21}^{-1}\Gamma_{11}\Gamma_{21}. \tag{3.68d}$$

If the number of oscillators of each group is equal, i.e., $n_1 = n_2 = n$*, then the critical points and the characteristic frequency* ω_H *at the critical point are determined by solving*

$$0 = \xi_i(\omega_\mathrm{H}) + [\mu_1 + \mathrm{i}(\omega_1 - \omega_\mathrm{H})]\,[\mu_2 + \mathrm{i}(\omega_2 - \omega_\mathrm{H})] \tag{3.69}$$

with the eigenvalues

$$\xi_i(\omega_\mathrm{H}) \in \bigcup_{i=1}^{4} \sigma\left(C_{2,i}(\omega_\mathrm{H})\right). \tag{3.70}$$

Before the claim is proven, a lemma to determine the determinant of block matrices is summarized. This lemma is subsequently exploited to simplify the necessary condition (H1) from the Hopf Theorem (see Theorem 2.9).

Lemma 3.2 ([124]) *Let* $A \in \mathbb{R}^{n_1 \times n_1}$, $B \in \mathbb{R}^{n_2 \times n_1}$, $C \in \mathbb{R}^{n_1 \times n_2}$, $D \in \mathbb{R}^{n_2 \times n_2}$, A *and* D *invertible and* $n_1, n_2 \in \mathbb{N}$*. Then the determinant of the block matrix consisting of* A*,* B*,* C *and* D *is given by*

$$\det \begin{bmatrix} A & B \\ C & D \end{bmatrix} = \det(A)\det\left(D - CA^{-1}B\right) = \det(D)\det\left(A - BD^{-1}C\right).$$

With this, Theorem 3.6 can be proven.

Proof. The proof focuses on the derivation of the critical point of an Andronov-Hopf bifurcation by showing that the system matrix of the two coupled groups of oscillators has an eigenvalue on the imaginary axis. For this, the determinant of the system matrix of coupled Andronov-Hopf oscillators is analyzed by exploiting its block structure. First, the system matrix (3.59), i.e.,

$$A_n = \begin{bmatrix} \mu_1 + \mathrm{i}\omega_1 & \gamma_{12} & \gamma_{13} & \cdots & \gamma_{1n} \\ \gamma_{21} & \mu_2 + \mathrm{i}\omega_2 & \gamma_{23} & \cdots & \gamma_{2n} \\ \gamma_{31} & \gamma_{32} & \mu_3 + \mathrm{i}\omega_3 & \cdots & \gamma_{3n} \\ \vdots & \vdots & \vdots & \ddots & \vdots \\ \gamma_{n1} & \gamma_{n2} & \gamma_{n3} & \cdots & \mu_n + \mathrm{i}\omega_n \end{bmatrix},$$

is rewritten in terms of the blocks. Second, Lemma 3.2 is applied to determine the characteristic polynomial and the terms are sorted. Third, it is shown that the result is a lower order system of nonlinear equations in terms of the eigenvalues, so that the claim follows.

First, the system matrix (3.59) is rewritten into a block matrix by sorting the oscillators into groups. Following (3.66), the adjacency matrix Γ consists of the self-coupling matrices Γ_{11} and Γ_{22} and the cross-coupling matrices Γ_{12} and Γ_{21}. With these consideration, the system is given by

$$A_{\mathrm{G},2} = \begin{bmatrix} (\mu_1 + \mathrm{i}\omega_1) I_n & 0 \\ 0 & (\mu_2 + \mathrm{i}\omega_2) I_n \end{bmatrix} + \begin{bmatrix} \Gamma_{11} & \Gamma_{12} \\ \Gamma_{21} & \Gamma_{22} \end{bmatrix}. \tag{3.71}$$

with the identity matrix $I_n \in \mathbb{R}^{n \times n}$. To derive the critical point, the characteristic polynomial of system matrix (3.71) is computed, which polynomial reads

$$P_{A_{\mathrm{G},2}} = \det(A_{2n} - \lambda I_{2n}) = \det\left(\begin{bmatrix} \Xi_1 & \Gamma_{12} \\ \Gamma_{21} & \Xi_2 \end{bmatrix} \right) \tag{3.72}$$

with $\Xi_i = \chi_i I_n + \Gamma_{ii}$ and $\chi_i = \mu_i - \lambda_i + \mathrm{i}\omega_i$ for all $i = 1, 2$.

Second, as (3.72) has a block structure, Lemma 3.2 is employed, which yields

$$0 = \det(\Xi_1) \det\left(\Xi_2 - \Gamma_{21} \Xi_1^{-1} \Gamma_{12}\right). \tag{3.73a}$$

or

$$0 = \det(\Xi_2) \det\left(\Xi_1 - \Gamma_{12} \Xi_2^{-1} \Gamma_{21}\right). \tag{3.73b}$$

In particular, (3.73) is only satisfied, if and only if $\det(\Xi_1) \neq 0$ or $\det(\Xi_2) \neq 0$. Subsequently, only (3.73a) is investigated as the approach for (3.73b) is similar. Asserting that the number of oscillators in the two groups are equivalent, i.e., $n_1 = n_2$, (3.73a) can be modified as follows

$$\begin{aligned} 0 &= \det(\Xi_1) \det(\Xi_2 - \Gamma_{21} \Xi_1^{-1} \Gamma_{12}) \\ &= \det(\Xi_1) \det\left(\Gamma_{21} \left(\Gamma_{21}^{-1} \Xi_2 \Gamma_{12}^{-1} - \Xi_1^{-1}\right) \Gamma_{12}\right) \\ &= \det(\Xi_1) \det(\Gamma_{21}) \det(\Gamma_{12}) \det\left(\Gamma_{21}^{-1} \Xi_2 \Gamma_{12}^{-1} - \Xi_1^{-1}\right) \end{aligned} \tag{3.74}$$

Depending on multiplying Ξ_1 to left or right side, two different solutions are obtained. If Ξ_1 is multiplied to the right side, (3.74) results in

$$0 = \det(\Gamma_{21}) \det(\Gamma_{12}) \det\left(\Gamma_{21}^{-1}\Xi_2\Gamma_{12}^{-1}\Xi_1 - I_n\right) = \det\left(\Xi_2\Gamma_{12}^{(-1)}\Xi_1\Gamma_{12} - \Gamma_{21}\Gamma_{12}\right),$$

while by multiplying Ξ_1 to the left side

$$0 = \det(\Gamma_{21}) \det(\Gamma_{12}) \det\left(\Xi_1\Gamma_{21}^{-1}\Xi_2\Gamma_{12}^{-1} - I_n\right) = \det\left(\Gamma_{21}\Xi_1\Gamma_{21}^{(-1)}\Xi_2 - \Gamma_{21}\Gamma_{12}\right)$$

is obtained. Inserting $\Xi_i = \chi_i I_n + \Gamma_{ii}$ with $\chi_i = \mu_i - \lambda_i + \mathrm{i}\omega_i$ for all $i = 1, 2$ and sorting terms results in

$$0 = \det\left(\chi_1\chi_2 I_n + C_{2,1}\right), \tag{3.75a}$$
$$0 = \det\left(\chi_1\chi_2 I_n + C_{2,2}\right) \tag{3.75b}$$

with the auxiliary matrices

$$C_{2,1} = \chi_1\Gamma_{22} + \chi_2\Gamma_{11}^{(12)} + \Gamma_{22}\Gamma_{11}^{(12)} - \Gamma_{21}\Gamma_{12}$$
$$C_{2,2} = \chi_1\Gamma_{22} + \chi_2\Gamma_{11}^{(21)} + \Gamma_{11}^{(21)}\Gamma_{22} - \Gamma_{21}\Gamma_{12}$$

Here, the transformed self-coupling matrices $\Gamma_{11}^{(12)}$ and $\Gamma_{11}^{(21)}$ are given by (3.68a) and (3.68b).

Third, (3.75) is rewritten as a system of nonlinear equations. This is done by employing the Jordan decompositions, see, e.g., [75],

$$C_{2,1} = W_{C_{2,1}}\Lambda_{C_{2,1}}W_{C_{2,1}}^{-1},$$
$$C_{2,2} = W_{C_{2,2}}\Lambda_{C_{2,2}}W_{C_{2,2}}^{-1}$$

with the Jordan normal forms $\Lambda_{C_{2,1}} \in \mathbb{R}^{n_1\times n_1}$ and $\Lambda_{C_{2,2}} \in \mathbb{R}^{n_1\times n_1}$ and the transformation matrices $W_{C_{2,1}} \in \mathbb{R}^{n_1\times n_1}$ and $W_{C_{2,2}} \in \mathbb{R}^{n_1\times n_1}$, which implies

$$0 = \det\left(W_{C_{2,1}}\left(\chi_1\chi_2 I_n + \Lambda_{C_{2,1}}\right)W_{C_{2,1}}^{-1}\right),$$
$$0 = \det\left(W_{C_{2,2}}\left(\chi_1\chi_2 I_n + \Lambda_{C_{2,2}}\right)W_{C_{2,2}}^{-1}\right).$$

It turns out that $\chi_1\chi_2$ influences the eigenvalues of matrices $C_{2,1}$ and $C_{2,1}$. Hence, (3.75) is satisfied, if

$$0 = \xi(\lambda) + (\mu_1 + \mathrm{i}\omega_1 - \lambda)(\mu_2 + \mathrm{i}\omega_2 - \lambda) \tag{3.76}$$

with the eigenvalues $\xi(\lambda) \in \sigma(C_{2,1}) \cup \sigma(C_{2,2})$ holds true. In particular, by imposing $\lambda = \mathrm{i}\omega_\mathrm{H}$ with the characteristic frequency $\omega_\mathrm{H} > 0$ and solving (3.76) for the characteristic frequency and bifurcation parameter $\xi(\lambda)$, the system matrix (3.71) has an eigenvalue on the imaginary axis. This results in (3.69) and concludes the proof. □

Eq. (3.68) demonstrates the influence of the cross-coupling matrices Γ_{12} and Γ_{21} on the self-coupling matrices Γ_{11} and Γ_{22}. As the cross-coupling matrices (and their inverses) are multiplied to the self-coupling matrices, (3.68) can be viewed as a change of coordinates of self-coupling matrix of one group to the other group in terms of the cross-coupling. In addition, similar results can also be determined for three coupled groups under certain conditions.

Proposition 3.3 *Consider the network* (3.5) *consisting of Andronov-Hopf oscillators and assert that this network can be sorted into three groups of oscillators with the adjacency matrix of this network given by*

$$\Gamma = \begin{bmatrix} \Gamma_{11} & \Gamma_{12} & \Gamma_{13} \\ \Gamma_{21} & \Gamma_{22} & \Gamma_{23} \\ \Gamma_{31} & \Gamma_{32} & \Gamma_{33} \end{bmatrix}. \tag{3.77}$$

In addition denote the auxiliary matrix

$$\begin{aligned} C_3(\omega_\mathrm{H}) = {} & [\mu_1 + \mathrm{i}(\omega_1 - \omega_\mathrm{H})][\mu_2 + \mathrm{i}(\omega_2 - \omega_\mathrm{H})]\Gamma_{33}^{(31)} + [\mu_2 + \mathrm{i}(\omega_2 - \omega_\mathrm{H})][\mu_3 + \mathrm{i}(\omega_3 - \omega_\mathrm{H})]\Gamma_{11} \\ & + [\mu_1 + \mathrm{i}(\omega_1 - \omega_\mathrm{H})][\mu_3 + \mathrm{i}(\omega_3 - \omega_\mathrm{H})]\Gamma_{22}^{(12)} + [\mu_1 + \mathrm{i}(\omega_1 - \omega_\mathrm{H})]\Gamma_{22}^{(12)}\Gamma_{33}^{(31)} \\ & + [\mu_2 + \mathrm{i}(\omega_2 - \omega_\mathrm{H})](\Gamma_{11}\Gamma_{33}^{(31)} - \Gamma_{13}\Gamma_{31}) + [\mu_2 + \mathrm{i}(\omega_2 - \omega_\mathrm{H})](\Gamma_{22}^{(12)}\Gamma_{11} - \Gamma_{12}\Gamma_{21}) \\ & + \Gamma_{22}^{(12)}\Gamma_{11}\Gamma_{33}^{(31)} + \Gamma_{12}\Gamma_{23}\Gamma_{31} - \Gamma_{22}^{(12)}\Gamma_{13}\Gamma_{31} - \Gamma_{12}\Gamma_{21}\Gamma_{33}^{(31)}. \end{aligned} \tag{3.78}$$

If the number of oscillators of each group is equal, i.e., $n_1 = n_2 = n_3 = n$, and $\Gamma_{32} = 0$, then the critical points and the characteristic frequency ω_H at the critical point are determined by solving

$$0 = \xi_i(\omega_\mathrm{H}) + [\mu_1 + \mathrm{i}(\omega_1 - \omega_\mathrm{H})][\mu_2 + \mathrm{i}(\omega_2 - \omega_\mathrm{H})][\mu_3 + \mathrm{i}(\omega_3 - \omega_\mathrm{H})] \tag{3.79}$$

with the eigenvalues

$$\xi_i(\omega_\mathrm{H}) \in \sigma\left(C_3(\omega_\mathrm{H})\right) \tag{3.80}$$

and the transformed self-coupling matrices

$$\Gamma_{22}^{(12)} = \Gamma_{12}\Gamma_{22}\Gamma_{12}^{-1}, \tag{3.81a}$$

$$\Gamma_{33}^{(31)} = \Gamma_{31}^{-1}\Gamma_{33}\Gamma_{31}. \tag{3.81b}$$

Proof. The proof follows the same route as the proof of Theorem 3.6.

First, the system matrix (3.59) for three groups is rewritten as the block matrix

$$A_{3n} = \begin{bmatrix} (\mu_1 + \mathrm{i}\omega_1)I_n & 0 & 0 \\ 0 & (\mu_2 + \mathrm{i}\omega_2)I_n & 0 \\ 0 & 0 & (\mu_3 + \mathrm{i}\omega_3)I_n \end{bmatrix} + \begin{bmatrix} \Gamma_{11} & \Gamma_{12} & \Gamma_{13} \\ \Gamma_{21} & \Gamma_{22} & \Gamma_{23} \\ \Gamma_{31} & \Gamma_{32} & \Gamma_{33} \end{bmatrix} \tag{3.82}$$

with the identity matrix $I_n \in \mathbb{R}^{n\times n}$. To determine the critical point, the characteristic polynomial of (3.82) has to be computed, which reads

$$P_{A_{\mathrm{G},3}} = \det(A_{3n} - \lambda I_{3n}) = \det\left(\begin{bmatrix} \Xi_1 & \Gamma_{12} & \Gamma_{13} \\ \Gamma_{21} & \Xi_2 & \Gamma_{23} \\ \Gamma_{31} & \Gamma_{32} & \Xi_3 \end{bmatrix}\right) \tag{3.83}$$

with $\Xi_i = \chi_i I_n + \Gamma_{ii}$ and $\chi_i = \mu_i - \lambda_i + \mathrm{i}\omega_i$ for all $i = 1, 2, 3$.

Second, as (3.83) has a block structure, Lemma 3.2 is employed twice and terms are sorted in similar manner as in the proof of Theorem 3.6. This results in

$$\begin{aligned} P_{A_{\mathrm{G},3}} = {} & \det(\Xi_1)^{-1} \det(\tilde{\Xi}_2) \det(\Gamma_{21}) \det(\Gamma_{12}) \det(\Gamma_{31}) \det(\Gamma_{13}) \\ & \times \det\left[\Xi_1\Gamma_{31}^{-1}\Xi_3\Gamma_{13}^{-1}\Xi_1 - \Xi_1 - (\Xi_1\Gamma_{31}^{-1}\Gamma_{32}\Gamma_{12}^{-1} - I)\tilde{\Xi}_2^{-1}(\Gamma_{21}^{-1}\Gamma_{23}\Gamma_{13}^{-1}\Xi_1 - I)\right] \end{aligned} \tag{3.84}$$

with the matrix $\tilde{\Xi}_2 = \Gamma_{21}^{-1}\Xi_2\Gamma_{12}^{-1} - \Xi_1^{-1}$. Asserting $\Gamma_{32} = 0$ in (3.84) and sorting terms, yields

$$P_{A_{\mathrm{G},3}} = \det\left[\chi_1\chi_2\chi_3 + C_3\right], \tag{3.85}$$

where the auxiliary matrix reads

$$\begin{aligned} C_3 = {} & \chi_1\chi_2\Gamma_{33}^{(31)} + \chi_2\chi_3\Gamma_{11} + \chi_1\chi_3\Gamma_{22}^{(12)} + \chi_1\Gamma_{22}^{(12)}\Gamma_{33}^{(31)} + \chi_2(\Gamma_{11}\Gamma_{33}^{(31)} - \Gamma_{13}\Gamma_{31}) \\ & + \chi_3(\Gamma_{22}^{(12)}\Gamma_{11} - \Gamma_{12}\Gamma_{21}) + \Gamma_{22}^{(12)}\Gamma_{11}\Gamma_{33}^{(31)} + \Gamma_{12}\Gamma_{23}\Gamma_{31} - \Gamma_{22}^{(12)}\Gamma_{13}\Gamma_{31} - \Gamma_{12}\Gamma_{21}\Gamma_{33}^{(31)}, \end{aligned}$$

while the transformed self-coupling matrices $\Gamma_{22}^{(12)}$ and $\Gamma_{33}^{(31)}$ are given by (3.81).

Third, (3.85) is rewritten as a system of nonlinear equations. This is done by employing the Jordan decomposition, see, e.g., [75], on $C_3(\lambda)$,

$$C_3 = W_{C_3}\Lambda_{C_3}W_{C_3}^{-1}$$

with the Jordan normal form $\Lambda_{C_3} \in \mathbb{R}^{n_1\times n_1}$ and the transformation matrix $W_{C_3} \in \mathbb{R}^{n_1\times n_1}$, which implies

$$0 = \det\left(W_{C_3}\left(\chi_1\chi_2\chi_3 I_n + \Lambda_{C_3}\right)W_{C_3}^{-1}\right).$$

It turns out that $\chi_1\chi_2\chi_3$ influences the eigenvalues of matrices C_3. Hence, (3.85) is satisfied, if

$$0 = \xi(\lambda) + (\mu_1 + \mathrm{i}\omega_1 - \lambda)\,(\mu_2 + \mathrm{i}\omega_2 - \lambda)\,(\mu_3 + \mathrm{i}\omega_3 - \lambda) \tag{3.86}$$

with the eigenvalues $\xi(\lambda) \in \sigma(C_3(\lambda))$. In particular, by imposing $\lambda = \mathrm{i}\omega_{\mathrm{H}}$ with the characteristic frequency $\omega_{\mathrm{H}} > 0$ and solving (3.86) for the characteristic frequency and a bifurcation parameter, the system matrix (3.82) has an eigenvalue on the imaginary axis. This results in (3.79) and concludes the proof. □

Finally, some results motivated by Proposition 3.1 are presented, which reduces a network of $m \in \mathbb{N}$ groups of Andronov-Hopf oscillators to a network consisting of m Andronov-Hopf oscillators. For this, it is assumed that there is no self-coupling, so that $\Gamma_{ii} = 0$ for all $i = 1, 2, m$, and that the groups are assumed to be coupled in a cycle graph. To prepare the proof of this, the characteristic polynomial of groups of oscillators coupled in a cycle graph is determined.

Lemma 3.3 *Consider the block matrix consisting of $m \in \mathbb{N}$ blocks*

$$A_{\mathrm{G},m} = \begin{bmatrix} \chi_1 I_{n_1} & \Gamma_{12} & 0 & \cdots & 0 & 0 \\ 0 & \chi_2 I_{n_2} & \Gamma_{23} & \cdots & 0 & 0 \\ 0 & 0 & \chi_3 I_{n_3} & \cdots & 0 & 0 \\ \vdots & \vdots & \vdots & \ddots & \vdots & \vdots \\ 0 & 0 & 0 & \cdots & \chi_{m-1} I_{n_{m-1}} & \Gamma_{m-1,m} \\ \Gamma_{m,1} & 0 & 0 & \cdots & 0 & \chi_m I_{n_m} \end{bmatrix} \in \mathbb{C}^{n \times n}, \tag{3.87}$$

with the cross-coupling matrices $\Gamma_{i,j} \in \mathbb{R}^{n_i \times n_j}$, the generalized damping coefficient $\chi_k \in \mathbb{C}$, the size n_k of the k-th block, and the size $n = \sum_{l=1}^{m} n_l$ of the block matrix for all $(i,j) \in \{(1,2),(2,3),\ldots,(m-1,m),(m,1)\}$ and $k = 1, 2, \ldots, m$. Then the determinant of (3.87) *is given by*

$$\det(A_{\mathrm{G},m}) = \prod_{i=1}^{m-1} \chi_i^{n_i} \det\left(\chi_m I_{n_m} - (-1)^m \Gamma_{m,1} \prod_{i=1}^{m-1} \chi_i^{-1} \Gamma_{i,(i+1)} \right). \tag{3.88}$$

Proof. To prove the claim, the determinant of (3.87) is determined by induction. For the induction start, the determinant for $m = 2$ is derived. Then it is shown in the inductive step that the determinant for m can be reduced to the determinant for $m - 1$.

Induction Start: Consider two coupled groups without self-coupling, i.e., $\Gamma_{11} = \Gamma_{22} = 0$, so that the system matrix is given by

$$A_{\mathrm{G},2} = \begin{bmatrix} (\mu_1 - \lambda + \mathrm{i}\omega_1) I_{n_1} & \Gamma_{12} \\ \Gamma_{21} & (\mu_2 - \lambda + \mathrm{i}\omega_2) I_{n_2} \end{bmatrix}.$$

The determinant can be determined by computing

$$\det(A_{\mathrm{G},2}) = \det\left(\begin{bmatrix} \chi_1 I_{n_1} & \Gamma_{12} \\ \Gamma_{21} & \chi_2 I_{n_2} \end{bmatrix} \right) \tag{3.89}$$

with $\chi_i \in \mathbb{C}$ and the size n_i of the i-th group of oscillators for all $i = 1, 2$. After employing Lemma 3.2, (3.89) is simplified to

$$\det(A_{\mathrm{G},2}) = \chi_1^{n_1} \det(\chi_2 I_{n_2} - \chi_1^{-1} \Gamma_{21} \Gamma_{12}). \tag{3.90}$$

Inductive Step: Second, consider (3.87) for $m > 2$. Its determinant reads

$$\det(A_{\mathrm{G},m}) = \det\left(\begin{bmatrix} \chi_1 I_{n_1} & \Gamma_{12} & 0 & \cdots & 0 & 0 \\ 0 & \chi_2 I_{n_2} & \Gamma_{23} & \cdots & 0 & 0 \\ 0 & 0 & \chi_3 I_{n_3} & \cdots & 0 & 0 \\ \vdots & \vdots & \vdots & \ddots & \vdots & \vdots \\ 0 & 0 & 0 & \cdots & \chi_{m-1} I_{n_{m-1}} & \Gamma_{m-1,m} \\ \Gamma_{m,1} & 0 & 0 & \cdots & 0 & \chi_m I_{n_m} \end{bmatrix}\right). \tag{3.91}$$

After employing Lemma 3.2, (3.91) is simplified to

$$\det(A_{\mathrm{G},m}) = \chi_1^{n_1} \det\left(\begin{bmatrix} \chi_2 I_{n_2} & \Gamma_{23} & \cdots & 0 & 0 \\ 0 & \chi_3 I_{n_3} & \cdots & 0 & 0 \\ \vdots & \vdots & \ddots & \vdots & \vdots \\ 0 & 0 & \cdots & \chi_{m-1} I_{n_{m-1}} & \Gamma_{m-1,m} \\ -\chi_1^{-1}\Gamma_{m,1}\Gamma_{12} & 0 & \cdots & 0 & \chi_m I_{n_m} \end{bmatrix}\right)$$

With this, it follows that the determinant for m can be reduced to the determinant for $m-1$. Thus, after employing this step $m-1$ times, the determinant (3.91) can be reduced to (3.89) and hence the claim follows directly. □

Remark 3.3 *Following Lemma 3.2, it can be shown by varying the initial block in the inductive step that the determinant is symmetric to the cyclic group $\mathbb{Z}_m$, e.g.,*

$$\begin{aligned} \det(A_{\mathrm{G},m}) &= \prod_{i=1}^{m} \chi_i^{n_i} \det\left[\chi_m I_{n_m} - (-1)^m \Gamma_{m,1} \prod_{i=1}^{m-1} \left(\chi_i^{-1}\Gamma_{i,(i+1)}\right)\right] \\ &= \prod_{i=2}^{m} \chi_i^{n_i} \det\left[\chi_1 I_{n_1} - (-1)^m \Gamma_{12} \prod_{i=2}^{m-1} \left(\chi_i^{-1}\Gamma_{i,(i+1)}\right) \chi_m^{-1}\Gamma_{m,1}\right]. \end{aligned}$$

Hence, it is implied that the upper limit of the magnitude of the spectrum $\sigma(A_{\mathrm{G},m})$ without zero is given by the size of the smallest group, i.e.,

$$|\sigma(A_{\mathrm{G},m}) \setminus \{0\}| \leq \min\{n_1, n_2, \ldots, n_m\}.$$

With this preparation, the following theorem can be stated.

Theorem 3.7 *Consider the network* (3.5) *and assume that there are $m \in \mathbb{N}$ groups of oscillators, that are coupled in a m-cycle graph, i.e., the adjacency matrix is given by*

$$\Gamma = \begin{bmatrix} 0 & \Gamma_{12} & 0 & \cdots & 0 & 0 \\ 0 & 0 & \Gamma_{23} & \cdots & 0 & 0 \\ 0 & 0 & 0 & \cdots & 0 & 0 \\ \vdots & \vdots & \vdots & \ddots & \vdots & \vdots \\ 0 & 0 & 0 & \cdots & 0 & \Gamma_{m-1,m} \\ \Gamma_{m,1} & 0 & 0 & \cdots & 0 & 0 \end{bmatrix} \in \mathbb{R}^{n\times n},$$

with the cross-coupling matrices $\Gamma_{i,j} \in \mathbb{R}^{n_i \times n_j}$*, the size* n_k *of the k-th group, and the size* $n = \sum_l^m n_l$ *of the network for all* $(i,j) \in \{(1,2),(2,3),\ldots,(m-1,m),(m,1)\}$ *and* $k = 1,2,\ldots,m$*. In addition, assume that the bifurcation parameter is given by* $\lambda_\mathrm{o} \in \sigma(\Gamma_{m,1}\prod_{i=1}^{m-1}\Gamma_{i,(i+1)})$*. Then the critical points of the coupled groups of oscillators are equal to the critical points of oscillators coupled in a cycle graph.*

Remark 3.4 *The bifurcation parameters* λ_o *describe the amplification of the cross-coupling matrices after the output of an oscillator is traveled across the m-cycle graph. In addition, following Remark 3.3, there are* $\min\{n_1, n_2, \ldots, n_m\}$ *bifurcations parameters.*

Proof. The following proof is based on simplifying the characteristic polynomial of the m groups of oscillators coupled in a cycle graph by employing Lemma 3.3.

The characteristic polynomial of the system matrix $A_{\mathrm{G},m}$ of the coupled groups can be obtained by computing the determinant of (3.87), where the generalized damping coefficient is given by $\chi_i = \mu_i - \lambda + \mathrm{i}\omega_i$. Thus, following Lemma 3.3, the characteristic polynomial of $A_{\mathrm{G},m}$ reads

$$P_{A_{\mathrm{G},m}}(\lambda) = \prod_{i=1}^{m-1} \chi_i^{n_i} \det\left(\chi_m I_{n_m} + (-1)^m \Gamma_{m,1} \prod_{i=1}^{m-1} \chi_i^{-1} \Gamma_{i,(i+1)}\right).$$

After factoring out the coefficients χ_i for all $i = 1,2,\ldots,m-1$, the characteristic polynomial simplifies to

$$P_{A_{\mathrm{G},m}}(\lambda) = \prod_{i=1}^{m-1} \chi_i^{n_i - n_m} \det\left(\prod_{i=1}^{m} \chi_i I_{n_m} - (-1)^m \Gamma_{m,1} \prod_{i=1}^{m-1} \Gamma_{i,(i+1)}\right).$$

Solving $P_{A_{\mathrm{G},m}}(\lambda) = 0$, reduces to

$$0 = \det\left(\prod_{i=1}^{m} \chi_i I_{n_m} - (-1)^m \Gamma_{m,1} \prod_{i=1}^{m-1} \Gamma_{i,(i+1)}\right) \tag{3.92}$$

Eq. (3.92) can be simplified by employing the Jordan decomposition, see, e.g., [75],

$$\Gamma_{m,1} \prod_{i=1}^{m-1} \Gamma_{i,(i+1)} = W_\mathrm{o} \Lambda_\mathrm{o} W_\mathrm{o}^{-1}$$

with the Jordan normal form $\Lambda_\mathrm{o} \in \mathbb{R}^{n\times n}$ and transformation matrix $W_\mathrm{o} \in \mathbb{R}^{n\times n}$, which simplifies to

$$0 = \det\left(W_\mathrm{o}\left(\prod_{i=1}^{m} \chi_i I_{n_m} - (-1)^m \Lambda_\mathrm{o}\right) W_\mathrm{o}^{-1}\right). \tag{3.93}$$

It turns out that $\prod_{i=1}^m \chi_i$ influences the eigenvalues of matrices $\Gamma_{m,1}\prod_{i=1}^{m-1}\Gamma_{i,(i+1)}$. Hence, (3.93) is satisfied, if

$$0 = \prod_{i=1}^{m} (\mu_i - \lambda + \mathrm{i}\omega_i) - (-1)^m \lambda_\mathrm{o}$$

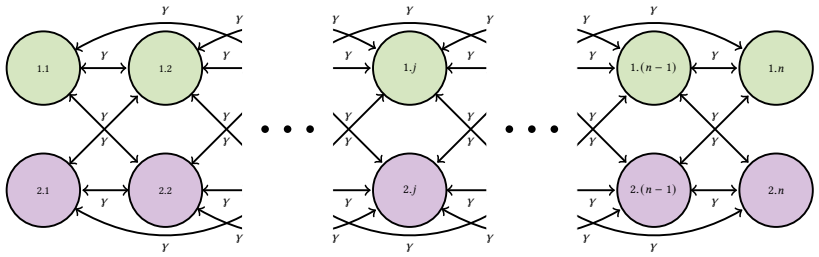

Figure 3.7.: Network topology of the two coupled groups indicated by the different colors of the vertices indicate different groups.

with the eigenvalues $\lambda_o \in \sigma(\Gamma_{m,1} \prod_{i=1}^{m-1} \Gamma_{i,(i+1)})$. It follows that the characteristic polynomial of m groups of oscillators coupled in a cycle graph is the same as the characteristic polynomial of m oscillators coupled in a cycle graph, so that the critical points are equal, if the bifurcation parameter is assumed to be the eigenvalue λ_o. This concludes the proof. □

To conclude the bifurcation analysis of injectively coupled Andronov-Hopf oscillators, the critical point of two coupled groups of oscillators is evaluated numerically.

Example 3.5 *The results of the bifurcation analysis from Theorem 3.6 are verified numerically. For this, consider the network topology is depicted in Figure 3.7, so that the self-coupling and cross-coupling matrices are given by*

$$\Gamma_{ii} = \begin{bmatrix} 0 & \gamma & \gamma & \cdots & 0 & 0 \\ \gamma & 0 & \gamma & \cdots & 0 & 0 \\ \gamma & \gamma & 0 & \cdots & 0 & 0 \\ \vdots & \vdots & \vdots & \ddots & \vdots & \vdots \\ 0 & 0 & 0 & \cdots & 0 & \gamma \\ 0 & 0 & 0 & \cdots & \gamma & 0 \end{bmatrix} \in \mathbb{R}^{n \times n},$$

$$\Gamma_{ij} = \begin{bmatrix} 0 & \gamma & 0 & \cdots & 0 & 0 \\ \gamma & 0 & \gamma & \cdots & 0 & 0 \\ 0 & \gamma & 0 & \cdots & 0 & 0 \\ \vdots & \vdots & \vdots & \ddots & \vdots & \vdots \\ 0 & 0 & 0 & \cdots & 0 & \gamma \\ 0 & 0 & 0 & \cdots & \gamma & 0 \end{bmatrix} \in \mathbb{R}^{n \times n}$$

with the coupling strength $\gamma \in [-5, 5]$ and the number $n \in \{10, 20, 50\}$ of oscillators in a group for all $i, j = 1, 2$. In addition, the parameters of the Andronov-Hopf oscillators are given by the damping coefficients $\mu_1 = -3\,\frac{1}{s}$ and $\mu_2 = -4\,\frac{1}{s}$ and the natural frequencies $\omega_1 = 3\,\frac{1}{s}$ and $\omega_2 = 4\,\frac{1}{s}$. To evaluate the results of Theorem 3.6, the minimal absolute value of the real-part of the eigenvalues of the system matrix $A_{G,2}$ of two coupled groups of oscillators and the roots of (3.69) *are computed in terms of the coupling strength γ. For this, denote*

$$\eta_2(\omega_H) = \min \left| \mathrm{Re} \left\{ \sigma \left[C_{2,1} + (\mu_1 + \mathrm{i}\omega_1 - \mathrm{i}\omega_H)\,(\mu_2 + \mathrm{i}\omega_2 - \mathrm{i}\omega_H)\, I_{2n} \right] \right\} \right|.$$

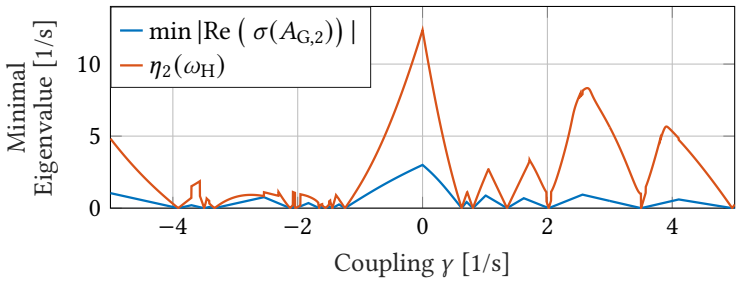

(a) Each group has $n = 10$ oscillators.

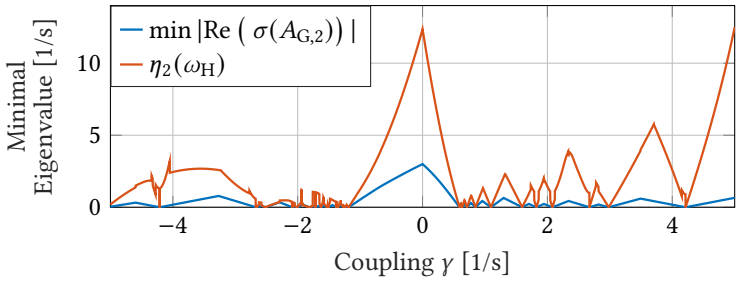

(b) Each group has $n = 20$ oscillators.

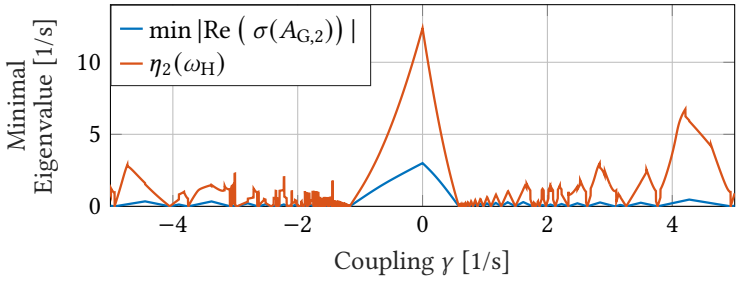

(c) Each group has $n = 50$ oscillators.

Figure 3.8.: Comparison between $\eta_2(\omega_H)$ and the minimal real-part of the eigenvalues of the system matrix $A_{G,2}$ for different number n of oscillators. The characteristic frequency ω_H is determined by taking the imaginary part determined of the eigenvalue of the system matrix $A_{G,2}$ with the minimal real-part.

Here, the characteristic frequency ω_H is determined by taking the imaginary part of the eigenvalue of the system matrix $A_{G,2}$ with the smallest absolute value of the real-part.

The results are visualized in Figure 3.8. It is showcased that $\eta(\omega_H)$ vanishes, if the system matrix $A_{G,2}$ has an eigenvalue located on the imaginary axis. Hence, the critical points of two coupled groups can also be determined by solving (3.69)*. This implies that only n eigenvalues (in comparison to 2n states) are inducing bifurcations in the two coupled groups, so that the number of computations can be reduced by applying Theorem 3.6. In particular, this decreases the computation time substantially as the QR algorithm has, e.g., a complexity of $O(l)^3$ with the size $l \in \mathbb{N}$ of a square matrix [38].*

3.1.2. Two Diffusively Coupled Oscillators

In contrast to injective coupling, where the amplitudes of the outputs are coupled, diffusive coupling is characterized by coupling the difference of the amplitudes of the output. This coupling will complicate the analytic investigation, so that only the number of critical points is subsequently determined for two diffusively coupled Andronov-Hopf oscillators. For this, the real-valued coordinates of the Andronov-Hopf oscillators are used to ensure that a real-valued polynomial emerges, so that the number of zeros can be easier analyzed. Two diffusively coupled Andronov-Hopf oscillators in real-valued coordinates are governed by

$$\frac{\mathrm{d}}{\mathrm{d}t}\begin{bmatrix}\boldsymbol{x}\\ \boldsymbol{y}\end{bmatrix} = \boldsymbol{f}(\boldsymbol{x},\boldsymbol{y}), \qquad t>0, \qquad \boldsymbol{x}(0)=\boldsymbol{x}_0, \qquad \boldsymbol{y}(0)=\boldsymbol{y}_0 \tag{3.94a}$$

with

$$\boldsymbol{f}(\boldsymbol{x},\boldsymbol{y}) = \begin{bmatrix} \mu_1 x_1 - \omega_1 x_2 - (x_1^2+x_2^2)x_1 - \xi_{12}\Delta_1 \\ \mu_1 x_2 + \omega_1 x_1 - (x_1^2+x_2^2)x_2 - \xi_{12}\Delta_2 \\ \mu_2 y_1 - \omega_2 y_2 - (y_1^2+y_2^2)y_1 + \xi_{21}\Delta_1 \\ \mu_2 y_2 + \omega_2 y_1 - (y_1^2+y_2^2)y_2 + \xi_{21}\Delta_2 \end{bmatrix}. \tag{3.94b}$$

Herein, the vectors are given by the state vectors $\boldsymbol{x}(t), \boldsymbol{y}(t) \in \mathbb{R}^2$, the difference vectors $\boldsymbol{\Delta}(t) = \boldsymbol{x}(t) - \boldsymbol{y}(t) \in \mathbb{R}^2$, and the initial conditions $\boldsymbol{x}_0, \boldsymbol{y}_0 \in \mathbb{R}^2$. Additional parameters are given by the damping coefficients $\mu_1, \mu_2 \in \mathbb{R}$, the natural frequencies $\omega_1, \omega_2 > 0$, and the coupling coefficients $\xi_{12}, \xi_{21} \in \mathbb{R}$. In particular, it directly follows from (3.94b) that diffusive coupling also influences the damping coefficient of the oscillator. Thus, the bifurcation analysis is going to be more complicated, so that conditions on the critical point for an Andronov-Hopf bifurcation are investigated first.

Lemma 3.4 ([156]) *Let either μ_1, μ_2, ξ_{12}, or ξ_{21} be the bifurcation parameter and assume $\xi_{12}+\xi_{21} \neq \mu_1+\mu_2$. Then the critical point for an Andronov-Hopf bifurcation of system* (3.94) *is determined by solving $g_1(\mu_1,\mu_2,\xi_{12},\xi_{21}) = 0$ with*

$$\begin{aligned} g_1 = &-\mu_2\xi_{12}^3 - (\mu_1+2\mu_2)\xi_{12}^2\xi_{21} - (2\mu_1+\mu_2)\xi_{12}\xi_{21}^2 - \mu_1\xi_{21}^3 + (3\mu_1+2\mu_2)\mu_2\xi_{12}^2 + (2\mu_1+3\mu_2)\mu_1\xi_{21}^2 \\ &+ \left[2(\mu_1^2+3\mu_1\mu_2+\mu_2^2) + (\omega_1-\omega_2)^2\right]\xi_{12}\xi_{21} - \left[(\mu_1+\mu_2)(3\mu_1+\mu_2) + (\omega_1-\omega_2)^2\right]\mu_2\xi_{12} \\ &- \left[(\mu_1+\mu_2)(\mu_1+3\mu_2) + (\omega_1-\omega_2)^2\right]\mu_1\xi_{21} + \mu_1\mu_2\left[(\mu_1+\mu_2)^2 + (\omega_1-\omega_2)^2\right]. \end{aligned} \tag{3.95}$$

In addition, the characteristic frequency at the critical point is given by

$$\omega_{\mathrm{C}} = \sqrt{\frac{c_{1,12}\mu_1 + c_{1,21}\mu_2 - c_{2,12}\xi_{12} - c_{2,21}\xi_{21}}{\mu_1+\mu_2-\xi_{12}-\xi_{21}}}. \tag{3.96}$$

with $c_{1,ij} = \mu_j^2 + \omega_j^2 + \xi_{ji}^2 + \xi_{ij}\xi_{ji}$ and $c_{2,ij} = \mu_j^2 + 2\mu_i\mu_j + \omega_j^2$.

Proof. To prove the claim, condition (H1) of Theorem 2.9 is analyzed. Note that this is done by assuming that the parameters μ_1, μ_2, ξ_{12}, and ξ_{21} are the bifurcations parameters.

The equilibrium of (3.94) is given by $\boldsymbol{z}_{\mathrm{eq}} = \mathbf{0}$, since $\boldsymbol{f}(\mathbf{0}) = \mathbf{0}$. With this, the system matrix of the linearized system reads

$$A = \left.\frac{\partial \boldsymbol{f}(\boldsymbol{z})}{\partial \boldsymbol{z}}\right|_{\boldsymbol{z}_{\mathrm{eq}}} = \begin{bmatrix} \mu_{1,\xi_{12}} & -\omega_1 & \xi_{12} & 0 \\ \omega_1 & \mu_{1,\xi_{12}} & 0 & \xi_{12} \\ \xi_{21} & 0 & \mu_{2,\xi_{21}} & -\omega_2 \\ 0 & \xi_{21} & \omega_2 & \mu_{2,\xi_{21}} \end{bmatrix} \tag{3.97}$$

with $\mu_{i,\xi_{ij}} = \mu_i - \xi_{ij}$. The eigenvalues of the matrix A can be determined by solving the characteristic polynomial

$$P_A(\lambda) = \lambda^4 + a_3\lambda^3 + a_2\lambda^2 + a_1\lambda + a_0 \tag{3.98}$$

with the coefficients

$$\begin{aligned} a_0 &= \mu_1^2\mu_2^2 + \omega_1^2\omega_2^2 + \left(\xi_{21}^2 + \omega_2^2 - 2\mu_2\xi_{21}\right)\mu_1^2 + \left(\xi_{12}^2 + \omega_1^2 - 2\mu_1\xi_{12}\right)\mu_2^2 + \left(\xi_{21}\omega_1 + \xi_{12}\omega_2\right)^2 \\ &\quad - 2\left(\mu_1\xi_{12}\omega_2^2 - \mu_1\mu_2\xi_{12}\xi_{21} + \mu_2\xi_{21}\omega_1^2\right), \qquad (3.99a) \\ a_1 &= 2\left\{2\mu_1\mu_2\left(\xi_{12} + \xi_{21}\right) + \left(\mu_1^2 + \omega_1^2\right)\xi_{21} + \left(\mu_2^2 + \omega_2^2\right)\xi_{12} - \left[\mu_2^2 + \omega_2^2 + \left(\xi_{12} + \xi_{21}\right)\xi_{21}\right]\mu_1\right. \\ &\quad \left. - \left[\mu_1^2 + \omega_1^2 + \left(\xi_{12} + \xi_{21}\right)\xi_{12}\right]\mu_2\right\}, \qquad (3.99b) \\ a_2 &= \left(\mu_1 + \mu_2\right)^2 + \left(\xi_{12} + \xi_{21}\right)^2 + \omega_1^2 + \omega_2^2 \\ &\quad - 2\left[\mu_1\mu_2 - \left(\xi_{12} + 2\xi_{21}\right)\mu_1 - \left(2\xi_{12} + \xi_{21}\right)\mu_2\right], \qquad (3.99c) \\ a_3 &= -2\left(\mu_1 + \mu_2 - \xi_{12} - \xi_{21}\right). \qquad (3.99d) \end{aligned}$$

Here, the necessary condition (H1) of the Hopf Theorem (see Theorem 2.9) is shown by comparing the coefficients of (3.98) with the coefficients of a quartic polynomial that has two arbitrary eigenvalues and a pair of complex conjugated eigenvalues on the imaginary axis located at $\mathrm{i}\omega_{\mathrm{C}}$ with $\omega_{\mathrm{C}} \in \mathbb{R}$. The latter polynomial reads

$$P_{\mathrm{H}}(\lambda) = \left(\lambda^2 + s_1\lambda + s_0\right)\left(\lambda^2 + \omega_{\mathrm{C}}^2\right) = \lambda^4 + s_0\lambda^3 + \left(s_1 + \omega_{\mathrm{C}}^2\right)\lambda^2 + s_0\omega_{\mathrm{C}}^2\lambda + s_1\omega_{\mathrm{C}}^2$$

with the coefficients $s_1, s_0 \in \mathbb{R}$. Comparing the coefficients results in

$$a_3 = s_0, \qquad a_2 = s_1 + \omega_{\mathrm{C}}^2, \qquad a_1 = s_0\omega_{\mathrm{C}}^2, \qquad a_0 = s_1\omega_{\mathrm{C}}^2.$$

Solving this system of equations, yields

$$\begin{aligned} 0 &= \frac{g_1(\mu_1, \mu_2, \xi_{12}, \xi_{21})\, g_2(\mu_1, \mu_2, \xi_{12}, \xi_{21})}{g_3(\mu_1, \mu_2, \xi_{12}, \xi_{21})}, \qquad (3.100a) \\ s_1 &= -2\left(\mu_1 + \mu_2 - \xi_{12} - \xi_{21}\right), \qquad (3.100b) \\ s_0 &= \frac{1}{\mu_1 + \mu_2 - \xi_{12} - \xi_{21}}\left\{\left(\mu_1 + \mu_2\right)^3 - \left(\xi_{12} + \xi_{21}\right)^3 - \xi_{12}\omega_1^2 - \xi_{21}\omega_2^2 - \left(3\xi_{12} + 4\xi_{21} - \mu_2\right)\mu_1^2\right. \\ &\quad - \left(4\xi_{12} + 3\xi_{21} - \mu_1\right)\mu_2^2 - 8\left(\xi_{12} + \xi_{21}\right)\mu_1\mu_2 + \left[\left(\xi_{12} + \xi_{21}\right)\left(3\xi_{12} + 4\xi_{21}\right) + \omega_1^2\right]\mu_1 \\ &\quad \left. + \left[\left(\xi_{12} + \xi_{21}\right)\left(4\xi_{12} + 3\xi_{21}\right) + \omega_2^2\right]\mu_2\right\}, \qquad (3.100c) \end{aligned}$$

and (3.96). Herein, the functions g_2 and g_3 read

$$g_2 = \left(\mu_1 + \mu_2 - \xi_{12} - \xi_{21}\right)^2 + \left(\omega_1 + \omega_2\right)^2, \tag{3.101}$$

$$g_3 = \mu_1 + \mu_2 - \xi_{12} - \xi_{21}, \tag{3.102}$$

while the function g_1 is given by (3.95). Eq. (3.102) implies $\xi_{12} + \xi_{21} \neq \mu_1 + \mu_2$ and that all roots of (3.101) are complex-valued, since $g_2 = 0$ results in

$$\xi_{12} + \xi_{21} = \mu_1 + \mu_2 \pm \mathrm{i}\left(\omega_1 + \omega_2\right).$$

This equations cannot be solved, since the parameters are real-valued. As a consequence, the critical points are only obtained by capturing the roots of (3.95), i.e., $g_1(\mu_1, \mu_2, \xi_{12}, \xi_{21}) = 0$. □

Remark 3.5 *The stability and uniqueness of the limit cycle of the system* (3.94) *is easily shown by denoting the Lyapunov function candidate by* $V = \boldsymbol{\chi}^{\mathrm{T}}\boldsymbol{\chi} \in \mathbb{R}$ *with* $\boldsymbol{\chi} = [\boldsymbol{x}^{\mathrm{T}}, \boldsymbol{y}^{\mathrm{T}}]^{\mathrm{T}}$, *which is positive definite for all* $\boldsymbol{\chi} \in \mathbb{R}^4$. *In addition, its rate of change along a solution trajectory reads*

$$\dot{V} = \boldsymbol{\chi}^{\mathrm{T}}(A + A^{\mathrm{T}})\boldsymbol{\chi} - \|\boldsymbol{\chi}\|_2^4 \leq -\zeta\|\boldsymbol{\chi}\|_2^2 - \|\boldsymbol{\chi}\|_2^4. \tag{3.103}$$

Herein, the upper bound is denoted by $\zeta \in \mathbb{R}$ *and the system matrix* A *given by* (3.97). *If* $\zeta \geq 0$ *holds true,* $-\zeta\|\boldsymbol{\chi}\|_2^2$ *becomes negative definite, so that Theorem 2.7 is satisfied and it follows that* (3.94) *is asymptotically stable. Hence, a stable and unique limit cycle emerges, if all eigenvalues are located on the left half complex plane and one pair of complex conjugated eigenvalues crosses the imaginary axis by varying the bifurcation parameter, since the dominant eigenvalues at this critical point are then purely imaginary. Moreover, the system* (3.94) *will desynchronize, if an additional pair of complex-conjugated eigenvalues travels from the left half to the right half complex plane by varying the bifurcation parameter, since the bifurcation parameter is not influencing the nonlinearity, i.e., the cubic nonlinearity is independent of* μ_1, μ_2, ξ_{12}, *and* ξ_{21}. *With this, an asymptotically stable sub-manifold can be found, so that after surpassing the critical point an additional limit cycle emerges and the system desynchronizes.*

For the remainder of this section, the solutions of (3.95) are discussed by asserting that either coupling or damping coefficient are the bifurcation parameters. For this, different scenarios are discussed: symmetric damping coefficient and symmetric coupling, asymmetric damping coefficient and symmetric coupling, and symmetric damping coefficient and asymmetric coupling.

Coupling as Bifurcation Parameter

Subsequently, the bifurcations induced by varying the symmetric coupling ξ are analyzed. In this case (3.95) reduced to a cubic polynomial, which is given by

$$\begin{aligned} g_1 = {} & 4\left(\mu_1 + \mu_2\right)\xi^3 - \left[4\left(\mu_1^2 + 3\mu_2\mu_1 + \mu_2^2\right) + \left(\omega_1 - \omega_2\right)^2\right]\xi^2 \\ & + \left(\mu_1 + \mu_2\right)\left[\mu_1^2 + 6\mu_2\mu_1 + \mu_2^2 + \left(\omega_1 - \omega_2\right)^2\right]\xi - \left[\left(\mu_1 + \mu_2\right)^2 + \left(\omega_1 - \omega_2\right)^2\right]\mu_1\mu_2. \end{aligned} \tag{3.104}$$

In particular, it is only necessary to investigate the number of real-valued zeros of (3.104), since the bifurcation parameter ξ is real-valued. This is done by applying Proposition 2.1 to analyze the cubic polynomial (3.104). With this, the discriminant of (3.104) reads

$$D_{g_1,\xi} = \frac{(\mu_1 - \mu_2)^2 \omega_\Delta^2}{27648\,(\mu_1 + \mu_2)^4} h(\mu_1, \mu_2) \tag{3.105}$$

with

$$\begin{aligned} h(\mu_1) = {} & 8\mu_1^6 + 3\left(5\omega_\Delta^2 + 8\mu_2^2\right)\mu_1^4 \\ & + 6\left(\omega_\Delta^4 - 13\omega_\Delta^2\mu_2^2 + 4\mu_2^4\right)\mu_1^2 - \left(\omega_\Delta^2 - 8\mu_2^2\right)\left(\omega_\Delta^2 + \mu_2^2\right)^2 . \end{aligned} \tag{3.106}$$

Thus, the number of real-valued zeros of (3.104) varies for two different scenarios: First, there are three real-valued zeros, where two are equivalent, if the damping coefficient is symmetric, i.e., $\mu_1 = \mu_2 = \mu$. Then the necessary condition is satisfied in two cases. This has been analyzed in [7] for $\mu = 1$. Second, if $\mu_1 \neq \mu_2$, there are either one or three critical points. In this case, the sign of (3.106) has to be analyzed, since $\frac{(\mu_1-\mu_2)^2\omega_\Delta^2}{27648(\mu_1+\mu_2)^4} > 0$ holds true. These two scenarios are analyzed in detail subsequently.

Symmetric Damping and Symmetric Coupling Let the damping coefficient be symmetric, i.e., $\mu_1 = \mu_2 = \mu$. Inserting this into the polynomial (3.104) to determine the critical point, the characteristic frequency (3.96) together with the coefficients (3.100) of the remaining polynomial $P_\mathrm{R} = \lambda^2 + s_1\lambda + s_0$, yield

$$g_1(\xi) = -(\mu - \xi)^2\left[4\mu(\mu - 2\xi) + (\omega_1 - \omega_2)^2\right], \tag{3.107a}$$

$$\omega_\mathrm{C} = \sqrt{\frac{2\mu(\mu - 2\xi) + \omega_1^2 + \omega_2^2}{2}}, \tag{3.107b}$$

$$s_1 = -4(\mu - \xi), \tag{3.107c}$$

$$s_0 = \frac{1}{2}\left(10\mu^2 - 20\mu\xi + 8\xi^2 + \omega_1^2 + \omega_2^2\right). \tag{3.107d}$$

In particular, the critical points can be derived directly from (3.107a) to obtain

$$\xi_{1,\mathrm{crit}} = \frac{4\mu^2 + (\omega_1 - \omega_2)^2}{8\mu}, \tag{3.108a}$$

$$\xi_{2,\mathrm{crit}} = \mu. \tag{3.108b}$$

Inserting (3.108) into (3.107b) yields the characteristic frequencies

$$\omega_{\mathrm{C},1} = \frac{\omega_1 + \omega_2}{2}, \tag{3.109a}$$

$$\omega_{\mathrm{C},2} = \sqrt{\frac{\omega_1 + \omega_2}{2} - \mu^2}. \tag{3.109b}$$

It is reported in [7] that there is only one critical point, if $\mu = 1$ is asserted. Thus, the sufficient condition (H2) of Theorem 2.9 has to be analyzed. The results are summarized in the following proposition.

Proposition 3.4 *Let $\mu = \mu_1 = \mu_2$ and $\xi = \xi_{12} = \xi_{21}$. Additionally, assume that the coupling strength ξ is the bifurcation parameter and denote*

$$\mu_0^{\pm} = \sqrt{\frac{4\omega_2\omega_1 - (\omega_1 - \omega_2)^2 \pm \sqrt{(\omega_1 - 3\omega_2)\,(\omega_2 - 3\omega_1)\,(\omega_1 + \omega_2)^2}}{8}}. \tag{3.110}$$

Then the critical points of the system (3.94) *and their respective characteristic frequencies are given by* (3.108) *and* (3.109).

In addition, the critical point (3.108a) *is an Andronov-Hopf bifurcation, which induces*

1. *a limit cycle, if*

$$\mu < 0 \wedge \frac{|\omega_1 - \omega_2|}{2} < |\mu| \wedge \left\{ \omega_2 \notin \left(\frac{1}{3}\omega_1, 3\omega_1\right) \right. \\ \left. \vee \left[\omega_2 \in \left(\frac{1}{3}\omega_1, 3\omega_1\right) \wedge \mu \notin \left(\mu_0^-, \mu_0^+\right) \right] \right\} \tag{3.111a}$$

2. *amplitude death, if*

$$\mu > 0 \wedge \frac{|\omega_1 - \omega_2|}{2} > |\mu| \wedge \left\{ \omega_2 \notin \left(\frac{1}{3}\omega_1, 3\omega_1\right) \right. \\ \left. \vee \left[\omega_2 \in \left(\frac{1}{3}\omega_1, 3\omega_1\right) \wedge \mu \notin \left(\mu_0^-, \mu_0^+\right) \right] \right\} \tag{3.111b}$$

3. *synchronization, if*

$$\mu > 0 \wedge \frac{|\omega_1 - \omega_2|}{2} < |\mu| \wedge \left\{ \omega_2 \notin \left(\frac{1}{3}\omega_1, 3\omega_1\right) \right. \\ \left. \vee \left[\omega_2 \in \left(\frac{1}{3}\omega_1, 3\omega_1\right) \wedge \mu \notin \left(\mu_0^-, \mu_0^+\right] \right\} \right] \tag{3.111c}$$

4. *desynchronization, if*

$$\mu < 0 \wedge \frac{|\omega_1 - \omega_2|}{2} > |\mu| \wedge \left\{ \omega_2 \notin \left(\frac{1}{3}\omega_1, 3\omega_1\right) \right. \\ \left. \vee \left[\omega_2 \in \left(\frac{1}{3}\omega_1, 3\omega_1\right) \wedge \mu \notin \left(\mu_0^-, \mu_0^+\right) \right] \right\} \tag{3.111d}$$

Proof. In the following, the crossing condition (H2) of Theorem 2.9 is investigated for two diffusively coupled Andronov-Hopf oscillators with identical damping coefficient and symmetric coupling. The crossing condition (H2) for the potential critical points is investigated individually as follows: The location of the remaining eigenvalues of (3.94) is analyzed. These can be determined by solving the quadratic polynomial $P_{\mathrm{R}} = \lambda^2 + s_1\lambda + s_0$

with the parameters s_1 and s_2 given by (3.100b) and (3.100a). For this analysis, the real-part of the remaining eigenvalues is investigated by applying the Routh-Hurwitz Criterion on $P_\mathrm{R} = \lambda^2 + s_1\lambda + s_0$ (see Theorem 2.4). Then the sensitivity (2.14) is analyzed, so that the qualitative behavior of (3.94) can be deduced.

First, the crossing condition (H2) for the critical point (3.108a) is analyzed. Inserting (3.108a) into (3.107c) and (3.107d), yields

$$s_1(\xi_{1,\mathrm{crit}}) = \frac{(\omega_1-\omega_2)^2 - 4\mu^2}{2\mu}, \tag{3.112a}$$

$$s_0(\xi_{1,\mathrm{crit}}) = \frac{\left[16\mu^4 - 4[(\omega_1-\omega_2)^2 - 4\omega_1\omega_2]\mu^2 + (\omega_1-\omega_2)^4\right]}{16\mu^2}. \tag{3.112b}$$

Then the sign of s_1 is determined by solving (3.112a) for μ. In contrast, the sign of (3.112b) is obtained by analyzing the zeros of the numerator with respect to the damping coefficient μ, since its denominator is positive for all $\mu \in \mathbb{R}$. The numerator of (3.112b) is a biquadratic polynomial that approaches to (positive) infinity, i.e., $\lim_{\mu\to\pm\infty} s_0(\xi_{1,\mathrm{crit}}) = \infty$. In addition, (3.112b) has zeros for all $\mu \in \mathbb{R}$, if $\omega_2 \notin (\omega_2^-, \omega_2^+)$ with $\omega_2^\pm = (3 \pm \sqrt{8})\omega_1$, since the coefficients of (3.112b) have alternating signs in this case. Moreover, (3.112b) is real-valued, if $(\omega_1 - 3\omega_2)(\omega_2 - 3\omega_1) > 0$. This implies $\omega_2 \in (\frac{1}{3}\omega_1, 3\omega_1)$. In particular, $3 - \sqrt{8} < 1/3$ and $3 + \sqrt{8} > 1/3$ holds true, such that (3.112b) has real-valued positive zeros for all $\omega_2 \in (\frac{1}{3}\omega_1, 3\omega_1)$. With these considerations, the signs of the coefficients $s_1(\xi_{1,\mathrm{crit}})$ and $s_0(\xi_{1,\mathrm{crit}})$ are given by

$$s_1(\xi_{1,\mathrm{crit}}) = \begin{cases} > 0, & \text{if } \mu > 0 \wedge \frac{|\omega_1-\omega_2|}{2} > |\mu| \\ > 0, & \text{if } \mu < 0 \wedge \frac{|\omega_1-\omega_2|}{2} < |\mu| \\ < 0, & \text{if } \mu < 0 \wedge \frac{|\omega_1-\omega_2|}{2} > |\mu| \\ < 0, & \text{if } \mu > 0 \wedge \frac{|\omega_1-\omega_2|}{2} < |\mu| \end{cases},$$

$$s_0(\xi_{1,\mathrm{crit}}) = \begin{cases} > 0, & \text{if } \omega_2 \notin \left(\frac{1}{3}\omega_1, 3\omega_1\right) \\ > 0, & \text{if } \omega_2 \in \left(\frac{1}{3}\omega_1, 3\omega_1\right) \wedge \mu \notin \left(\mu_0^-, \mu_0^+\right) \\ = 0, & \text{if } \omega_2 \in \left(\frac{1}{3}\omega_1, 3\omega_1\right) \wedge \mu \in \{\mu_0^-\mu_0^+\} \\ < 0, & \text{if } \omega_2 \in \left(\frac{1}{3}\omega_1, 3\omega_1\right) \wedge \mu \in \left(\mu_0^-\mu_0^+\right) \end{cases}$$

with $\mu_0^\pm$ given by (3.110). Thus, the zeros of the quadratic polynomial are located on the left complex half plane, if

$$\left[\left(\mu > 0 \wedge \frac{|\omega_1-\omega_2|}{2} > |\mu|\right) \vee \left(\mu < 0 \wedge \frac{|\omega_1-\omega_2|}{2} < |\mu|\right)\right] \wedge \left[\left(\omega_2 \in \left(\frac{1}{3}\omega_1, 3\omega_1\right) \wedge \mu \notin \left(\mu_0^-, \mu_0^+\right)\right) \vee \omega_2 \notin \left(\frac{1}{3}\omega_1, 3\omega_1\right)\right],$$

and on the right complex half plane, if

$$\left[\left(\mu > 0 \wedge \frac{|\omega_1 - \omega_2|}{2} < |\mu|\right) \vee \left(\mu < 0 \wedge \frac{|\omega_1 - \omega_2|}{2} > |\mu|\right)\right] \wedge \left[\left(\omega_2 \in \left(\frac{1}{3}\omega_1, 3\omega_1\right) \wedge \mu \notin \left(\mu_0^-, \mu_0^+\right)\right) \vee \omega_2 \notin \left(\frac{1}{3}\omega_1, 3\omega_1\right)\right].$$

Following the Hopf Theorem (see Theorem 2.9), the sensitivity d is computed by (2.14), i.e.,

$$d = \frac{\mathrm{d}}{\mathrm{d}\xi} \left(\mathrm{Re}\ \lambda(\xi)\right) |_{\xi=\xi_{\mathrm{crit}}}.$$

Assuming that $\mu_1 = \mu_2 = \mu$, $\xi_1 = \xi_2 = \xi$ hold true, inserting the characteristic polynomial (3.98) into (2.14) and considering the numerator of the result, yields

$$\begin{aligned}\mathrm{num}(d) = &-\left(2\mu^2 + \omega_1^2 + \omega_2^2\right)^2 \mu^2 + 2\left(2\mu^2 + \omega_1^2 + \omega_2^2\right)\left(5\mu^2 + \omega_1^2 + \omega_2^2 + \omega_1\omega_2\right)\mu\xi \\ &- \left[32\mu^4 + 2\left(7\omega_2^2 + 6\omega_1\omega_2 + 7\omega_1^2\right)\mu^2 + \left(\omega_1^2 - \omega_2^2\right)\left(\omega_1^2 + \omega_2^2\right)\right]\xi^2 \\ &+ 4\left[4\mu^2 + (\omega_1 + \omega_2)^2\right]\mu\xi^3 - \left[12\mu^4 + \left(\omega_1^2 + \omega_2^2\right)^2\right]\omega_{\mathrm{C}}^2 \\ &+ 2\left(20\mu^2 - \omega_1^2 - \omega_2^2 - 6\omega_1\omega_2\right)\mu\xi\omega_{\mathrm{C}}^2 + 6\left[(\omega_1 + \omega_2)^2 - 8\mu^2\right]\xi^2\omega_{\mathrm{C}}^2 + 16\mu\xi^3\omega_{\mathrm{C}}^2 \\ &+ 4\left(-3\mu^2 + \omega_1^2 + \omega_2^2\right)\omega_{\mathrm{C}}^4 + 20\mu\xi\omega_{\mathrm{C}}^4 - 16\xi^2\omega_{\mathrm{C}}^4 - 4\omega_{\mathrm{C}}^6.\end{aligned}$$

Inserting the critical point $\xi_{1,\mathrm{crit}}$ and the characteristic frequency $\omega_{\mathrm{C},1}$ results in

$$\mathrm{num}(d_{\mathrm{crit},1}) = -\overbrace{\frac{(\omega_1 + \omega_2)^2}{128\mu^2}}^{>0}\left(4\mu^2 - (\omega_1 - \omega_2)^2\right) \times \underbrace{\left(16\mu^4 + 4[(\omega_1 + \omega_2)^2 + 4\omega_1\omega_2]\mu^2 + (\omega_1 - \omega_2)^4\right)}_{>0}. \quad (3.113)$$

By considering the conditions on (3.112a), the sign of (3.113) is given by

$$\mathrm{num}(d_{\mathrm{crit},1}) = \begin{cases} > 0, & \text{if } \frac{|\omega_1 - \omega_2|}{2} > |\mu|, \\ < 0, & \text{if } \frac{|\omega_1 - \omega_2|}{2} < |\mu|, \end{cases}$$

so that (3.111) follows.

Second, the crossing condition (H2) for the critical point (3.108b) is analyzed. In this case, the coefficients (3.107c) and (3.107d) are given by

$$s_1(\xi_{2,\mathrm{crit}}) = 0, \qquad s_0(\xi_{2,\mathrm{crit}}) = \frac{\omega_1^2 + \omega_2^2 - 2\mu^2}{2}.$$

This implies that the zeros of the quadratic polynomial are on the imaginary axis if $|\mu| < \sqrt{\omega_1^2 + \omega_2^2/2}$. Otherwise, the quadratic polynomial has one positive real-valued

zero and one negative real-valued zero. In addition, the characteristic frequency (3.108a) becomes imaginary in this case, such that two eigenvalues are on the left half complex plane and two eigenvalues are on the right half complex plane. From this, it follows that (3.108b) cannot induce an Andronov-Hopf bifurcation, since the sufficient condition is violated. □

Remark 3.6 *If the sufficient condition (H2) of Theorem 2.9 is violated, the emerging bifurcation is not an Andronov-Hopf bifurcation. For* (3.94) *with* $\mu_1 = \mu_2 = \mu$ *and* $\xi_1 = \xi_2 = \xi$*, this condition is violated, if* $|\mu| = |\omega_1 + \omega_2|/2$ *holds true. In this case, both critical points* (3.108a) *and* (3.108b) *become equivalent and all eigenvalues are purely imaginary, so that the necessary condition of a Hopf-Hopf bifurcation is satisfied [48]. This bifurcation induces the qualitative change of bifurcation described in Proposition 3.4.*

Asymmetric Damping and Symmetric Coupling Subsequently, the number of critical points of (3.94) for asymmetric damping coefficients, i.e., $\mu_1 \neq \mu_2$, is determined by analyzing the sign of (3.106), which reads

$$h(\mu_1) = 8\mu_1^6 + 3\left(5\omega_\Delta^2 + 8\mu_2^2\right)\mu_1^4 + 6\left(\omega_\Delta^4 - 13\omega_\Delta^2\mu_2^2 + 4\mu_2^4\right)\mu_1^2 - \left(\omega_\Delta^2 - 8\mu_2^2\right)\left(\omega_\Delta^2 + \mu_2^2\right)^2.$$

The results are summarized in the following proposition.

Proposition 3.5 ([156]) *Let* $\xi_{12} = \xi_{21} = \xi$ *and assume that the coupling strength* ξ *is the bifurcation parameter. Additionally, denote the frequency difference and the intervals by* $\omega_\Delta = \omega_1 - \omega_2$ *and*

$$\mathcal{I}_0 = \left(\eta_1^+, \infty\right), \qquad \mathcal{I}_1 = \left(0, \frac{1}{\sqrt{8}}\right), \qquad \mathcal{I}_2 = \left(\frac{1}{\sqrt{8}}, \eta_1^+\right)$$

with the constants

$$\eta_1^+ = \frac{1}{2}\sqrt{\frac{17}{4} + 3\sqrt{13}\cos\left(\frac{1}{3}\cos^{-1}\left(\frac{673}{208\sqrt{13}}\right)\right)}. \tag{3.114}$$

Moreover, denote the positive roots of h from (3.106) *by* $\mu_{1,i}$ *for all* $i = 1, 2, 3$ *and assume that the zeros* $\mu_{1,i}$ *are sorted by the magnitude of their real part beginning with the largest value. Then system* (3.94) *has*

1. *one critical point, if*

$$\left|\tfrac{\mu_2}{\omega_\Delta}\right| \in \mathcal{I}_0 \cup \mathcal{I}_2 \cup \left(\frac{1}{2}, \infty\right), \tag{3.115a}$$

$$\left|\tfrac{\mu_2}{\omega_\Delta}\right| \in \mathcal{I}_1 \wedge |\mu_1| \notin \left(0, \mu_{1,1}\right), \tag{3.115b}$$

$$\left|\tfrac{\mu_2}{\omega_\Delta}\right| \in \mathcal{I}_2 \cap \left(0, \frac{1}{2}\right) \wedge |\mu_1| \notin \left(\mu_{1,2}, \mu_{1,1}\right). \tag{3.115c}$$

2. three critical points, if

$$\left|\frac{\mu_2}{\omega_\Delta}\right| \in \mathcal{I}_1 \wedge |\mu_1| \in \left(0, \mu_{1,1}\right), \tag{3.116a}$$

$$\left|\frac{\mu_2}{\omega_\Delta}\right| \in \mathcal{I}_2 \cap \left(0, \tfrac{1}{2}\right) \wedge |\mu_1| \in \left(\mu_{1,2}, \mu_{1,1}\right). \tag{3.116b}$$

Before the claim is proven, Descartes' rule of signs is summarized because it is needed for the proof.

Theorem 3.8 (Descartes' Rule of Signs, [139]) *Let*

$$P(x) = a_0 x^{b_0} + a_1 x^{b_1} + \ldots + a_n x^{b_n}$$

denote a polynomial with nonzero real coefficients a_i, where the b_i are integers satisfying $0 \leq b_0 < b_1 < b_2 < \ldots < b_n$. Then the number of positive real zeros of $P(x)$ (counted with multiplicities) is either equal to the number of variations in sign in the sequence $\{a_0, a_1, \ldots, a_n\}$ of the coefficients or less than that by an even integer. The number of negative zeros of $P(x)$ (counted with multiplicities) is either equal to the number of variations in sign in the sequence of the coefficients of $P(-x)$ or less than that by an even integer.

Proof. As elaborated, the number of real-valued solutions of (3.95) is determined by the sign of its discriminant $D_{\tilde{\xi}}$, which is given by (3.105). This will be analyzed by investigating the domain of (3.106) with respect to μ_1 and μ_2. The proof is structured as follows: First, the limit at infinity of (3.106) in terms μ_1 is derived. With this, the sign of (3.106) can be determined, if μ_1 is large enough. Second, the number and the sign of the real-valued zeros of (3.106) are derived. The latter is done by reducing (3.106) to a cubic polynomial using the substitution $z_1 = \mu_1^2$, so that the sign of (3.106) is determined by its limit at infinity for all μ, provided that (3.106) is a Hurwitz polynomial with respect to z_1.

First, note that (3.106) approaches positive infinity for $\mu_1 \longrightarrow \pm\infty$. From this it follows that the polynomial (3.104), which determines the critical points of the system (3.94), has only one real-valued zero, if μ_1 is large enough.

Second, the number of real-valued zeros of (3.106) is obtained by computing its discriminant with respect to z_1, which reads

$$D_{h,z_1} = -\frac{729\omega_\Delta^4\mu_2^2\left(\omega_\Delta^2 - 4\mu_2^2\right)^3}{1024}. \tag{3.117}$$

Hence, if $|\mu_2| \leq \frac{1}{2}|\omega_\Delta|$ holds true, (3.106) has three real-valued solutions with respect to z_1. Following the Routh-Hurwitz Criterion (see Theorem 2.4), the number of zeros of (3.106) with positive real parts is determined by the number of sign changes of the series $(\Delta_{0,0}, \Delta_{1,0}, \Delta_{2,0}, \Delta_{3,0})$ with $\Delta_{3,0} = 8$ and

$$\Delta_{0,0} = -\left(\omega_\Delta^2 - 8\mu_2^2\right)\left(\omega_\Delta^2 + \mu_2^2\right)^2, \tag{3.118a}$$

$$\Delta_{1,0} = 6\left(\Delta\omega^4 - 13\Delta\omega^2\mu_2^2 + 4\mu_2^4\right), \tag{3.118b}$$

$$\Delta_{2,0} = \frac{49\Delta\omega^6 - 537\Delta\omega^4\mu_2^2 - 816\Delta\omega^2\mu_2^4 + 256\mu_2^6}{3\left(\Delta\omega^4 - 13\Delta\omega^2\mu_2^2 + 4\mu_2^4\right)}. \tag{3.118c}$$

Subsequently, the domains, in which (3.118) are positive, are derived with respect to μ_2. For this, denote $\eta = \mu_2/\omega_\Delta$:

Note that (3.118a) is increasing in terms of μ_2, but it is negative all for $|\eta| < 1/\sqrt{8}$.

The zeros of (3.118b) are given by $|\eta_2^\pm| = \frac{3\pm\sqrt{17}}{4}$, which implies that (3.118b) approaches positive infinity for $\mu_2 \to \pm\infty$. Thus, (3.118b) is negative for all $|\eta| \in (|\eta_2^-|, |\eta_2^+|)$.

The sign of (3.118c) is investigated by analyzing the numerator and denominator individually. Note that the sign changes of the denominator are given by the sign changes of (3.118b). Additionally, the zeros of the numerator are given by the square root of the real-valued zeros of a cubic polynomial, since by substituting $z_2 = \mu_2^2$ the numerator becomes a cubic polynomial, whose discriminant reads

$$D_{\Delta_{3,0},z_2} = -\frac{79827687}{67108864}\omega_\Delta^{12} < 0.$$

Note that there are two complex-valued zeros of (3.118c) with respect to μ_2, since it has one negative zero with respect to z_2. This is a consequence of Theorem 3.8, which implies that (3.118c) has zero or two positive, real-valued zeros and one negative, real-valued zero.

The results on the signs of $(\Delta_{0,0}, \Delta_{1,0}, \Delta_{2,0}, \Delta_{3,0})$ are summarized in Table 3.1. With these considerations, the signs of (3.118) are given by

$$\Delta_{0,0} \begin{cases} > 0, \text{ if } \left|\frac{\mu_2}{\omega_\Delta}\right| \notin \left(0, \frac{1}{\sqrt{8}}\right), \\ < 0, \text{ if } \left|\frac{\mu_2}{\omega_\Delta}\right| \in \left(0, \frac{1}{\sqrt{8}}\right), \end{cases}$$

$$\Delta_{1,0} \begin{cases} > 0, \text{ if } \left|\frac{\mu_2}{\omega_\Delta}\right| \notin \left(\eta_2^-, \eta_2^+\right), \\ < 0, \text{ if } \left|\frac{\mu_2}{\omega_\Delta}\right| \in \left(\eta_2^-, \eta_2^+\right), \end{cases}$$

$$\Delta_{2,0} \begin{cases} > 0, \text{ if } \left|\frac{\mu_2}{\omega_\Delta}\right| \notin \left(\eta_2^-, c^-\right) \cup \left(\eta_2^+, c^+\right), \\ < 0, \text{ if } \left|\frac{\mu_2}{\omega_\Delta}\right| \in \left(\eta_2^-, c^-\right) \cup \left(\eta_2^+, c^+\right). \end{cases}$$

Table 3.1.: Illustration of the signs of the series $(\Delta_{0,0}, \Delta_{1,0}, \Delta_{2,0}, \Delta_{3,0})$ and the number of sign changes m_{sign} in terms of the corresponding intervals of the absolute value of the normalized damping coefficient $|\mu_2/\omega_\Delta|$. Note that the positive and negative signs are abbreviated by P and N, respectively.

Interval	$\Delta_{0,0}$	$\Delta_{1,0}$	$\Delta_{2,0}$	$\Delta_{3,0}$	m_{sign}
$(0, \eta_2^-)$	N	P	P	P	1
(η_2^-, η_1^-)	N	N	N	P	1
$(\eta_1^-, \frac{1}{\sqrt{8}})$	N	N	P	P	1
$(\frac{1}{\sqrt{8}}, \eta_2^+)$	P	N	P	P	2
(η_2^+, η_1^+)	P	P	N	P	2
(η_1^+, ∞)	P	P	P	P	0

Herein, η_1^+ is determined by (3.114), while η_1^- reads

$$\eta_1^- = \frac{1}{2}\sqrt{\frac{17}{4} - 3\sqrt{13}\sin\left(\frac{\pi}{6} - \frac{1}{3}\cos^{-1}\left(\frac{673}{208\sqrt{13}}\right)\right)}.$$

Then the number of zeros with positive real part is given by

$$m_{\text{sign}} = \begin{cases} 0, \text{ if } \left|\frac{\mu_2}{\omega_\Delta}\right| \in \mathcal{I}_0 = \left(\eta_1^+, \infty\right), \\ 1, \text{ if } \left|\frac{\mu_2}{\omega_\Delta}\right| \in \mathcal{I}_1 = \left(0, \frac{1}{\sqrt{8}}\right), \\ 2, \text{ if } \left|\frac{\mu_2}{\omega_\Delta}\right| \in \mathcal{I}_2 = \left(\frac{1}{\sqrt{8}}, \eta_1^+\right). \end{cases}$$

In particular, note that a detailed description of the sign changes is given in Table 3.1.

With these considerations, it is possible to compare the number of positive zeros with the number of real-valued zeros, which implies the conditions on the number of critical points formulated in (3.115) and (3.116). □

Remark 3.7 *The discriminant of g with respect to the damping coefficients μ_1 and μ_2 has the same structure. Hence, conditions for μ_1 are similar to the conditions* (3.115) *and* (3.116).

To analyze the frequency tunability of diffusively coupled oscillators with respect to symmetric coupling, the results of Proposition 3.5 are investigated numerically. Its critical points can be computed in terms of three trigonometric solutions [100] or one hyperbolic solution [57]. The analytic investigation of the frequency tunability is thus difficult, so that a numerical path is followed.

Example 3.6 *Subsequently, the results of Proposition 3.5 and its implication on the bifurcations of two diffusively coupled Andronov-Hopf oscillators are verified numerically. This is done by analyzing the critical points $\xi_{\text{H},i}$, their characteristic frequencies $\omega_{i,\text{C}}$ and the corresponding crossing condition for all $i = 1, 2, 3$. In particular, the crossing condition (H2) from the Hopf Theorem (see Theorem 2.9) is evaluated by determining the sensitivity $d_{\text{H},i}$ at the respective critical point $\xi_{\text{H},i}$ for all $i = 1, 2, 3$ by evaluating* (3.104) *for $\xi = \xi_{12} = \xi_{21}$. Hence, the sensitivity is determined by*

$$d = \frac{\mathrm{d}}{\mathrm{d}\xi}\left(\operatorname{Re}\lambda(\xi)\right)|_{\mu=\xi_{\text{H}}}.$$

Additionally, the tunability of the characteristic frequencies $\omega_{i,\text{C}}$ are investigated by controlling the asymmetry between the oscillators. This is done by fixing the damping coefficient μ_1 and varying the damping coefficient μ_2.

To investigate the different bifurcation behaviors, which are predicted in Proposition 3.5, the number of bifurcations of (3.94) *and the corresponding changes are evaluated as a function of μ_1 and μ_2 numerically. Here, the numerical values of the natural frequencies are assumed to be given by $\omega_1 = 1\,\frac{1}{\text{s}}$ and $\omega_1 = 2\,\frac{1}{\text{s}}$. The resulting bifurcation diagram is depicted in Figure 3.9. In particular, it is possible to identify three different bifurcation behaviors for the*

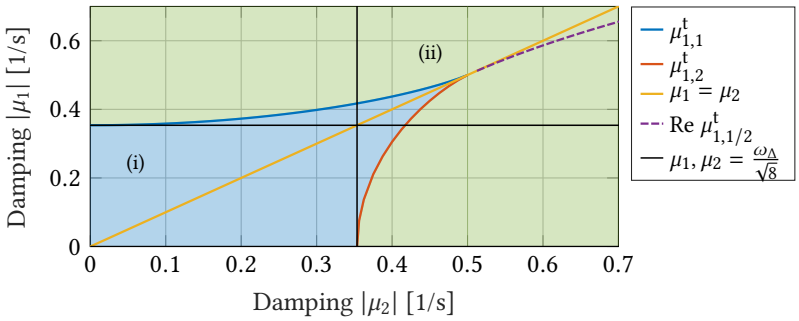

Figure 3.9.: Bifurcation diagram of two diffusively coupled Andronov-Hopf oscillators with symmetric coupling. The number of critical points are marked as follows: Three different critical points are obtained in (i). One unique critical point is marked by (ii). Three critical points with two identical critical points are given by the solid lines.

example. These behaviors can be distinguished by the change of the number of critical points. In particular, the change of the number of critical points is given by (i) the change from three critical point to one critical point, (ii) the change from one critical point over three critical points to one critical point, and (iii) only one critical point. Hence, the critical point ξ_H, the characteristic frequency ω_C and the sensitivity d_H are evaluated for three different damping coefficient $\mu_1 \in \{-1/\sqrt{10}, -3/\sqrt{20}, -1/\sqrt{2}\}\ \frac{1}{s}$.

The results for $\mu_1 = -1/\sqrt{10}\ \frac{1}{s}$, $\mu_1 = -\sqrt{3/20}\ \frac{1}{s}$, and $\mu_1 = -1/\sqrt{2}\ \frac{1}{s}$ are shown in Figures 3.10, 3.11, and 3.12. In particular, the number of critical points and their corresponding changes agree with the analytical results. In addition, the sensitivity d_H is not vanishing for every case so that the crossing condition (H2) of Theorem 2.9 is satisfied. Combining the sign of the sensitivity d_H with the sign of the critical point ξ_H, implies that the first and second pair of complex conjugated eigenvalues, which cross the imaginary axis, are traveling from the left half complex plane to the right half complex plane, if $\mu_1, \mu_2 < 0$. While the third pair of complex conjugated eigenvalues, which cross the imaginary axis, are traveling from the right half complex plane to the left half complex plane, if $\mu_1, \mu_2 < 0$. Hence, the oscillators are always synchronized, if the coupling ξ is strong enough.

Moreover, the simulations imply that the characteristic frequency ω_C of (3.94) *can be controlled in the tunable interval constraint by the natural frequencies ω_1 and ω_2 by changing the damping coefficient μ_1 and μ_2. Similar to injective coupling, the characteristic frequency ω_C is closer to the natural frequency of the oscillator that has the larger absolute value of the damping. In addition, note that the system* (3.94) *should have a unique critical point for sensor applications. This comes from the fact that the complete tunable interval becomes exploitable, since the sub-critical regime is constrained by the first pair of complex conjugated pair of eigenvalues, which travel from the left half to the right half complex plane.*

Damping as Bifurcation Parameter

For the following analysis, it is assumed that one of the damping coefficients μ_1 or μ_2, respectively, is the bifurcation parameter. With this, the polynomial (3.95) to determine the

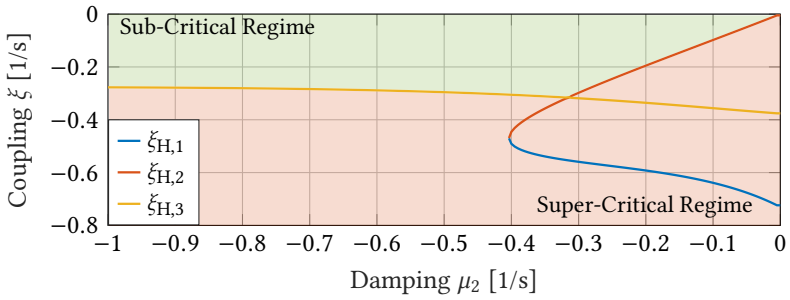

(a) Critical coupling strength $\xi_{H,i}$ as a function of the damping coefficient μ_2 for all $i = 1, 2, 3$.

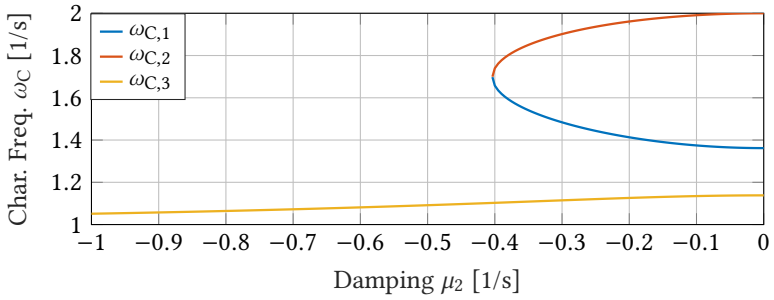

(b) Characteristic frequency $\omega_{C,i}$ as a function of the damping coefficient μ_2 for all $i = 1, 2, 3$.

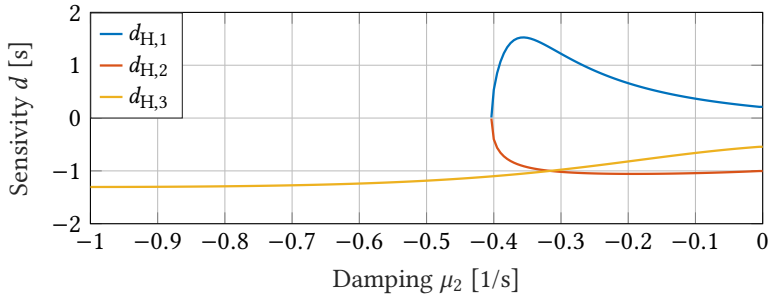

(c) Sensitivity $d_{H,i}$ of the eigenvalues on the imaginary axis as a function of the damping coefficient μ_2 for all $i = 1, 2, 3$.

Figure 3.10.: Critical coupling strength $\xi_{H,i}$, characteristic frequency $\omega_{C,i}$, and sensitivity $d_{H,i}$ with $\mu_1 = -1/\sqrt{10}\ \frac{1}{s}$ in terms of the damping coefficient μ_2 for all $i = 1, 2, 3$.

critical points is also a cubic polynomial. However, instead of analyzing its discriminant, the analysis is first of all simplified by asserting that the damping coefficient is symmetric, i.e., $\mu_1 = \mu_2 = \mu$. Then the polynomial (3.95) to determine the critical points reduces to

$$g_1(\mu) = 4\mu^4 - 8\xi_\Sigma\mu^3 + \left[5\xi_\Sigma^2 + \omega_\Delta^2\right]\mu^2 - \left[\xi_\Sigma^2 + \omega_\Delta^2\right]\xi_\Sigma\mu + \xi_{12}\xi_{21}\omega_\Delta^2 \tag{3.119}$$

with $\xi_\Sigma = \xi_{12} + \xi_{21}$ and $\omega_\Delta = \omega_1 - \omega_2$. In this case, the zeros of (3.119) can be easily derived with the transformation $\mu = z + \frac{\xi_\Sigma}{2}$. This results in

$$g_1(z) = 4z^4 - \left(\xi_\Sigma^2 - \omega_\Delta^2\right)z^2 - \frac{\xi_\Delta^2\omega_\Delta^2}{4}$$

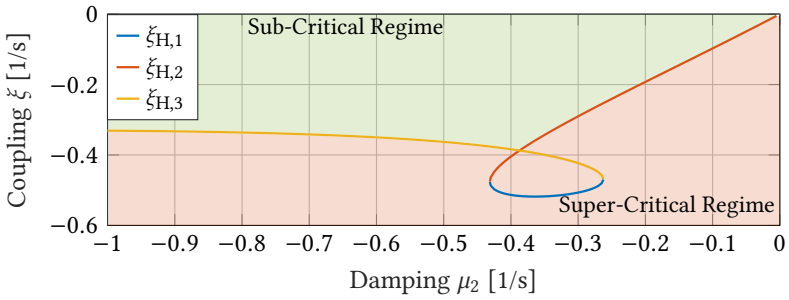

(a) Critical coupling strength $\xi_{H,i}$ as a function of the damping coefficient μ_2 for all $i = 1, 2, 3$.

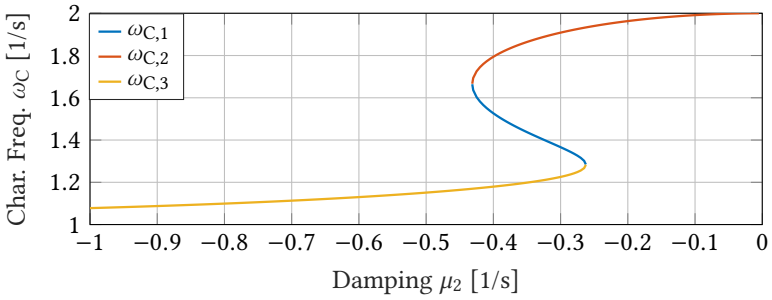

(b) Characteristic frequency $\omega_{C,i}$ as a function of the damping coefficient μ_2 for all $i = 1, 2, 3$.

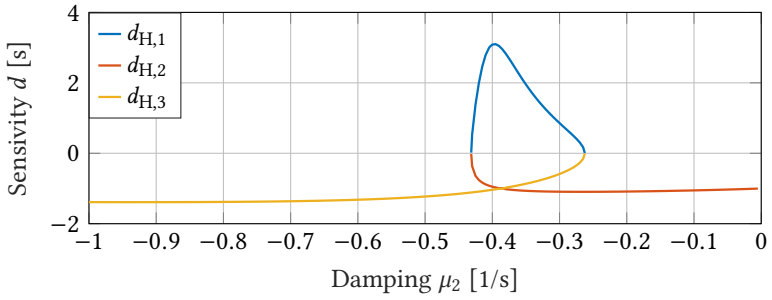

(c) Sensitivity $d_{H,i}$ of the eigenvalues on the imaginary axis as a function of the damping coefficient μ_2 for all $i = 1, 2, 3$.

Figure 3.11.: Critical coupling strength $\xi_{H,i}$, characteristic frequency $\omega_{C,i}$, and sensitivity $d_{H,i}$ with $\mu_1 = -3/\sqrt{20}\ \frac{1}{s}$ in terms of the damping coefficient μ_2 for all $i = 1, 2, 3$.

with $\xi_\Delta = \xi_{12} - \xi_{21}$. Hence, the zeros of (3.119) are determined as

$$\mu_{H,1}^{\pm} = \frac{\xi_\Sigma}{2} \pm \sqrt{\frac{\xi_\Sigma^2 - \omega_\Delta^2 + \sqrt{\left[\xi_\Sigma^2 - \omega_\Delta^2\right]^2 + 4\omega_\Delta^2 \xi_\Delta^2}}{8}}, \tag{3.120a}$$

$$\mu_{H,2}^{\pm} = \frac{\xi_\Sigma}{2} \pm \sqrt{\frac{\xi_\Sigma^2 - \omega_\Delta^2 - \sqrt{\left[\xi_\Sigma^2 - \omega_\Delta^2\right]^2 + 4\omega_\Delta^2 \xi_\Delta^2}}{8}}. \tag{3.120b}$$

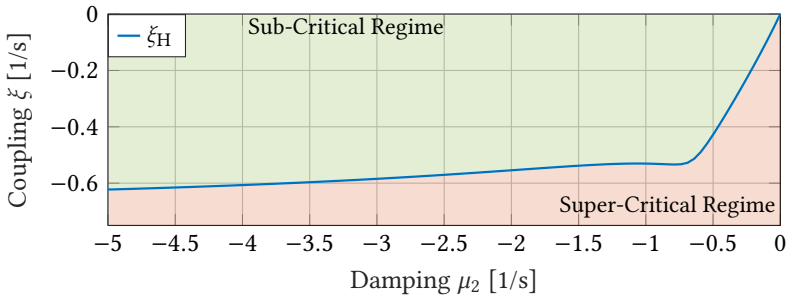

(a) Critical coupling strength ξ_H as a function of the damping coefficient μ_2.

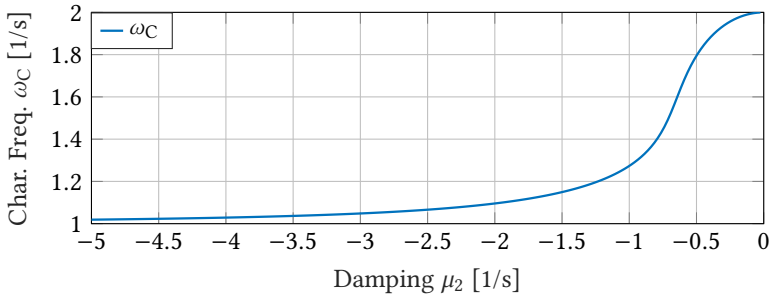

(b) Characteristic frequency ω_C as a function of the damping coefficient μ_2.

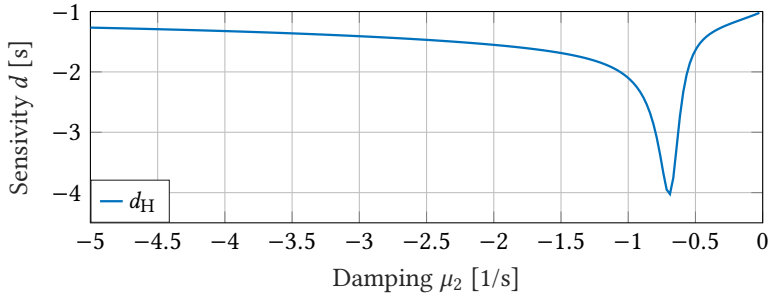

(c) Sensitivity d of the eigenvalues on the imaginary axis as a function of the damping coefficient μ_2.

Figure 3.12.: Critical coupling strength ξ_H, characteristic frequency ω_C, and sensitivity d_H with $\mu_1 = -1/\sqrt{2}\ \frac{1}{s}$ in terms of the damping coefficient μ_2.

Eq. (3.120b) yields are complex values as

$$\xi_\Sigma^2 - \omega_\Delta^2 \leq \sqrt{\left[\xi_\Sigma^2 - \omega_\Delta^2\right]^2 + 4\omega_\Delta^2 \xi_\Delta^2}, \tag{3.121}$$

so that the critical point (3.120b) becomes invalid. In addition, the crossing condition (H2) of the Hopf Theorem (see Theorem 2.9) can be investigated analytically with the analytic solution (3.120a) of the critical point.

Proposition 3.6 ([156]) *Let $\mu_1 = \mu_2 = \mu$, $\xi_{12} \neq \xi_{21}$, and assume that the damping coefficient μ is the bifurcation parameter. Then system* (3.94) *has two Andronov-Hopf bifurcations. The corresponding critical points are given by* (3.120a).

Proof. Subsequently, the crossing condition (H2) of Hopf Theorem (see Theorem 2.9) is analyzed. This is done by evaluating the sensitivity d given by

$$d = \frac{\mathrm{d}}{\mathrm{d}\mu} \left(\operatorname{Re} \lambda(\mu)\right) |_{\mu=\mu_{\mathrm{H}}}.$$

The sensitivity d is derived by inserting $\mu_1 = \mu_2 = \mu$ into (3.98). After simplifying and substituting $\lambda - \mu = \eta$, the characteristic polynomial reads

$$\begin{aligned} P_A = \left(\xi_{21}\omega_1 + \xi_{12}\omega_2\right)^2 + \omega_1^2\omega_2^2 - 2\left(\xi_{21}\omega_1^2 + \xi_{12}\omega_2^2\right)\eta \\ - \left[\left(\xi_{12} + \xi_{21}\right)^2 + \omega_1^2 + \omega_2^2\right]\eta^2 + 2\left(\xi_{12} + \xi_{21}\right)\eta^3 + \eta^4. \end{aligned} \tag{3.122}$$

Taking the derivative of (3.122) with respect to the bifurcation parameter μ and setting the resulting equation to zero, yields

$$0 = \left(1 - \tfrac{\mathrm{d}\lambda}{\mathrm{d}\mu}\right) \frac{\mathrm{d}P_A}{\mathrm{d}\eta}(\mu, \lambda). \tag{3.123}$$

As the derivative $\frac{\mathrm{d}P_A}{\mathrm{d}\eta}(\mu, \lambda) \in \mathbb{R}$ is independent of $\frac{\mathrm{d}\lambda}{\mathrm{d}\mu}$, eq. (3.123) implies $\frac{\mathrm{d}\lambda}{\mathrm{d}\mu} = 1$. Therefore, the crossing condition is satisfied for all critical points since the sensitivity reads

$$d = 1. \tag{3.124}$$

In addition, the sign of (3.124) implies that the eigenvalues are always traveling from the left complex half plane to the right complex half plane as the damping coefficient is increased. □

Combining Remark 3.5 and Proposition 3.6, the qualitative behavior of the solutions of (3.94) can evaluated.

Lemma 3.5 ([156]) *Let $\mu_1 = \mu_2 = \mu$, $\xi_{12} \neq \xi_{21}$ and $\mu_{\mathrm{H}}^{\pm}$ be given by* (3.120a). *Then* (3.94)

1. *is asymptotically stable, if $\mu \in (-\infty, \mu_{\mathrm{H}}^{-}]$,*
2. *has a unique limit cycle, if $\mu \in (\mu_{\mathrm{H}}^{-}, \mu_{\mathrm{H}}^{+}]$,*
3. *has two limit cycles, if $\mu \in (\mu_{\mathrm{H}}^{+}, \infty)$.*

Proof. The claim is shown by analyzing the location of the remaining eigenvalues at the critical point. This is done in two steps: First, it is shown, that all eigenvalues of the system matrix (3.97) are complex-valued. Second, it is determined, if the remaining two eigenvalues at the critical points (3.120a) are located on the right half or the left half complex plane.

Note that $\frac{\mathrm{d}\lambda}{\mathrm{d}\mu} = 1$ holds true for all $\mu \in \mathbb{R}$. Hence, if there is one μ, for which all eigenvalues are complex-valued, it follows for all $\mu \in \mathbb{R}$ that all eigenvalues are complex-valued. Thus,

assume that $\mu = 0$ is a critical point, which is satisfied, if $g_1(0) = 0$ with g_1 given by (3.119) holds true. Thus,

$$g_1(0) = \xi_{12}\xi_{21}\omega_\Delta$$

implies

$$\xi_{12} = 0 \vee \xi_{21} = 0 \vee \omega = \omega_1 = \omega_2. \tag{3.125}$$

In addition, the coefficients (3.99) of the characteristic polynomial $P_A = \lambda^4 + a_3\lambda^3 + a_2\lambda^2 + a_1\lambda + a_0$ reduce to

$$\begin{aligned} a_0 &= (\xi_{21}\omega_1 + \xi_{12}\omega_2)^2 + \omega_2^2\omega_1^2, & a_1 &= 2\left(\xi_{21}\omega_1^2 + \xi_{12}\omega_2^2\right), \\ a_2 &= (\xi_{12} + \xi_{21})^2 + \omega_1^2 + \omega_2^2, & a_3 &= 2\left(\xi_{12} + \xi_{21}\right) \end{aligned}$$

and the eigenvalues hence read

$$\lambda_1^\pm = -\frac{\xi_\Sigma - \mathrm{i}\omega_\Sigma}{2} \pm \frac{w}{2}, \tag{3.126a}$$

$$\lambda_2^\pm = -\frac{\xi_\Sigma + \mathrm{i}\omega_\Sigma}{2} \pm \frac{w}{2} \tag{3.126b}$$

with

$$w = \sqrt{(\xi_{12} + \xi_{21})^2 - (\omega_1 - \omega_2)^2 + \mathrm{i}2\,(\omega_1 - \omega_2)\,(\xi_{12} - \xi_{21})} \tag{3.127}$$

$$\tag{3.128}$$

Inserting (3.125) into (3.127), results in

$$w = \begin{cases} \xi_{21} - \mathrm{i}(\omega_1 - \omega_2), & \text{if } \xi_{12} = 0 \\ \xi_{12} + \mathrm{i}(\omega_1 - \omega_2), & \text{if } \xi_{21} = 0 \\ \xi_{12} + \xi_{21}, & \text{if } \omega = \omega_1 = \omega_2 \end{cases}.$$

so that the eigenvalues of the system matrix (3.97) at the critical point are given by

$$\lambda_1^\pm = \begin{cases} -\frac{\xi_{21} \mp \xi_{21} - \mathrm{i}(\omega_\Sigma \pm \omega_\Delta)}{2} & \text{if } \xi_{12} = 0 \\ -\frac{\xi_{12} \mp \xi_{12} - \mathrm{i}(\omega_\Sigma \pm \omega_\Delta)}{2} & \text{if } \xi_{21} = 0 \\ -\frac{\xi_\Sigma \mp \xi_\Sigma - \mathrm{i}2\omega}{2} & \text{if } \omega = \omega_1 = \omega_2 \end{cases},$$

$$\lambda_2^\pm = \begin{cases} -\frac{\xi_{21} \mp \xi_{21} + (\mathrm{i}\omega_\Sigma \mp \omega_\Delta)}{2} & \text{if } \xi_{12} = 0 \\ -\frac{\xi_{12} \mp \xi_{12} + \mathrm{i}(\omega_\Sigma \mp \omega_\Delta)}{2} & \text{if } \xi_{21} = 0 \\ -\frac{\xi_\Sigma \mp \xi_\Sigma + \mathrm{i}2\omega}{2} & \text{if } \omega = \omega_1 = \omega_2 \end{cases}.$$

Obviously, all eigenvalues at the critical point are complex-valued for μ, if $\omega > 0$, which is always satisfied.

Second, the sign of the real part of the pair of eigenvalues with non-zero real part is analyzed. This is done by investigating the location of the remaining eigenvalues, which

are determined by $P_\mathrm{R} = \lambda^2 + s_1\lambda + s_0$ with the coefficients s_1 and s_0 given by (3.100b) and (3.100c), i.e.,

$$\begin{aligned} s_1 &= -2\left(\mu_1 + \mu_2 - \xi_{12} - \xi_{21}\right), \\ s_0 &= \frac{1}{\mu_1 + \mu_2 - \xi_{12} - \xi_{21}} \left\{ \left(\mu_1 + \mu_2\right)^3 - \left(\xi_{12} + \xi_{21}\right)^3 - \xi_{12}\omega_1^2 - \xi_{21}\omega_2^2 - \left(3\xi_{12} + 4\xi_{21} - \mu_2\right)\mu_1^2 \right. \\ &\quad - \left(4\xi_{12} + 3\xi_{21} - \mu_1\right)\mu_2^2 - 8\left(\xi_{12} + \xi_{21}\right)\mu_1\mu_2 + \left[\left(\xi_{12} + \xi_{21}\right)\left(3\xi_{12} + 4\xi_{21}\right) + \omega_1^2\right]\mu_1 \\ &\quad \left. + \left[\left(\xi_{12} + \xi_{21}\right)\left(4\xi_{12} + 3\xi_{21}\right) + \omega_2^2\right]\mu_2 \right\}, \end{aligned}$$

Inserting (3.120a) into (3.100b) results in

$$s_1|_{\mu=\mu_{\mathrm{H},1}^{\pm}} = \mp\sqrt{\frac{\xi_\Sigma^2 - \omega_\Delta^2 + \sqrt{\left[\xi_\Sigma^2 - \omega_\Delta^2\right]^2 + 4\omega_\Delta^2\xi_\Delta^2}}{2}}. \tag{3.129}$$

In addition, $s_0 > 0$, since (3.99) has two pairs of complex conjugated eigenvalues. From (3.129), it follows that $\operatorname{sign}(s_1|_{\mu=\mu_{\mathrm{H},1}^-}) = 1$ at $\mu = \mu_{\mathrm{H},1}^-$ and $\operatorname{sign}(s_1|_{\mu=\mu_{\mathrm{H},1}^+}) = -1$ at $\mu = \mu_{\mathrm{H},1}^+$. Combined with (3.124), the first pair of eigenvalues crosses the imaginary axis after surpassing $\mu_{\mathrm{H},1}^-$, since the remaining two zeros of (3.98) have a negative real part at $\mu = \mu_{\mathrm{H},1}^-$. Moreover, a second pair of eigenvalues crosses the axis imaginary after surpassing $\mu_{\mathrm{H},1}^+$, since the remaining zeros of (3.98) have a positive real part at $\mu = \mu_{\mathrm{H},1}^+$. □

The characteristic frequency is analyzed with these results. This can be done by inserting the critical points (3.120a) into

$$\omega_\mathrm{C} = \sqrt{\frac{\left(c_{1,12} + c_{1,21}\right)\mu - c_{2,12}\xi_{12} - c_{2,21}\xi_{21}}{2\mu - \xi_{12} - \xi_{21}}},$$

which results in

$$\omega_{\mathrm{C},1}^{\pm} = \sqrt{\frac{4g_\mathrm{C}^2 - \xi_\Sigma^2}{4} \pm \frac{\left(\xi_\Delta \pm 2g_\mathrm{C}\right)\omega_1^2 - \left(\xi_\Delta \mp 2g_\mathrm{C}\right)\omega_2^2}{g_\mathrm{C}}} \tag{3.130}$$

given

$$g_\mathrm{C}(\xi_{12}, \xi_{21}) = \sqrt{\frac{\xi_\Sigma^2 - \omega_\Delta^2 + \sqrt{\left[\xi_\Sigma^2 - \omega_\Delta^2\right]^2 + 4\omega_\Delta^2\xi_\Delta^2}}{8}}.$$

The limits of (3.130) are determined by inserting $\xi_{12} = 0$ or $\xi_{12} = 0$. This yields

$$\omega_{\mathrm{C},1}^- = \begin{cases} \omega_1, & \text{if } \xi_{12} = 0 \\ \omega_2, & \text{if } \xi_{21} = 0 \end{cases}, \qquad \omega_{\mathrm{C},1}^+ = \begin{cases} \omega_1, & \text{if } \xi_{21} = 0 \\ \omega_2, & \text{if } \xi_{12} = 0 \end{cases}.$$

Example 3.7 *To conclude this section, the tunability in the sub-critical regime with negative coupling is analyzed by simulating the characteristic frequency ω_C^- at the critical point μ_H^-. The parameters of* (3.94) *are given by $\omega_1 = 10\,\frac{1}{\mathrm{s}}$ and $\omega_2 = 20\,\frac{1}{\mathrm{s}}$. The result is shown in Figure 3.13. As expected, the characteristic frequency ω_C^- is tunable inside the interval (ω_1, ω_2) by controlling the coupling ξ_{12} and ξ_{21}.*

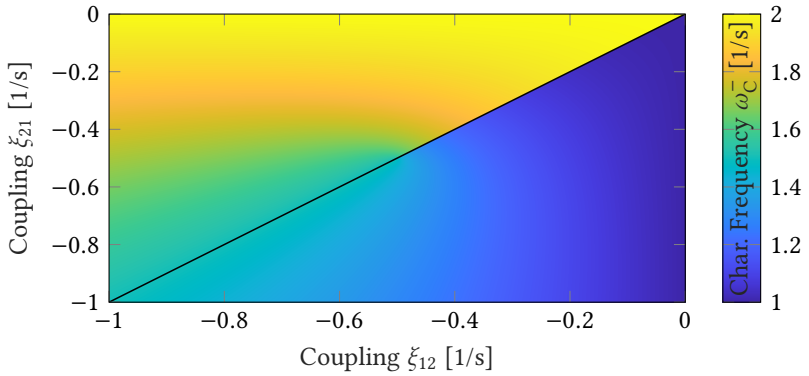

Figure 3.13.: Frequency tunability induced by asymmetric coupling. In particular, the characteristic frequency ω_C^- at the critical damping coefficient μ_H^- is given as a function the coupling ξ_{12} and ξ_{21}.

3.2. Delayed Feedback

By introducing a delayed feedback, the dynamics of oscillators can change fundamentally. For instance, it is observed in [106, 107] that two diffusively coupled Andronov-Hopf oscillators become frequency tunable by introducing time delay. Similarly, it is shown numerically in [43] that the frequency of injectively coupled Andronov-Hopf oscillators with delayed coupling is tunable. Yet, it is not clear from [43, 106, 107], if the characteristic frequency becomes tunable by coupling via delayed signals or a controllable time delay.

The tunability enhancement by introducing a controllable delay is subsequently investigated by analyzing the bifurcation of the complex-valued representation (3.1) with additional delayed feedback. In addition, denote $z_\tau(t) = z(t-\tau)$ with a positive delay $\tau \geq 0$, so that the Andronov-Hopf oscillator with additional delayed feedback is governed by

$$\dot{z} = f(z, z_\tau), \qquad t > 0, \qquad z(\theta) = z_0(\theta), \qquad \theta \in [-\tau, 0] \tag{3.131a}$$

with

$$f(z, z_\tau) = (\mu + \mathrm{i}\omega)z + (\eta + \mathrm{i}\nu)z_\tau - |z|^2 z, \tag{3.131b}$$

the state $z(t) \in \mathbb{C}$ and initial condition $z_0(\theta) \in \mathbb{C}$. Herein, the parameters are given by natural frequencies ω, $\nu > 0$ and the damping coefficient μ, $\eta \in \mathbb{R}$. The results of the bifurcation analysis are summarized subsequently.

Theorem 3.9 ([152]) *Let the delay τ be the bifurcation parameter and assume that $\sqrt{\eta^2+\nu^2} \geq |\mu|$. Then the critical points and characteristic frequencies of system* (3.131) *are given by*

$$\tau_{H,k}^+ = \frac{2\pi k + \arccos\left(-\frac{\operatorname{sign}(\eta)\mu}{\sqrt{\eta^2+\nu^2}}\right) + \varphi}{\omega - \operatorname{sign}(\eta)\sqrt{\eta^2+\nu^2-\mu^2}} \tag{3.132a}$$

$$\omega_C^+ = \omega - \operatorname{sign}(\eta)\sqrt{\eta^2+\nu^2-\mu^2}, \tag{3.132b}$$

and

$$\tau_{\mathrm{H},k}^{-} = \frac{2\pi k - \arccos\left(-\frac{\operatorname{sign}(\eta)\mu}{\sqrt{\eta^2+\nu^2}}\right) + \varphi}{\omega + \operatorname{sign}(\eta)\sqrt{\eta^2+\nu^2-\mu^2}}, \tag{3.133a}$$

$$\omega_{\mathrm{C}}^{-} = \omega + \operatorname{sign}(\eta)\sqrt{\eta^2+\nu^2-\mu^2} \tag{3.133b}$$

for all $k \in \mathbb{N}_0$*. Herein, the phase reads*

$$\varphi = \begin{cases} \arctan\left(\frac{\nu}{\eta}\right), & \text{if } \eta > 0 \\ \pi - \arctan\left(\frac{\nu}{\eta}\right), & \text{if } \eta < 0. \end{cases} \tag{3.134}$$

Moreover, these bifurcations are Andronov-Hopf bifurcations if $\tau_{\mathrm{H},k}^{-} < \tau_{\mathrm{H},k}^{+}$ *for all* $k \in \mathbb{N}_0$ *holds true, and the system* (3.131) *is asymptotically stable for* $\tau \in \mathcal{M}_\tau \cap \mathbb{R}_{\geq 0}$ *with*

$$\mathcal{M}_\tau = \begin{cases} [0, \tau_{\mathrm{H},0}^{-}] \cup \bigcup_{k=0}^{\infty} [\tau_{\mathrm{H},k}^{+}, \tau_{\mathrm{H},k+1}^{-}], & \text{if } \eta > 0 \\ \bigcup_{k=0}^{\infty} [\tau_{\mathrm{H},k}^{-}, \tau_{\mathrm{H},k}^{+}], & \text{if } \eta < 0. \end{cases} \tag{3.135}$$

Proof. This proof is based on the Hopf Theorem (see Theorem 2.9). For this, the bifurcation parameter is assumed to be the delay τ.

(H1) The linearization of (3.131) is obtained by substituting the equilibrium z_{eq} of (3.131) into the Jacobian of $f(z, z_\tau)$, i.e., $a_0 = \partial_z f(z, z_\tau)|_{z=z_{\mathrm{eq}}}$ and $a_1 = \partial_{z=z_\tau} f(z, z_\tau)|_{z_{\mathrm{eq}}}$. The equilibrium z_{eq} is determined by solving $f(z_{\mathrm{eq}}, z_{\mathrm{eq}}) = 0$, which yields $z_{\mathrm{eq}} = 0$. Hence, the linearized system is given by

$$\Delta\dot{z} = a_0 \Delta z + a_1 \Delta z_\tau \tag{3.136}$$

with the parameters $a_0 = \mu + \mathrm{i}\omega \in \mathbb{C}$ and $a_1 = \eta + \mathrm{i}\nu \in \mathbb{C}$. It should be noted that the stability of (3.136) has been discussed in detail in [141]. Following [114] and [95], the characteristic function of (3.136) is given by

$$f_{\mathrm{CF}}(\lambda) = \lambda - \left(\mu + \eta \mathrm{e}^{-\lambda\tau}\right) - \mathrm{i}\left(\omega + \nu \mathrm{e}^{-\lambda\tau}\right). \tag{3.137}$$

In particular, (3.137) has to have a pair of eigenvalues with zero real part. These are determined by inserting the ansatz $\lambda = \mathrm{i}\omega_{\mathrm{C}}$ with the characteristic frequency $\omega_{\mathrm{C}} \in \mathbb{R}$ and Euler's formula $\mathrm{e}^{-\mathrm{i}\omega_{\mathrm{C}}\tau} = \cos(\omega_{\mathrm{C}}\tau) - \mathrm{i}\sin(\omega_{\mathrm{C}}\tau)$ into (3.137). Splitting real and imaginary part yields

$$0 = \mu + \eta\cos(\omega_{\mathrm{C}}\tau) + \nu\sin(\omega_{\mathrm{C}}\tau), \tag{3.138a}$$

$$0 = \omega_{\mathrm{C}} - \omega + \eta\sin(\omega_{\mathrm{C}}\tau) - \nu\cos(\omega_{\mathrm{C}}\tau). \tag{3.138b}$$

After inserting the relationships

$$\nu\sin(\omega_{\mathrm{C}}\tau) + \eta\cos(\omega_{\mathrm{C}}\tau) = \sqrt{\eta^2+\nu^2}\ \cos\left(\omega_{\mathrm{C}}\tau - \varphi\right),$$

$$\eta\sin(\omega_{\mathrm{C}}\tau) - \nu\cos(\omega_{\mathrm{C}}\tau) = \sqrt{\eta^2+\nu^2}\ \sin\left(\omega_{\mathrm{C}}\tau - \varphi\right),$$

with φ given by (3.134), equations (3.138) can be solved for the delay τ and the characteristic frequency ω_C. This results in (3.132) and (3.133). In particular, the delay τ is real-valued, if $\sqrt{\eta^2 + \nu^2} \geq |\mu|$, since (3.138a) can be rewritten as

$$\cos(\omega_C \tau - \varphi) = -\frac{\mu}{\sqrt{\eta^2 + \nu^2}}$$

with φ given by (3.134).

(H2) Second, by varying the bifurcation parameter τ, the complex conjugated eigenvalues move in the complex plane. In particular, the location and its sensitivity is important to deduce the properties of the bifurcation. To determine the location of the eigenvalues of (3.131) before surpassing the first critical point, assume that the delay τ approaches 0, so that the eigenvalues of (3.131) have to approach

$$\lambda = (\mu + \eta) + \mathrm{i}(\omega + \nu). \tag{3.139}$$

Hence, the location before surpassing the first critical point is determined by analyzing the real part of (3.139). If $\mu + \eta < 0$, the eigenvalues of (3.136) are negative. In this case, the system (3.131) is asymptotically stable. In contrast to this, if $\mu + \eta > 0$, at least one eigenvalue of (3.136) is positive. In particular, the uniqueness of the eigenvalue (3.139) implies that only one eigenvalue of (3.136) has a positive real-part, so that a limit cycle has to emerges. To determine the change induced by the bifurcation, the sensitivity of the eigenvalues on the imaginary axis has to be investigated. With this, the asymptotically stable and oscillating regimes of (3.131) can be characterized. The sensitivity is derived by setting (3.137) to zero, i.e., $f_{CF}(\lambda) = 0$, and taking the derivative of this equation with respect to the delay τ. Solving the result for $\frac{\mathrm{d}\lambda}{\mathrm{d}\tau}$ and inserting the ansatz $\lambda = \mathrm{i}\omega_C$, yields

$$\lambda_{\tau_H}^{(1)} = \left.\frac{\mathrm{d}\lambda}{\mathrm{d}\tau}\right|_{\lambda=\mathrm{i}\omega_C} = \frac{\omega_C}{c_1}\left[\omega_C - \omega - \mathrm{i}\left(\tau\eta^2 + \tau\nu^2 - \mu\right)\right] \tag{3.140}$$

with the constant

$$c_1 = 1 - 2\mu\tau + \left(\eta^2 + \nu^2\right)\tau^2.$$

The real part of (3.140) is given by

$$\mu_{\tau_H}^{(1)} = \mathrm{Re}\,\lambda_{\tau_H}^{(1)} = \frac{\omega_C(\omega_C - \omega)}{c_1}. \tag{3.141}$$

In particular, the constant c_1 is positive, since

$$c_1 \geq 1 - 2\mu\tau + \mu^2\tau^2 = (1 - \mu\tau)^2 \geq 0.$$

Hence, (3.141) satisfies

$$\mu_{\tau_H}^{(1)} \begin{cases} > 0, & \text{if } \omega_C > \omega, \\ < 0, & \text{if } \omega_C < \omega. \end{cases} \tag{3.142}$$

Combining the location of the eigenvalues before the first critical point is surpassed with eqns. (3.132) and (3.142), implies that the set of asymptotic stable regimes reads $\mathcal{M}_{\mathrm{s}}^{\mathrm{O}} = \mathcal{M}_{\tau}^{\mathrm{O}} \cap \mathbb{R}_{\geq 0}$ with

$$\mathcal{M}_{\tau}^{\mathrm{O}} = \begin{cases} [0, \tau_{\mathrm{H},0}^{-}) \cup \bigcup_{k=0}^{\infty} (\tau_{\mathrm{H},k}^{+}, \tau_{\mathrm{H},k+1}^{-}), & \text{if } \eta > 0, \\ \bigcup_{k=0}^{\infty} (\tau_{\mathrm{H},k}^{-}, \tau_{\mathrm{H},k}^{+}), & \text{if } \eta < 0. \end{cases}$$

Note that compared to (3.135) the set $\mathcal{M}_{\tau}^{\mathrm{O}}$ consists of open intervals, since the stability of (3.131) at the critical point cannot be deduced from the eigenvalues. In addition, it can happen that the interval $(\tau_{\mathrm{H},k}^{+}, \tau_{\mathrm{H},k+1}^{-})$ is empty, i.e., when $\tau_{\mathrm{H},k}^{+} > \tau_{\mathrm{H},k+1}^{-}$ if $\eta > 0$.

(H3) Third, the stability of the system (3.131) at the critical point $\tau_{\mathrm{H},k}^{\pm}$ is analyzed by using the comparison approach, e.g., see [114]. For this, (3.131) is transformed into a real-valued system with $x_1 = \operatorname{Re} z$ and $x_2 = \operatorname{Im} z$, which yields

$$\dot{\boldsymbol{x}} = \begin{bmatrix} \mu & -\omega \\ \omega & \mu \end{bmatrix} \boldsymbol{x} + \begin{bmatrix} \eta & -\nu \\ \nu & \eta \end{bmatrix} \boldsymbol{x}_{\tau_{\mathrm{H},k}^{\pm}} - \|\boldsymbol{x}\|_2^2 \boldsymbol{x} \tag{3.143}$$

with the euclidean norm $\|\cdot\|_2$. In particular, the previous analysis of the eigenvalues still holds true for (3.143). Thus, the linearized, delayed system (3.136) is bounded by a finite dimensional, linear system, so that the trajectory of (3.143) can be overestimated by

$$\boldsymbol{x}(t) \leq \mathrm{e}^{a_{\mathrm{comp}} t} \boldsymbol{x}_0 \tag{3.144}$$

with the identity matrix $I \in \mathbb{R}^{2\times 2}$ and the real part of the maximum eigenvalue

$$a_{\mathrm{comp}} \geq \operatorname{Re}\{\max\left[\sigma(\mathcal{A})\right]\}.$$

with the system operator from (3.143). Herein, the spectrum of $\mathcal{A}$ denote by $\sigma(\mathcal{A})$. This overestimation is valid, since asymptotic and exponential stability are equivalent for delayed and undelayed linear ODEs [95]. With these considerations, a Lyapunov-Razumikhin candidate function can be defined by $V = \boldsymbol{x}^{\mathrm{T}} P \boldsymbol{x}$ with a positive definite matrix $P \in \mathbb{R}^{2\times 2}$. This candidate satisfies $\min[\sigma(P)]\|\boldsymbol{x}\|_2^2 \leq V \leq \max[\sigma(P)]\|\boldsymbol{x}\|_2^2$ and its rate of change along a solution trajectory of (3.143) is given by

$$\begin{aligned} \dot{V} = &\left(\boldsymbol{x}^{\mathrm{T}} \begin{bmatrix} \mu & -\omega \\ \omega & \mu \end{bmatrix}^{\mathrm{T}} + \boldsymbol{x}_{\tau_{\mathrm{H},k}^{\pm}}^{\mathrm{T}} \begin{bmatrix} \eta & -\nu \\ \nu & \eta \end{bmatrix}^{\mathrm{T}} \right) P \boldsymbol{x} \\ &+ \boldsymbol{x}^{\mathrm{T}} P \left(\begin{bmatrix} \mu & -\omega \\ \omega & \mu \end{bmatrix} \boldsymbol{x} + \begin{bmatrix} \eta & -\nu \\ \nu & \eta \end{bmatrix} \boldsymbol{x}_{\tau_{\mathrm{H},k}^{\pm}} \right) - \|\boldsymbol{x}\|^2 \boldsymbol{x}^{\mathrm{T}} P \boldsymbol{x} \\ &\leq (2 a_{\mathrm{comp}} - \|\boldsymbol{x}\|^2) \boldsymbol{x}^{\mathrm{T}} P \boldsymbol{x}. \end{aligned}$$

Hence, the system (3.131) at the critical point $\tau_{\mathrm{H},k}^{\pm}$ is asymptotically stable if

$$\operatorname{Re}\{\max\left[\sigma\left(\mathcal{A}\right)\right]\} = 0.$$

In particular, this is satisfied on the boundaries of $\mathcal{M}_{\mathrm{s}}^{\mathrm{O}}$, which yields (3.135). This concludes the proof. □

As expected Theorem 3.9 suggests that a delay can destabilize or stabilize the system (3.131). For an oscillator this can be viewed as an interference between the oscillations and the delayed feedback. In addition, the characteristic frequency ω_C of the system (3.131) becomes tunable by assigning the delay τ, the damping coefficient η, and the frequency ν accordingly. This can be explained by interpreting a single oscillator with delayed feedback as two coupled oscillators, where amplitude and phase of the coupled signals can be controlled. By assigning the amplitude and phase of the coupled signal, the characteristic frequency ω_C can be decreased or increased. To conclude the chapter, the results are numerically verified:

Example 3.8 *Subsequently, the characteristic frequency of* (3.131) *is investigated numerically. In particular, the analysis focuses on the numerical validation of the asymptotically stable regimes of* (3.131)*. The parameters are given by* $\omega = 100\,\frac{1}{s}$, $\mu = -10\,\frac{1}{s}$, $\nu = 0\,\frac{1}{s}$, *and* $\eta \in [-10, -50]\,\frac{1}{s}$. *It has to be stressed that* (3.131) *is asymptotically stable, if* $\tau = 0$, *since the real-part of the eigenvalue is given by* $\mu + \eta \in [-20, -60]\,\frac{1}{s}$.

The results are shown in Figure 3.14 and 3.15. Herein, the characteristic frequencies ω_C^- *and* ω_C^+ *are illustrated in Figure 3.14. For the numerical parameters, the characteristic frequency* ω_C^- *decreases by increasing the damping coefficient* η. *While, the frequency* ω_C^+ *increases by increasing the damping coefficient* η. *In the sub-critical regime, the characteristic frequency* ω_C^+ *is unlimited, since* $\tau_{H,k}^- < \tau_{H,k+1}^-$ *is satisfied for all* η, *and the frequency* ω_C^- *has a lower limit. This limit reads* $\tau_{H,k}^+ > \tau_{H,k+1}^-$. *In addition, the different regimes are depicted in Figure 3.15 and examples of the different regimes are illustrated in Figure 3.16. The parameters of these regimes are depicted by the different makers in Figure 3.15.*

Example 3.9 *In the following, the first eigenvalue, which crosses the imaginary axis as the delay* τ *is increased, is evaluated. For this, the parameters are given by* $\omega = 20\,\frac{1}{s}$, $\mu = -5\,\frac{1}{s}$, $\nu = 0\,\frac{1}{s}$, *and* $\eta \in [-5, -15]\,\frac{1}{s}$. *The results are illustrated in Figure 3.17. Herein, the real part* $\mu_\lambda = \mathrm{Re}\,\lambda$ *and the critical points* $\tau_{H,0}^+$, $\tau_{H,1}^-$, *and* $\tau_{H,1}^+$ *are shown in Figure 3.17a. As the delay* τ *is increased, the real part* μ_λ *of the first eigenvalue becomes zero for the critical points* $\tau_{H,0}^+$ *and* $\tau_{H,1}^-$. *If the delay* τ *is further increased,* μ_λ *remains non-zero, so that a different eigenvalue has to induce the Andronov-Hopf bifurcation. From this, it follows that, if the delay satisfies* $\tau = \tau_{H,k}^+ = \tau_{H,k+1}^-$, *the system has two eigenvalues on the imaginary axis and*

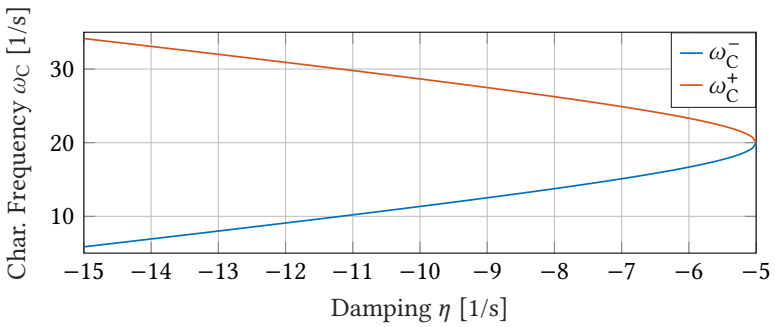

Figure 3.14.: Characteristic frequencies ω_C^+ and ω_C^- at the critical point $\tau_{H,k}^+$ and $\tau_{H,k}^-$ as a function of the damping coefficient η for all $k \in \mathbb{N}$.

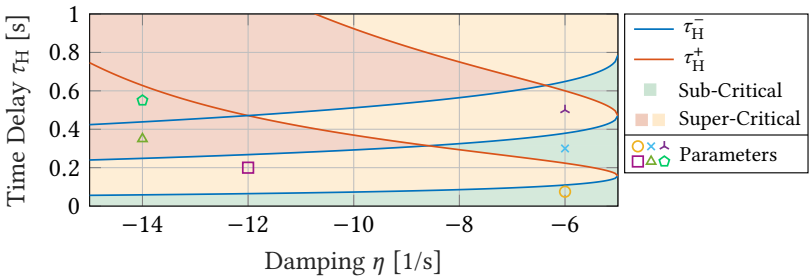

Figure 3.15.: Critical delay τ_H and the different regimes in terms of the damping coefficient η. In addition, the parameters of the results in Figure 3.16 simulation are marked by a circle, a cross, a star, a square, a triangle, and a pentagon.

thus two different characteristic frequencies, because a Hopf-Hopf bifurcation emerges. For a single oscillator, the neighborhood of the critical point of the Hopf-Hopf bifurcation has to be avoided, since the frequency of the external stimuli cannot be reconstructed in this case. Moreover, the imaginary part $\omega_\lambda = \operatorname{Im}\lambda$ of the first eigenvalue is shown in Figure 3.17b. In comparison to the natural frequency ω, the frequency ω_λ is decreased around the critical point $\tau_{H,0}^-$ and increased around the critical point $\tau_{H,0}^+$. Thus, the tunability of this system is also achieved in both the sub-critical and super-critical regime.

Example 3.10 *Finally, the amplitude response of the harmonically excited, delayed Andronov-Hopf oscillator is numerically investigated. This oscillator is governed by*

$$\dot{z} = (\mu + \mathrm{i}\omega)z + (\eta + \mathrm{i}\nu)z_\tau - |z|^2 z + F_{ex}\mathrm{e}^{\mathrm{i}(\omega_{ex}t)} \tag{3.145}$$

with the state $z \in \mathbb{C}$, the delay $\tau > 0$, the damping coefficient $\mu, \eta \in \mathbb{R}$, the natural frequencies $\omega, \nu > 0$, the external frequency $\omega_{ex} > 0$, and the complex-valued amplitude $F_{ex} \in \mathbb{C}$. Note that the amplitude response is computed by evaluating the steady state of (3.145)*. This can be done, e.g., by asserting a 1:1 phase lock, such that the trajectory of* (3.145) *reads*

$$z = \rho\mathrm{e}^{\mathrm{i}\omega_{ex}t} \tag{3.146}$$

with the complex-valued amplitude $\rho(t) \in \mathbb{C}$. Inserting (3.146) *into* (3.145) *and simplifying the expression, results in*

$$\dot{\rho} = [\mu + \mathrm{i}(\omega - \omega_{ex}) + \eta\mathrm{e}^{-\mathrm{i}\omega_{ex}\tau} + \mathrm{i}\nu\mathrm{e}^{-\mathrm{i}\omega_{ex}\tau}]\rho - \rho^3 + F_{ex}. \tag{3.147}$$

By asserting $\dot{\rho}$ the amplitude response of (3.147) *can be computed. In particular, subtracting F_{ex} and taking the absolute value squared, simplifies the steady state equations to*

$$\begin{aligned} 0 = |\rho|^6 - 2\left[\mu + \eta\cos(\omega_{ex}\tau) + \nu\sin(\omega_{ex}\tau)\right]|\rho|^4 + \big[(\mu + \eta\cos(\omega_{ex}\tau) + \nu\sin(\omega_{ex}\tau))^2 \\ + (\omega - \omega_{ex} - \eta\sin(\omega_{ex}\tau) + \nu\cos(\omega_{ex}\tau))^2\big]|\rho|^2 - |F_{ex}|^2. \end{aligned} \tag{3.148}$$

Note that this equation might have multiple real-valued solutions. For the purpose of this example, the number of solutions of (3.148) *at the critical point is analyzed. This is done by inserting* (3.138) *into* (3.148)*, which yields*

$$0 = |\rho|^6 + (\omega_C - \omega_{ex})^2|\rho|^2 - |F_{ex}|^2. \tag{3.149}$$

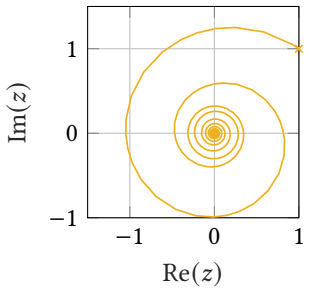

(a) Phase plane for the parameters $\eta = -6\,\frac{1}{\mathrm{s}}$ and $\tau = 0.1\,\mathrm{s}$.

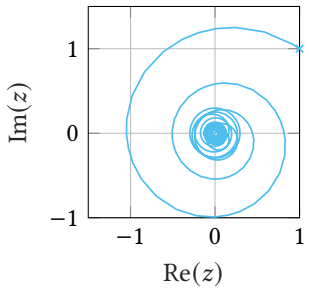

(b) Phase plane for the parameters $\eta = -6\,\frac{1}{\mathrm{s}}$ and $\tau = 0.3\,\mathrm{s}$.

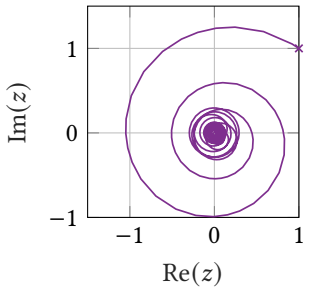

(c) Phase plane for the parameters $\eta = -6\,\frac{1}{\mathrm{s}}$ and $\tau = 0.5\,\mathrm{s}$.

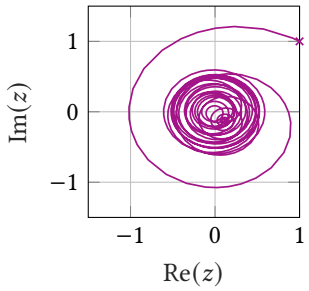

(d) Phase plane for the parameters $\eta = -12\,\frac{1}{\mathrm{s}}$ and $\tau = 0.2\,\mathrm{s}$.

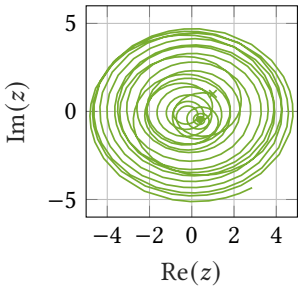

(e) Phase plane for the parameters $\eta = -14\,\frac{1}{\mathrm{s}}$ and $\tau = 0.35\,\mathrm{s}$.

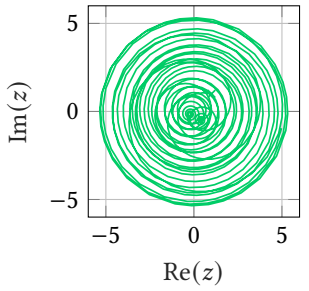

(f) Phase plane for the parameters $\eta = -14\,\frac{1}{\mathrm{s}}$ and $\tau = 0.55\,\mathrm{s}$.

Figure 3.16.: Phase plot of an Andronov-Hopf oscillator with damping coefficient η given by system (3.131) in different operation regimes. The parameters of the delay τ and the damping coefficient η of the operation regimes are marked in Figure 3.15, respectively.

Employing Theorem 3.8 on (3.149) *implies that the equilibrium of* (3.147) *is unique and real-valued. To illustrate this,* (3.149) *is evaluated numerically as a function of the external frequency* ω_{ex}. *The numerical parameters are given by the frequencies* $\omega = 20\,\frac{1}{\mathrm{s}}$, $\nu = 0\,\frac{1}{\mathrm{s}}$, *the damping coefficient* $\mu = -5\,\frac{1}{\mathrm{s}}$, $\eta \in \{-5, -5.6, -7.1\}\,\frac{1}{\mathrm{s}}$ *and the amplitude* $F_{\mathrm{ex}} = 10^{-1}$. *From this, it follows that the characteristic frequencies read* $\omega_{\mathrm{C}} \in \{15, 17.5, 20, 22.5, 25\}\,\frac{1}{\mathrm{s}}$. *The result is depicted in Figure 3.18. It is demonstrated that* (3.149) *will have its global maximum, if* $\omega_{\mathrm{ex}} = \omega_{\mathrm{C}}$ *holds. However, there will be multiple maxima, if the* (3.131) *is to close a Hopf-Hopf bifurcation.*

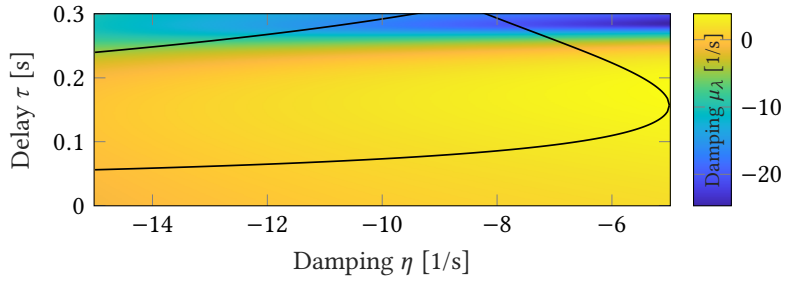

(a) Real part μ_λ of the eigenvalue that induces the first Andronov-Hopf bifurcation as a function of the delay τ and the damping coefficient η.

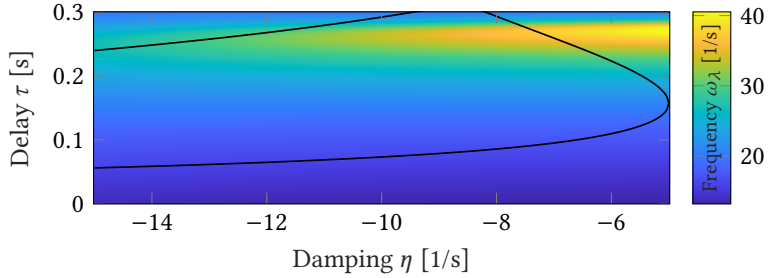

(b) Imaginary part ω_λ of the eigenvalue that induces the first Andronov-Hopf bifurcation as a function of the delay τ and the damping coefficient η.

Figure 3.17.: Colormaps of the real part $\mu_\lambda = \operatorname{Re}\lambda$ and imaginary part $\omega_\lambda = \operatorname{Im}\lambda$ of the eigenvalue that induces the first Andronov-Hopf bifurcation as a function of the delay τ and the damping coefficient η. In addition, the critical delays $\tau^+_{\mathrm{H},0}$, $\tau^+_{\mathrm{H},1}$, and $\tau^-_{\mathrm{H},1}$ are depicted by the black solid line.

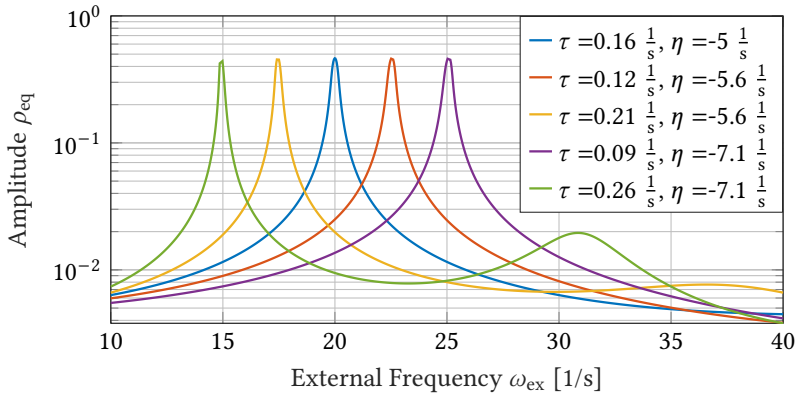

Figure 3.18.: Amplitude response of (3.131) as a function of the external frequency ω_{ex} for various parameter sets.

4. Sensing with an Andronov-Hopf Bifurcation

The present is based on the preliminary work of the author in [148]. A superordinate controller is designed for a neuromorphic acoustic sensor to enable in-sensor signal processing. This acoustic sensor is assumed to consist of an array of oscillators, which exhibit at least a controllable Andronov-Hopf bifurcation (see Figure 4.1). By controlling the bifurcation parameter, the compression can be modified to add redundant information of the measurement to its spectrum, which simplifies the recognition of noisy signals [70]. In addition, the frequency-selectivity of oscillators can be adjusted. With this each oscillator satisfies the sampling property of the Dirac impulse on the frequency domain [66], so that the oscillators only react in a (small) frequency band and they can be associated to (different) frequencies (see Figure 4.2b). Thus, the neuromorphic acoustic sensor transforms the stimuli into the frequency domain over time, which is subsequently called in-sensor Fourier transform. By introducing frequency tunability in this array of oscillators, sampling in the frequency domain is enabled, since each oscillator can sample multiple frequencies. In comparison to this neuromorphic acoustic sensor, the pre-processing of the hearing perception is done in the cochlea, where the response of the Basilar membrane can be interpreted as a Fourier transform over space (see Figure 4.2a). This comes from the fact that its cross-section changes its geometry and stiffness over space resulting in a varying characteristic frequencies [50, 121]. In contrast to these approaches, the processing in classical automatic speech recognition is performed in a feedforward structure, where a

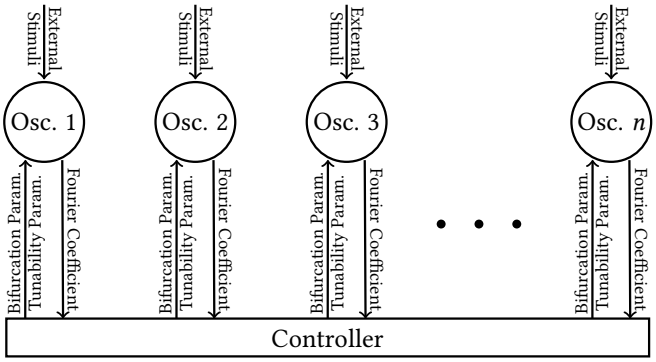

Figure 4.1.: Sketch of a neuromorphic acoustic sensor consisting of n oscillators with a frequency-selective response. The output of the i-th oscillator for $i = 1, 2, \ldots, n$ is associated to a frequency component, the bifurcation parameter and the tunability parameter of the i-th oscillator tunes its response, and each oscillator is excited by the external stimuli.

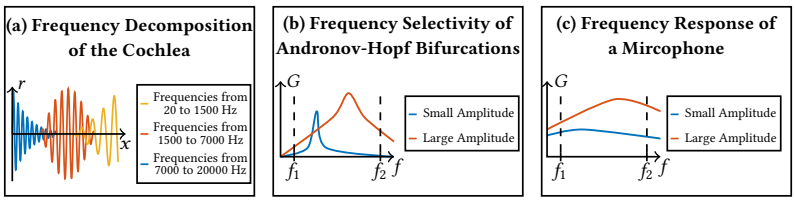

Figure 4.2.: Comparison between the signal measurement of the cochlea, the bio-inspired approach, and the technological speech processing. (a) In the cochlea, the external stimuli is decomposed over space in into its Fourier coefficients. (b) In the bio-inspired approach, an Andronov-Hopf bifurcation is used to mimic the functionality of the cochlea. With this, the frequency-selectivity can be used to sample the Fourier coefficients over the time. (c) In the technological speech processing, the external stimuli is measured by a microphone, which has a linear transfer function. After this, the signal is transformed into the frequency domain. (Figures 4.2(a) and 4.2(b) are from Ref. [148], used under Creative Commons CC-BY license.)

microphone with a linear transfer function transduces the external stimuli (see Figure 4.2c). This signal is then transformed into the frequency domain [2].

To implement sampling in the frequency domain, two major problems have to be resolved. First, it has to be shown that the response of an Andronov-Hopf oscillator to an unknown input is unique after transients have decayed. This implies that the frequency response to an unknown input can be reconstructed by the response of an array of oscillators, which exhibit at least one Andronov-Hopf bifurcation. This, however, might be impaired by the compressive nonlinearity of the Andronov-Hopf oscillator, since it can induce multiple (attractive) steady states. In contrast to the Andronov-Hopf oscillator, the uniqueness of the response of the linear oscillators directly from its linearity, since a linear system has a unique response to an input. Second, the convergence time of neuromorphic microphone might be too slow in practice. This comes from the fact that the vowel time can be as fast as 10 ms [12, 39] and automatic speech recognition usually processes acoustic signals in a time frame of 20 ms to 30 ms [102]. In particular, this convergence speed might not be feasible, if the bifurcation parameter of the oscillator is too close to the critical point.

In this chapter, these two problems are addressed. This is done by analyzing the steady state of the Andronov-Hopf oscillator evoked by an external stimuli. In addition, the convergence time of two different designs of neuromorphic acoustic sensors is analyzed as the in-sensor Fourier transform can be implemented by either a large number of oscillators each with constant frequency or a frequency tunable oscillator according to Definition 3.1. In particular, a tunable characteristic enables a degree of freedom in designing sampling algorithms, since it has to be asserted that the external stimuli is stationary (for the oscillator), so that the sequence of sampled frequencies can be assigned arbitrary. Thus, it is both possible to define a benchmark for sampling the frequency domain and to investigate other algorithms. For instance, the premise of reinforcement learning can be applied for this application.

4.1. Response of an Andronov-Hopf Oscillator to Harmonic Stimuli

In the following, the response of an Andronov-Hopf oscillator to harmonic stimuli is investigated and it is shown that the oscillator (4.1) has an unique frequency response after transients have decayed, if it is excited by an unknown external stimuli. For this, consider the Andronov-Hopf oscillator

$$\dot{z} = (\mu + \mathrm{i}\omega)z - \eta|z|^2 z + u, \qquad z(0) = z_0, \qquad t > 0 \tag{4.1}$$

with the state $z(t) \in \mathbb{C}$, the external input $u(t) \in \mathbb{C}$ and the initial conditions $z_0 \in \mathbb{C}$. The parameters are given by the linear damping coefficient $\mu \in \mathbb{R}$, the cubic damping coefficient $\eta > 0$ and the angular frequency $\omega > 0$.

The response of (4.1) is analyzed by rewriting the state z and the external stimuli u by the truncated Fourier series

$$z = \sum_{k=0}^{n} q_k \mathrm{e}^{\mathrm{i}k\nu_\Delta t}, \tag{4.2a}$$

$$u = \sum_{k=0}^{n} F_k \mathrm{e}^{\mathrm{i}k\nu_\Delta t} \tag{4.2b}$$

with the Fourier coefficients $q_k(t) \in \mathbb{C}$, $F_k(t) \in \mathbb{C}$, the fundamental frequency $\nu_\Delta > 0$ and the number of Fourier coefficients $n \in \mathbb{N}$ for all $k = 0, 1, \ldots, n$ [17, 32, 33]. The temporal evolution of the Fourier series of z is derived by inserting (4.2) into (4.1), solving the result for $\dot{q}_k$, and comparing the frequency components $\mathrm{e}^{\mathrm{i}k\nu_\Delta t}$. This yields

$$\dot{\boldsymbol{q}} = A\boldsymbol{q} - \boldsymbol{f}(\boldsymbol{q}) + \boldsymbol{F} \tag{4.3}$$

with the vector of the Fourier coefficients $\boldsymbol{q} = [q_0, q_1, \ldots, q_n]^{\mathrm{T}} \in \mathbb{C}^{n+1}$, $\boldsymbol{F} = [F_0, F_1, \ldots, F_n]^{\mathrm{T}} \in \mathbb{C}^{n+1}$, and the vector-valued nonlinearity $\boldsymbol{f}(\boldsymbol{q}) \in \mathbb{C}^{n+1}$ for all $k = 0, 1 \ldots, n$. Herein, the system matrix reads

$$A = \begin{bmatrix} \mu + \mathrm{i}\omega & 0 & \cdots & 0 \\ 0 & \mu + \mathrm{i}(\omega - \nu_\Delta) & \cdots & 0 \\ \vdots & \vdots & \ddots & \vdots \\ 0 & 0 & \cdots & \mu + \mathrm{i}(\omega - n\nu_\Delta) \end{bmatrix} \in \mathbb{R}^{(n+1)\times(n+1)}. \tag{4.4}$$

The system (4.4) is subsequently called envelope model of (4.1). To analyze the response of the system (4.1) or (4.3) respectively, to an external input u, the nonlinearity $\boldsymbol{f}$ has to be determined. This can be done by comparing the frequency components $\mathrm{e}^{\mathrm{i}k\nu_\Delta t}$ of

$$z|z|^2 = \underbrace{\left(\sum_{k=0}^{n} q_k \mathrm{e}^{\mathrm{i}k\nu_\Delta t}\right)}_{=z} \underbrace{\left(\sum_{k=0}^{n} q_k \mathrm{e}^{\mathrm{i}k\nu_\Delta t}\right)}_{=z} \underbrace{\left(\sum_{k=0}^{n} q_k^* \mathrm{e}^{-\mathrm{i}k\nu_\Delta t}\right)}_{=z^*} \tag{4.5}$$

with the complex conjugate q_k^* of the Fourier coefficients q_k for all $k = 0, 1 \ldots, n$. If (4.1) is frequency-selective, the coupling between the Fourier coefficients will (approximately) vanish, so that the nonlinearity (4.5) results in

$$|z|^2 z \approx \sum_{k=0}^{n} |q_k|^2 q_k \mathrm{e}^{\mathrm{i}k\nu_\Delta}.$$

With this, it follows that the Fourier coefficients q_k can be analyzed individually. Indeed, any oscillator exhibiting an Andronov-Hopf bifurcation is frequency-selective, if its bifurcation parameter is in a neighborhood of the critical point [26, 27, 40, 41, 92, 103]. In this case, (4.4) can be approximated by the uncoupled envelope model

$$\dot{q}_k = [\mu + \mathrm{i}(\omega - k\nu_\Delta)]\, q_k - |q_k|^2 q_k + F_k \tag{4.6}$$

with $k = 0, 1, \ldots, n$. Subsequently, the uniqueness of the steady states of the envelope model (4.4) is investigated by analyzing the uncoupled case (4.6). Asserting $\dot{q}_k = 0$, results in

$$0 = [\mu + \mathrm{i}(\omega - k\nu_\Delta)]\, q_{\mathrm{eq},k} - |q_{\mathrm{eq},k}|^2 q_{\mathrm{eq},k} + F_{\mathrm{eq},k} \tag{4.7}$$

with $F_{\mathrm{eq},k} \in \mathbb{C}$ for all $k = 0, 1, \ldots, n$. Hence, there are three possible zeros, which are subsequently analyzed by inserting polar coordinates $q_{\mathrm{eq},k} = r_{\mathrm{eq},k}\mathrm{e}^{\mathrm{i}\varphi_{\mathrm{eq},k}}$ and $F_{\mathrm{eq},k} = \rho_{\mathrm{eq},k}\mathrm{e}^{\mathrm{i}\phi_{\mathrm{eq},k}}$ with amplitudes $r_{\mathrm{eq},k}, \rho_{\mathrm{eq},k} \geq 0$ and phases $\varphi_{\mathrm{eq},k}, \phi_{\mathrm{eq},k} \in [0, 2\pi)$ in (4.7). This results in

$$0 = \left([\mu + \mathrm{i}(\omega - k\nu_\Delta)] - r_{\mathrm{eq},k}^2 \right) r_{\mathrm{eq},k}\mathrm{e}^{\mathrm{i}\varphi_{\mathrm{eq},k}} + \rho_{\mathrm{eq},k}\mathrm{e}^{\mathrm{i}\phi_{\mathrm{eq},k}}. \tag{4.8}$$

The phases $\varphi_{\mathrm{eq},k}$ are determined by computing the phase of (4.8) and the amplitudes $r_{\mathrm{eq},k}$ are derived by sorting terms and taking the absolute value squared of (4.8). This yields

$$\varphi_{\mathrm{eq},k} = \arctan\left[\frac{\sqrt{\mu^2 + \omega_{\Delta,k}^2}\sin(\varphi)}{r_{\mathrm{eq}}^2 - \sqrt{\mu^2 + \omega_{\Delta,k}^2}\cos(\varphi)} \right] + \phi_{\mathrm{eq},k}, \tag{4.9a}$$

$$0 = r_{\mathrm{eq},k}^6 - 2\mu r_{\mathrm{eq},k}^4 + [\mu^2 + \omega_{\Delta,k}^2] r_{\mathrm{eq},k}^2 - \rho_{\mathrm{ex},k}^2 \tag{4.9b}$$

with the phase $\varphi = \arctan(\omega_\Delta/\mu)$ of the complex-valued coefficient $\mu + \mathrm{i}\omega_{\Delta,k}$ and the difference frequency $\omega_{\Delta,k} = \omega - k\nu_\Delta$. Thus, the number of solutions of (4.7) is given by the number of positive, real-valued solutions of (4.9b). Indeed, (4.9b) has only one positive, real-valued solution. This is proven, e.g., by substituting $x = r_{\mathrm{eq},k}^2$ and applying Descartes' Rule of Signs (see Theorem 3.8). In particular, there is only one change of signs, if $\mu < 0$ and $\omega_{\Delta,k}, \rho_{\mathrm{ex},k} \in \mathbb{R}$ is satisfied. This implies that (4.7) has a unique, positive, real-valued zero. Hence, the response of an oscillator exhibiting an Andronov-Hopf bifurcation to a harmonic excitation is unique, if the respective bifurcation parameter is a neighborhood of the critical point.

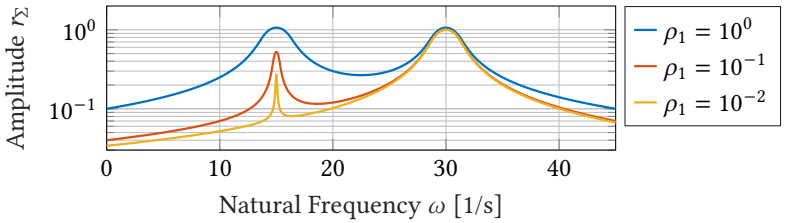

(a) Amplitude response r_Σ of the original envelope model (4.3) for small amplitudes.

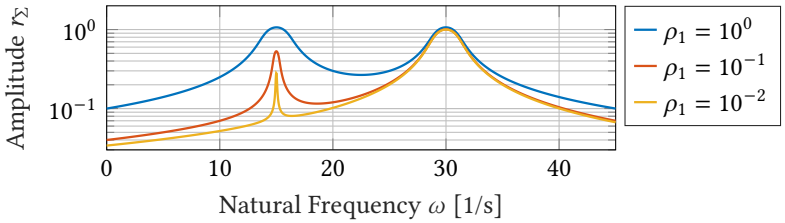

(b) Amplitude response r_Σ of the uncoupled envelope model (4.6) for small amplitudes.

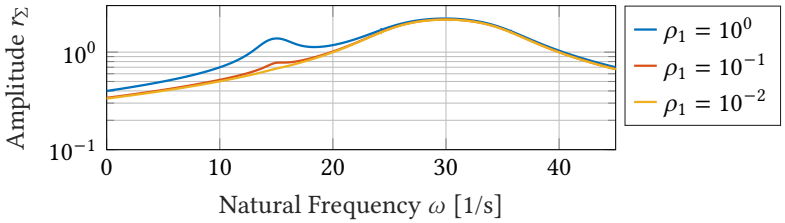

(c) Amplitude response r_Σ of the original envelope model (4.3) for large amplitudes.

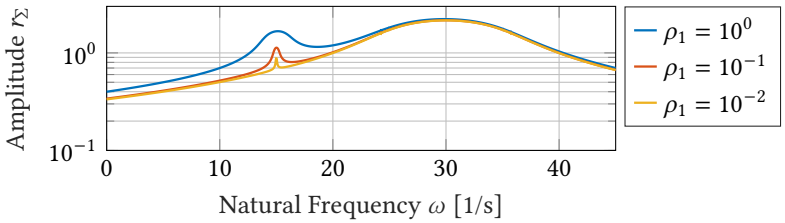

(d) Amplitude response r_Σ of the uncoupled envelope model (4.6) for large amplitudes.

Figure 4.3.: Comparison between the amplitude responses $r_\Sigma = r_1 + r_2$ of (4.3) and (4.6) as a function of the characteristic frequency ω and external amplitudes ρ_1 and ρ_2 at the critical point.

Example 4.1 *The results are verified numerically by comparing the steady state of the original envelope model* (4.3) *and the uncoupled envelope model* (4.6) *for different natural frequency* ω*. For this, the external stimuli is assumed to be a two-tone signal*

$$u = \rho_1 e^{i\nu_\Delta t} + \rho_2 e^{i2\nu_\Delta t} \tag{4.10}$$

with the amplitudes $\rho_1, \rho_2 > 0$ and the fundamental frequency $\nu_\Delta > 0$, so that the original envelope model (4.3) *reads*

$$0 = [\mu + \mathrm{i}(\omega - \nu_\Delta)]\, q_1 - |q_1|^2 q_1 - 2|q_2|^2 q_1 + \rho_1, \tag{4.11}$$

$$0 = [\mu + \mathrm{i}(\omega + 2\nu_\Delta)]\, q_2 - 2|q_1|^2 q_2 - |q_2|^2 q_2 + \rho_2. \tag{4.12}$$

The numerical parameters are given by the fundamental frequency $\nu_\Delta = 10$ and the amplitudes $\rho_1 \in \{10^0, 10^{-1}, 10^{-2}\}$ and $\rho_2 \in \{10^0, 10^{-1}\}$. The results of the computation are depicted in Figure 4.3. It is demonstrated in Figures 4.3a and 4.3b that the uncoupled envelope model (4.6) *approximates the original envelope model* (4.3)*, if the excitation amplitudes are small enough. In contrast, the approximation is not valid, if the excitation amplitudes are too large, as visualized in Figures 4.3c and 4.3d. This comes from the fact that large amplitudes are changing the critical point of the system, so that the frequency-selectivity of oscillator* (4.1) *is impaired and thus the assumption on the frequency-selectivity is violated.*

4.2. Implementing the In-Sensor Fourier Transform

Subsequently, the implementation of the in-sensor Fourier transform for an array of oscillators or a frequency tunable oscillator is discussed. To access the Fourier coefficients $\boldsymbol{q}$, amplitude demodulation is employed, since the important information of the external input can be accessed with this demodulation. This comes from the fact that relevant features of the acoustic signal, i.e., the energy, the spectral detail, and the periodicity, are determined by using amplitude demodulation [102]. Thus, the sampled spectrum can be directly used for automatic speech recognition. By exploiting the frequency-selectivity of oscillator (4.1), the amplitude demodulation is approximated by

$$|z|^2 = \left(\sum_{k=0}^{n} q_k \mathrm{e}^{\mathrm{i}k\nu_\Delta t}\right)\left(\sum_{k=0}^{n} q_k^* \mathrm{e}^{-\mathrm{i}k\nu_\Delta t}\right) \approx \sum_{k=0}^{n} |q_k|^2 \approx \begin{cases} |q_k|^2, & \text{if } \omega \approx k\nu_\Delta \\ 0, & \text{else} \end{cases}. \tag{4.13}$$

The Fourier coefficients $\boldsymbol{q}$ are determined by the envelope of (4.1), if an integer multiple of the fundamental frequency ν_Δ is equal to the natural frequency ω of (4.1). This implies that the output of a neuromorphic acoustic sensor consisting of an array of frequency-selective oscillators can reconstruct the frequency domain $\mathcal{F}$ and thus the spectrum of the external stimuli. However, the spectrum of the external stimuli and the output of a neuromorphic acoustic sensor are functions in terms of time t and the frequency ω, so that the neuromorphic acoustic sensor can only be implemented after discretizing the spectrum of the external stimuli over time t and frequency ω.

On the one hand, the spectrum of the external stimuli has to be discretized over ω, since the spectrum is a map from $\mathbb{R}$ to $\mathbb{C}$, so that infinitely many samples or oscillators are needed to determine the spectrum completely. Thus, it has to be assumed that the spectrum of the external stimuli is constrained on a frequency domain $\mathcal{F} = [\omega_{\min}, \omega_{\max}]$ with the minimal frequency and the maximum frequency $0 < \omega_{\min} < \omega_{\max}$ and that it is discretized in $n_\omega + 1$ subintervals defined by $[\omega_k, \omega_{k+1}]$ for all $k = 0, 1, \ldots, n_\omega$. Subsequently, the subintervals

are assumed to be equidistant (in the frequency domain) so that $\omega_k = \omega_{\min} + k\omega_s$ with $\omega_s = \frac{\omega_{\max}-\omega_{\min}}{n_\omega+1}$. On the other hand, following the results of Section 4.1 the amplitude of the Fourier coefficient $\boldsymbol{F}$ of the external stimuli is deduced from an approximation of the steady state $z_{\text{eq}}(\omega)$ of the oscillator (4.1), since the convergence time of (4.1) is not finite. For this, it has to be assumed that the time scales of the oscillator (4.1) and the external stimuli can be separated, i.e., (4.1) changes much faster that the external stimuli. With this, the external stimuli can be discretized in time t, i.e., $t = lT_s$ for all $l \in \mathbb{N}$. The conditions to sample the frequency domain with a neuromorphic acoustic sensor are subsequently summarized:

Assumption 4.1 *To sample the frequency domain with a neuromorphic acoustic sensor consisting of an array of oscillators. The following assumptions have to be fulfilled:*

(S1) The oscillators have to be frequency-selective.

(S2) The time scales of the oscillators and the external stimuli can be separated.

With these considerations, the output of a neuromorphic acoustic sensor can be denoted as follows

$$\mathrm{h}[l,k] = [\delta_{-1}(\omega - \omega_{\min} - k\omega_\Delta) - \delta_{-1}(\omega - \omega_{\min} - (k+1)\omega_\Delta)]\, q_k[l]$$

with the Heavyside function

$$\delta_{-1}(\omega) = \begin{cases} 1, & \text{if } \omega > 0 \\ 0, & \text{else} \end{cases}$$

and the Fourier coefficients $q_k[l]$ for all $k = 0, 1, \ldots, n_\omega$ and $l \in \mathbb{N}$. In contrast, the output of a neuromorphic acoustic sensor, which is continuous in ω, is denoted by $\mathrm{h}_{\text{eq}}[l](\omega)$. Subsequently, different algorithms to implement the in-sensor Fourier transform in a neuromorphic acoustic sensor are discussed. This is done by analyzing the convergence time of the in-sensor Fourier transform implemented by an array of untunable oscillators or a frequency tunable oscillator. To this end, sequential sampling and a sampling approach based on reinforcement learning are introduced for neuromorphic acoustic sensor consisting of a frequency tunable oscillator.

Algorithm 1: Array of Untunable Oscillators

Subsequently, the convergence time of a neuromorphic acoustic sensor consisting of many oscillators with constant and different characteristic frequencies is investigated. After applying amplitude demodulation (4.13), the convergence time of the in-sensor Fourier transform can be determined by computing the distance between (4.6) and its steady state. For this, denote the relative distance from (4.6) and its steady state by $p_z = q_k/q_{\text{eq},k}$. The solution of (4.6) is approximated by the real part $\mu < 0$ of its dominant eigenvalue and the

sampling time $T_\mathrm{s} > 0$. Assuming that the initial conditions are given by $q_{k,0} = 0$, the upper boundary of (4.6) is given by [4]

$$q_k < q_{\mathrm{eq},k} \left(1 - \mathrm{e}^{\mu T_\mathrm{s}}\right),$$

so that the relative distance reads

$$p_z = 1 - \mathrm{e}^{\mu T_\mathrm{s}}. \tag{4.14}$$

Hence, the relative distance p_z can be viewed as the accuracy of the measured Fourier coefficient. For instance, relevant values of p_z read [4]

$$p_z = \begin{cases} 95,0\%, & \text{if } |\mu| T_\mathrm{s} = 3 \\ 98,1\%, & \text{if } |\mu| T_\mathrm{s} = 4 \\ 99,3\%, & \text{if } |\mu| T_\mathrm{s} = 5 \end{cases}. \tag{4.15}$$

To estimate the convergence time, (4.14) is solved for the sampling time

$$T_\mathrm{s} = \frac{\ln\left(1 - p_z\right)}{\mu}.$$

In addition, it is useful to denote the convergence number $m_\mathrm{conv} = |\mu| T_\mathrm{s} > 0$ to characterize the convergence independently of μ and T_s. Combined with (4.15), a simple relationship between sampling time T_s and accuracy emerges, which is given by

$$T_\mathrm{s} = \frac{m_\mathrm{conv}}{|\mu|}. \tag{4.16}$$

Hence, the real part μ of the dominant eigenvalue can be used to tune the convergence time of the in-sensor Fourier transform.

Additionally, the real part μ of the dominant eigenvalue changes the bandwidth of an oscillator. To demonstrate this, the 3-dB bandwidth $f_\mathrm{3dB} > 0$ is determined by setting the Q-factor Q_th of a damped oscillator and the experimentally determined Q-factor Q_exp equal, i.e., $Q_\mathrm{th} = Q_\mathrm{exp}$. The Q-factor of a damped oscillator is given by [52]

$$Q_\mathrm{th} = \left|\frac{\omega_\mathrm{C}}{\mu_\mathrm{C}}\right| \tag{4.17}$$

with the imaginary part $\omega_\mathrm{C} \in \mathbb{R}$ of the dominant eigenvalue. While the experimentally determined Q-factor reads [45]

$$Q_\mathrm{exp} = \frac{f_\mathrm{C}}{f_\mathrm{3dB}} \tag{4.18}$$

with the 2π-normalized characteristic frequency $f_\mathrm{C} = \omega_\mathrm{C}/(2\pi)$. Asserting $Q_\mathrm{th} = Q_\mathrm{exp}$ and sorting terms results in

$$f_\mathrm{3dB} = \frac{|\mu_\mathrm{C}|}{2\pi}. \tag{4.19}$$

Finally, (4.19) is inserted into (4.16), which results in

$$T_\mathrm{s} = \frac{m_\mathrm{conv}}{2\pi f_\mathrm{3dB}}. \tag{4.20}$$

Hence, the 3-dB bandwidth f_3dB and the convergence time T are anti-proportional, so that the sampling of the frequency domain is either fast or accurate.

Algorithm 2: Sequential Sampling

To implement Algorithm 2, the neuromorphic acoustic sensor has to consist of a frequency tunable oscillator. Then the discretized frequency domain $\mathcal{F}$ is sampled by decreasing or increasing the natural frequency ω, since the frequency response can be demodulated by (4.13). The procedure of Algorithm 2, is summarized as follows. First, the lower (or upper, respectively) limit of the frequency domain $\mathcal{F}$ is chosen and it is sampled for a sampling time $T_\mathrm{s} > 0$. Second, the natural frequency is increased (or decreased, respectively) by ω_s and this frequency is sampled. This is repeated until every frequency in the frequency domain $\mathcal{F}$ is sampled. Afterwards the characteristic frequency of the oscillator is set back to its initial value. In particular, the sampling T_s satisfies (4.14), so that the convergence time of one iteration reads

$$T_\mathrm{seq} = (n_\omega + 1)T_\mathrm{s}$$

with the convergence time of the system $T_\mathrm{s} > 0$. Note that T_s can be approximated with (4.16). As the convergence time of Algorithm 2, can be easily determined and it is closely related to the sampling of the time domain, it can be subsequently considered to be the benchmark for an in-sensor Fourier transform with tunable oscillators.

Algorithm 3: Sampling based on Reinforcement Learning

Because the convergence time $T_\mathrm{s} > 0$ of an oscillator close to its critical point is rather slow, important information of the external stimuli can be missed by a neuromorphic acoustic sensor consisting of a frequency tunable oscillator. For instance, the vowels can be as fast as 10 ms [12, 39], so that the frequency domain has to be sampled in a restricted time interval. This issue can be resolved by noting that main measures of information of acoustic signals are its fundamental frequency and its harmonics [102]. For instance, vowels in speech can be characterized with these measures [102, 117]. Hence, only the most dominant Fourier coefficients have to be determined, which implies that the output of the neuromorphic acoustic sensor has to be maximized and the spectrum of an acoustic can be reconstructed by solving

$$\max_{\omega\in\mathcal{F}} \mathrm{h}[l](\omega) = \max_{k\in\{0,1,\ldots,n_\omega\}} \mathrm{h}[l,k]. \tag{4.21}$$

To solve (4.21), gradient-based methods are not suitable as the spectrum of the vowel is only supported on its fundamental frequency and its harmonics. Hence, the gradient is

large, if the sampled frequency is in a neighborhood of the fundamental frequency or its harmonics. Otherwise the gradient will vanish.

To avoid gradient-based methods, the optimization problem is reformulated based on the discretized output $\mathrm{h}[l,k]$ of the neuromorphic acoustic sensor. With this, (4.21) is similar to the multi-armed bandit, see, e.g., [73, 88, 115], where the Fourier coefficients can be interpreted as the probabilities for winning. In particular, this model is suitable, if the equilibrium value of the Fourier coefficient is only approximated. Hence, the optimization (4.21) can be, e.g., solved by using reinforcement learning [88].

For this, a variation of the epsilon-greedy strategy is applied to determine $n_{\max} > 0$ maxima of (4.21). With this approach, either the frequency domain $\mathcal{F}$ is explored or (4.21) is optimized based on a value function Q, which represents the knowledge of the explored frequency domain. In particular, the optimization phase can be used to determine the correct amplitude. The choice of these actions is based on a policy π and the set of possible actions is given by $\mathcal{A} = \{0, 1, \ldots, n_\omega\}$. For this approach, the action is the sampled frequency, so that the policy can be interpreted as a strategy to choose the characteristic frequency. In addition, the value function is given by

$$Q[l+1,k] = aQ[l,k] + bp[l], \qquad l > 0, \qquad Q[0,k] = Q_0[k] \tag{4.22}$$

with the initial condition $Q_0[l,k] \in \mathbb{R}$ for the time instances $l \in \mathbb{N}$ and the discretized frequency $k \in \{0, 1, \ldots, n_\omega\}$. The parameters are given by the forgetting rate $a \in [0,1)$ and the constant $b > 0$ for all $l \in \mathbb{N}$ and $k \in \mathcal{A}$. In particular, the forgetting rate a represents the speed in which the learned information is forgotten. In addition, the reward $p[l]$ is assumed to be the measured Fourier coefficient q_k, which can be determined by amplitude demodulation (4.13), so that the reward reads $p[l] = |z(lT_\mathrm{s})|$. Finally, the policy of the epsilon-greedy strategy is asserted to be

$$\pi[Q[l,k]] = \begin{cases} \text{random action from } \mathcal{A}, & \text{if } (i-1)m_\mathrm{s} \leq l < im_\mathrm{ex} \\ \text{exploiting } n_{\max} \text{ maxima of } Q[l,k], & \text{if } im_\mathrm{ex} \leq l < im_\mathrm{s} \end{cases}$$

with the number of explorations $m_\mathrm{ex} \in \mathbb{N}$, the number of samples $m_\mathrm{s} \in \mathbb{N}$ for the time instances $l \in \mathbb{N}$. Particularly, the policy chooses the Fourier coefficient, which is measured in the next time step. Thus, the optimizer is purely greedy, if $m_\mathrm{ex} = 0$, and purely exploratory, if $m_\mathrm{ex} = m_\mathrm{s}$. To implement this algorithm, the policy is separated into a exploration phase and a exploitation phase, so that a larger sampling time is used to improve the accuracy of the discovered maxima in the exploitation phase. With this, the sampling time T_s can be decreased drastically, while increasing the accuracy of the sampled maxima. The policy π is constructed as follows: A permutation $\mathcal{P}(\mathcal{A})$ of the set of action $\mathcal{A}$ constructed. Then the actions are draw sequentially from $\mathcal{P}(\mathcal{A})$. After the set of permutation $\mathcal{P}(\mathcal{A})$ is empty, a new permutation is constructed based on $\mathcal{A}$. With this policy, it is possible to randomize the sequence of sampled frequencies, so that it might be possible to decrease the number of explorations m_ex.

To choose the parameters a and b of (4.22) properly, the analytic solution of (4.22) is analyzed, which reads

$$Q[l,k] = a^l Q[0,k] + \frac{b}{1-a} p[l].$$

From this, it follows that (4.22) converges, if $a \in [0,1)$ and $b = 1 - a$. Moreover, the distance between (4.22) and its steady state is given by

$$p_Q = 1 - a^l.$$

Thus, it is subsequently assumed that the forgetting rate a has to be small, i.e., $a \ll 1$, since (4.22) is then converge after sampling all frequencies at least ones. To compare the performance between Algorithm 2 and Algorithm 3, the time until one iteration of the reinforcement learning algorithm terminates, has to be evaluated. This is given by

$$T_{\mathrm{RF}} = m_{\mathrm{s}} T_{\mathrm{s}}$$

with the numbers of samples $m_{\mathrm{s}} \in \mathbb{N}$ in one iteration. Because the algorithm is motivated by the multi-armed bandit problem, the sampling time can be decreased substantially in comparison to the convergence time of the system, i.e., $T_{\mathrm{s}} \ll T_{\mathrm{s}}$. However, more samples have to be done, which implies $m_{\mathrm{s}} > m_{\omega} + 1$.

4.3. Numerical Evaluation

Subsequently, Algorithm 2 and Algorithm 3 are compared. For this, the parameters of the oscillator (4.1) and the algorithma are given in Table A.1 in Appendix A. In particular, the interval length ω_{Δ} and the limits of the frequency domain $\mathcal{F}$ imply that 10 frequencies are measured, i.e., $n_{\omega} = 9$. On the one hand, Algorithm 2 has a convergence number $m_{\mathrm{conv}}^{\mathrm{seq}}$, which yields a time frame of $T_{\mathrm{seq}} = 50\,\mathrm{ms}$ for each iteration. In addition, the convergence number $m_{\mathrm{conv}}^{\mathrm{seq}}$ implies that each frequency is converged to 98.1%. On the other hand, Algorithm 3 is simulated 1000 times and the average and confidence interval given by three times the standard deviation is analyzed, since this algorithm is based on a probability distribution. This implies that 99.8% of all solutions are element of the confidence interval. In addition, it is assumed that Algorithm 3 also samples the complete Frequency domain $\mathcal{F}$ in the exploration phase and then maximizes the discovered maxima in the exploitation phase. For this, the time T_{RF} is assumed to be at maximum T_{seq}.

To compare the performance of the algorithms the accuracy of the sampled frequency domain $\mathcal{F}$ is analyzed with respect to the convergence number $m_{\mathrm{s}}^{\mathrm{RF}}$, a given convergence time T_{RF}, and the number of maxima $n_{\max}$. This is done by exciting (4.1) with three different, external stimuli – a time-varying signal, a two-tone signal, and a harmonic input with a harmonic distortion. These stimuli are given by

$$\begin{aligned}
u_{\mathrm{tv}} &= \rho(t) \mathrm{e}^{\mathrm{i}[\nu(t)t + \phi(t)]}, \\
u_{\mathrm{tt}} &= \rho_{1,\mathrm{tt}} \mathrm{e}^{\mathrm{i}(\omega_{1,\mathrm{tt}} t + \varphi_{1,\mathrm{tt}})} + \rho_{2,\mathrm{tt}} \mathrm{e}^{\mathrm{i}(\omega_{2,\mathrm{tt}} t + \varphi_{2,\mathrm{tt}})}, \\
u_{\mathrm{hd}} &= \rho_{1,\mathrm{hd}} \mathrm{e}^{\mathrm{i}(\omega_{1,\mathrm{hd}} t + \varphi_{1,\mathrm{hd}})} + \rho_{2,\mathrm{hd}} \mathrm{e}^{\mathrm{i}(\omega_{2,\mathrm{hd}} t + \varphi_{2,\mathrm{hd}})}
\end{aligned}$$

Table 4.1.: Comparison between the convergence time per iteration of the algorithms for the three different scenarios.

Convergence Time	Scenario 1	Scenario 2	Scenario 3
T_s	5 ms	5 ms	5 ms
T_seq	50 ms	50 ms	50 ms
$T_{\mathrm{RF},1}$	50 ms $100\% \cdot T_\mathrm{seq}$	50 ms $100\% \cdot T_\mathrm{seq}$	50 ms $100\% \cdot T_\mathrm{seq}$
$T_{\mathrm{RF},2}$	43.75 ms $87.5\% \cdot T_\mathrm{seq}$	50 ms $100\% \cdot T_\mathrm{seq}$	50 ms $100\% \cdot T_\mathrm{seq}$
$T_{\mathrm{RF},3}$	37.5 ms $75\% \cdot T_\mathrm{seq}$	50 ms $100\% \cdot T_\mathrm{seq}$	50 ms $100\% \cdot T_\mathrm{seq}$
$T_{\mathrm{RF},4}$	25 ms $50\% \cdot T_\mathrm{seq}$	37.5 ms $75\% \cdot T_\mathrm{seq}$	37.5 ms $75\% \cdot T_\mathrm{seq}$

with

$$\rho(t) = \begin{cases} \rho_{1,\mathrm{tv}}, & \text{if } t < t_\mathrm{th} \\ \rho_{2,\mathrm{tv}}, & \text{if } t \geq t_\mathrm{th} \end{cases}, \quad \nu(t) = \begin{cases} \omega_{1,\mathrm{tv}}, & \text{if } t < t_\mathrm{th} \\ \omega_{2,\mathrm{tv}}, & \text{if } t \geq t_\mathrm{th} \end{cases}, \quad \phi(t) = \begin{cases} \varphi_{1,\mathrm{tv}}, & \text{if } t < t_\mathrm{th} \\ \varphi_{2,\mathrm{tv}}, & \text{if } t \geq t_\mathrm{th} \end{cases}.$$

The parameters are given by the threshold $t_\mathrm{th} > 0$, the amplitudes $\rho_{i,\mathrm{tv}}, \rho_{i,\mathrm{tt}}, \rho_{i,\mathrm{hd}} > 0$, the frequencies $\omega_{i,\mathrm{tv}}, \omega_{i,\mathrm{tt}}, \omega_{i,\mathrm{hd}} > 0$, and the phases $\varphi_{i,\mathrm{tv}}, \varphi_{i,\mathrm{tt}}, \varphi_{i,\mathrm{hd}} \in [0, 2\pi)$. In addition, these scenarios are evaluated for four different parameter sets of the Algorithm 3. The numerical values are given by Table A.2 in Appendix A, and the threshold t_th is assumed to be equivalent to the convergence time of Algorithm 2 and Algorithm 3, respectively. In particular, the convergence of Algorithm 3 is verified for the first parameter set by assigning Algorithm 3 to be purely exploratory and a convergence number equivalent to Algorithm 2 and a comparison between the convergence time of Algorithm 2 and Algorithm 3 is depicted in Table 4.1.

Example 4.2 (Scenario 1: Time Varying Signal) *The results of Scenario 1 are illustrated in Figure 4.4. It turns out that by choosing the convergence number $m^{\mathrm{RF}}_{\mathrm{conv},1}$, the results of both algorithms are identical. This is depicted in Figure 4.4a. In contrast to this, the convergence numbers $m^{\mathrm{RF}}_{\mathrm{conv},2}$, $m^{\mathrm{RF}}_{\mathrm{conv},3}$, and $m^{\mathrm{RF}}_{\mathrm{conv},4}$ are smaller than the convergence numbers $m^{\mathrm{seq}}_{\mathrm{conv},1}$. With this, it is possible to increase the number of samples in Algorithm 3, so that the spectrum is first estimated and then the maxima of the estimation are investigated for a longer time period. Thereby, it becomes possible to sample the maxima in a shorter time, while preserving the accuracy of Algorithm 2. This is illustrated in Figures 4.4b, 4.4c, and 4.4d. In particular, the convergence time can be decreased by down to 50% in this scenario.*

Example 4.3 (Scenario 2: Two-Tone Signal) *The results of Scenario 2 are shown in Figure 4.5. In particular, it can be observed that both algorithms can reconstruct the frequency response of two-tone signal. By decreasing the convergence number $m^{\mathrm{RF}}_{\mathrm{conv}}$ and thus increasing*

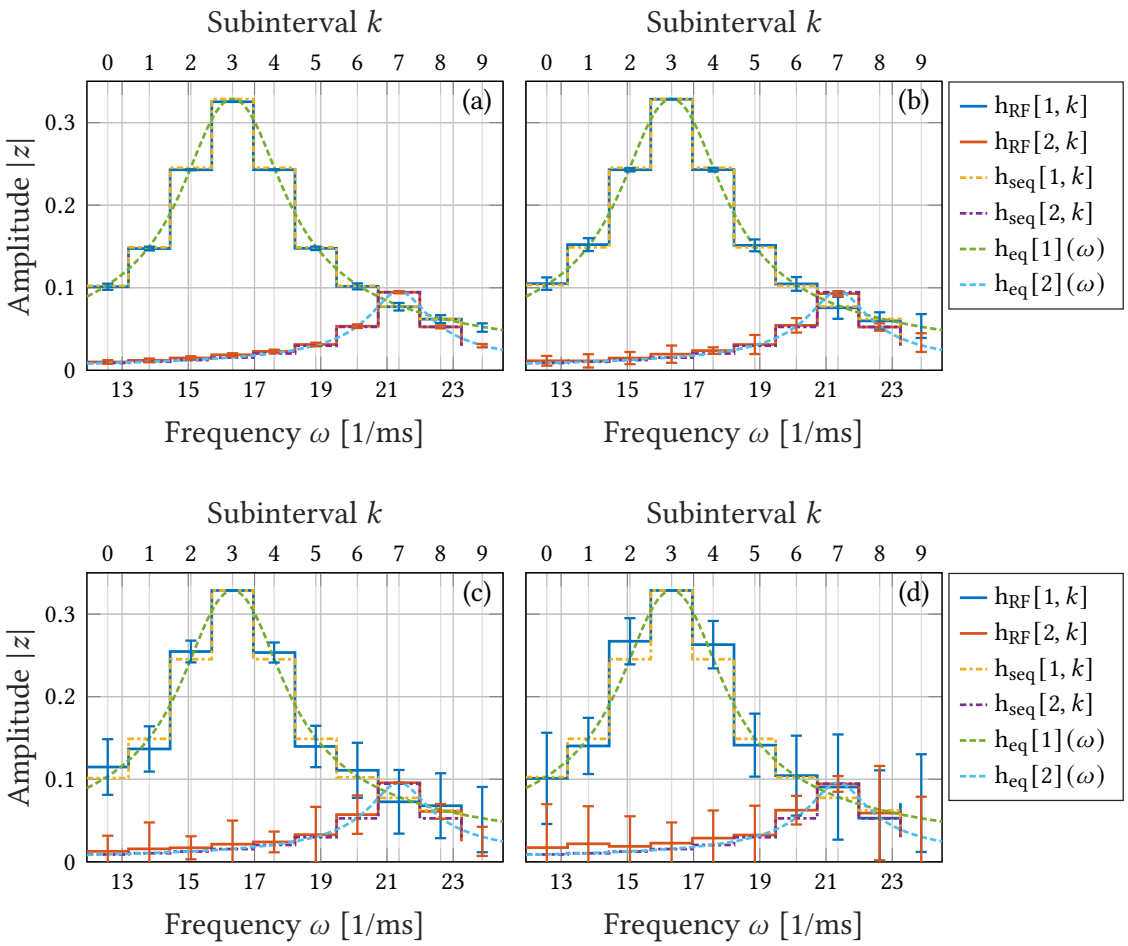

Figure 4.4.: Comparison between the sampled frequency responses $h_{seq}[l,k]$ and $h_{RF}[l,k]$ of Algorithm 2 and Algorithm 3 and the (continuous) frequency response $h_{eq}[l](\omega)$ of oscillator (4.1) exited by a time varying signal after two iterations. The sampling time of Algorithm 3 is given by $T_{RF,1} = T_{seq}$ (for (a)), $T_{RF,2} = 0.875 \cdot T_{seq}$ (for (b)), $T_{RF,3} = 0.75 \cdot T_{seq}$ (for (c)), and $T_{RF,4} = 0.5 \cdot T_{seq}$ (for (d)).

the time of exploitation of the maxima, the convergence time can be decreased. For instance, the maxima are robustly identified by decreasing the convergence number as depicted in Figures 4.5b and 4.5c. Additionally, the convergence time T_{RF}^{tt} can be decreased resulting in Figure 4.5d.

Example 4.4 (Scenario 3: Harmonic Disturbance) *The results of Scenario 3 are shown in Figure 4.6. It is demonstrated that by choosing the parameters accordingly the accuracy and the convergence time can be improved by using Algorithm 3. This is depicted in 4.6b, 4.6c and, 4.6d.*

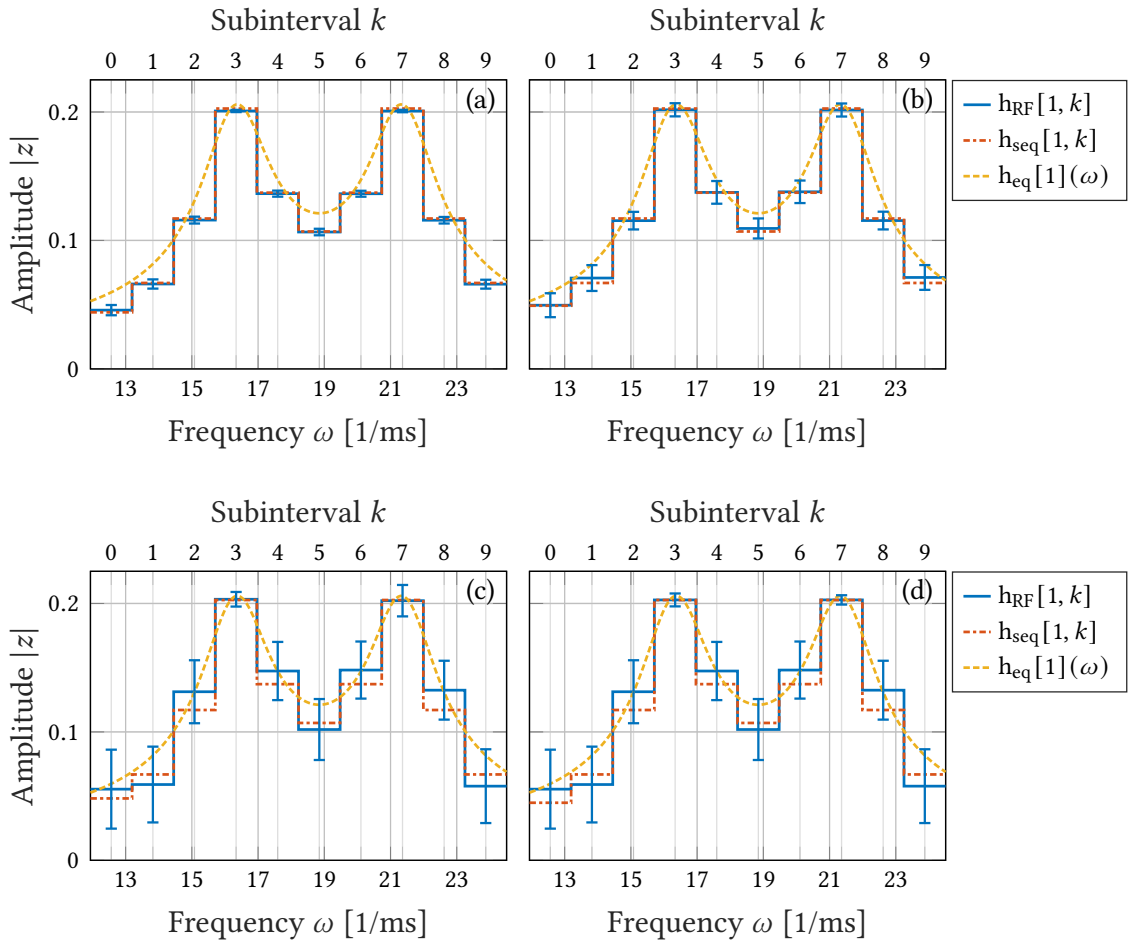

Figure 4.5.: Comparison between the sampled frequency responses $h_{seq}[1,k]$ and $h_{RF}[1,k]$ of Algorithm 2 and Algorithm 3 and the (continuous) frequency response $h_{eq}[1](\omega)$ of oscillator (4.1) exited by a two tone signal after one iterations. The sampling time of Algorithm 3 is given by $T_{RF,1} = T_{RF,2} = T_{RF,3} = T_{seq}$ (for (a), (b),(c)) and $T_{RF,4} = 0.75 \cdot T_{seq}$ (for (d)).

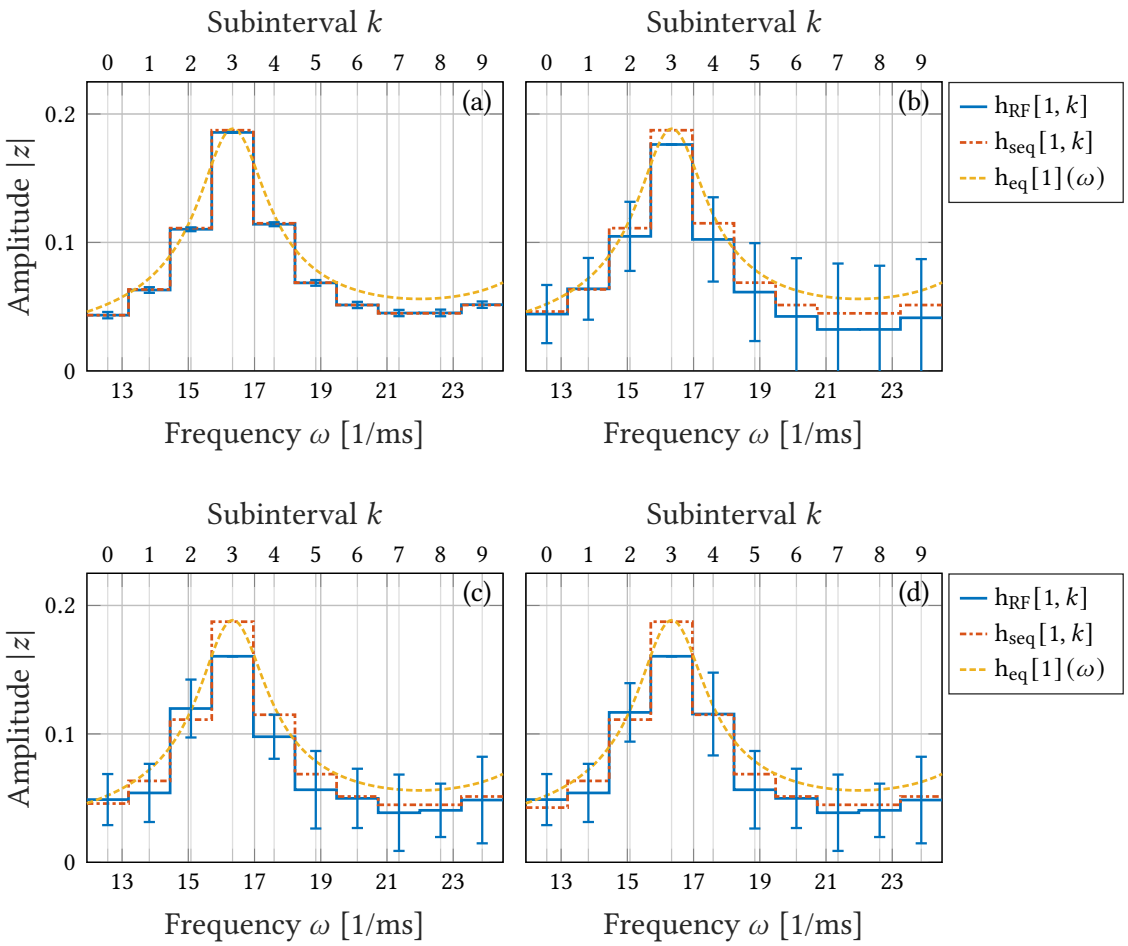

Figure 4.6.: Comparison between the sampled frequency responses $h_{seq}[1,k]$ and $h_{RF}[1,k]$ of Algorithm 2 and Algorithm 3 and the (continuous) frequency response $h_{eq}[1](\omega)$ of oscillator (4.1) exited by a two tone signal after one iterations. The sampling time of Algorithm 3 is given by $T_{RF,1} = T_{RF,2} = T_{RF,3} = T_{seq}$ (for (a), (b),(c)) and $T_{RF,4} = 0.75 \cdot T_{seq}$ (for (d)).

Part III.

A Neuromorphic Smart Sensing System

5. Modeling of the MEMS

Subsequently, a microelectromechanical systems (MEMS) is investigated that serves as sensor. Its geometry is given by either a cantilever or two coupled beams. The MEMS converts the sound pressure into an electrical signal with an piezoelectric strain gauge and it can be thermally actuated by an aluminum wire. By assigning the actuation accordingly, controllable Andronov-Hopf bifurcations and frequency tunability can be induced in this system. Thus, the scope of this part is to employ the controller design of Chapter 3. In the subsequent chapter, a mathematical model of the MEMS unifying the two designs is derived to prepare the investigations. This is done by modeling the MEMS with two coupled partial differential equations (PDE). To simplify the analysis in Chapter 6, the PDE is approximated by employing the Rayleigh-Ritz method and the Galerkin method.

5.1. Bio-Inspired Setup and Experimental Results

The considered MEMS is a silicon (Si) structure, which has a length from 750 µm to 1350 µm. It is fabricated on a 4 inch Si-wafer [108], where a layer of silicon-oxid (SiO_2) is deposited using plasma enhanced chemical vapor deposition (PECVD). This SiO_2-layer acts as an electric insulator. On top of the SiO_2-layer, the thermal actuator is implemented by depositing Al-wires using magnetron sputtering. To realize the piezoelectric strain gauge in the MEMS, high doped p++ boron implantation is used, and a Wheatstone bridge is utilized to measure the voltage of the piezoelectric strain gauge. From this measurement, the deflection of the MEMS can be deduced. The thickness of the MEMS is tuned by etching out the Si-layer with potassium hydroxide (KOH). For further details regarding the fabrication process the reader is referred to [62, 108].

By changing the geometry of the MEMS, certain properties can be modified. A selection of designs is sketched in Figure 5.1. On the one hand, a cantilevered MEMS is shown in Figures 5.1a. It has a constant natural frequency, which is assigned in the fabrication process by choosing the length, the width, and the height of the MEMS. On the other hand, a clamped-clamped design is visualized in Figure 5.1b. This design consists of a cantilever for sensing and a clamped beam for tuning. These beams are coupled by fixing the tip of the cantilever to a side of the clamped beam. By doing this, a geometric nonlinearity can be induced even for small displacements [47, 155], so that the characteristic frequency of this design can be adjusted by a small pre-deflection.

Experimental results imply that this MEMS can be used to implement neuromorphic acoustic sensor, when the MEMS is operated in a feedback loop (see Figure 5.2). Here, the

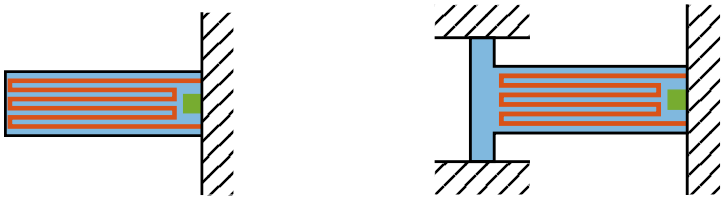

(a) Sketch of a cantilevered MEMS [81].

(b) Sketch of a clamped-clamped MEMS [47].

Figure 5.1.: Examples of different designs for the considered, thermally actuated MEMS. Here, the carrier, the thermal actuator, and the piezoelectric strain gauge are sketched in blue, red, and green.

MEMS tranduces an external input into an electric signal, which can be measured in the Wheatstone bridge. Then the output of the MEMS is filtered by a high pass to remove noise and the high pass filtered signal is forwarded to a field programmable gate array (FPGA), where the feedback signal is generated. The processing of the high pass filtered signal can, e.g., involve amplification and adding an additional DC-voltage. With this, Andronov-Hopf bifurcations emerge, which can be controlled by adjusting the DC-voltage and the amplification of the high pass filtered signal [80, 82, 81, 136, 153, 155]. To evaluate the experimental results, a mathematical model of the MEMS is derived in this chapter.

5.2. Continuum Model of the MEMS

To analyze the emergence of controllable bifurcations in the sensory scheme involving the MEMS from Figure 5.2, a mathematical model of the MEMS has to be derived. For this, the mechanical and thermodynamic subsystems are modeled separately and are then coupled by the Duhamel-Neumann law.

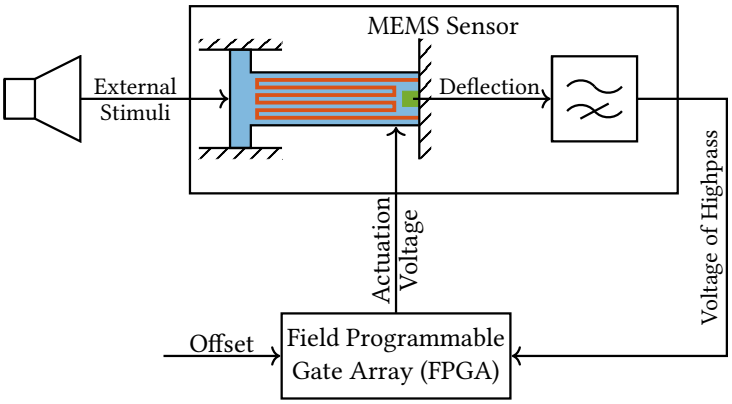

Figure 5.2.: Bio-inspired setup of the a single MEMS sensor.

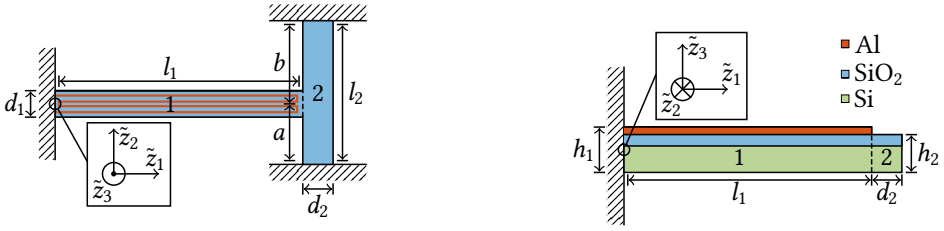

(a) Sketch of the MEMS in the $\tilde{z}_1\tilde{z}_2$-plane.+

(b) Sketch of the MEMS in the $\tilde{z}_1\tilde{z}_3$-plane.

Figure 5.3.: Sketch of the mechanical subsystem of the clamped-clamped MEMS.

5.2.1. Mechanical Subsystem

In the following, the mechanical subsystem of the cantilevered MEMS and clamped-clamped MEMS are modeled. This is done as follows: First, some mechanical preliminaries are summarized. Second, the clamped-clamped beam is modeled by a cantilevered Bernoulli beam, where an additional force acts on tip of the cantilever. Third, the dynamics of the mechanical subsystem are derived by employing the extended Hamiltonian principle on the cantilever.

Preliminaries

Subsequently, geometrical and mechanical preliminaries are discussed by defining a coordinate system for the clamped-clamped MEMS and introducing the extended Hamiltonian principle.

Let the coordinate system be a right-handed coordinate system with the coordinates $\tilde{z} = [\tilde{z}_1, \tilde{z}_2, \tilde{z}_3]^{\mathrm{T}} \in \mathbb{R}^3$ and assume that the clamped-clamped MEMS consists a cantilever and a clamped beam. Both beams are composed of a Si-layer and a SiO_2-layer and Al-wires deposited only on the cantilever. Sketches of the $\tilde{z}_1\tilde{z}_2$-plane and $\tilde{z}_1\tilde{z}_3$-plane of the clamped-clamped MEMS are provided in Figure 5.3. The length, the height, and the width are denoted by $l_i > 0$, $h_i > 0$, and $d_i > 0$ for all $i = 1, 2$ with 1 and 2 labeling the cantilever and the clamped beam, respectively, and the distances from the middle of the tip of the cantilever to both ends of the clamped beam are denoted by $a > 0$ and $b > 0$. In addition, the material for the material layer and the Al-wires is assumed to be isotropic and homogeneous.

To model a deformable body, the extended Hamiltonian principle can be employed. This principle is based on making a line integral involving the stored kinetic and potential energy extremal. In particular, applying calculus of variations implies

$$0 = \int_{t_1}^{t_2} \delta W_{\mathrm{pot}}(t) - \delta W_{\mathrm{kin}}(t) + \delta W_{\mathrm{NC}}(t)\, \mathrm{d}t, \tag{5.1a}$$

$$0 = \delta\tilde{\boldsymbol{w}}(\tilde{\boldsymbol{z}}, t), \qquad \tilde{\boldsymbol{z}} \in \mathcal{S}, \quad \forall t \in [t_1, t_2], \tag{5.1b}$$

$$0 = \delta\tilde{\boldsymbol{w}}(\tilde{\boldsymbol{z}}, t_1) = \delta\tilde{\boldsymbol{w}}(\tilde{\boldsymbol{z}}, t_2), \qquad \tilde{\boldsymbol{z}} \in \mathcal{V}(\tilde{\boldsymbol{z}}) \tag{5.1c}$$

with the displacement $\tilde{\boldsymbol{w}}(\tilde{z},t) = [\tilde{w}_1(\tilde{z},t), \tilde{w}_2(\tilde{z},t), \tilde{w}_3(\tilde{z},t)]^{\mathrm{T}} \in \mathbb{R}^3$ of the point $[\tilde{z}_1, 0, 0]^{\mathrm{T}} \in \mathbb{R}^3$, the time instances $t_1 < t_2$, the potential energy $W_{\mathrm{pot}}(t) \in \mathbb{R}$, the kinetic energy $W_{\mathrm{kin}}(t) \in \mathbb{R}$, the virtual work $W_{\mathrm{NC}}(t) \in \mathbb{R}$ of the non-conservative forces, the volume $\mathcal{V}(\tilde{\boldsymbol{z}}) \subset \mathbb{R}^3$ of the mechanical system, and the set $\mathcal{S} \subset \mathbb{R}^3$ of the boundary conditions for all $i = 1, 2, 3$ [44, 94, 110]. Note that δ is called the variational operator [44, 110]. To solve (5.1), the potential energy, the kinetic energy and virtual work of the non-conservative forces have to be determined and the fundamental lemma of the calculus of variations can be employed. This lemma is subsequently summarized.

Lemma 5.1 (Fundamental Lemma of the Calculus of Variations [110]) *Let $g(x) \in \mathbb{R}$ be an arbitrary function and assume that $f(x) \in \mathbb{R}$ be integrable. If*

$$\int_a^b f(x)g(x)\mathrm{d}x = 0$$

is satisfied, it follows that $f(x) = 0$ for all $x \in (a, b) \subset \mathbb{R}$.

In addition, by assuming that the material is homogeneous and isotropic, the potential energy, the kinetic energy and virtual work of the non-conservative forces are given by [110]

$$W_{\mathrm{pot}} = \frac{1}{2}\int_{\mathcal{V}} \sum_{i=1}^{3}\sum_{j=1}^{3} \sigma_{ij}e_{ij}\,\mathrm{d}V, \tag{5.2a}$$

$$W_{\mathrm{kin}} = \frac{1}{2}\int_{\mathcal{V}} \rho\left(v_1^2 + v_2^2 + v_3^2\right)\,\mathrm{d}V, \tag{5.2b}$$

$$W_{\mathrm{NC}} = \int_{\mathcal{V}} \boldsymbol{f}\cdot\tilde{\boldsymbol{w}}\,\mathrm{d}V + [\boldsymbol{F}\cdot\tilde{\boldsymbol{w}}]\,|_{\tilde{\boldsymbol{w}}\in\partial\mathcal{S}} \tag{5.2c}$$

with the velocity $\boldsymbol{v}(\tilde{z},t) = [\partial_t\tilde{w}_1(\tilde{z},t), \partial_t\tilde{w}_2(\tilde{z},t), \partial_t\tilde{w}_3(\tilde{z},t)]^{\mathrm{T}} \in \mathbb{R}^3$, body force $\boldsymbol{f}(\tilde{\boldsymbol{z}},t) \in \mathbb{R}^3$, the force $\boldsymbol{F}(t) \in \mathbb{R}^3$ acting on $\mathcal{S}$, the mechanical stress $\sigma_{ij}(\tilde{z},t) > 0$, the infinitesimal strain $e_{ij}(\tilde{z},t) > 0$, and the density $\rho > 0$ for all $i, j = 1, 2, 3$.

To describe the deformation in thermoelastic medium, the Duhamel-Neumann law is considered. This law extends Hooke's law to thermoelasticity. Assuming that the material isotropic, the stress of a thermoelastic medium is given by [53, 101, 110]

$$\sigma_{ij}(\tilde{z},t) = Ee_{ij}(\tilde{z},t) - E\alpha_i\tilde{\theta}(\tilde{z},t)\delta_0\,[i-j] \tag{5.3}$$

with the ambient temperature $\tilde{\theta}(\tilde{z},t) \in \mathbb{R}$, the Young's modulus $E > 0$, the linear heat expansion coefficient $\alpha_i > 0$, and the discrete Dirac impulse [101]

$$\delta_0\,[i-j] = \begin{cases} 1, & \text{if } i = j, \\ 0, & \text{else.} \end{cases}$$

Finally, the mechanical strain is described by the deformation of the material in terms of the time. The deformation of a material is determined by the change of the distances between two arbitrary points of this material, such that the strain reads [110]

$$\epsilon_{ij} = \frac{1}{2}\left(\partial_{\tilde{z}_j} p_i + \partial_{\tilde{z}_i} p_j + \partial_{\tilde{z}_j}\boldsymbol{p}\partial_{\tilde{z}_i}\boldsymbol{p}\right)$$

with the deflections $\boldsymbol{p}(\tilde{z}, t) = [p_1(\tilde{z}, t), p_2(\tilde{z}, t), p_3(\tilde{z}, t)]^{\mathrm{T}} \in \mathbb{R}^3$ to a point $[\tilde{z}_1, \tilde{z}_2, \tilde{z}_3]^{\mathrm{T}} \in \mathbb{R}^3$ along the $\tilde{z}_1$-, $\tilde{z}_2$-, and $\tilde{z}_3$-coordinates. By considering the infinitesimal strain e_{ij}, i.e., the strain between two points infinitely close to each other, the quadratic derivative vanishes providing

$$e_{ij} = \frac{1}{2}\left(\partial_{\tilde{z}_j} p_i + \partial_{\tilde{z}_i} p_j\right). \tag{5.4}$$

With these preliminaries, the potential and the kinetic energy can be determined in thermoelastic homogeneous and isotropic media.

Interaction between the Cantilever and the Clamped Beam

To model the interaction between the cantilever and the clamped beam, it is assumed that a point force is acting on the tip of the cantilever, which can be modeled as a spring (see Figure 5.4a). The spring constant can be determined by asserting the Bernoulli assumption on the clamped beam, since this beam is long, slender and consists of an isotropic and homogeneous material.

Assumption 5.1 (Bernoulli Assumptions [44]) *A long and slender beam satisfies the following assumptions:*

(B1) The material is homogeneous and isotropic.

(B2) If a plane section within the beam was plain before bending, the section will remain plane after bending.

(B3) The deformation of a beam is not changing the length of the neutral plane of a beam, i.e., the torsion of this plane is negligible.

(B4) The stresses with respect to $\tilde{z}_2$ and $\tilde{z}_3$ are negligible, i.e., $\sigma_{22} = \sigma_{33} = \sigma_{23} = \sigma_{32} = 0$.

With these assumptions, the mechanical stress in the beam in the z_1- and z_3-direction vanishes (see Figure 5.3a). Hence, the rotation of these axis can be neglected and the resulting force of the rotation around these axis can be omitted, so that the spring force is given by the deflection of the clamped beam in the z_2-direction. The absolute value of the force is determined by the displacement of the clamped beam at the interconnection between the cantilever and the clamped beam [46], which reads

$$F_{\mathrm{Sp}} = \frac{3l_2}{a^2 b^2}\overline{E_2 I_{\tilde{z}_2}} p_3$$

with the pre-deflection $p_3 \in \mathbb{R}$ at the tip of the cantilever and the effective parameter $\overline{E_2 I_{\tilde{z}_2}} = E_{21} I_{\tilde{z}_2,1} + E_{22} I_{\tilde{z}_2,2}$. Additional parameter for the clamped beam are given by the Young's modulus $E_{2i} > 0$ and the second moment of inertia

$$I_{\tilde{z}_2,1} = \frac{d_2}{3}\left[\left(h_{21} + \frac{h_2}{2}\right)^3 + \frac{h_2^3}{8}\right], \qquad I_{\tilde{z}_2,2} = \frac{d_2}{3}\left[\frac{h_2^3}{8} - \left(h_{21} - \frac{h_1}{2}\right)^3\right]$$

with the heights $h_{21} > 0$ for all $i = 1, 2$ labeling the Si-layer and SiO_2-layer, respectively. With this, the spring constant is determined by

$$c_{\mathrm{Sp}} = \frac{3 l_2}{a^2 b^2} \overline{E_2 I_{\tilde{z}_2}}.$$

Following Assumption (B4), the interaction between the clamped beam and the cantilever are derived by determining the direction of their movements. On the one hand, the clamped beam can only move in z_2- und z_3-direction. Hence, the resulting force acts in these directions. On the other hand, the directions of movement of the cantilever follow z_1- und z_3-axis. Hence, the direction of the spring force cannot be parallel to the movement direction of the cantilever, so that it has to be separated into a parallel and orthogonal component of the movement direction of the tip of the cantilever (see Figure 5.4b). This implies that the spring forces acting on the tip of the cantilever reads

$$F_\perp = F_{\mathrm{Sp}} \cos(\varphi) \approx c_{\mathrm{Sp}} p_3 + \frac{c_{\mathrm{Sp}}}{2 l_1^2} p_3^3, \tag{5.5a}$$

$$F_\parallel = F_{\mathrm{Sp}} \sin(\varphi) \approx -\frac{c_{\mathrm{Sp}}}{l_1} p_3^2 \tag{5.5b}$$

with the angle $\varphi \in [0, 2\pi)$, the length of the cantilever $l_1 > 0$, the truncated Taylor series of a cosine and sine $\cos(\varphi) \approx 1 + \varphi^2/2$, $\sin(\varphi) \approx \varphi$, and the approximation of the angle $\varphi \approx p_3 / l_1$. In particular, the forces $F_\perp$ and $F_\parallel$ only act on the tip of the cantilever, so that these forces are subsequently embedded into the boundary conditions of the PDE of the cantilever. With this, the PDE of the clamped-clamped MEMS can be reduced to the PDE of the cantilevered MEMS by asserting that $c_{\mathrm{Sp}} = 0$.

Dynamics of Mechanical Subsystem

In the following, the dynamics of the cantilevered MEMS are derived by employing the extended Hamiltonian principle. It follows from the Bernoulli assumptions that the

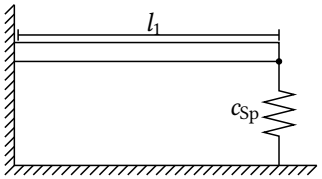

(a) Sketch of the MEMS in equilibrium.

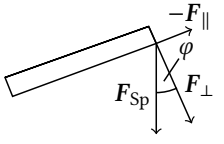

(b) Sketch of the forces on the tip of the MEMS.

Figure 5.4.: Sketch of the preliminary assumptions of the clamped-clamped MEMS.

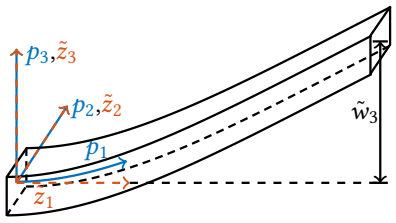

Figure 5.5.: Sketch of the coordinate system of the cantilevered MEMS.

deflection of the cantilever is described in the (initial) right-handed coordinate system of the MEMS (see Figure 5.5), by

$$p_1(\tilde{z}, t) = \tilde{w}_1(\tilde{z}_1, t) - \tilde{z}_3 \partial_{\tilde{z}_1} \tilde{w}_3(\tilde{z}_1, t), \tag{5.6a}$$
$$p_2(\tilde{z}, t) = 0, \tag{5.6b}$$
$$p_3(\tilde{z}, t) = \tilde{w}_3(\tilde{z}_1, t), \tag{5.6c}$$

The volume of the cantilevered MEMS is sketched in Figure 5.6 and it is defined by

$$\mathcal{V} = \mathcal{V}_1 \cup \mathcal{V}_2 \cup \mathcal{V}_3$$

with the volumes of the Si-layer, SiO_3-layer, and the aluminum wires

$$\mathcal{V}_1 = \left\{ \tilde{z} \in \mathbb{R}^3 \,\middle|\, 0 \leq \tilde{z}_1 \leq l_1 \wedge -\frac{d_1}{2} \leq \tilde{z}_2 \leq \frac{d_1}{2} \wedge -\frac{h_1}{2} \leq \tilde{z}_3 \leq h_{11} - \frac{h_1}{2} \right\},$$
$$\mathcal{V}_2 = \left\{ \tilde{z} \in \mathbb{R}^3 \,\middle|\, 0 \leq \tilde{z}_1 \leq l_1 \wedge -\frac{d_1}{2} \leq \tilde{z}_2 \leq \frac{d_1}{2} \wedge h_{11} - \frac{h_1}{2} \leq \tilde{z}_3 \leq \frac{h_1}{2} - h_{13} \right\},$$
$$\mathcal{V}_3 = \bigcup_{i=1}^{n_{\mathrm{Al}}} \left\{ \tilde{z} \in \mathbb{R}^3 \,\middle|\, 0 \leq \tilde{z}_1 \leq l_1 \wedge -\frac{d_{\mathrm{Al}}}{2} \leq \tilde{z}_2 - \tilde{z}_{2,n_{\mathrm{Al}},i} \leq \frac{d_{\mathrm{Al}}}{2} \wedge \frac{h_1}{2} - h_{13} \leq \tilde{z}_3 \leq \frac{h_1}{2} \right\},$$

the height h_{13} of the Si-layer, the height $h_{13} > 0$ of the Al-wires, the width $d_{\mathrm{Al}} > 0$ of the Al-wires, the position $\tilde{z}_{2,n_{\mathrm{Al}},i} \in [-\frac{d_1}{2}, \frac{d_1}{2}]$ of the Al-wires and the number $n_{\mathrm{Al}} \in \mathbb{N}$ of Al-wires for all $i = 1, 2, \ldots, n_{\mathrm{Al}}$. In addition, it is assumed that the cantilever only undergoes bending [110, Example 4.3]

$$\tilde{w}_1(\tilde{z}, t) = 0, \qquad \forall \tilde{z} \in \mathcal{V}, \qquad \forall t \in [t_1, t_2]. \tag{5.7}$$

With these assumptions, the potential energy (5.2a) and kinetic energy (5.2b) for the cantilever in the MEMS can be determined.

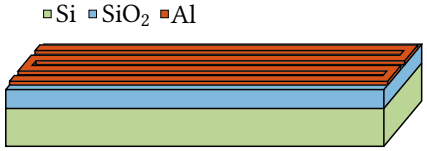

Figure 5.6.: Sketch of the volume of the cantilevered MEMS.

By inserting (5.6) and (5.7) into (5.4), the mechanical strain e_{ij} of the cantilever results in

$$e_{ij}(\tilde{z}_1, t) = \begin{cases} -\tilde{z}_3 \partial_{\tilde{z}_1}^2 \tilde{w}_3(\tilde{z}_1, t), & \text{if } i = j = 1 \\ 0, & \text{else} \end{cases}. \tag{5.8}$$

The mechanical stress σ_{ij} follows by substituting (5.8) in (5.3), which yields

$$\sigma_{ij}(\tilde{z}, t) = \begin{cases} E_{1k} e_{11}(\tilde{z}, t) - E_{1k} \alpha_{1k} \tilde{\theta}(\tilde{z}_1, t), & \text{if } i = j = 1 \\ 0, & \text{else} \end{cases} \tag{5.9}$$

with the Young's modulus $E_{1k} > 0$ and the thermal expansion constant $\alpha_{1k} > 0$ for all $k = 1, 2, 3$ labeling the Si-layer, SiO_2-layer and the Al-wires, respectively. Herein, it can be assumed that the temperature difference $\tilde{\theta}$ only depends on time t and coordinate $\tilde{z}_1$, as the MEMS is very slim with $h_1 \ll l_1$, so that the dependency on the coordinates $\tilde{z}_2$ and $\tilde{z}_3$ can be neglected. After inserting (5.8) and (5.9) into (5.2a), the potential energy can be evaluated to

$$\begin{aligned} W_{\text{pot}} &= \int_{\mathcal{V}} \sigma_{11} e_{11} \, \mathrm{d}V \\ &= \frac{1}{2} \int_0^{l_i} d_1 \int_{-\frac{h_1}{2}}^{h_{11}-\frac{h}{2}} E_1 \left(\partial_{\tilde{z}_1}^2 \tilde{w}_3 \right)^2 \tilde{z}_3^2 + E_1 \alpha_1 \tilde{\theta} \partial_{\tilde{z}_1}^2 \tilde{w}_3 \, \tilde{z}_3 \, \mathrm{d}\tilde{z}_3 \, \mathrm{d}\tilde{z}_1 \\ &\quad + \frac{1}{2} \int_0^{l_i} d_1 \int_{h_{11}-\frac{h_1}{2}}^{\frac{h_1}{2}-h_{13}} E_2 \left(\partial_{\tilde{z}_1}^2 \tilde{w}_3 \right)^2 \tilde{z}_3^2 + E_2 \alpha_2 \tilde{\theta} \partial_{\tilde{z}_1}^2 \tilde{w}_3 \, \tilde{z}_3 \, \mathrm{d}\tilde{z}_3 \, \mathrm{d}\tilde{z}_1 \\ &\quad + \frac{1}{2} \int_0^{l_i} d_{\text{Al}} n_{\text{Al}} \int_{\frac{h_1}{2}-h_{13}}^{\frac{h_1}{2}} E_3 \left(\partial_{\tilde{z}_1}^2 \tilde{w}_3 \right)^2 \tilde{z}_3^2 + E_3 \alpha_3 \tilde{\theta} \partial_{\tilde{z}_1}^2 \tilde{w}_3 \, \tilde{z}_3 \, \mathrm{d}\tilde{z}_3 \, \mathrm{d}\tilde{z}_1 \\ &= \int_0^{l_i} \frac{\overline{E_1 I_{\tilde{z}_1}}}{2} \left(\partial_{\tilde{z}_1}^2 \tilde{w}_3 \right)^2 + \frac{\overline{E_1 \alpha_1 S_{\tilde{z}_1}}}{2} \tilde{\theta}_i \partial_{\tilde{z}_1}^2 \tilde{w}_3 \, \mathrm{d}\tilde{z}_1 \end{aligned} \tag{5.10}$$

with the effective Young's modulus $\overline{E_1 I_{\tilde{z}_1}} = E_{11} I_{\tilde{z}_1,1} + E_{12} I_{\tilde{z}_1,2} + E_{13} I_{\tilde{z}_1,3}$ and the effective thermal expansion constant $\overline{E_1 \alpha_1 S_{\tilde{z}_1}} = E_{11} \alpha_{11} S_{\tilde{z}_1,1} + E_{12} \alpha_{12} S_{\tilde{z}_1,2} + E_{13} \alpha_{13} S_{\tilde{z}_1,3}$. Herein, the first moment of inertia $S_{\tilde{z}_1,i}$ and the second moment of inertia $I_{\tilde{z}_1,i} > 0$ for all $i = 1, 2, 3$ are given by

$$\begin{aligned} S_{z_1,1} &= \frac{d_1}{2} \left[\left(h_{11} - \frac{h_1}{2} \right)^2 - \frac{h_1^2}{4} \right], & I_{z_1,1} &= \frac{d_1}{3} \left[\left(h_{11} + \frac{h_1}{2} \right)^3 + \frac{h_1^3}{8} \right], \\ S_{z_1,2} &= \frac{d_1}{2} \left[\left(\frac{h_1}{2} - h_{13} \right)^2 - \left(h_{11} - \frac{h_1}{2} \right)^2 \right], & I_{z_1,2} &= \frac{d_1}{3} \left[\left(\frac{h_1}{2} - h_{13} \right)^3 - \left(h_{11} - \frac{h}{2} \right)^3 \right], \\ S_{z_1,3} &= \frac{d_{\text{Al}} n_{\text{Al},i}}{2} \left[\left(\frac{h_1}{2} \right)^2 - \left(\frac{h_1}{2} - h_{13} \right)^2 \right], & I_{z_1,3,} &= \frac{d_{\text{Al}} n_{\text{Al},i}}{3} \left[\left(\frac{h_1}{2} \right)^3 - \left(\frac{h_1}{2} - h_{13} \right)^3 \right]. \end{aligned}$$

The kinetic energy is derived by substituting (5.6) and (5.7) in (5.2b), which results in

$$
\begin{aligned}
W_{\text{kin}} &= \int_{\mathcal{V}} \frac{\tilde{\rho}_1(\tilde{z}_3)}{2} \left[(\partial_t p_1)^2 + (\partial_t p_2)^2 + (\partial_t p_3)^2 \right] \, \mathrm{d}V \\
&= \int_{\mathcal{V}} \frac{\tilde{\rho}_1(\tilde{z}_3)}{2} \left[(\partial_t \tilde{w}_3)^2 + \left(\tilde{z}_3 \partial_t \partial_{\tilde{z}_1} \tilde{w}_3 \right)^2 \right] \, \mathrm{d}V \\
&= \int_0^{l_1} \frac{\overline{\rho_1 A_{\tilde{z}_1}}}{2} (\partial_t \tilde{w}_3)^2 + \frac{\overline{\rho_1 I_{\tilde{z}_1}}}{2} \left(\partial_t \partial_{\tilde{z}_1} \tilde{w}_3 \right)^2 \, \mathrm{d}\tilde{z}_1.
\end{aligned} \tag{5.11}
$$

with the effective densities $\overline{\rho_1 A_{\tilde{z}_1}} = \rho_{11} A_{\tilde{z}_1,1} + \rho_{12} A_{\tilde{z}_1,2} + \rho_{13} A_{\tilde{z}_1,3}$, $\overline{\rho_1 I_{\tilde{z}_1}} = \rho_{11} I_{\tilde{z}_1,1} + \rho_{12} I_{\tilde{z}_1,2} + \rho_{13} I_{\tilde{z}_1,3}$, the cross-sections $A_{\tilde{z}_1} = h_1 d_1$, $A_{\tilde{z}_1,i} = h_{1i} d_1$, $A_{\tilde{z}_1,i} = h_{3i} n_{\text{Al}} d_{\text{Al}}$, and the densities

$$
\tilde{\rho}_1 = \begin{cases} \rho_{11}, & \text{if } \tilde{z}_3 \in \left[-\frac{h_1}{2}, h_{11} - \frac{h_1}{2} \right) \\ \rho_{12}, & \text{if } \tilde{z}_3 \in \left[h_{11} - \frac{h_1}{2}, \frac{h_1}{2} - h_{12} \right] \\ \rho_{13}, & \text{if } \tilde{z}_3 \in \left[\frac{h_1}{2} - h_{12}, \frac{h_1}{2} \right] \end{cases},
$$

$\rho_{1i} > 0$ for all $i = 1, 2, 3$. To simplify (5.11), the effective density $\overline{\rho_1 I_{\tilde{z}_1}}$ is neglected, since $\overline{\rho_1 I_{\tilde{z}_1}} \ll \overline{\rho_1 A_{\tilde{z}_1}}$ holds true. Finally, the virtual work of the non-conservative forces of the MEMS is determined by

$$
W_{\text{NC}} = \int_0^{l_1} A_{\tilde{z}_1} f_3 \tilde{w}_3 \, \mathrm{d}\tilde{z}_1 + F_3 \tilde{w}_3(l_1)
$$

The body force f_1 and f_2 and the forces F_1 and F_2 are neglected, because the MEMS is modeled as a purely bending Bernoulli beam. In addition, the force F is given by (5.5a), so that the virtual work of the non-conservative forces results in

$$
W_{\text{NC}} = -\int_0^{l_1} f_3 \tilde{w}_3 \, \mathrm{d}\tilde{z}_1 + F_\perp \tilde{w}_3(l_1) \tag{5.12}
$$

Using the variational operator δ on the potential energy[1] (5.10), the kinetic energy (5.11), and the virtual work (5.12) of the non-conservative forces, applying integration by parts, and inserting the conditions (5.1b) and (5.1c), yields

$$
\begin{aligned}
J_{\text{pot}} &= \int_{t_1}^{t_2} \delta W_{\text{pot}} \, \mathrm{d}t \\
&= \int_{t_1}^{t_2} \left[\left(\overline{E_1 \alpha_1 S_{\tilde{z}_1}} \tilde{\theta} + \overline{E_1 I_{\tilde{z}_1}} \partial_{\tilde{z}_1}^2 \tilde{w}_3 \right) \delta \partial_{\tilde{z}_1} \tilde{w}_3 \right]_0^{l_1} \, \mathrm{d}t \\
&\quad - \int_{t_1}^{t_2} \left[\left(\overline{E_1 \alpha_1 S_{\tilde{z}_1}} \partial_{\tilde{z}_1} \tilde{\theta} + \overline{E_1 I_{\tilde{z}_1}} \partial_{\tilde{z}_1}^3 \tilde{w}_3 \right) \delta \tilde{w}_3 \right]_0^{l_1} \, \mathrm{d}t \\
&\quad + \int_{t_1}^{t_2} \int_0^{l_1} \left(\overline{E_1 \alpha_1 S_{\tilde{z}_1}} \partial_{\tilde{z}_1}^2 \tilde{\theta} + \overline{E_1 I_{\tilde{z}_1}} \partial_{\tilde{z}_1}^4 \tilde{w}_3 \right) \delta \tilde{w}_3 \, \mathrm{d}\tilde{z}_1 \, \mathrm{d}t,
\end{aligned} \tag{5.13a}
$$

[1] To obtain δW_{pot}, the approach of [101, Section 5.3] is followed.

$$J_{\text{kin}} = \int_{t_1}^{t_2} \delta W_{\text{kin}} \, \mathrm{d}t = \int_{t_1}^{t_2} \int_0^{l_1} \overline{\rho_1 A_{\tilde{z}_1}} \partial_t \tilde{w}_3 \delta \partial_t \tilde{w}_3 \, \mathrm{d}\tilde{z}_1 \, \mathrm{d}t$$
$$= \int_{t_1}^{t_2} \int_0^{l_1} -\overline{\rho_1 A_{\tilde{z}_1}} \partial_t^2 \tilde{w}_3 \delta \tilde{w}_3 \, \mathrm{d}\tilde{z}_1 \, \mathrm{d}t, \tag{5.13b}$$
$$J_{\text{NC}} = \int_{t_1}^{t_2} \delta W_{\text{NC}} \, \mathrm{d}t$$
$$= \int_{t_1}^{t_2} F_3 \delta \tilde{w}_3(l_1) \, \mathrm{d}t - \int_{t_1}^{t_2} \int_0^{l_1} A_{z_1} f_3 \delta \tilde{w}_3 \, \mathrm{d}\tilde{z}_1 \, \mathrm{d}t. \tag{5.13c}$$

The conditions of the boundaries at the tip and the fixed end of the cantilevered MEMS are constraint by [116]

$$\delta \tilde{w}_3(0) = 0, \qquad \delta \partial_{\tilde{z}_1} \tilde{w}_3(0) = 0, \qquad \delta \tilde{w}_3(l_1) \neq 0, \qquad \delta \partial_{\tilde{z}_1} \tilde{w}_3(l_1) \neq 0.$$

Hence, substituting (5.13) into (5.1), asserting that the body force is given by $f_3 = \mu \partial_t \tilde{w}_3 - F_{\text{ex}}(t)$, and employing the fundamental lemma of calculus of variations (see Lemma 5.1) results in

$$0 = \overline{E_1 I_{\tilde{z}_1}} \partial_{\tilde{z}_1}^4 \tilde{w}_3 + \overline{\rho_1 A_{\tilde{z}_1}} \partial_t^2 \tilde{w}_3 + \overline{E_1 \alpha_1 S_{\tilde{z}_1}} \partial_{\tilde{z}_1}^2 \tilde{\theta} + \mu \partial_t \tilde{w}_3 - A_{z_1} F_{\text{ex}}. \tag{5.14}$$

with the boundary conditions

$$0 = [\tilde{w}_3] \,|_{\tilde{z}_1 = 0}, \tag{5.15a}$$
$$0 = \left[\partial_{\tilde{z}_1} \tilde{w}_3\right]_{\tilde{z}_1 = 0}, \tag{5.15b}$$
$$0 = \left[\overline{E_1 \alpha_1 S_{\tilde{z}_1}} \tilde{\theta} + \overline{E_1 I_{\tilde{z}_1}} \partial_{\tilde{z}_1}^2 \tilde{w}_3\right] \Big|_{\tilde{z}_1 = l_1}, \tag{5.15c}$$
$$0 = \left[\overline{E_1 I_{\tilde{z}_1}} \partial_{\tilde{z}_1}^3 \tilde{w}_3 + \overline{E_1 \alpha_1 S_{\tilde{z}_1}} \partial_{\tilde{z}_1} \tilde{\theta} + 2\left(c_{\text{Sp}} \tilde{w}_3 + \frac{c_{\text{Sp}}}{l_1^2} \tilde{w}_3^3\right)\right] \Big|_{\tilde{z}_1 = l_1}. \tag{5.15d}$$

Finally, the piezoelectric strain gauge layer is modeled. This is done by assuming a point measurement at the position $\tilde{z}_{1,\text{meas}} \in (0, l_1)$ of the piezoelectric gauge and a linear relationship between strain ϵ_{11} and the derivative $\partial_{\tilde{z}_1} \tilde{w}_3$ of the deflection with respect to $\tilde{z}_1$. This can be written as

$$y(t) = \tilde{\kappa} \partial_{\tilde{z}_1} \tilde{w}_3(\tilde{z}_1, t)|_{\tilde{z}_1 = \tilde{z}_{1,\text{meas}}}$$

with the transfer factor $\tilde{\kappa} > 0$.

5.2.2. Thermodynamic Subsystem

Subsequently, the thermodynamic subsystem for the MEMS model is derived. This is done by using the generalized equation for heat conduction in a thermoelastic, homogeneous, and isotropic medium. Following [53, 101], heat conduction in a thermoelastic medium is connected to the entropy, since the transportation of heat from areas of high temperature

to areas of low temperature is spontaneous and irreversible. Hence, heat conduction can be determined by considering the flow of entropy. In addition, it is assumed that the heat is a functions in terms of the direction $\tilde{z}_1$ and the time t as the mechanical subsystem is also dependent of them. To describe the change of the entropy, the local form of the second law of thermodynamics is used. This yields

$$\frac{\mathrm{d}s}{\mathrm{d}t} = -\frac{1}{T}\left(\partial_{\tilde{z}_1} q - \frac{P}{V}\right) \tag{5.16}$$

with the entropy $s(\tilde{z}_1, t) \in \mathbb{R}$, the heat flow $q(\tilde{z}_1, t) \in \mathbb{R}$, the generated heat $P(\tilde{z}_1, t) > 0$, and the volume $V > 0$ [101]. In a thermoelastic system, the entropy can be described by

$$s = E\alpha e_{11} + \frac{c_e \rho}{T_0}\tilde{\theta} \tag{5.17}$$

with the specific heat at constant strain $c_e > 0$, ambient temperature $T_0 > 0$, temperature difference $\tilde{\theta}(\tilde{z}_1, t) = \tilde{T}(\tilde{z}_1, t) - T_0 \in \mathbb{R}$, and the absolute temperature $\tilde{T}(\tilde{z}_1, t) \in \mathbb{R}$ of the medium [101]. In addition, the heat flow can be simplified by considering Fourier's law of heat conduction

$$q = -\lambda \partial_{\tilde{z}_1} \tilde{\theta} \tag{5.18}$$

with the thermal conductivity $\lambda > 0$ [53, 101]. Inserting (5.17) and (5.18) into (5.16), results in the nonlinear equation

$$\lambda \partial^2_{\tilde{z}_1} \tilde{\theta} - c_e \rho \partial_t \tilde{\theta} - \frac{E\alpha T_0}{1-\nu} \partial_t \epsilon_{11} \left(1 + \frac{\tilde{\theta}}{T_0}\right) = -\frac{P}{V} \tag{5.19}$$

with the Poisson ratio $\nu \in \mathbb{R}$. By inserting the strain (5.8) and by assuming $\tilde{\theta}/T_0 \ll 1$, (5.19) is simplified providing the linear equation for heat conduction in a thermoelastic homogeneous Bernoulli beam

$$\lambda \partial^2_{\tilde{z}_1} \tilde{\theta} - c_e \rho \partial_t \tilde{\theta} + \frac{E\alpha T_0}{1-\nu} \frac{\tilde{z}_3}{2} \partial^2_{\tilde{z}_1} \partial_t \tilde{w}_3 = -\frac{P}{V}. \tag{5.20}$$

To derive the mathematical model of the thermodynamic subsystem of the MEMS, (5.20) is adjusted as follows: On the one hand, the volume is asserted to be given by $V = A_{\tilde{z}_1} l_1$ and the generated heat P is assumed to be generated by the thermal actuator, so that it is is equal to the electric power P_E, which is transduced by the Al-wires. On the other hand, the heat conduction of the Si-layer and the SiO_2-layer has to be taken into account. Following [116], this is done by considering the effective parameters of the MEMS, which are derived by computing the integral over the cross-section of the cantilever of the MEMS. With this, the effective parameters read

$$\begin{aligned}
\overline{\lambda A_{\tilde{z}_1}} &= \lambda_1 A_{\tilde{z}_1,1} + \lambda_2 A_{\tilde{z}_1,2} + \lambda_3 A_{\tilde{z}_1,3}, \\
\overline{c_e \rho_1 A_{\tilde{z}_1}} &= c_{e,1}\rho_{11} A_{\tilde{z}_1,1} + c_{e,2}\rho_{12} A_{\tilde{z}_1,2} + c_{e,3}\rho_{12} A_{\tilde{z}_1,3}, \\
\overline{\frac{E_1 \alpha_1 S_{\tilde{z}_1}}{1-\nu}} &= \frac{\alpha_1 E_{11} S_{\tilde{z}_1,1}}{1-\nu_1} + \frac{\alpha_2 E_{12} S_{\tilde{z}_1,2}}{1-\nu_2} + \frac{\alpha_3 E_{13} S_{\tilde{z}_1,3}}{1-\nu_3}
\end{aligned}$$

with the thermal conductivity $\lambda_i > 0$, the specific heat at constant strain $c_{e,i} > 0$ and the Poisson ratio ν_i for all $i = 1, 2, 3$ labeling the Si-layer, the SiO_2-layer, and the Al-wires, respectively. The thermodynamic subsystem of the MEMS is thus governed by

$$\overline{\lambda A_{\tilde{z}_1}} \partial_{\tilde{z}_1}^2 \tilde{\theta} - \overline{c_e \rho_1 A_{\tilde{z}_1}} \partial_t \tilde{\theta} + \frac{\overline{E_1 \alpha_1 S_{\tilde{z}_1}}}{1-\nu} T_0 \partial_{\tilde{z}_1}^2 \partial_t \tilde{w}_3 = -\frac{P_\mathrm{E}}{l_1} \tag{5.21}$$

To determine the boundary conditions of the heat conduction, the thermodynamic properties of the MEMS model have to be characterized. For this, the mechanical subsystem of the MEMS is modeled by a cantilever, where a spring is attached to its free end, so that the energy transfer at the tip of the cantilever has to be adiabatic, since the cross-sectional area $A_{\tilde{z}_1}$ is small [116]. Hence, the heat flow vanishes at the tip of the cantilever [11], i.e.,

$$\dot{Q}(l_1, t) = -\overline{\lambda A_{\tilde{z}_1}} \tilde{\theta}(l_1, t) \approx 0$$

with the thermal conductivity between the cantilever and the surrounding air $\lambda_{l_1} > 0$. The clamped end of the cantilever is assumed to be isothermalsystem is called isothermal, if the temperature is constant , since it is fixed on a large silicon wafer [116]. This implies that the temperature at this point is equal to the reference temperature, i.e., $\tilde{\theta}(0, t) = 0$. With these assumptions, the boundary conditions are given by

$$0 = \tilde{\theta}|_{\tilde{z}_1 = 0}, \tag{5.22a}$$

$$0 = \partial_{\tilde{z}_1} \tilde{\theta}|_{\tilde{z}_1 = l_1}. \tag{5.22b}$$

In addition, (5.15b) and (5.15c) can be simplified by inserting these assumptions. This yields

$$0 = \left[\overline{E_1 I_{\tilde{z}_1}} \partial_{\tilde{z}_1}^3 \tilde{w}_3 + 2 \left(c_\mathrm{Sp} \tilde{w}_3 + \frac{c_\mathrm{Sp}}{l_1^2} \tilde{w}_3^3 \right) \right] \Bigg|_{\tilde{z}_1 = l_1}.$$

To model the generated heat, the electric power emitting from heater reads

$$P_{\mathrm{E},i} = iu \tag{5.23}$$

with the electric current $i(t) \in \mathbb{R}$ of the heater and the electric voltages $u(t) \in \mathbb{R}$ applied on the MEMS. The current $i(t)$ is obtained by employing Ohm's law, which yields

$$i = \frac{u}{R} \tag{5.24}$$

with the resistance of the heater given by

$$R = \frac{\sigma_\mathrm{Al}}{h_{13} d_\mathrm{Al}} n_\mathrm{Al} l$$

and the specific resistance $\sigma_\mathrm{Al} > 0$ of the Al-wires. Inserting (5.24) into (5.23), yields

$$P_{\mathrm{E},i} = \frac{1}{R} u^2.$$

5.2.3. Coupled System

In the following, the mathematical model of the MEMS in normalized coordinates is summarized. For this, let

$$z_1 = \frac{\tilde{z}_1}{l_1}, \qquad w_1 = \frac{\tilde{w}_1}{h_1}, \qquad \theta = \frac{\tilde{\theta}}{T_0}$$

and introduce the change of coordinates

$$\tilde{w}_1(\tilde{z}_1(z_1), t) = h_1 w_1(z_1, t), \qquad \tilde{\theta}(\tilde{z}_1(z_1), t) = T_0 \theta(z_1, t)$$

which provide

$$\partial_{\tilde{z}_1}^n \tilde{w}_1 = \frac{h_1}{l_1^n} \partial_{z_1}^n w_1, \qquad \partial_{\tilde{z}_1}^n \tilde{\theta} = \frac{T_0}{l_1^n} \partial_{z_1}^n \theta.$$

With this, the model of the MEMS is governed by

$$\begin{aligned} \overline{\rho_1 A_{\tilde{z}_1}} h_1 \partial_t^2 w_3 = &- \frac{\overline{E_1 I_{\tilde{z}_1}} h_1}{l_1^4} \partial_{z_1}^4 w_3 - h_1 A_{\tilde{z}_1} \mu \partial_t w_3 \\ &- \frac{\overline{E_1 \alpha_1 S_{\tilde{z}_1}} T_0}{l_1^2} \partial_{z_1}^2 \theta + A_{z_1} F_{\text{ex}}, \quad (z_1, t) \in (0,1) \times \mathbb{R}^+, \end{aligned} \tag{5.25a}$$

$$\overline{c_e \rho_1 A_{\tilde{z}_1}} T_0 \partial_t \theta = \frac{\overline{\lambda A_{\tilde{z}_1}} T_0}{l_1^2} \partial_{z_1}^2 \theta + \frac{\overline{E_1 \alpha_1 S_{\tilde{z}_1}}}{1-\nu} \frac{T_0 h_1}{2 l_1^2} \partial_{z_1}^2 \partial_t w_3 + \frac{u^2}{l_1 R}, \quad (z_1, t) \in (0,1) \times \mathbb{R}^+, \tag{5.25b}$$

$$y = \tilde{\kappa} \frac{h_1}{l} \partial_{z_1} w_3 |_{z_1 = z_{1,\text{meas}}} \tag{5.25c}$$

with the mixed boundary conditions

$$0 = [w_3] \,|_{z_1=0}, \tag{5.25d}$$

$$0 = \left[\partial_{z_1} w_3\right] \Big|_{z_1=0}, \tag{5.25e}$$

$$0 = \left[\overline{\alpha_1 S_{\tilde{z}_1}} T_0 \theta + \frac{\overline{E_1 I_{\tilde{z}_1}} h_1}{l_1^2} \partial_{z_1}^2 w_3 \right] \Bigg|_{z_1=1}, \tag{5.25f}$$

$$0 = \left[\frac{\overline{E_1 I_{\tilde{z}_1}}}{l_1^3} \partial_{z_1}^3 w_3 + 2 c_{\text{Sp}} \left(w_3 + \frac{h_1^2}{l_1^2} w_3^3 \right) \right] \Bigg|_{z_1=1}, \tag{5.25g}$$

$$0 = \theta|_{z_1=0}, \tag{5.25h}$$

$$0 = \partial_{z_1} \theta|_{z_1=1} \tag{5.25i}$$

and the initial conditions

$$w_3(z_1, 0) = w_{3,1,0}(z_1) \in \mathbb{R}, \qquad z_1 \in (0,1), \tag{5.25j}$$

$$\partial_t w_3(z_1, 0) = w_{3,2,0}(z_1) \in \mathbb{R}, \qquad z_1 \in (0,1), \tag{5.25k}$$

$$\theta(z_1, 0) = \theta_0(z_1) \in \mathbb{R} \qquad z_1 \in (0,1). \tag{5.25l}$$

Table 5.1.: Relevant material constants of silicon (Si), silicon-oxide (SiO_2), and Aluminum (Al) for the continuum model of the MEMS sensor.

Parameter		Value		
		Silicon (Si)	Silicon-oxide (SiO_2)	Aluminum (Al)
Young's Modulus	E [GPa]	170	$58.1 - 95.6$	70
Poisson's Ratio	ν	0.22	0.17	0.33
Density	ρ $[\frac{\text{kg}}{\text{m}^3}]$	$2,336$	$2,196 - 2,660$	$2,700$
Length	l [µm]	$750 - 1350$	$750 - 1350$	$750 - 1350$
Width	d [µm]	$150 - 700$	$150 - 700$	1
Height	h [µm]	$1 - 9$	$0.25 - 1$	1
Lin. Heat Expansion Coefficient	α $[\frac{\mu}{\text{K}}]$	$2,57 - 3,6$	0.56	$23 - 24$
Specific Heat at Constant Strain	c_e $[\frac{\text{J}}{\text{kg}\cdot\text{K}}]$	$691 - 825$	$742 - 1,243$	$837 - 984$
Heat Conductivity	λ $[\frac{\text{W}}{\text{m}\cdot\text{K}}]$	170	$1.3 - 1.5$	236
Specific Resistivity	σ [µΩ · m]	/	/	265

Example 5.1 *The parameter ranges of the effective parameter in terms of the material constants of the cantilevered MEMS are discussed. The relevant material constants of Si,* SiO_2*, and Al are summarized in Table 5.1. The values for silicon follow [58, 96, 128, 140], the values for silicon-oxide are taken from [65, 104], and the values for aluminum follow [21, 54, 128]. In addition, it is assumed that the geometry of the cantilevered MEMS is given by the length* $l = 900\,\mu m$*, the width* $d = 400\,\mu m$*, and the height* $h \in [0, 4]\,\mu m$ *and that the ambient temperature is equal to the room temperature, i.e.,* $T_0 = 300\,K$*. To determine the parameter range, the effective parameters are computed as a function of the height of the Si-layer and the minimum and maximum value of the material constants.*

The results are visualized in Figure 5.7. It turns out that the effective parameter of coupling from the thermodynamic subsystem to mechanical subsystem and the effective parameter of the self-coupling of the mechanical subsystem are in a similar order of magnitude. In contrast, this does not hold true for the effective parameter of the coupling from the mechanical subsystem to the thermodynamic subsystem and the self-coupling if the thermodynamic subsystem. Hence, the coupled PDEs can be sufficiently approximated by neglecting the coupling from the mechanical subsystem to the thermodynamic subsystem.

5.3. Approximation of the MEMS Model

To prepare the bifurcation analysis of the mathematical model of the MEMS, the coupled PDEs of the MEMS are simplified to a system of ODEs and the experimental parameter identification of the setup is discussed. This is done by approximating the coupled PDEs

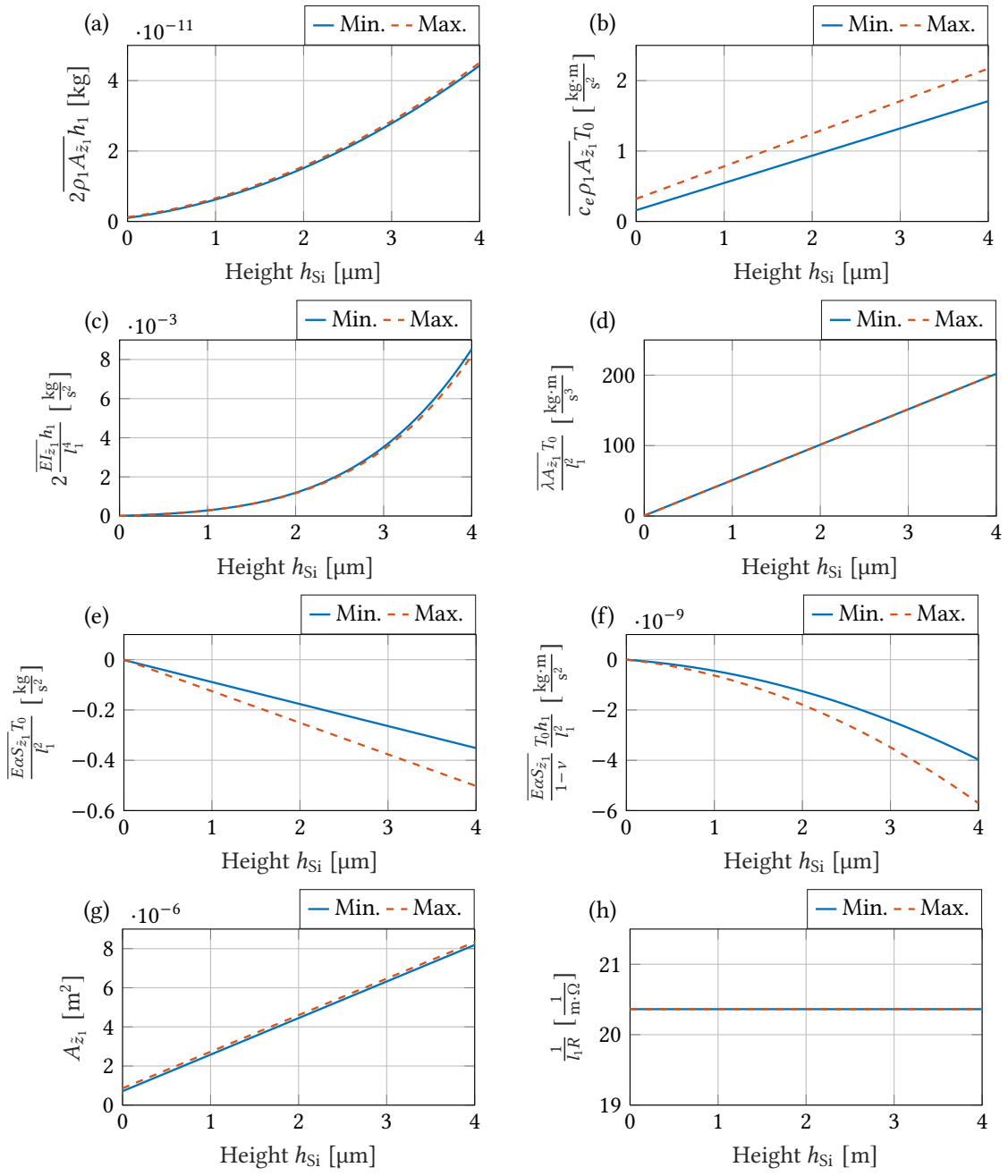

Figure 5.7.: Minimum and maximum of the effective parameters of (5.25) as a function of the height of the Si-layer. (a),(c),(e),(g) Parameter range of the mechanical subsystem. (b),(d),(f),(h) Parameter range of the thermodynamic subsystem.

with the Rayleigh-Ritz method and the Galerkin method. In particular, acoustic stimuli can only excite a few modes of the MEMS, so that these modes are mainly responsible for the observed dynamics of the MEMS. The so-called dominant mode model is derived by employing the Rayleigh-Ritz method to the mechanical subsystem and the Galerkin

method to the thermodynamic subsystem. To employ these methods, consider the ansatz

$$\tilde{w}_3 = \tilde{\psi}_{1,0} + \sum_{i=1}^{n_1} \tilde{x}_{1,i}\tilde{\psi}_{1,i}, \tag{5.26a}$$

$$\tilde{\theta} = \tilde{\psi}_{2,0} + \sum_{i=1}^{n_2} \tilde{x}_{2,i}\tilde{\psi}_{2,i} \tag{5.26b}$$

with the test functions $\tilde{\psi}_{j,i}(\tilde{z}_1) \in \mathbb{R}$, the coefficients $\tilde{x}_{j,i}(t) \in \mathbb{R}$, and the number of elements $n_j \in \mathbb{N}$ for all $i = 1, \ldots, n$ and $j = 1, 2$. The boundary condition (5.25d) and (5.25h), i.e., $\tilde{w}_3(0,t) = \tilde{\theta}(0,t) = 0$, implies that $\tilde{\psi}_{j,0}(z_1) = 0$ is satisfied.

5.3.1. Rayleigh-Ritz Method

The approximation of the mechanical subsystem of the clamped-clamped MEMS is derived by employing the Rayleigh-Ritz method. As this method approximates a PDE by considering the energy, the subsequent analysis is done by simplifying the extended Hamiltonian principle with the ansatz (5.26). Inserting (5.26) into the potential energy (5.10), the kinetic energy (5.11), and the virtual work (5.12) of the non-conservative forces results in

$$W_{\text{pot}} = \int_0^{l_1} \frac{\overline{E_1 I_{z_1}}}{2} \left[\sum_{i=1}^{n_1} \tilde{x}_{1,i} \frac{\mathrm{d}^2\tilde{\psi}_{1,i}}{\mathrm{d}z_1}\right]^2 + \overline{E_1\alpha_1 S_{z_1}} \left[\sum_{i=1}^{n_2} \tilde{x}_{2,i}\tilde{\psi}_{2,i}\right]\left[\sum_{i=1}^{n_1} \tilde{x}_{1,i} \frac{\mathrm{d}^2\tilde{\psi}_{1,i}}{\mathrm{d}z_1}\right] \mathrm{d}z_1,$$

$$W_{\text{kin}} = \frac{\overline{\rho_1 A_{z_1}}}{2} \int_0^{l_1} \left[\sum_{i=1}^{n_1} \frac{\mathrm{d}\tilde{x}_{1,i}}{\mathrm{d}t}\tilde{\psi}_{1,i}\right]^2 \mathrm{d}z_1,$$

$$W_{\text{NC}} = \int_0^{l_1} A_{z_1} f_3 \left[\sum_{i=1}^{n_1} \tilde{x}_{1,i}\tilde{\psi}_{1,i}\right] \mathrm{d}z_1 + c_{\text{Sp}} \left[\sum_{i=1}^{n_1} \tilde{x}_{1,i}\tilde{\psi}_{1,i}(l_1)\right]^2 + \frac{c_{\text{Sp}}}{2l_1} \left[\sum_{i=1}^{n_1} \tilde{x}_{1,i}\tilde{\psi}_{1,i}(l_1)\right]^4.$$

Then the dominate mode mode is derived by taking the variation of the integral of the energies over the time with respect to $\tilde{w}_{t,i}$ for all $i = 1, \ldots, n$. This results in

$$\begin{aligned}\tilde{J}_{\text{pot}} &= \int_{t_1}^{t_2} \delta W_{\text{pot}} \, \mathrm{d}t \\ &= \sum_{i=1}^{n}\sum_{j=1}^{n} \int_{t_1}^{t_2} \left(\overline{E_1 I_{z_1}} \left[\int_0^{l_1} \frac{\mathrm{d}^2\tilde{\psi}_{1,i}}{\mathrm{d}z_1}\frac{\mathrm{d}^2\tilde{\psi}_{1,j}}{\mathrm{d}z_1} \, \mathrm{d}z_1\right]\tilde{x}_{1,j} \right. \\ &\qquad \left. + \overline{E_1\alpha_1 S_{z_1}} \left[\int_0^{l_1} \tilde{\psi}_{2,j}\frac{\mathrm{d}^2\tilde{\psi}_{1,i}}{\mathrm{d}z_1} \, \mathrm{d}z_1\right]\tilde{x}_{2,j}\right) \delta\tilde{x}_{1,i}\mathrm{d}t, \end{aligned} \tag{5.27a}$$

$$\begin{aligned}\tilde{J}_{\text{kin}} &= \int_{t_1}^{t_2} \delta W_{\text{kin}} \, \mathrm{d}t \\ &= -\sum_{i=1}^{n}\sum_{j=1}^{n} \int_{t_1}^{t_2} \left(\overline{\rho_1 A_{z_1}} \left[\int_0^{l_1} \tilde{\psi}_{1,i}\tilde{\psi}_{1,j} \, \mathrm{d}z_1\right] \frac{\mathrm{d}^2\tilde{x}_{1,j}}{\mathrm{d}t}\right) \delta\tilde{x}_{1,i} \, \mathrm{d}t, \end{aligned} \tag{5.27b}$$

$$\begin{aligned}\tilde{J}_{\mathrm{NC}} &= \int_{t_1}^{t_2} \delta W_{\mathrm{NC}}\,\mathrm{d}t \\ &= \sum_{i=1}^{n}\left(\sum_{j=1}^{n}\int_{t_1}^{t_2} A_{z_1}\left[\int_0^{l_1} f_3\tilde{\psi}_{1,i}\,\mathrm{d}z_1\right]\mathrm{d}t + 2c_{\mathrm{Sp}}\left[\tilde{\psi}_{1,i}(l_1)\tilde{\psi}_{1,j}(l_1)\right]\tilde{x}_{1,j}\right. \\ &\qquad \left. + \sum_{i=1}^{n}\frac{2c_{\mathrm{Sp}}\tilde{w}_{z_1,i}(l_1)}{l_1}\left[\sum_{j=1}^{n}\tilde{\psi}_{1,j}(l_1)\tilde{x}_{1,j}\right]^3\right)\delta\tilde{x}_{1,i} \end{aligned} \tag{5.27c}$$

with the body force is given by $f_3 = \mu\partial_t\tilde{w}_3 - F_{\mathrm{ex}}(t)$. Inserting (5.27) into

$$\begin{aligned} 0 &= \int_{t_1}^{t_2} \delta W_{\mathrm{pot}}(t) - \delta W_{\mathrm{kin}}(t) + \delta W_{\mathrm{NC}}(t)\,\mathrm{d}t, \\ 0 &= \delta\tilde{\boldsymbol{w}}(\tilde{\boldsymbol{z}},t), && \tilde{\boldsymbol{z}}\in\mathcal{S}(\tilde{\boldsymbol{z}}), && \forall t\in[t_1,t_2], \\ 0 &= \delta\tilde{\boldsymbol{w}}(\tilde{\boldsymbol{z}},t_1) = \delta\tilde{\boldsymbol{w}}(\tilde{\boldsymbol{z}},t_2), && && \tilde{\boldsymbol{z}}\in\mathcal{V}(\tilde{\boldsymbol{z}}) \end{aligned}$$

and employing the fundamental lemma of calculus of variations (see Lemma 5.1), the approximation of the mechanical subsystem is obtained as

$$\mathcal{J}_{\mathrm{R},1}\ddot{\tilde{\boldsymbol{x}}}_1 = \left(\mathcal{J}_{\mathrm{R},2} + \mathcal{J}_{\mathrm{R},3}\right)\tilde{\boldsymbol{x}}_1 + \mathcal{J}_{\mathrm{R},4}\dot{\tilde{\boldsymbol{x}}}_1 + \mathcal{J}_{\mathrm{R},5}\tilde{\boldsymbol{x}}_2 + \boldsymbol{f}(\tilde{\boldsymbol{x}}_1) + \mathcal{J}_{\mathrm{R},6}F_{\mathrm{ex}}, \tag{5.28a}$$

$$y = \mathcal{J}_{\mathrm{R},y}\tilde{\boldsymbol{x}}_1. \tag{5.28b}$$

with the state vectors

$$\tilde{\boldsymbol{x}}_1 = [\tilde{x}_{11}, \tilde{x}_{12}, \ldots, \tilde{x}_{1n_1}]^{\mathrm{T}} \in \mathbb{R}^{n_1}, \qquad \tilde{\boldsymbol{x}}_2 = [\tilde{x}_{21}, \tilde{x}_{22}, \ldots, \tilde{x}_{2n_2}]^{\mathrm{T}} \in \mathbb{R}^{n_2}.$$

The matrices and the nonlinearity read

$$\mathcal{J}_{\mathrm{R},1} = \overline{\rho_1 A_{z_1}}\left[\int_0^{l_1}\tilde{\psi}_{1,i}\tilde{\psi}_{1,j}\,\mathrm{d}z_1\right]_{i,j=1,\ldots,n_1}, \tag{5.29a}$$

$$\mathcal{J}_{\mathrm{R},2} = -\overline{E_1 I_{z_1}}\left[\int_0^{l_1}\frac{\mathrm{d}^2\tilde{\psi}_{1,i}}{\mathrm{d}z_1}\frac{\mathrm{d}^2\tilde{\psi}_{1,j}}{\mathrm{d}z_1}\,\mathrm{d}z_1\right]_{i,j=1,\ldots,n_1}, \tag{5.29b}$$

$$\mathcal{J}_{\mathrm{R},3} = 2c_{\mathrm{Sp}}\left[\tilde{\psi}_{1,i}(l_1)\tilde{\psi}_{1,j}(l_1)\right]_{i,j=1,\ldots,n_1}, \tag{5.29c}$$

$$\mathcal{J}_{\mathrm{R},4} = -A_{z_1}\mu\left[\int_0^{l_1}\tilde{\psi}_{1,i}\tilde{\psi}_{1,j}\,\mathrm{d}z_1\right]_{i,j=1,\ldots,n_1}, \tag{5.29d}$$

$$\mathcal{J}_{\mathrm{R},5} = \overline{E_1\alpha_1 S_{z_1}}\left[\int_0^{l_1}\tilde{\psi}_{2,j}\frac{\mathrm{d}^2\tilde{\psi}_{1,i}}{\mathrm{d}z_1}\,\mathrm{d}z_1\right]_{i=1,\ldots,n_1,j=1,\ldots,n_2}, \tag{5.29e}$$

$$\mathcal{J}_{\mathrm{R},6} = A_{z_1}\left[\int_0^{l_1}\tilde{\psi}_{1,i}\,\mathrm{d}z_1\right]_{i=1,\ldots,n_1}, \tag{5.29f}$$

$$\mathcal{J}_{\mathrm{R},y} = \tilde{\kappa}\left[\left.\frac{\mathrm{d}\psi_{1,i}}{\mathrm{d}z_1}\right|_{\tilde{z}_1=\tilde{z}_{1,\mathrm{meas}}}\right]_{i=1,\ldots,n}, \tag{5.29g}$$

$$\boldsymbol{f}(\boldsymbol{w}_t) = -\frac{2c_{\mathrm{Sp}}}{l_1}\left[\tilde{\psi}_{1,i}(l_1)\left(\sum_{j=1}^{n}\tilde{\psi}_{1,j}(l_1)\tilde{x}_{1,j}\right)^3\right]_{i,j=1,\ldots,n_1}. \tag{5.29h}$$

The potential test functions $\tilde{\psi}_{1,i}$ have to satisfy the specified essential boundary conditions [110], which implies

$$0 = \left[\tilde{\psi}_{1,i}\right]\Big|_{z_1=0}, \tag{5.30a}$$

$$0 = \left[\partial_{z_1}\tilde{\psi}_{1,i}\right]\Big|_{z_1=0} \tag{5.30b}$$

for all $i = 1, \ldots, n_1$.

5.3.2. Galerkin Method

In contrast to the Rayleigh-Ritz method, the Galerkin method approximates a PDE by considering the weak form. For this, (5.21) is multiplied with the test function $\tilde{\phi}_{2j}$ and integrated over $\tilde{z}_1 \in [0, l]$, which yields

$$0 = -\overline{\lambda A_{\tilde{z}_1}} \int_0^{l_1} \tilde{\phi}_{2j}\partial_{\tilde{z}_1}^2\tilde{\theta}\mathrm{d}\tilde{z}_1 - \int_0^{l_1} \frac{\overline{E_1\alpha_1 S_{\tilde{z}_1}}}{1-\nu} T_0\tilde{\phi}_{2j}\partial_{\tilde{z}_1}^2\partial_t\tilde{w}_3 + \overline{c_e\rho_1 A_{\tilde{z}_1}}\tilde{\phi}_{2j}\partial_t\tilde{\theta} - \frac{u^2}{l_1 R}\tilde{\phi}_{2j}\mathrm{d}\tilde{z}_1.$$

Performing integration by parts, inserting (5.22) and (5.26) into the result, and sorting terms, results in

$$\begin{aligned} 0 = {} & \overline{\lambda A_{\tilde{z}_1}} \sum_{i=1}^{n_2} \tilde{\phi}_{2j}(0)\frac{\mathrm{d}\tilde{\theta}(0)}{\mathrm{d}\tilde{z}_1} + \overline{\lambda A_{\tilde{z}_1}} \sum_{i=1}^{n_2} \tilde{x}_{2,i}\int_0^{l_1} \frac{\mathrm{d}\tilde{\phi}_{2j}}{\mathrm{d}\tilde{z}_1}\frac{\mathrm{d}\tilde{\psi}_{2,i}}{\mathrm{d}\tilde{z}_1}\mathrm{d}z_1 \\ & - \frac{\overline{E_1\alpha_1 S_{\tilde{z}_1}}}{1-\nu} T_0 \sum_{i=1}^{n_1} \frac{\mathrm{d}\tilde{x}_{1,i}}{\mathrm{d}t}\int_0^{l_1} \tilde{\phi}_{2j}\frac{\mathrm{d}^2\tilde{\psi}_{1,i}}{\mathrm{d}\tilde{z}_1}\mathrm{d}z_1 - \overline{c_e\rho_1 A_{\tilde{z}_1}} \sum_{i=1}^{n_2} \frac{\mathrm{d}\tilde{x}_{2,i}}{\mathrm{d}t}\int_0^{l_1} \tilde{\phi}_{2j}\tilde{\psi}_{2,i}\mathrm{d}z_1 \\ & - \frac{u^2}{l_1 R}\int_0^{l_1} \tilde{\phi}_{2j}\mathrm{d}z_1. \end{aligned}$$

Evalutation of this expression for each $j = 1, 2, \ldots, n_2$ yields the reduced order system

$$\mathcal{J}_{\mathrm{G},1}\dot{\tilde{\boldsymbol{x}}}_2 = \mathcal{J}_{\mathrm{G},2}\dot{\tilde{\boldsymbol{x}}}_1 + \mathcal{J}_{\mathrm{G},3}\tilde{\boldsymbol{x}}_2 + \frac{\mathcal{J}_{\mathrm{G},4}}{R}u^2,$$

with the matrices

$$\mathcal{J}_{\mathrm{G},1} = \overline{c_e\rho_1 A_{\tilde{z}_1}}\left[\int_0^{l_1} \phi_{2i}\phi_{2j}\,\mathrm{d}z_1\right]_{i,j=1,\ldots,n_2}, \tag{5.31a}$$

$$\mathcal{J}_{\mathrm{G},2} = -\frac{\overline{E_1\alpha_1 S_{\tilde{z}_1}}}{1-\nu} T_0\left[\int_0^{l_1} \phi_{2i}\frac{\mathrm{d}^2\phi_{1j}}{\mathrm{d}z_1^2}\,\mathrm{d}z_1\right]_{i=1,\ldots,n_2,j=1,\ldots,n_1}, \tag{5.31b}$$

$$\mathcal{J}_{\mathrm{G},3} = \overline{\lambda A_{\tilde{z}_1}}\left[\int_0^{l_1} \frac{\mathrm{d}\phi_{2i}}{\mathrm{d}z_1^2}\frac{\mathrm{d}\phi_{2j}}{\mathrm{d}z_1^2}\,\mathrm{d}z_1\right]_{i,j=1,\ldots,n_2}, \tag{5.31c}$$

$$\mathcal{J}_{\mathrm{G},4} = \left[\frac{1}{l_1 R}\int_0^{l_1} \phi_{2i}\,\mathrm{d}z_1\right]_{i=1,\ldots,n_2} \tag{5.31d}$$

and the boundary condition

$$\tilde{\phi}_{2j}(0) = 0 \tag{5.32}$$

for all $j = 1, 2, \ldots, n_2$.

5.3.3. Eigenfunctions as Test Functions

Subsequently, the test functions $\tilde{\phi}_{1,i}$ and $\tilde{\phi}_{2,i}$ are assumed to the eigenfunctions of the Bernoulli beam for $\tilde{\phi}_{1,i}$, see, e.g., [37, Appendix C], and the eigenfunctions of the heat conduction for $\tilde{\phi}_{2,i}$, see, e.g., [98, Section 5.3], as these functions satisfy the boundary conditions (5.30) and (5.32) and the resulting matrices can be easily interpreted physically. These test functions are read

$$\begin{aligned}\phi_{1i}(z_1) =& c_{\mathrm{M}} \left\{ \left[\cosh\left(\lambda_i \frac{\tilde{z}_1}{l_1}\right) - \cos\left(\lambda_i \frac{\tilde{z}_1}{l_1}\right) \right] \right. \\ &\left. + \frac{\cos(\lambda_i) + \cosh(\lambda_i)}{\sin(\lambda_i) + \sinh(\lambda_i)} \left[\sin\left(\lambda_i \frac{\tilde{z}_1}{l_1}\right) - \sinh\left(\lambda_i \frac{\tilde{z}_1}{l_1}\right) \right] \right\}, \end{aligned} \tag{5.33a}$$

$$\phi_{2j}(z_1) = c_{\mathrm{T}} \sin\left(\frac{(2j-1)\pi \tilde{z}_1}{2 l_1}\right) \tag{5.33b}$$

with the coefficients $c_{\mathrm{M}}, c_{\mathrm{T}} \in \mathbb{R}$ and the parameter $\lambda_i > 0$ for all $i = 1, 2, \ldots, n_1$ and $j = 1, 2, \ldots, n_2$. The parameter λ_i is obtained by solving

$$\cos(\lambda_i)\cosh(\lambda_i) + 1 = 0.$$

Inserting (5.33) into (5.29) and (5.31) and evaluating the integrals, results in

$$\mathcal{J}_{\mathrm{R},1,ij} = \begin{cases} \frac{l_1 c_{\mathrm{M}}^2 \overline{\rho_1 A_{z_1}}}{4\lambda_i [\sin(\lambda_i)+\sinh(\lambda_i)]^2} \left\{ 4\lambda_i \left[\sin(\lambda_i) + \sinh(\lambda_i)\right]^2 \right. \\ \qquad -6\cosh(\lambda_i)\left[2\sin(\lambda_i) + \sin(2\lambda_i)\cosh(\lambda_i)\right] \\ \left. \qquad +6\cos(\lambda_i)\left[2\sinh(\lambda_i) + \cos(\lambda_i)\sinh(2\lambda_i)\right] \right\}, & \text{if } i = j \\ 0, & \text{if } i \neq j \end{cases}, \tag{5.34a}$$

$$\mathcal{J}_{\mathrm{R},2,ij} = \begin{cases} -\frac{c_{\mathrm{M}}^2 \lambda_i^3 \overline{E_1 I_{z_1}}}{4 l_1^3 [\sin(\lambda_i)+\sinh(\lambda_i)]^2} \left\{ \sin(2\lambda_i) + 4\lambda_i \left(\sin(\lambda_i) + \sinh(\lambda_i)\right)^2 \right. \\ \qquad -2\cos(\lambda_i)\left[2\sinh(\lambda_i) + \cos(\lambda_i)\sinh(2\lambda_i)\right] \\ \left. \qquad +4\sin(\lambda_i)\cosh(\lambda_i) + \sin(2\lambda_i)\cosh(2\lambda_i)\right\}, & \text{if } i = j \\ 0, & \text{if } i \neq j \end{cases}, \tag{5.34b}$$

$$\begin{aligned}\mathcal{J}_{\mathrm{R},3,ij} = 2 c_{\mathrm{M}}^2 c_{\mathrm{Sp}} &\left\{ \left[\cosh(\lambda_i) - \cos(\lambda_i)\right] + \frac{\cos(\lambda_i) + \cosh(\lambda_i)}{\sin(\lambda_i) + \sinh(\lambda_i)} \left[\sin(\lambda_i) - \sinh(\lambda_i)\right] \right\} \\ &\times \left\{ \left[\cosh(\lambda_j) - \cos(\lambda_j)\right] + \frac{\cos(\lambda_j) + \cosh(\lambda_j)}{\sin(\lambda_j) + \sinh(\lambda_j)} \left[\sin(\lambda_j) - \sinh(\lambda_j)\right] \right\}, \end{aligned} \tag{5.34c}$$

$$\mathcal{J}_{\mathrm{R},4,ij} = \begin{cases} -\frac{l_1 c_{\mathrm{M}}^2 A_{z_1} \mu}{4\lambda_i (\sin[\lambda_i]+\sinh(\lambda_i))^2} \left\{ 4\lambda_i \left[\sin(\lambda_i) + \sinh(\lambda_i)\right]^2 \right. \\ \qquad -6\cosh(\lambda_i)\left[2\sin(\lambda_i) + \sin(2\lambda_i)\cosh(\lambda_i)\right] \\ \qquad \left. +6\cos(\lambda_i)\left[2\sinh(\lambda_i) + \cos(\lambda_i)\sinh(2\lambda_i)\right]\right\}, & \text{if } i = j \\ 0, & \text{if } i \neq j \end{cases}, \tag{5.34d}$$

$$\mathcal{J}_{\mathrm{R},5,ij} = \frac{4 c_{\mathrm{M}} c_{\mathrm{T}} \lambda_j^2 \overline{E_1 \alpha_1 S_{z_1}}}{l_1 \left[\pi^4 (1-2i)^4 - 16\lambda_j^4\right] \left[\sin(\lambda_j) + \sinh(\lambda_j)\right]} \tag{5.34e}$$

$$\times \left\{ \pi^3 (2i-1)^3 \left[\sin(\lambda_j) + \sinh(\lambda_j)\right] + 8(-1)^i \lambda_j^3 \sin(\lambda_j)\sinh(\lambda_j) \right\}, \tag{5.34f}$$

$$\mathcal{J}_{\mathrm{R},6,i} = \frac{8 l_1 c_{\mathrm{M}} A_{z_1} \sin^2\left(\frac{\lambda_i}{2}\right) \sinh^2\left[\frac{\lambda_i}{2}\right]}{\lambda_i \left(\sin(\lambda_i) + \sinh(\lambda_i)\right)}, \tag{5.34g}$$

$$\mathcal{J}_{\mathrm{R},y,i} = \frac{c_{\mathrm{M}} \lambda_i \tilde{\kappa}}{l_1} \left\{ \left[\sinh\left(\lambda_i \frac{\tilde{z}_1}{l_1}\right) + \sin\left(\lambda_i \frac{\tilde{z}_1}{l_1}\right) \right] \right.$$

$$\left. + \frac{\cos(\lambda_i) + \cosh(\lambda_i)}{\sin(\lambda_i) + \sinh(\lambda_i)} \left[\cos\left(\lambda_i \frac{\tilde{z}_1}{l_1}\right) - \cosh\left(\lambda_i \frac{\tilde{z}_1}{l_1}\right) \right] \right\}, \tag{5.34h}$$

$$\mathcal{J}_{\mathrm{G},1,ij} = \begin{cases} \frac{c_{\mathrm{T}} l_1 \overline{c_e \rho_1 A_{\tilde{z}_1}}}{2}, & \text{if } i = j \\ 0, & \text{if } i \neq j \end{cases}, \tag{5.34i}$$

$$\mathcal{J}_{\mathrm{G},2,ij} = -\frac{4 c_{\mathrm{M}} c_{\mathrm{T}} \lambda_j^2 T_0}{l_1 \left[\pi^4 (1-2i)^4 - 16\lambda_j^4\right] \left[\sin(\lambda_j) + \sinh(\lambda_j)\right]} \frac{\overline{E_1 \alpha_1 S_{\tilde{z}_1}}}{1-\nu}$$

$$\times \left\{ \pi^3 (2i-1)^3 \left[\sin(\lambda_j) + \sinh(\lambda_j)\right] + 8(-1)^i \lambda_j^3 \sin(\lambda_j)\sinh(\lambda_j) \right\}, \tag{5.34j}$$

$$\mathcal{J}_{\mathrm{G},3,ij} = \begin{cases} \frac{c_{\mathrm{T}} \overline{\lambda A_{\tilde{z}_1}}}{2 l_1}, & \text{if } i = j \\ 0, & \text{if } i \neq j \end{cases}, \tag{5.34k}$$

$$\mathcal{J}_{\mathrm{G},4,i} = \frac{2 c_T}{(2i-1)\pi R}. \tag{5.34l}$$

5.3.4. State Space Representation

The approximation governing the clamped-clamped thermoelastic MEMS is given by

$$\dot{\boldsymbol{x}}_1 = \boldsymbol{x}_2, \qquad t > 0, \quad \boldsymbol{x}_1(0) = \boldsymbol{x}_{10}, \tag{5.35a}$$

$$\mathcal{J}_{\mathrm{R},1} \dot{\boldsymbol{x}}_2 = \left(\mathcal{J}_{\mathrm{R},2} + \mathcal{J}_{\mathrm{R},3}\right) \boldsymbol{x}_1 + \boldsymbol{f}(\boldsymbol{x}_1) + \mathcal{J}_{\mathrm{R},4} \boldsymbol{x}_2 + \mathcal{J}_{\mathrm{R},5} \boldsymbol{x}_3 + \mathcal{J}_{\mathrm{R},6} F_{\mathrm{ex}}, \quad t > 0, \quad \boldsymbol{x}_2(0) = \boldsymbol{x}_{20}, \tag{5.35b}$$

$$\mathcal{J}_{\mathrm{G},1} \dot{\boldsymbol{x}}_3 = \mathcal{J}_{\mathrm{G},2} \boldsymbol{x}_2 + \mathcal{J}_{\mathrm{G},3} \boldsymbol{x}_3 + \mathcal{J}_{\mathrm{G},4} u_{\mathrm{act}}^2, \qquad t > 0, \quad \boldsymbol{x}_3(0) = \boldsymbol{x}_{30}, \tag{5.35c}$$

$$y = \mathcal{J}_{\mathrm{R},y} \boldsymbol{x}_1, \qquad t \geq 0 \tag{5.35d}$$

with the deflection vector $\boldsymbol{x}_1 = \tilde{\boldsymbol{x}}_1$, velocity vector $\tilde{\boldsymbol{x}}_2 = \dot{\tilde{\boldsymbol{x}}}_1$, the temperature vector $\boldsymbol{x}_3(t) = \tilde{\boldsymbol{x}}_2$, the output $y(t) \in \mathbb{R}$, the actuation voltage $u_{\mathrm{act}}(t) \in \mathbb{R}$, the external input $F_{\mathrm{ex}}(t) \in \mathbb{R}$, and the initial conditions $\boldsymbol{x}_{10}, \boldsymbol{x}_{20} \in \mathbb{R}^{n_1}$ and $\boldsymbol{x}_{30} \in \mathbb{R}^{n_2}$.

5.3.5. Parameter Identification

Following [47, 81], the approximation can be truncated after the first mode. This can be done since the bandwidth of acoustic stimuli is limited to a bandwidth from 20 Hz to 20 kHz, so that only the first mode of the mechanical subsystem of the MEMS is excited. With this, the parameters of the MEMS can be easily determined experimentally. Inserting $n = 1$ in (5.35), neglecting $\mathcal{J}_{G,2}$ and sorting terms, results in

$$\dot{\boldsymbol{x}} = \begin{bmatrix} x_2 \\ -c_1 x_1 - c_3 x_1^3 - \mu x_2 + \alpha x_3 + \frac{1}{m} F_{\text{ex}} \\ -\beta x_3 + \zeta u_{\text{act}}^2 \end{bmatrix} \qquad t > 0, \qquad \boldsymbol{x}(0) = \boldsymbol{x}_0, \tag{5.36a}$$

$$y = \kappa x_1, \qquad t \geq 0 \tag{5.36b}$$

with the deflection $x_1(t) \in \mathbb{R}$, the velocity $x_2(t) \in \mathbb{R}$, and the temperature $x_3(t) \in \mathbb{R}$. Additional parameters are given by the linear spring constant $c_1 > 0$, the cubic spring constant $c_3 > 0$, the damping $\mu > 0$, the mass $m > 0$, the transfer factors $\alpha, \zeta > 0$, the time constant $\beta > 0$, and the calibration factor $\kappa > 0$. From (5.36) it follows that the geometric nonlinearity can be approximated by a Duffing oscillator.

In particular, the parameters of (5.36) can be easily determined experimentally [47, 81]. For this, the signal acquisition and signal generation is done by the laser Doppler vibrometer *PSV-500* from Polytec GmbH and the vibrometer is set up to measure the deflection at the tip of the MEMS. With this, the parameters are determined as follows: First, the spring constants c_1 and c_3 and the damping μ are determined by exciting the MEMS acoustically using frequency chirps for multiple DC-voltages $u_{\text{DC}} = u_{\text{act}}$. After determining the characteristic frequency by maximizing the frequency responses of the MEMS and the steady state of the deflection $x_{1,\text{eq}}$, the spring constants are obtained by fitting the measured data with

$$\omega_{\text{C}} = \sqrt{c_1 + 3c_2 x_{1,\text{eq}}^2}.$$

The damping μ is determined by computing the Q-factor Q_0 from the 3-dB bandwidth of the frequency responses and fitting $\mu = \frac{\omega_{\text{C}}}{Q_0}$. Second, the calibration factor κ is determined by exciting the MEMS acoustically with a single tone stimuli, where the frequency of the generated signal is given by the characteristic frequency of the MEMS. With this, the calibration factor κ is obtained by dividing the steady state of the deflection x_1 with the steady state of the output y. Third, the resistance R of the Al-wires is measured from PCB using a multimeter. Fourth, the time constant β and the product between the transfer factors α and γ are determined by evaluating the response of the MEMS to thermal actuation. For this, the actuation voltage is chosen to be a square wave with an amplitude 500 mV and a frequency 1 Hz. Then the time constant β is the inverse of the rise time, which is obtained by measuring the time until the deflection reached 63% of its maximum. In contrast, the transfer factors α and γ is determined by using

$$\alpha\gamma = \frac{4\beta(\pi\omega R)^2}{u_{\text{DC}}^2} x_{1,\text{eq}}.$$

with the measured steady state $x_{1,\text{eq}} \in \mathbb{R}$ of the deflection.

Example 5.2 *The MEMS model* (5.36) *with the identified parameters and the approximated MEMS model* (5.35) *are compared by determining the parameters of the first mode and simulating the evolution of their deflection. For this, a (cantilevered) MEMS from [81, Table 1] is considered. The parameters of* (5.36) *are summarized in Table 5.2 and geometry of the MEMS is given by* $l_{1,\text{meas}} = 350\,\mu m$, $d_{\text{meas}} = 150\,\mu m$, *and* $h_{\text{meas}} \in [1.25, 1.45]\,\mu m$. *To determine the matrices* (5.34), *it is assumed that the measurement error of the length and the width of this MEMS is in several micrometers, while the error of the height is upto 1 micrometer. Hence, the geometry of the theoretical MEMS is asserted to be given by the length* $l_{1,\text{th}} = 350\,\mu m$, *the width* $d_{\text{th}} = 150\,\mu m$, *the number* $n_{\text{Al}} = 6$ *of the Al-wires, the width* $d_{\text{Al}} = 2\,\mu m$ *of the Al-wires, and the height* $h_{\text{th}} = 1.45\,\mu m$ *of the MEMS consisting of* $h_{1,\text{th}} = 0.55\,\mu m$, $h_{2,\text{th}} = 0.4\,\mu m$, *and* $h_{3,\text{th}} = 0.5\,\mu m$ *with* $i = 1, 2, 3$ *labeling the Si-layer,* SiO_3*-layer and the Al-wires, respectively. In addition, the material constants follow Table 5.1, while the constants of the test functions* (5.33) *read* $c_{\text{M}} = 1$ *and* $c_{\text{T}} = 1$.

The evolution of the deflection is visualized in Figure 5.8. For this, the modes of the mechanical and thermodynamic subsystem are given by $n_1, n_2 = 1, 3$ *and it is assumed that the deflection of the MEMS is measured at tip. It is showcased that it is sufficient to approximate the equilibrium of mechanical subsystem by truncating the approximation* (5.26a) *after the first*

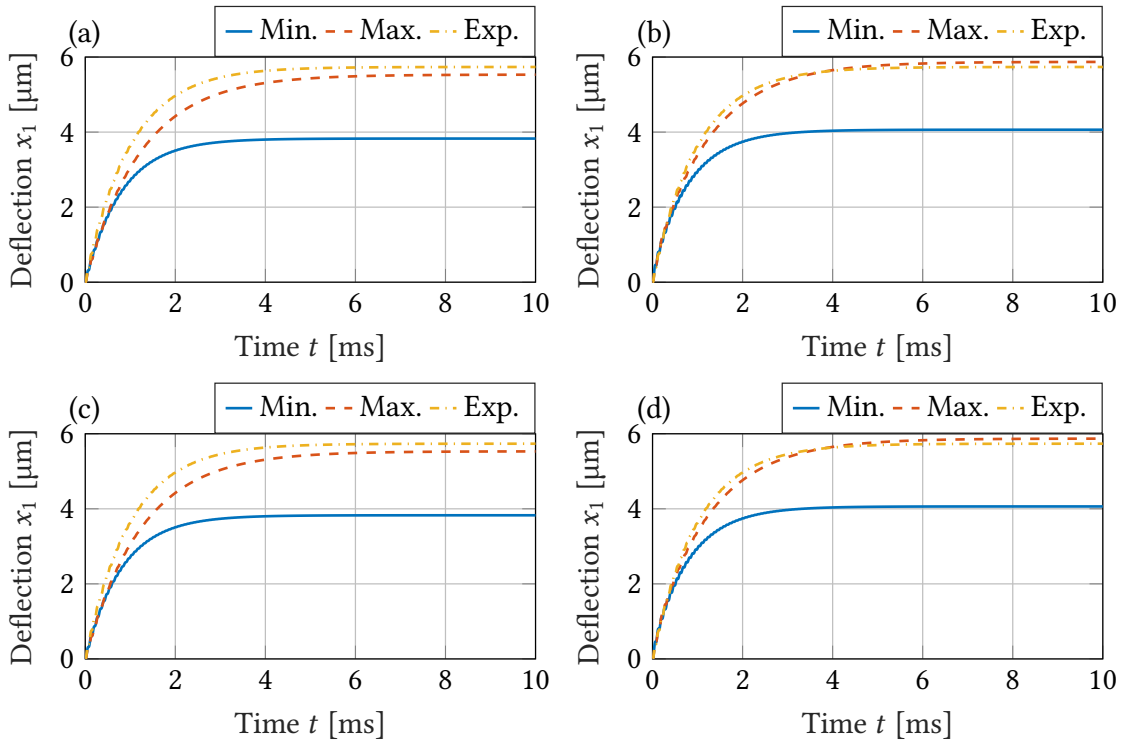

Figure 5.8.: Comparison between of the evolution of the deflection x_1 of the MEMS model (5.36) with the estimated parameters and the approximated MEMS model (5.35) for different modes $n_1 = 1, 3$ of the mechanical subsystem and $n_2 = 1, 3$ of the thermodynamic subsystem. (a) The modes of the subsystems are given by $n_1 = 1$ and $n_2 = 1$. (b) The modes of the subsystems read $n_1 = 1$ and $n_2 = 3$. (c) The modes of the subsystems are given by $n_1 = 3$ and $n_2 = 1$. (d) The modes of the subsystems read $n_1 = 3$ and $n_2 = 3$.

mode. In contrast, the influence of the thermodynamic subsystem can only be reproduced by considering multiple elements of the approximation (5.26b).

Based on these results, the parameters of the approximation (5.35) *are analyzed for* $n_1 = 1$ *and* $n_2 = 3$. *For this, the parameters* (5.34) *are evaluated by considering the deflections* $\boldsymbol{x}_1$, *the velocities* $\boldsymbol{x}_2$, *and the temperatures* $\boldsymbol{x}_3$ *at the tip of the cantilevered MEMS. This is done by transforming the states with*

$$\bar{x}_{1,i} = \phi_{1,i}(l_1)x_{1,i}, \qquad \bar{x}_{2,i} = \phi_{1,i}(l_1)x_{2,i}, \qquad \bar{x}_{3,i} = \phi_{2,i}(l_1)x_{3,i},$$

so that the MEMS at the tip is governed by

$$\begin{aligned}
\dot{\bar{\boldsymbol{x}}}_1 &= \bar{\boldsymbol{x}}_2, && t>0, \quad \bar{\boldsymbol{x}}_1(0) = \bar{\boldsymbol{x}}_{10},\\
\dot{\bar{\boldsymbol{x}}}_2 &= \left(\bar{\mathcal{J}}_{\mathrm{R},2} + \bar{\mathcal{J}}_{\mathrm{R},3}\right)\bar{\boldsymbol{x}}_1 + \bar{\mathcal{J}}_{\mathrm{R},4}\bar{\boldsymbol{x}}_2 + \bar{\mathcal{J}}_{\mathrm{R},5}\bar{\boldsymbol{x}}_3 + \bar{\mathcal{J}}_{\mathrm{R},6}F_{\mathrm{ex}}, && t>0, \quad \bar{\boldsymbol{x}}_2(0) = \bar{\boldsymbol{x}}_{20},\\
\dot{\bar{\boldsymbol{x}}}_3 &= \bar{\mathcal{J}}_{\mathrm{G},2}\bar{\boldsymbol{x}}_2 + \bar{\mathcal{J}}_{\mathrm{G},3}\bar{\boldsymbol{x}}_3 + \bar{\mathcal{J}}_{\mathrm{G},4}u_{\mathrm{act}}^2, && t>0, \quad \bar{\boldsymbol{x}}_3(0) = \bar{\boldsymbol{x}}_{30},\\
y &= \bar{\mathcal{J}}_{\mathrm{R},y}\bar{\boldsymbol{x}}_1, && t\geq 0.
\end{aligned}$$

Here, the matrices are given by

$$\begin{aligned}
\bar{\mathcal{J}}_{\mathrm{R},2,ij} &= (\mathcal{J}_{\mathrm{R},1}^{-1})_{ij}\mathcal{J}_{\mathrm{R},2,ij}, & \bar{\mathcal{J}}_{\mathrm{R},3,ij} &= (\mathcal{J}_{\mathrm{R},1}^{-1})_{ij}\mathcal{J}_{\mathrm{R},3,ij},\\
\bar{\mathcal{J}}_{\mathrm{R},4,ij} &= (\mathcal{J}_{\mathrm{R},1}^{-1})_{ij}\mathcal{J}_{\mathrm{R},4,ii}, & \bar{\mathcal{J}}_{\mathrm{R},5,ij} &= \frac{\phi_{2,j}(l_1)}{\phi_{1,i}(l_1)}(\mathcal{J}_{\mathrm{R},1}^{-1})_{ij}\mathcal{J}_{\mathrm{R},5,ij},\\
\bar{\mathcal{J}}_{\mathrm{R},6,i} &= \frac{1}{\phi_{1,i}(l_1)}\sum_{j=1}^{n_1}(\mathcal{J}_{\mathrm{R},1}^{-1})_{ij}\mathcal{J}_{\mathrm{R},6,j}, & \bar{\mathcal{J}}_{\mathrm{R},y,i} &= \phi_{1,i}(l_1)\mathcal{J}_{\mathrm{R},y,i},\\
\bar{\mathcal{J}}_{\mathrm{G},2,ij} &= \frac{\phi_{1,j}(l_1)}{\phi_{2,i}(l_1)}(\mathcal{J}_{\mathrm{G},1}^{-1})_{ij}\mathcal{J}_{\mathrm{G},2,ij}, & \bar{\mathcal{J}}_{\mathrm{G},3,ij} &= (\mathcal{J}_{\mathrm{G},1}^{-1})_{ij}\mathcal{J}_{\mathrm{G},3,ij},\\
\bar{\mathcal{J}}_{\mathrm{G},4,i} &= \frac{1}{\phi_{2,i}(l_1)}\sum_{j=1}^{n_2}(\mathcal{J}_{\mathrm{G},1}^{-1})_{ij}\mathcal{J}_{\mathrm{G},4,j}, & &
\end{aligned}$$

where $(\mathcal{J}_{\mathrm{R},1}^{-1})_{ij}$ *and* $(\mathcal{J}_{\mathrm{G},1}^{-1})_{ij}$ *denote the i-th column and the j-th row of* $\mathcal{J}_{\mathrm{R},1}^{-1}$ *and* $\mathcal{J}_{\mathrm{G},1}^{-1}$, *respectively. The comparison between the parameters are shown in Table 5.2. It turns out that the time*

Table 5.2.: Comparison between the identified and the computed parameters of the first mode of the MEMS model.

Parameter	Experiment	Theory		
	Mode 1	Mode 1	Mode 2	Mode 3
$\bar{\mathcal{J}}_{\mathrm{R},2,ii}/c_1$ $\frac{1}{\mathrm{s}^2}$	7.9604×10^9	$7.42 \times 10^9 - 8.159 \times 10^9$	/	/
$\bar{\mathcal{J}}_{\mathrm{G},2,ii}/\beta$ $\frac{1}{\mathrm{s}}$	1006.6	$803.774 - 1239.565$	$7,233 - 11,156$	$20,094 - 30,989$
$\bar{\mathcal{J}}_{\mathrm{R},5,ij}/\alpha$ $\frac{\mathrm{m}}{\mathrm{s}^2\cdot\mathrm{K}}$	749.37	$824.64 - 1083.24$	$1222.24 - 1605.54$	$678.74 - 891.59$
$\bar{\mathcal{J}}_{\mathrm{G},4,ij}/\zeta$ $\frac{\mathrm{K}}{\mathrm{s}\cdot\mathrm{V}^2}$	68,141	$33,980 - 52,447$	$11,327 - 17,482$	$6,796 - 10,489$
$\bar{\mathcal{J}}_{\mathrm{R},5,ij}\bar{\mathcal{J}}_{\mathrm{G},4,ij}/\alpha\zeta$ $\frac{\mathrm{Mm}}{\mathrm{s}^3\cdot\mathrm{V}^2}$	51.06	$28.02 - 56.81$	$13.84 - 28.07$	$4.6127 - 9.3519$

constants c_1 and β are in between the minimum and maximum value of $\bar{\mathcal{J}}_{\mathrm{R},2,ii}$ and $\bar{\mathcal{J}}_{\mathrm{G},2,ii}$. In contrast to this, the transfer factors α and ζ are not predicted by the theoretical parameters $\bar{\mathcal{J}}_{\mathrm{R},5,ij}$ and $\bar{\mathcal{J}}_{\mathrm{G},4,ij}$. Moreover, the product $\alpha\zeta$ has to be larger than the product of the theoretical parameters as the equilibrium cannot be reproduced by the approximation (5.35) *with $n_1 = n_2 = 1$. This comes form the fact that the experimental model* (5.36) *is obtained by truncating the approximation* (5.35) *after the first mode and fitting the measurements onto the parameters. Hence, the contribution of the higher modes have to be compensated by the transfer factors α and ζ.*

6. Bifurcation and Tunability Analysis of the MEMS

In this chapter, the dynamics of a bio-inspired oscillator model consisting of the MEMS model and a high pass filter is investigated by analyzing the bifurcations in the oscillator from Chapter 5. The controller design proposed in Chapter 3 is employed on this oscillator model. With this, the results of the controller design for the Andronov-Hopf oscillator can be compared with a more complicated model. The chapter is structured as follows: First, preliminaries are introduced. Second, the bifurcations induced by proportional feedback are analyzed. It is demonstrated that two controllable Andronov-Hopf bifurcations are induced by assigning the feedback strength accordingly. Third, as the oscillator exhibits Andronov-Hopf bifurcations, the controller of the MEMS is extended to a network of injectively coupled MEMS, two diffusively coupled MEMS, and a (single) MEMS with delayed feedback to verify the results of Chapter 3. In particular, the tunability enhancement of the characteristic frequency of these controllers are compared to the enhancements for the Andronov-Hopf oscillator.

6.1. Preliminaries

Subsequently, the bio-inspired oscillator model consisting of the MEMS model and a high pass filter is introduced and it is linearized around its equilibrium.

6.1.1. Mathematical Model of the Bio-Inspired Oscillator

The considered oscillator model is based on the MEMS model (5.36) and an additional high pass filter to remove the offset of the output of the MEMS. The high pass filter given by $g_{\mathrm{HP}}(s) = Ts/(1+Ts)$ with the time constant $T > 0$. The output of the high pass is then

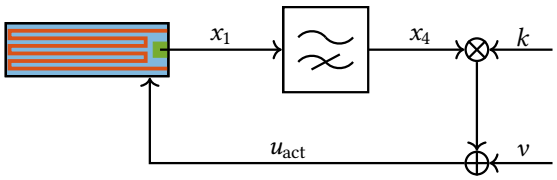

Figure 6.1.: Sketch of the setup represented by the bio-inspired oscillator.

forwarded into the FPGA, where it can be amplified by the feedback strength $k \in \mathbb{R}$ and it can be added with additional signals $v(t) \in \mathbb{R}$. The resulting signal $u_{\text{act}} = kx_4 + v$ is the fed into the thermal actuator. A sketch of this setup is depicted in Figure 6.1. With these considerations,the bio-inspired oscillator model is governed by

$$\dot{\boldsymbol{x}} = \boldsymbol{f}(\boldsymbol{x}, v), \qquad t > 0, \qquad \boldsymbol{x}(0) = \boldsymbol{x}_0, \tag{6.1a}$$

$$y = h(\boldsymbol{x}) = x_4, \qquad t \geq 0 \tag{6.1b}$$

with

$$\boldsymbol{f}(\boldsymbol{x}, v) = \begin{bmatrix} x_2 \\ -c_1 x_1 - c_3 x_1^3 - \mu x_2 + \alpha x_3 \\ -\beta x_3 + \zeta (k x_4 + v)^2 \\ -\frac{1}{T} x_4 + \kappa x_2 \end{bmatrix}, \tag{6.1c}$$

the state vector $\boldsymbol{x}(t) = [x_1(t), x_2(t), x_3(t), x_4(t)]^{\mathrm{T}} \in \mathbb{R}^4$, the output $y(t) \in \mathbb{R}$. The state vector composed of the deflection $x_1(t) \in \mathbb{R}$, the velocity $x_2(t) \in \mathbb{R}$, the temperatures $x_3(t) \in \mathbb{R}$ and the voltage of the high pass $x_4(t) \in \mathbb{R}$. Additional parameters are given by the spring constants $c_1 = \omega_0^2 > 0$, $c_3 \geq 0$, the damping $\mu = \omega_0 / Q_0 > 0$, the natural frequency $\omega_0 > 0$, the Q-factor $Q_0 > 0$, the transfer factors $\alpha > 0$, $\zeta = \gamma / R^2 > 0$, $\kappa > 0$, $\gamma > 0$, the resistance $R > 0$, the time constants $\beta > 0$, and initial conditions $\boldsymbol{x}_0 \in \mathbb{R}^4$.

6.1.2. Linearization of the Oscillator Model

To simplify the bifurcation analysis, the mathematical model (6.1) is linearized around an steady state.

Lemma 6.1 ([155]) *Let $v(t) = u_{\text{DC}} \in \mathbb{R}$. Then the oscillator* (6.1) *has a unique steady state given by*

$$\boldsymbol{x}_{\text{eq}} = \begin{bmatrix} \sqrt{\frac{4p}{3}} \sinh\left(\frac{1}{3} \operatorname{arsinh}\left(\frac{q}{2}\sqrt[3]{\frac{3}{p}}\right)\right) & 0 & \frac{\zeta}{\beta} u_{\text{DC}}^2 & 0 \end{bmatrix}^{\mathrm{T}} \tag{6.2}$$

with the coefficients $p = \frac{c_1}{c_3}$, $q = -\frac{\alpha\zeta}{\beta c_3} u_{\text{DC}}^2$.

Proof. To prove the claim, the steady state $(\boldsymbol{x}_{\text{eq}}, u_{\text{DC}})$ of (6.1) is analyzed by following Definition 2.1. Considering $\boldsymbol{f}(\boldsymbol{x}_{\text{eq}}, v)) = \boldsymbol{0}$, the steady states are determined by solving

$$0 = x_{2,\text{eq}}, \tag{6.3a}$$

$$0 = -c_1 x_{1,\text{eq}} - c_3 x_{1,\text{eq}}^3 - \mu x_{2,\text{eq}} + \alpha x_{3,\text{eq}}, \tag{6.3b}$$

$$0 = -\beta x_{3,\text{eq}} + \zeta (k x_{4,\text{eq}} + u_{\text{DC}})^2, \tag{6.3c}$$

$$0 = -\frac{1}{T} x_{4,\text{eq}} + \kappa x_{2,\text{eq}}. \tag{6.3d}$$

From (6.3a), (6.3c) and (6.3d), the values $x_{2,\mathrm{eq}}$, $x_{3,\mathrm{eq}}$ and $x_{4,\mathrm{eq}}$ follow immediately. After inserting these solutions into (6.3b), the cubic polynomial

$$P_{\mathrm{eq}}(x_{1,\mathrm{eq}}) = x_{1,\mathrm{eq}}^3 + p x_{1,\mathrm{eq}} - q \tag{6.4}$$

is obtained with the coefficients $p = \frac{c_1}{c_3}$ and $q = \frac{\alpha\zeta}{\beta c_3} u_{\mathrm{DC}}^2$. Note that a cubic polynomial has in general 3 different roots. However, only the real-valued roots are of interest here. Using Proposition 2.1 and inserting p and q into the polynomial discriminant (2.11b) yields

$$D_{\mathrm{eq}} = \frac{c_1^3}{c_3^3} + \frac{\alpha^2\zeta^2}{\beta^2 c_3^2} u_{\mathrm{DC}}^4 > 0$$

Comparing this with (2.11a) shows that (6.4) has only one unique, real-valued solution, which implies that (6.1) has only one unique equilibrium. The value $x_{1,\mathrm{eq}}$ can be determined by the sinh-solution of a cubic equation following [57] since $p > 0$. This yields

$$x_{1,\mathrm{eq}} = \sqrt{\frac{4p}{3}} \sinh\left(\frac{1}{3}\operatorname{arsinh}\left(\frac{q}{2}\sqrt[3]{\frac{3}{p}}\right)\right)$$

and concludes the proof. □

Following Theorem 2.2, the system matrix, the input matrix, and the output matrix of the linearization of (6.1) around the steady state (6.2) reads

$$A = \frac{\partial f}{\partial \boldsymbol{x}}(\boldsymbol{x}_{\mathrm{eq}}, \boldsymbol{u}_{\mathrm{eq}}) = \begin{bmatrix} 0 & 1 & 0 & 0 \\ -\Omega^2 & -\mu & \alpha & 0 \\ 0 & 0 & -\beta & 2\zeta u_{\mathrm{DC}} k \\ 0 & \kappa & 0 & -\frac{1}{T} \end{bmatrix}, \tag{6.5a}$$

$$\boldsymbol{b}^{\mathrm{T}} = \frac{\partial f}{\partial v}^{\mathrm{T}}(\boldsymbol{x}_{\mathrm{eq}}, \boldsymbol{u}_{\mathrm{eq}}) = \begin{bmatrix} 0 & 0 & 2\zeta & 0 \end{bmatrix}, \tag{6.5b}$$

$$\boldsymbol{c} = \frac{\partial h}{\partial \boldsymbol{x}} = \begin{bmatrix} 0 & 0 & 0 & 1 \end{bmatrix} \tag{6.5c}$$

with the natural frequency $\Omega = (c_1 + 3c_3 x_{1,\mathrm{eq}}^2)^{1/2}$.

To conclude the preliminaries, the characteristic polynomial and the transfer matrix of the linearization of the oscillator (6.1) around (6.2) are derived. Note that the transfer function of the open loop system is given by $g(s)|_{k=0} = \boldsymbol{c}(sI - A|_{k=0})^{-1}\boldsymbol{b}$. The characteristic polynomial and the transfer function read

$$P(\lambda) = \lambda^4 + a_3\lambda^3 + a_2\lambda^2 + (a_1 - b_1 k)\lambda + a_0, \tag{6.6a}$$

$$g(s) = \frac{b_1 s}{s^4 + a_3 s^3 + a_2 s^2 + (a_1 - b_1 k)s + a_0}, \tag{6.6b}$$

with the coefficients

$$a_0 = \frac{\beta\Omega^2}{T}, \tag{6.7a}$$

$$a_1 = \beta\Omega^2 + \frac{\beta\mu}{T} + \frac{\Omega^2}{T}, \tag{6.7b}$$

$$a_2 = \frac{\beta}{T} + \beta\mu + \frac{\mu}{T} + \Omega^2, \tag{6.7c}$$

$$a_3 = \beta + \mu + \frac{1}{T}, \tag{6.7d}$$

$$b_1 = 2\alpha\kappa\zeta u_{\mathrm{DC}}. \tag{6.7e}$$

6.2. Bifurcation and Tunability Analysis of the Bio-Inspired Oscillator

Subsequently, the bifurcations and frequency tunability of the bio-inspired oscillator model (6.1) under different controllers are analyzed.

6.2.1. Frequency Tunability induced by DC-Voltage

In the following, the influence of the DC-voltage u_{DC} on the natural frequency of the bio-inspired oscillator (6.1) is analyzed. Following Lemma 6.2, it is implied that the natural Ω can be increased by assigning the DC-voltage u_{DC} accordingly. This is visualized by evaluating the (normalized) frequency $f = \Omega/(2\pi)$ from (6.5a) as a function of the DC-voltage u_{DC}. The parameters used for the numerical simulation are summarized in Table A.3, respectively.

The frequency tunability of (6.1) is illustrated in Figure 6.2 and it can be explained by considering the geometry of the clamped-clamped MEMS, which can be separated into a sensing part and a tuning part (see Figure 6.3). With this, a geometric nonlinearity is induced, so that the frequency becomes tunable [47]. Other designs to induce geometric nonlinearities in a MEMS are discussed, e.g., in [3, 30, 77, 78, 79, 133, 134, 143].

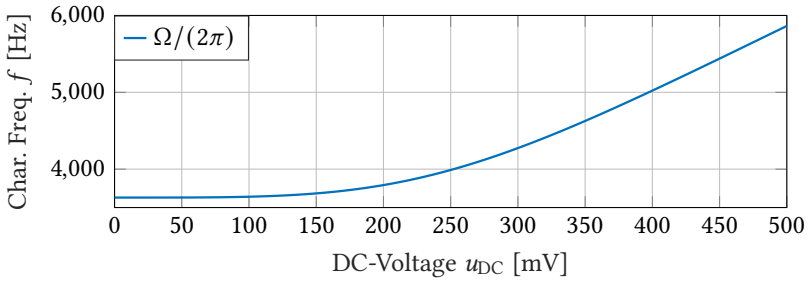

Figure 6.2.: Natural frequency Ω in terms of the DC-voltage u_{DC}.

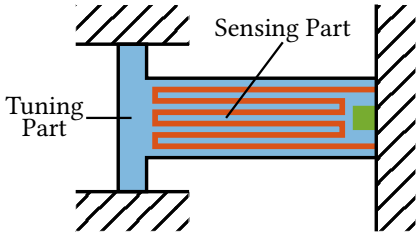

Figure 6.3.: Geometry of the clamped-clamped MEMS.

6.2.2. Emergence of Controllable Andronov-Hopf Bifurcations

To employ the controllers designed in Chapter 3, it has to be shown that the oscillator (6.1) exhibits a controllable Andronov-Hopf bifurcation. This is shown in the subsequent theorem.

Theorem 6.1 ([153]) *The system* (6.1) *undergoes two Andronov-Hopf bifurcations depending on the feedback gain k with the critical points and the characteristic frequencies given by*

$$k_{\mathrm{H}}^{\pm} = \frac{2a_1 - a_2 a_3 \pm a_3\sqrt{a_2^2 - 4a_0}}{2b_1}, \tag{6.8a}$$

$$\omega_{\mathrm{C}}^{\pm} = \sqrt{\frac{a_2 \pm \sqrt{a_2^2 - 4a_0}}{2}}. \tag{6.8b}$$

Proof. The proof follows the necessary condition (H1) and the crossing condition (H2) of the Hopf Theorem (see Theorem 2.9).

(H1) The critical feedback strength k_{H}^{+} and k_{H}^{-} and the characteristic frequencies ω_{C}^{+} and $\omega_{\mathrm{C}}^{-}$are derived by comparing the characteristic polynomial (6.6a) with a quartic polynomial with a pair of complex conjugated, purely imaginary zeros. This quartic polynomial is given by

$$P_{\mathrm{H},4}(\lambda) = (\lambda^2 + \omega_{\mathrm{C}}^2)(\lambda^2 + p_{\mathrm{H}}\lambda + q_{\mathrm{H}})$$

with the coefficients $p_{\mathrm{H}}, q_{\mathrm{H}} \in \mathbb{R}$ and the characteristic frequency $\omega_{\mathrm{C}} > 0$. Comparing the coefficients between both polynomials yields

$$a_0 = q_{\mathrm{H}}\omega_{\mathrm{C}}^2, \tag{6.9a}$$

$$a_1 + b_1 k_{\mathrm{H}} = p_{\mathrm{H}}\omega_{\mathrm{C}}^2, \tag{6.9b}$$

$$a_2 = q_{\mathrm{H}} + \omega_{\mathrm{C}}^2, \tag{6.9c}$$

$$a_3 = p_{\mathrm{H}}. \tag{6.9d}$$

After solving the nonlinear system of equation (6.9), the coefficients $p_{\mathrm{H}}, q_{\mathrm{H}}$, the characteristic frequency ω_{C}, and the critical feedback strength k_{H} are obtained as

$$p_{\mathrm{H}} = a_3, \qquad q_{\mathrm{H}}^{\pm} = \frac{a_2 \pm \sqrt{a_2^2 - 4a_0}}{2},$$
$$k_{\mathrm{H}}^{\pm} = \frac{2a_1 - a_2 a_3 \pm a_3\sqrt{a_2^2 - 4a_0}}{2b_1}, \qquad \omega_{\mathrm{C}}^{\pm} = \sqrt{\frac{a_2 \pm \sqrt{a_2^2 - 4a_0}}{2}}.$$

(H2) To characterize the limit cycle the location of the eigenvalues and the crossing condition are investigated. The location of the eigenvalues is analyzed by showing that the quadratic polynomial $p_2(\lambda) = \lambda^2 + p_{\mathrm{H}}\lambda + q_{\mathrm{H}}$ satisfies the necessary and sufficient condition for a Hurwitz polynomial, i.e., $p_{\mathrm{H}} > 0$ and $q_{\mathrm{H}} > 0$. As $p_{\mathrm{H}} \in \mathbb{R}$, $q_{\mathrm{H}} \in \mathbb{R}$, $a_2 > 0$, and $a_0 > 0$ has to be satisfied, it is implied that that $a_2^2 > 4a_0$ holds true. Hence, it follows that $p_{\mathrm{H}} > 0$ and $q_{\mathrm{H}} > 0$ is satisfied, so that $p_2(\lambda)$ is a Hurwitz polynomial.

Second, the crossing condition is investigated by analyzing the sensitivity of the complex conjugated eigenvalues located on the imaginary axis. The sensitivity reads

$$d_{\mathrm{H}} = \mathrm{Re}\left.\frac{\mathrm{d}\lambda}{\mathrm{d}k}\right|_{\lambda=\mathrm{i}\omega_{\mathrm{C}}} = \frac{(a_2 - \omega_{\mathrm{C}}^2)\, b_1 \omega_{\mathrm{C}}^2}{(a_3\omega_{\mathrm{C}}^2 - kb_1 - a_2)^2 + (\omega_{\mathrm{C}}^2 - a_2)^2\omega_{\mathrm{C}}^2}. \tag{6.10}$$

Note that the sign of (6.10) is determined by its numerator since the denominator is always positive. Thus, the sign of (6.10) is always positive, if

$$a_2 - \omega_{\mathrm{C}}^2 = \frac{a_2 \mp \sqrt{a_2^2 - 4a_0}}{2} > 0.$$

This is satisfied, since $a_2^2 > 4a_0$ holds true. □

6.3. Frequency Tunability Enhancing Controller Design

As the oscillator (6.1) exhibits two controllable Andronov-Hopf bifurcations, the controller developed in Chapter 3 can be employed to enhance the frequency tunability of the oscillator, if the bifurcation parameter k is in the neighborhood of the critical point $k_{\mathrm{H}}^{\pm}$. Subsequently, the tunability enhancement of the two coupled oscillators of the form (6.1) and an oscillator with a controllable delay is analyzed.

6.3.1. Controller based on Injectively Coupling

In the following, the frequency tunability enhancements by coupling oscillators of the form (6.1) injectively is analyzed. A sketch of two injectively coupled oscillator is illustrated in Figure 6.4 and the i-th Andronov-Hopf oscillator is governed by

$$\begin{aligned} \dot{\boldsymbol{x}}_i &= \boldsymbol{f}_i(\boldsymbol{\chi}), & t &> 0, & \boldsymbol{x}_i(0) &= \boldsymbol{x}_{i,0}, \\ y &= x_{4,i}, & t &\geq 0 \end{aligned}$$

with

$$\boldsymbol{f}_i(\boldsymbol{\chi}) = \begin{bmatrix} x_{2,i} \\ -c_{1,i}x_{1,i} - c_{3,i}x_{1,i}^3 - \mu_i x_{2,i} + \alpha_i x_{3,i} \\ -\beta_i x_{3,i} + \zeta_i \left(u_{\mathrm{DC}} + \sum_{j=1}^{n} k_{ij} x_{4j} \right)^2 \\ -\frac{1}{T_i} x_{4,i} + \kappa_i x_{2,i} \end{bmatrix}.$$

the state vector $\boldsymbol{\chi} = [\boldsymbol{x}_1^{\mathrm{T}}, \boldsymbol{x}_2^{\mathrm{T}}, \ldots, \boldsymbol{x}_n^{\mathrm{T}}]^{\mathrm{T}}$ of the network, the feedback matrix $K = [k_{ij}]_{i,j=1,\ldots,n}$, and the number $n \in \mathbb{N}$ of oscillator for all $i = 1, 2, \ldots, n$. To analyze the tunability enhancements, the necessary conditions (H1) of the Hopf Theorem (see Theorem 2.9) is investigated. The analysis is structured as follows: First, conditions are derived to determine the critical points of two coupled groups of (arbitrary) oscillators. To achieve this, it is asserted that both groups of oscillator, see, e.g., Definition 3.2, exhibit at least one Andronov-Hopf bifurcation, if the oscillators are uncoupled. Second, the emergence of Andronov-Hopf bifurcations of two coupled groups consisting of the bio-inspired oscillator (6.1a) are investigated. It turns out that the necessary conditions for the emergence of an Andronov-Hopf bifurcation are satisfied in three cases. Third, it is analyzed whether these three bifurcation points induce a Hopf-Hopf bifurcation, see, e.g., [48, 76].

Theoretical Results

The critical points of two coupled groups are determined by exploiting the structure of the linearization of (6.1). In particular, the exploited structure is induced in the following way:

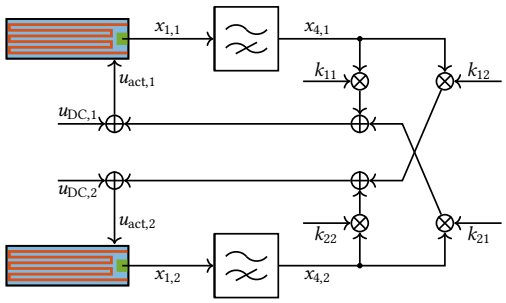

Figure 6.4.: Sketch of two injectively coupled, bio-inspired oscillators (6.1).

Assumption 6.1 ([149]) *For a network composed of oscillators the following assumptions are imposed:*

(A1) The equilibria of the decoupled oscillators are invariant to coupling, i.e., they remain the sole equilibria of the coupled nonlinear system, and the system matrix is influenced by the adjacency matrix.

(A2) For each uncoupled oscillator there exists a critical value $k_{\mathrm{H},ii}$ of the self-feedback strength so that it undergoes at least one Andronov-Hopf bifurcation.

Assumption (A1) implies that the transfer matrix of the coupled system is obtained by coupling the transfer functions of the uncoupled oscillators. A consequence of (A2) is that the linearized system matrix A_{ii} has a pair of complex conjugated eigenvalues on the imaginary axis for the feedback strength $k_{ii} = k_{\mathrm{H},ii}$. With this, the necessary condition (H1) of the Hopf Theorem (see Theorem 2.9) for two coupled groups of oscillators is summarized as follows.

Theorem 6.2 ([149]) *Consider two groups composed of $n_1 \in \mathbb{N}$ and $n_2 \in \mathbb{N}$ oscillators, respectively, so that the dimension of the coupled network is $n = n_1 + n_2$. Let the transfer function of an individual (linearized) oscillator (with respect to its controllable input), the self-coupling matrices, and the cross-coupling matrices be given by $g_i(s) \in \mathbb{C}$, $K_{ii} = k_{ii} I \in \mathbb{R}^{n_i \times n_i}$ with $k_{ii} \in \mathbb{R}$, and $K_{ij} \in \mathbb{R}^{n_i \times n_j}$ for all $i, j = 1, 2$ and $i \neq j$. Assume that the eigenvalues $\lambda_k \in \mathbb{R}$, $k = 1, \ldots, n_2$ of the matrix $K_{21}K_{12} \in \mathbb{R}^{n_2 \times n_2}$ are real-valued and the bifurcation parameters. Then the bifurcation points λ_{H} of the Andronov-Hopf bifurcations of the two groups of oscillators are determined by*

$$\lambda_{\mathrm{H}} = q_{11}^2 + q_{12}^2 - q_{21}^2 - q_{22}^2, \tag{6.11}$$

with the constants $q_{11}, q_{12}, q_{21}, q_{22} \in \mathbb{R}$ computed from

$$0 = g_1(\mathrm{i}\omega_{\mathrm{C}}) - g_2(\mathrm{i}\omega_{\mathrm{C}}) + [k_{11} - k_{22} + 2(q_{21} - \mathrm{i}q_{12})] g_1(\mathrm{i}\omega_{\mathrm{C}}) g_2(\mathrm{i}\omega_{\mathrm{C}}), \tag{6.12a}$$

$$0 = 1 - [k_{11} + q_{11} + q_{21} - \mathrm{i}\,(q_{12} + q_{22})]\, g_1(\mathrm{i}\omega_{\mathrm{C}}), \tag{6.12b}$$

$$0 = q_{11} q_{22} - q_{21} q_{12} \tag{6.12c}$$

with $\omega_{\mathrm{C}} \in \mathbb{R}$ the characteristic frequency at the critical point.

Remark 6.1 *Eqn.* (6.11) *must be interpreted in the sense that at least one eigenvalue λ_k of the matrix $K_{21}K_{12}$ must take the value λ_{H}. Note that this also enables us to deduce information about the topology.*

Proof. To prove the claim, it has to be shown that the transfer matrix of the network has a complex conjugated pair of eigenvalues on the imaginary axis. This is done in 3 steps: First, the transfer matrix from output to input of the network is derived depending on the coupling in terms of the adjacency matrix K. Second, the adjacency matrix K is shifted by a diagonal matrix $Q \in \mathbb{C}^{n \times n}$ so that $\tilde{K} = K + Q$ becomes singular. Third, this shift introduces a linear pseudo-feedback into each transfer function. This is then used to show

that the transfer function of the network has a complex conjugated pair of eigenvalues on the imaginary axis in terms of the eigenvalues λ_{H} of the matrix $K_{12}K_{21}$.

Denote the self-coupling matrix and cross-coupling matrix of the two groups by $K_{11} = k_{11}I$, $K_{22} = k_{22}I$, K_{12} and K_{21}. Then the transfer matrix of the coupled groups from output $\boldsymbol{y} = [y_1, y_2, \ldots, y_n]^{\mathrm{T}}$ to input $\Delta\boldsymbol{v} = [\Delta v_1, \Delta v_2, \ldots, \Delta v_n]^{\mathrm{T}}$ reads

$$H(s) = \begin{bmatrix} \frac{1-k_{11}g_1(s)}{g_1(s)} I_{n_1} & 0 \\ 0 & \frac{1-k_{22}g_2(s)}{g_2(s)} I_{n_2} \end{bmatrix} - \underbrace{\begin{bmatrix} 0 & K_{12} \\ K_{21} & 0 \end{bmatrix}}_{=K_{\mathrm{ND}}}.$$

By choosing this rather uncommon transfer matrix the effects of the cross-coupling K_{ND} can be investigated directly, since the zeros of $H(s)$ are the poles and thus at least a subset of the eigenvalues of the network. Hence, the aim is to show that $H(s)$ has two complex conjugated zeros on the imaginary axis. To express this behavior, assume that there exists an asymmetric shift given by

$$\tilde{K} = K_{ND} - \underbrace{\begin{bmatrix} (q_1^* + q_2^*) I_{n_1} & 0 \\ 0 & (q_1 - q_2) I_{n_2} \end{bmatrix}}_{=Q} \tag{6.13}$$

with the constants $q_1 = q_{11} + \mathrm{i}q_{12} \in \mathbb{C}$, $q_2 = q_{21} + \mathrm{i}q_{22} \in \mathbb{C}$. Herein, z^* denotes the complex conjugate of a complex number $z \in \mathbb{C}$. To satisfy the necessary condition of an Andronov-Hopf bifurcation, it has to be imposed that $\tilde{K}$ is singular, such that a rank drop argument can be used for the transfer matrix $H(s)$. Following Lemma 3.2 the determinant of $\tilde{K}$ can be simplified to

$$\det \tilde{K} = \frac{n_1}{n_2} \det \left[\left(q_1^* + q_2^*\right) (q_1 - q_2)\, I_{n_2} - K_{21}K_{12} \right].$$

Assuming that at least one eigenvalue of $H(s)$ is not influenced by the cross-coupling matrices implies $\det \tilde{K} = 0$. This is achieved by setting $\left(q_1^* + q_2^*\right)(q_1 - q_2)$ to the eigenvalues $\lambda_k \in \sigma(K_{21}K_{12})$ of $K_{21}K_{12}$ for all $k = 1, , \ldots, n_2$, which yields

$$\lambda_k = q_{11}^2 + q_{12}^2 - q_{21}^2 - q_{22}^2 + \mathrm{i}2(q_{12}q_{21} - q_{11}q_{22})$$

where the imaginary part must vanish since the eigenvalues are assumed to be real-valued. Hence, $q_{11}q_{22} = q_{12}q_{21}$ must be satisfied implying (6.11).

Now, it has to be shown that the transfer matrix $H(s)$ is locally singular for $s \in \{\pm\mathrm{i}\omega_{\mathrm{C}}\}$[1]. For this, the Jordan decomposition of $\tilde{K} = W^*\Lambda W$ is used with the Jordan matrix $\Lambda \in \mathbb{R}^{n\times n}$

[1]Without loss of generality, it can be assumed that $s = \mathrm{i}\omega_{\mathrm{C}}$, since the transfer matrix of the network $H(s)$ is composed of rational functions $g_1(s)$ and $g_2(s)$ with real-valued coefficients, so that complex-valued zeros and poles can only occur in complex conjugated pairs. Particularly, this fact is not changed by adding or subtracting the complex-valued matrix Q, since $H(s)$ is not changed by these manipulations.

and a transformation matrix $W \in \mathbb{R}^{n\times n}$ [75]. For the output-to-input transfer function of the network, this implies

$$\begin{aligned} H(s) &= \begin{bmatrix} \frac{1-k_{11}g_1(s)}{g_1(s)} I_{n_1} & 0 \\ 0 & \frac{1-k_{22}g_2(s)}{g_2(s)} I_{n_2} \end{bmatrix} - Q - \tilde{K} \\ &= \begin{bmatrix} \frac{1-k_{11}g_1(s)}{g_1(s)} I_{n_1} & 0 \\ 0 & \frac{1-k_{22}g_2(s)}{g_2(s)} I_{n_2} \end{bmatrix} - Q - W^* \Lambda W \end{aligned}$$

By imposing

$$\begin{aligned} &\begin{bmatrix} \frac{1-k_{11}g_1(s)}{g_1(s)} I_{n_1} & 0 \\ 0 & \frac{1-k_{22}g_2(s)}{g_2(s)} I_{n_2} \end{bmatrix} - Q \\ &= \begin{bmatrix} \frac{1-(k_{11}+q_1^*+q_2^*)g_1(s)}{g_1(s)} I_{n_1} & 0 \\ 0 & \frac{1-(k_{22}+q_1-q_2)g_2(s)}{g_2(s)} I_{n_2} \end{bmatrix} \overset{!}{=} h(s) I_n, \qquad \forall s \in \{\pm \mathrm{i}\omega_\mathrm{C}\}, \end{aligned}$$

the transfer matrix is simplified to

$$H(s) = W^* \left(h(s) I - \Lambda \right) W,$$

respectively. If $h(s)$ vanishes for $s \in \{\pm \mathrm{i}\omega_\mathrm{C}\}$, then $H(s)$ is singular, because Λ is singular for all $s \in \mathbb{C}$. This analysis implies the following conditions

$$\begin{aligned} 0 &= \frac{1 - \left[k_{11} + q_1^* + q_2^*\right] g_1(\mathrm{i}\omega_\mathrm{C})}{g_1(\mathrm{i}\omega_\mathrm{C})} - \frac{1 - \left[k_{22} + q_1 - q_2\right] g_2(\mathrm{i}\omega_\mathrm{C})}{g_2(\mathrm{i}\omega_\mathrm{C})}, \\ 0 &= 1 - \left[k_{22} + q_{11} - q_{21} + \mathrm{i}(q_{12} - q_{22})\right] g_2(\mathrm{i}\omega_\mathrm{C}), \end{aligned}$$

which can be rearranged into (6.12a) and (6.12b) thus concluding the proof. □

The condition imposed on the real-valued eigenvalues of the product of the cross-coupling matrices $K_{12}K_{21}$ and the self-coupling matrices K_{12} and K_{22} is fulfilled for a rather large classes of networks, e.g., if

- the network is undirected so that the adjacency matrix becomes symmetric, i.e., $K = K^\mathrm{T}$,
- the size of one group is 1.

Moreover, with similar arguments as in Theorem 6.2, the bifurcation point of identical oscillators in symmetric networks can be generalized, e.g., see [127, Proposition 1]. This is elaborated subsequently.

Proposition 6.1 ([149]) *Consider a single group consisting of $n \in \mathbb{N}$ oscillators and denote the self-coupling matrix by $K \in \mathbb{R}^{n\times n}$. In addition, assume that the Assumptions (A1) and (A2) are satisfied and that the eigenvalues of the self-coupling matrix $\lambda_i \in \sigma(K)$ are real-valued for all $i = 1, \ldots, n$. Then the critical points of each oscillator are given by $k_{\mathrm{H},i} = k + \lambda_i$.*

Proof. The proof follows the line of the proof of Theorem 6.2. However, in the case of one group the auxiliary matrix $Q \in \mathbb{C}^{n\times n}$ simplifies to a weighted identity matrix, i.e., $Q = qI_n$ with the weight $q \in \mathbb{R}$. Then by following the arguments of the proof of Theorem 6.2, the conditions

$$\tilde{K} = \det\left[qI_n - K\right], \tag{6.14}$$

$$G(s) = W^*\left(g(s)I - \Lambda\right)W \tag{6.15}$$

arise. Herein, the parameters are given by the Jordan decomposition $\tilde{K} = W^*\Lambda W$ and the transfer function $g(\lambda) \in \mathbb{C}$ of the oscillator. Thus, (6.14) and (6.15) have a rank drop, if $q = \lambda_i$ and $k_{\mathrm{H},i} = k + \lambda_i$ for all $i = 1, \ldots, n$. The critical point and the feedback strength of the oscillators are then given by $k_{\mathrm{H}} \in \mathbb{R}$ and $k \in \mathbb{R}$. This concludes the proof. □

Remark 6.2 *The results of Proposition 6.1 can be strengthened by assuming that the uncoupled oscillators are passive, i.e., the unforced oscillator possesses a stable limit cycle and the feedback system satisfies the dissipation inequality*

$$\dot{S} \leq (k - k_{\mathrm{H}})y^2 - yh(y) + y\Delta v$$

with a nonlinearity $h(y) \in \mathbb{R}$. Then the critical point of the network becomes unique, i.e., only the minimal eigenvalue changes the critical point, and the network admits a stable limit cycle. For more details, see [127].

Andronov-Hopf Bifurcation

After substituting (6.6b) into (6.12), taking the numerator and splitting it into real and imaginary part, the resulting equations read

$$0 = [b_{11}b_{21}(k_{11} - k_{22} + 2q_{21}) - a_{21}b_{11} + a_{11}b_{21}]\omega_{\mathrm{C}}^2 + (a_{23}b_{11} - a_{13}b_{21})\omega_{\mathrm{C}}^4, \tag{6.16a}$$

$$0 = (b_{11} - b_{21})\omega_{\mathrm{C}}^5 + (a_{12}b_{21} - a_{22}b_{11})\omega_{\mathrm{C}}^3 + 2b_{11}b_{21}q_{12}\omega_{\mathrm{C}}^2 + (a_{20}b_{11} - a_{10}b_{21})\omega_{\mathrm{C}}, \tag{6.16b}$$

$$0 = a_{13}\omega_{\mathrm{C}}^3 + [b_{11}(k_{11} + q_{11} + q_{21}) - a_{11}]\omega_{\mathrm{C}}, \tag{6.16c}$$

$$0 = \omega_{\mathrm{C}}^4 - a_{12}\omega_{\mathrm{C}}^2 - b_{11}(q_{12} + q_{22})\omega_{\mathrm{C}} + a_{10}, \tag{6.16d}$$

$$0 = q_{11}q_{22} - q_{21}q_{12}. \tag{6.16e}$$

In the following, two different scenarios are analyzed: First, the emergence of bifurcations of two identical groups with different self-feedback and second the general case, i.e., the network consists of two non-identical groups of oscillators of the form (6.1), are investigated.

Identical Oscillators In the case of identical groups, (6.16) is simplified significantly. In addition, it is asserted that the feedback strengths k_{11} and k_{22} are non-identical, so that two groups can be identified and Theorem 6.2 can be employed. This results in

$$0 = b_2^2(k_{11} - k_{22} + 2q_{21})\omega_C^2, \tag{6.17a}$$
$$0 = 2b_2^2 q_{12}\omega_C^2, \tag{6.17b}$$
$$0 = a_3\omega_C^3 + (b_2k_{11} + b_2q_{11} + b_2q_{21} - a_1)\omega_C, \tag{6.17c}$$
$$0 = \omega_C^4 - a_2\omega_C^2 - b_2(q_{12} + q_{22})\omega_C + a_0, \tag{6.17d}$$
$$0 = q_{11}q_{22} - q_{21}q_{12}. \tag{6.17e}$$

Solving (6.17a)-(6.17d) for q_{11}, q_{12}, q_{21}, and q_{22}, yields

$$q_{11} = \frac{a_3\omega_C^2 - a_1}{b_1} + \frac{\tilde{k}_{11} + \tilde{k}_{22}}{2}, \quad q_{12} = 0,$$
$$q_{21} = -\frac{\tilde{k}_{11} - \tilde{k}_{22}}{2}, \qquad q_{22} = \frac{\omega_C^4 - a_2\omega_C^2 + a_0}{b_1\omega_C}$$

with the shifted self-feedback strengths $\tilde{k}_{ii} = k_{ii} + \lambda_{ii}$ and $\lambda_{ii} \in \sigma(K_{ii})$ for all $i = 1, 2$. Substituting this into (6.17e) and taking the numerator, provides

$$0 = \left[2a_3\omega_C^2 - a_1 + b_1(\tilde{k}_{11} + \tilde{k}_{22})\right]\left[\omega_C^4 - a_1\omega_C^2 + a_0\right].$$

It hence follows that there are three different parameter configurations satisfying the necessary condition of the Andronov-Hopf bifurcation, i.e.,

$$\lambda_H^{(1)} = \frac{\left(\omega_{C,1}^4 - a_2\omega_{C,1}^2 + a_0\right)^2}{b_1^2\omega_{C,1}^2} - \frac{\left(\tilde{k}_{11} - \tilde{k}_{22}\right)^2}{4}, \qquad \omega_{C,1}^2 = \frac{2a_1 - b_1(\tilde{k}_{11} + \tilde{k}_{22})}{2a_3}, \tag{6.18a}$$

$$\lambda_H^{(2)} = \frac{a_3\omega_{C,2}^2 - a_1 + b_1\tilde{k}_{11}}{b_1}\frac{a_3\omega_{C,2}^2 - a_1 + b_1\tilde{k}_{22}}{b_1}, \qquad \omega_{C,2}^2 = \frac{a_2 + \sqrt{a_2^2 - 4a_0}}{2}, \tag{6.18b}$$

$$\lambda_H^{(3)} = \frac{a_3\omega_{C,3}^2 - a_1 + b_1\tilde{k}_{11}}{b_1}\frac{a_3\omega_{C,3}^2 - a_1 + b_1\tilde{k}_{22}}{b_1}, \qquad \omega_{C,3}^2 = \frac{a_2 - \sqrt{a_2^2 - 4a_0}}{2}. \tag{6.18c}$$

The critical points given by (6.18b) and (6.18c) are closely related to the critical points of a single oscillator as predicted from Proposition 6.1. This can be illustrated by imposing $k_{11} = k_{22} = k$. Then the critical point will be given by $\lambda_H = (k_H - k)^2$ with k_H given by (6.8a). However, an additional bifurcation given by (6.18a) emerges. The critical point is given by (6.18a) and it is created by coupling the oscillators of the form (6.1).

Non-Identical Oscillators In the case of two non-identical groups of oscillators of the form (6.1), (6.16a)-(6.16d) are solved for q_{11}, q_{12}, q_{22}, and ω_C. After substituting the results into (6.16e), a polynomial of 3rd degree arises, so that the two coupled groups of oscillator (6.1) have either one or three critical points. In particular, the emergence of three critical points is considered subsequently. This assumption can be explained in two ways. First, by interpreting one oscillator as two Andronov-Hopf oscillators. This can be done since Theorem 6.1 implies that (6.1) can converge to two different sub-manifold described by the Andronov-Hopf oscillator. Thus, it is reasonable to consider the simpler bifurcation behavior of n injectively coupled Andronov-Hopf oscillators. Then Lemma 3.1 suggests that $n-1$ different Andronov-Hopf bifurcation can be controlled with the eigenvalues of the adjacency matrix. Second, the results on two coupled groups of identical oscillators can be considered.

With these analogies, it is implied that a network of two coupled groups of oscillators of the form (6.1) has three critical points. Hence, the cubic polynomial is solved by the method proposed in [100]. The resulting equations for q_{11}, q_{12}, q_{21}, q_{22} and ω_C are summarized in Appendix B.2.

Example 6.1 *Subsequently, the results of Theorem 6.2 are verified for a network of two groups of oscillators of the form* (6.1)*. The topology is visualized in Figure 6.5 and the numerical parameters are depicted in Table A.4 in Appendix A. Each group is visualized by a different color of the vertex, so that the one group consists of $n_1 = 2$ and the other group consists of $n_2 = 4$, respectively. In addition, Figure 6.5 implies that the self-coupling and cross-coupling matrices are given by*

$$K_{11} = 0, \qquad K_{12} = \begin{bmatrix} k & 0 & 0 & 0 \\ k & k & k & k \end{bmatrix}^{\mathrm{T}}, \qquad K_{21} = \begin{bmatrix} \tilde{k} & 0 & 0 & 0 \\ k & k & k & k \end{bmatrix}, \qquad K_{22} = 0$$

with the coupling strengths $k \in [-8, 3]$ and $\tilde{k} = |k|$. It has to be stressed that this network is not symmetric and that the product between the cross-coupling matrices is given by

$$K_{21}K_{12} = \begin{bmatrix} k|k| & k|k| \\ k^2 & 4k^2 \end{bmatrix}$$

with the spectrum

$$\sigma(K_{21}K_{12}) = \left\{ \frac{k\left(|k| + 4k \pm \sqrt{16k^2 - 4k|k| + |k|^2}\right)}{2} \right\} \tag{6.19}$$

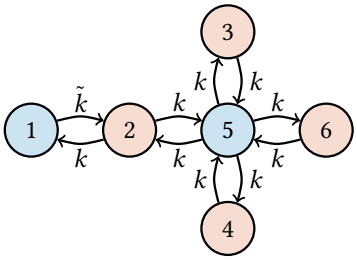

Figure 6.5.: Sketch of the network topology. Oscillators are colored in terms of the group they belong to.

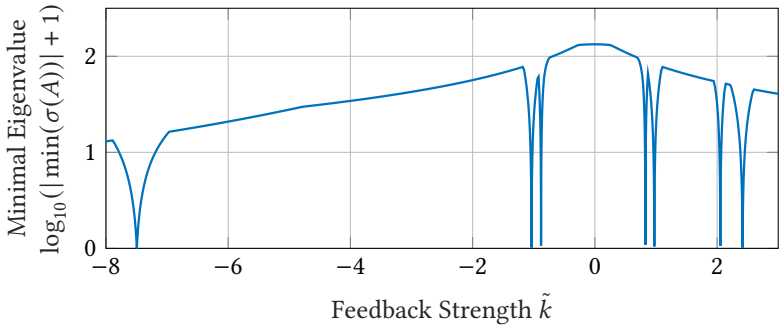

(a) Real part of the minimal eigenvalue of the system matrix A in terms of the coupling strengths $\tilde{k}$.

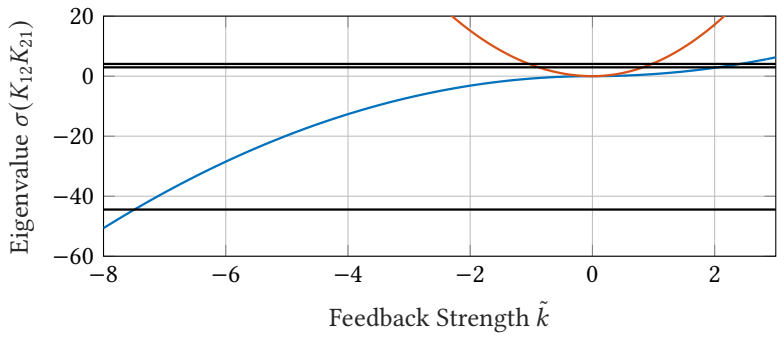

(b) Eigenvalues of the matrix $K_{21}K_{12}$ in terms of the coupling strengths $\tilde{k}$. Herein, the bifurcation points $\lambda_{\mathrm{H}}^{(i)}$, $i = 1, \ldots, 7$ are defined by the intersections of the blue and red curves with the critical points depicted black.

Figure 6.6.: Comparison between the real part of the minimal eigenvalue of the system matrix A and eigenvalues of matrix $K_{21}K_{12}$ in terms of the coupling strengths $\tilde{k}$.

Starting from $K_{21}K_{12}$ the characteristic polynomial is reduced to a quadratic polynomial. Thus, it is possible to determine the critical point analytically. In particular, there are 1 negative eigenvalue and 3 positive eigenvalues. While there are 2 positive and 1 negative critical points, so that the two groups have in 7 different critical points. This observation is shown in Figure 6.6. The resulting real part of the minimal eigenvalue of the system matrix in terms of the coupling strength is illustrated in Figure 6.6a, while the eigenvalues given by (6.19) *in terms of the parameter $\tilde{k}$ are depicted in Figure 6.6b. The numerical simulation align with the results of Theorem 6.2.*

Frequency Tunability

In addition to the emergence of the three Andronov-Hopf bifurcations, the three respective characteristic frequencies become tunable by controlling the asymmetry between the damping of the bifurcation. This is achieved by changing the self-feedback strengths k_{11} and k_{22} as the sensitivity in the physical setup is assigned by these parameter. For instance, the lower limit and upper limit of the characteristic frequencies is derived by applying first

Proposition 6.1 and then Theorem 6.2. In detail, Proposition 6.1 implies that the critical points and characteristic frequencies of one group will be given by the critical points and characteristic frequencies of the individual oscillators if the two groups are not coupled. Then by assuming that one group is in bifurcation, Theorem 6.2 implies that there is at least one critical point equal to zero. In this case, the characteristic frequency of the two groups is given by the characteristic frequencies (6.8b). In particular, these are the limits, since by increasing the cross-coupling and decreasing the self-coupling the characteristic frequency of the system will be shifted towards the characteristic frequency of the other group.

Hopf-Hopf Bifurcation

Due to the fact that there are three critical points the existence of a Hopf-Hopf bifurcation has to be analyzed. Subsequently, the Hopf-Hopf bifurcation is investigated in terms of the feedback strengths k_{11} and k_{22} and the natural frequencies ω_1 and ω_2 by imposing

$$\lambda_{\mathrm{H}}^{(i)} = \lambda_{\mathrm{H}}^{(j)} \tag{6.20}$$

with the critical points $\lambda_{\mathrm{H}}^{(i)}, \lambda_{\mathrm{H}}^{(j)}$ of the two coupled groups of oscillators of the form (6.1) for all $i, j = 1, 2, 3$ and $i \neq j$. In addition two different scenarios are discussed: First, two coupled groups of identical oscillators of the form (6.1) are analyzed. In this case, the feedback strengths k_{11} and k_{22} are discussed. Second, it is argued that it is not possible to derive an analytic equation with (6.20) for the two coupled non-identical MEMS sensors in terms of the feedback strengths k_{11} and k_{22} or the natural frequencies ω_1 and ω_2. Thus, the critical point of a Hopf-Hopf bifurcation is determined by exploiting a simple numerical algorithm.

Identical Oscillators After inserting (6.18a) and (6.18b) or (6.18a) and (6.18c) into (6.20), the equation results in the quartic polynomial

$$\begin{aligned} 0 = d_0 + d_1(k_{\mathrm{HH},11} + k_{\mathrm{HH},22}) + d_2(k_{\mathrm{HH},11} + k_{\mathrm{HH},22})^2 \\ - d_3(k_{\mathrm{HH},11} + k_{\mathrm{HH},22})^3 + d_4(k_{\mathrm{HH},11} + k_{\mathrm{HH},22})^4 \end{aligned} \tag{6.21}$$

with the coefficients

$$\begin{aligned} d_0 = & -16\left(a_{11} - a_{13}\omega_{\mathrm{C},i}^2\right)\left\{a_{13}a_{11}^2\omega_{\mathrm{C},i}^2\left(a_{13}^2 - 2a_{12} + \omega_{\mathrm{C},i}^2\right) - a_{10}^2a_{13}^3 + a_{11}^3\omega_{\mathrm{C},i}^2\right. \\ & \left. +2a_{10}a_{11}a_{13}^2\omega_{\mathrm{C},i}^2 + a_{13}^2a_{11}\omega_{\mathrm{C},i}^2\left[\omega_{\mathrm{C},i}^4 - (a_{13}^2 + 2a_{12})\omega_{\mathrm{C},i}^2 + a_{12}^2\right]\right\} \\ d_1 = & -8b_{11}\left\{a_{13}^3\omega_{\mathrm{C},i}^8 - a_{13}^3\left[a_{13}^2 + 2a_{12}\right]\omega_{\mathrm{C},i}^6 + a_{13}^3\left[a_{12}^2 + 2a_{10} + 4a_{11}a_{13}\right]\omega_{\mathrm{C},i}^4\right. \\ & \left. -a_{11}\left[4a_{11}^2 + 3a_{13}\left(a_{13}^2 - 2a_{12}\right)a_{11} + 2\left(a_{12}^2 + 2a_{10}\right)a_{13}^2\right]\omega_{\mathrm{C},i}^2 + a_{10}^2a_{13}^3\right\} \\ d_2 = & -4b_{11}^2\omega_{\mathrm{C},i}^2\left[a_{13}^2\left(-2a_{13}^2\omega_{\mathrm{C},i}^2 + a_{12}^2 + 2a_{10}\right) + 6a_{11}^2 + \left(3a_{13}^3 - 6a_{12}a_{13}\right)a_{11}\right] \\ d_3 = & \ 2\left(a_{13}^3 - 2a_{12}a_{13} + 4a_{11}\right)b_{11}^3\omega_{\mathrm{C},i}^2 \end{aligned}$$

for all $i = 2, 3$. The equation (6.21) can be solved for $k_{\mathrm{HH},11} + k_{\mathrm{HH},22}$ analytically [10, 13]. Similar results are obtained by inserting the critical points (6.18a) and (6.18c) into (6.20). However, a detailed discussion is omitted, since it follows by replacing $\omega_{\mathrm{C},2}$ with $\omega_{\mathrm{C},3}$.

Consider now the Hopf-Hopf bifurcation, which emerges from (6.18b) and (6.18c). This results in

$$k_{\mathrm{HH},11} + k_{\mathrm{HH},22} = \frac{2a_1 - a_2 a_3}{b_1}. \tag{6.22}$$

In addition, it follows from (6.21) and (6.22) that three purely imaginary pairs of complex conjugated eigenvalues cannot be obtained by assigning the feedback strengths $k_{\mathrm{HH},11}$ and $k_{\mathrm{HH},22}$. This comes from the fact that (6.21) and (6.22) are linearly dependent.

Example 6.2 *Subsequently, the Hopf-Hopf bifurcations of two coupled identical groups of oscillators of the form* (6.1) *are analyzed numerical. The parameters of these oscillators are given by oscillator 1 from Table A.4 in Appendix A. In particular, this system has in total 9 possible Hopf-Hopf bifurcations since there are one polynomial of degree 1 and two polynomials of degree 4. The numerical solution of these polynomials is given by*

- $k_{\mathrm{HH},1}^{(1,2)} = -2.19$, $k_{\mathrm{HH},2}^{(1,2)} = -2.119$, $k_{\mathrm{HH},3}^{(1,2)} = 0.53$, *and* $k_{\mathrm{HH},4}^{(1,2)} = 0.53$ *between the bifurcation* 1 *and bifurcation* 2,
- $k_{\mathrm{HH},1}^{(1,3)} = -2.11 + 4.47 \times 10^{-8}\mathrm{i}$, $k_{\mathrm{HH},2}^{(1,3)} = -2.11 - 4.47 \times 10^{-8}\mathrm{i}$, $k_{\mathrm{HH},3}^{(1,3)} = 0.521 + 0.165\mathrm{i}$, *and* $k_{\mathrm{HH},4}^{(1,3)} = 0.521 - 0.165\mathrm{i}$ *between the bifurcation* 1 *and bifurcation* 3,
- $k_{\mathrm{HH}}^{(2,3)} = -0.792$ *between the bifurcation* 2 *and bifurcation* 3.

For comparison, note that the critical feedback strengths of this oscillator are given by $k_{\mathrm{H},1} = 0.526$ *and* $k_{\mathrm{H},2} = -2.11$. *Hence, only the Hopf-Hopf bifurcation* $k_{\mathrm{HH}}^{(2,3)}$ *is valid in the sub-critical regime, since* $k_{\mathrm{H},12} \leq k_{\mathrm{HH}}^{(2,3)} \leq k_{\mathrm{H},11}$, *so that the critical coupling strength* $\lambda_{\mathrm{H}}^{(1)}$ *can be omitted for the analysis. The results are illustrated in Figure 6.7. This is done by determining the critical point of* $\lambda_{\mathrm{H}}^{(2)}$ *and* $\lambda_{\mathrm{H}}^{(3)}$ *in terms of the feedback k. In particularly, the location of the critical coupling strengths is changed by assigning a feedback k. For example, the coupling strength* $\lambda_{\mathrm{H}}^{(2)}$ *becomes dominant, i.e.,* $\lambda_{\mathrm{H}}^{(2)}$ *is smaller than* $\lambda_{\mathrm{H}}^{(3)}$, *if* $k > k_{\mathrm{HH},1}$. *From this it follows that it is possible to assign a dominant bifurcation by choosing the feedback strength k, accordingly.*

Non-Identical Oscillators To derive an equation for the Hopf-Hopf bifurcation (6.20) has to be solved for a design parameter, e.g., the feedback strengths k_i or the natural frequency ω_i for all $i = 1, 2$. However, the emerging equation is transcendental, so that it is not possible to determine an analytic solution. This comes from the fact that the second bifurcation parameter is an argument and a coefficient of the cosine. Hence, the critical points are determined numerically by applying

$$k_{ii,n+1} = k_{ii,n} + \eta_k \left(\lambda_{\mathrm{H}}^{(j)} - \lambda_{\mathrm{H}}^{(k)} \right), \tag{6.23a}$$

$$\omega_{i,n+1} = \omega_{i,n} - \eta_\omega \left(\lambda_{\mathrm{H}}^{(j)} - \lambda_{\mathrm{H}}^{(k)} \right) \tag{6.23b}$$

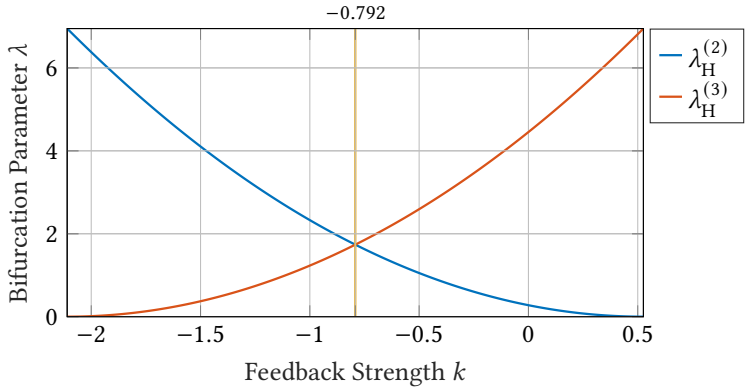

Figure 6.7.: Critical coupling strength of two coupled, identical, oscillators of the form (6.1) in terms of a symmetric feedback strength $k(= k_{11} = k_{22})$.

with the step size $\eta_k, \eta_\omega > 0$ and the iteration $n \in \mathbb{N}$ for all $i = 1, 2$, $j, k = 1, 2, 3$ and $j \neq k$. This algorithm is aborted, if the absolute values of the error $e = \lambda_{\mathrm{H}}^{(1)} - \lambda_{\mathrm{H}}^{(3)}$ are smaller than the threshold with respect to the natural frequency $\underline{e}_\omega > 0$ and the threshold with respect to the self-feedback $\underline{e}_k > 0$.

Example 6.3 *Subsequently, the characteristic frequencies $\omega_{\mathrm{C},1}$, $\omega_{\mathrm{C},2}$, and $\omega_{\mathrm{C},3}$ are analyzed numerically in terms of the feedback strengths $k_{11} \in [k_{\mathrm{H},12}, k_{\mathrm{H},11}]$ and $k_{22} \in [k_{\mathrm{H},22}, k_{\mathrm{H},21}]$. The parameters of these oscillators are given by oscillator 1 from Table A.4 in Appendix A. In addition, the Hopf-Hopf bifurcation between the first and third Andronov-Hopf bifurcation is computed numerically with* (6.23a) *as Example 6.2 suggests. The results are illustrated in Figure 6.8. Similar to the two coupled Andronov-Hopf oscillators, by adjusting the feedback strengths k_{11} and k_{22} the characteristic frequency can be tuned. Moreover, the Hopf-Hopf bifurcation is shown in Figures 6.8a and 6.8c by a red line. Particularly, the regime above the line is of interest since the bifurcation corresponding to the characteristic frequency $\omega_{\mathrm{C},1}$ is then dominant in this regime, so that this bifurcation is called tunable from now on. In addition, as expected from Example 6.2 it follows that the feedback strengths k_{11} and k_{22} influence, which bifurcation becomes dominant.*

Example 6.4 *Subsequently, the maximal difference between the natural frequencies ω_1 and ω_2 of two oscillators of the form* (6.1) *is evaluated numerically for different Q-factors, i.e.,$Q_i = 40, 80$ for all $i \in \{1, 2\}$. The remaining parameters of these oscillators are given by oscillator 1 from Table A.4 in Appendix A. For this, let $f = \omega/2\pi$. The analysis is done in two steps:*

First, the frequency interval $[\underline{f}, \bar{f}]$ with respect to the feedback strengths k_{11} and k_{22} is analyzed. For this, the results obtained in Example 6.2 are exploited, i.e., the relationship between the critical coupling strengths $k_{\mathrm{H},1}$ and $k_{\mathrm{H},2}$. This is done by determining the intersection of the critical points $k_{\mathrm{H},1}$ and $k_{\mathrm{H},2}$ numerically. Second, with (6.23b) *the frequency difference $\Delta f = |f_1 - f_2|$ is computed for the quantified regions. For this, the investigated interval is assumed to be the hearing range of humans, i.e., the interval $C = [20, 20000]$ Hz [121].*

For the two different values of the Q-factor, the critical feedback strengths of a single oscillator $k_{\mathrm{H},1}$ and $k_{\mathrm{H},2}$ are illustrated in Figure 6.9. The solid lines depict the critical feedback strengths

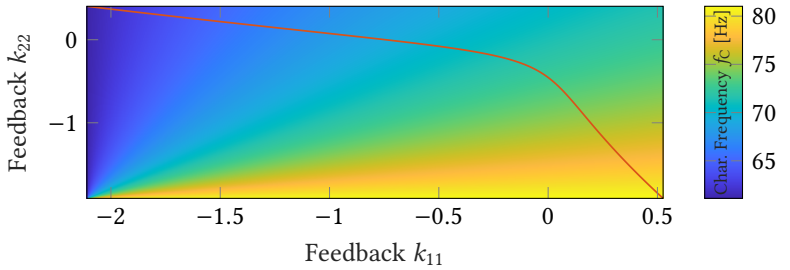

(a) Characteristic frequency $f_{C,1}$ in terms of the feedback strengths k_{11} and k_{22}. Herein, the Hopf-Hopf bifurcation between the first and third bifurcation is marked by the red line.

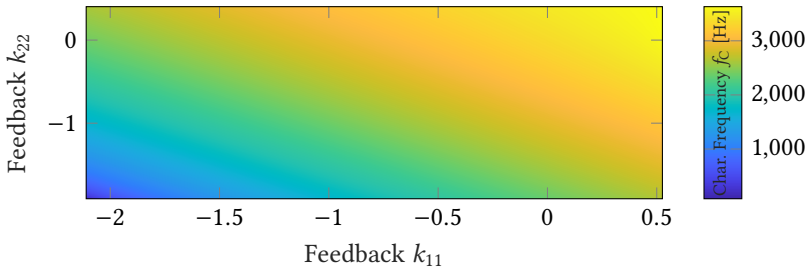

(b) Characteristic frequency $f_{C,2}$ in terms of the feedback strengths k_{11} and k_{22}.

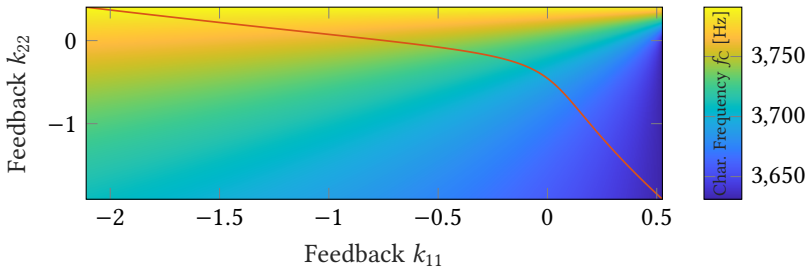

(c) Characteristic frequency $f_{C,3}$ in terms of the feedback strengths k_{11} and k_{22}. Herein, the Hopf-Hopf bifurcation between the first and third bifurcation is marked by the red line.

Figure 6.8.: Characteristic frequency f_C of the three bifurcations in terms of the feedback strengths k_{11} and k_{22}.

$k_{H,1}$ and $k_{H,2}$ of an oscillator shifted feedback. In contrast, the dashed lines depict the critical feedback strengths $k_{H,1}$ and $k_{H,2}$ of an oscillator, where the feedback strength k is shifted towards $k_{H,1}$, i.e., $k = 0.8 \times k_{H,1}$. For the oscillator without feedback, it turns out that $k_{H,1}$ is smaller than $k_{H,2}$ in an interval from approximately 63.8 Hz to 7295 Hz for $Q_i = 40$ and from approximately 62.1 Hz to 14555.6 Hz for $Q_i = 80$, respectively. These intervals are marked by the gray region in Figure 6.9. In particular, the critical point with the characteristic frequency $\omega_{C,1}$ has a smaller magnitude in these intervals. Hence, it is also the dominant bifurcation when coupling two identical oscillators, since the critical point of the two coupled identical oscillators is given by the square of the critical feedback strength of a oscillator. In contrast to the oscillator without feedback, the interval is enlarged by shifting the feedback k moving

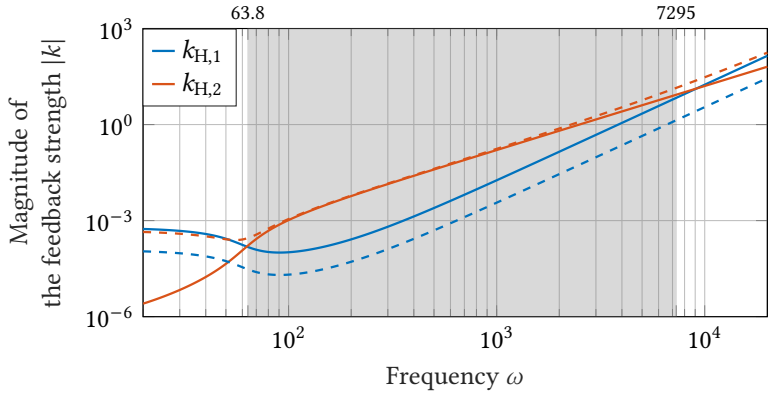

(a) Critical feedback strength k_H with $Q_1 = Q_2 = 40$.

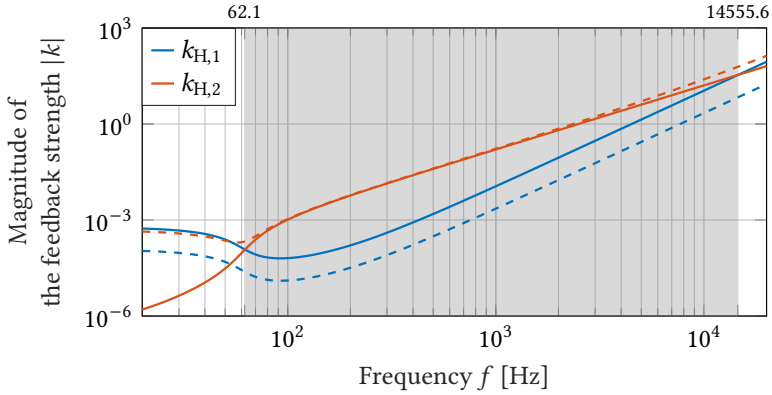

(b) Critical feedback strength k_H with $Q_1 = Q_2 = 80$.

Figure 6.9.: Comparison of between the maximal frequency difference and magnitude of the critical points for different Q-factors. The parameters are given by the feedback strengths $k_{11}(\omega) \in \{0,\ 0.8 \times k_{H,1}(\omega)\}$ and $k_{22} = 0$ and the Q-factors $Q_1 = Q_2 = 40$ for the top and $Q_1 = Q_2 = 80$ for the bottom. In addition, the solid lines depict the case without feedback and dashed lines depict the case with feedback and the natural frequency is given by $\omega = 2\pi f$.

closer to the critical point $k_{H,1}$. Thus, the tunable bifurcation becomes dominant for the whole interval C.

With this, the maximum frequency difference Δf can be evaluated. This is done by comparing the system without feedback, i.e., $k_{11} = k_{22} = 0$, and a system with a feedback moved close to the critical point of the first oscillator, i.e., $k_{11}(\omega) = 0.8 \times k_{H,1}(\omega)$ and $k_{22} = 0$. The results are illustrated in Figure 6.10. It turns out that the numerical method (6.23) converge, if the tunable bifurcation is dominant. From this, it can be concluded that the interval in which the tunable bifurcation is dominant, is increased by increasing the Q-factor Q or moving the feedback k closer to the critical feedback strength $k_{H,1}$.

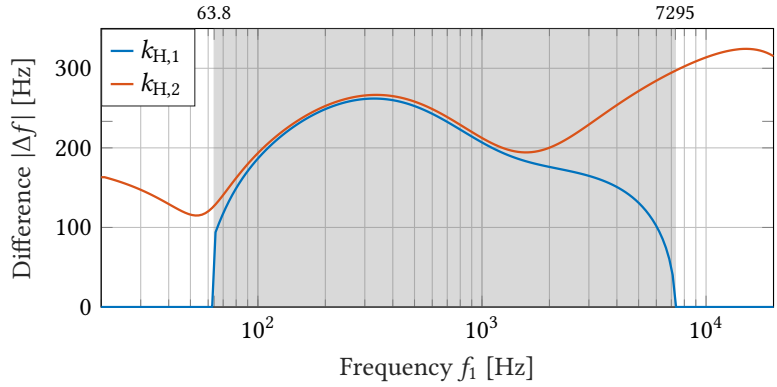

(a) Critical feedback strength k_H of a single oscillator in terms of the natural frequency f.

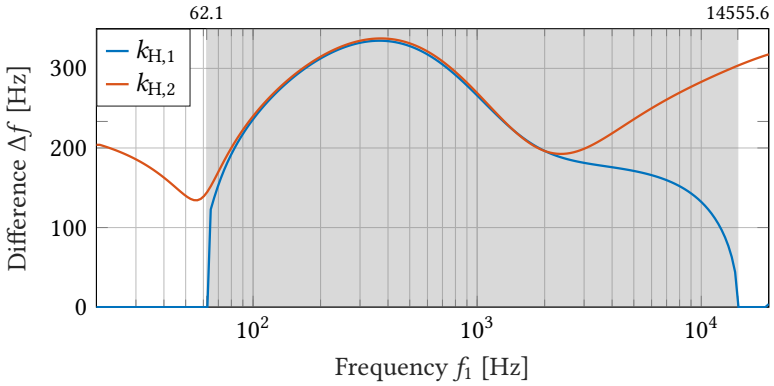

(b) Maximal frequency difference $\Delta f = |f_1 - f_2|$ in terms of the natural frequency f_1.

Figure 6.10.: Comparison of between the maximal frequency difference and magnitude of the critical points for different Q-factors. The parameters are given by the feedback strengths $k_{11}(\omega) \in \{0,\ 0.8 \times k_{H,1}(\omega)\}$ and $k_{22} = 0$ and the Q-factors $Q_1 = Q_2 = 40$ for the top and $Q_1 = Q_2 = 80$ for the bottom. In addition, the solid lines depict the case without feedback and dashed lines depict the case with feedback and the natural frequency is given by $\omega = 2\pi f$.

6.3.2. Controller based on Diffusive Coupling

Subsequently, tunability enhancements based on two diffusive coupled oscillators of the form (6.1) are analyzed. A sketch of the setup is illustrated in Figure 6.11. For this, the subsequent results are compared to the number of critical points of symmetrically coupled Andronov-Hopf oscillators from Proposition 3.5 and the frequency tunability at their critical point. Following Figure 6.11, the i-th oscillator is governed by

$$\dot{\boldsymbol{x}}_i = \boldsymbol{f}_i(\boldsymbol{\chi}), \qquad t > 0, \qquad \boldsymbol{x}_i(0) = \boldsymbol{x}_{i,0}, \tag{6.24a}$$

$$y_i = x_{4,i}, \qquad t \geq 0 \tag{6.24b}$$

with

$$f_i(\boldsymbol{\chi}) = \begin{bmatrix} x_{1,i} \\ -c_{1,i}x_{1,i} - c_{3,i}x_{1,i}^3 - \mu_i x_{2,i} + \alpha_i x_{3,i} \\ -\beta_i x_{3,i} + \zeta_i \left((\xi - k_{ii})\, x_{4,i} + \xi x_{4,j} + u_{\mathrm{DC},i} \right)^2 \\ -\frac{1}{T_i} x_{4,i} + \kappa x_{2,i} \end{bmatrix}, \tag{6.24c}$$

the state vector $\boldsymbol{\chi} = [\boldsymbol{x}_1^{\mathrm{T}}, \boldsymbol{x}_2^{\mathrm{T}}]^{\mathrm{T}}$ of the two coupled oscillators, and the coupling strength ξ for all $i, j = 1, 2$ and $i \neq j$. The analysis is structured as follows: First, analytical results are discussed by showing that the necessary condition (H1) of the Hopf Theorem (see Theorem 2.9) is satisfied by solving a polynomial of 6th order. Second, the number of real-valued solutions, the crossing condition (H2), and the frequency tunability are analyzed numerically.

Analytic Results

Necessary Condition of the Hopf Theorem To analyze the necessary condition (H1) of the Hopf Theorem (see Theorem 2.9) the critical point in terms of the coupling strength ξ is investigated. For this, the two diffusively coupled oscillators are linearized around the equilibrium (6.2) and the characteristic polynomial is determined as

$$\begin{aligned} P_{\mathrm{CF}}(\lambda) = \lambda^8 + \left[a_{12} + a_{22} + a_{13}a_{23}\right] \lambda^7 + \left[a_{13} + a_{23}\right] \lambda^6 \\ + c_5\lambda^5 + c_4\lambda^4 + c_3\lambda^3 + c_2\lambda^2 + c_1\lambda + a_{10}a_{20} \end{aligned} \tag{6.25}$$

with the parameters given by (6.7), i.e.,

$$a_{0i} = \frac{\beta_i \Omega_i^2}{T_i}, \quad a_{1i} = \beta_i \Omega_i^2 + \frac{\beta_i \mu_i}{T_i} + \frac{\Omega_i^2}{T_i}, \quad a_{2i} = \frac{\beta_i}{T_i} + \beta_i \mu_i + \frac{\mu_i}{T_i} + \Omega_i^2, \quad a_{3i} = \beta_i + \mu_i + \frac{1}{T_i},$$

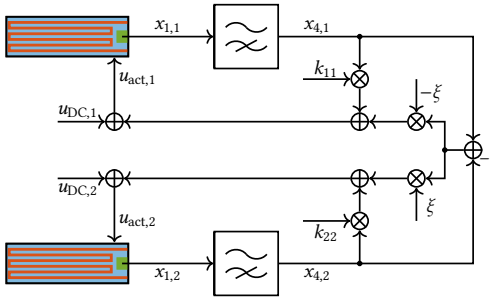

Figure 6.11.: Sketch of two diffusively coupled, bio-inspired oscillators (6.1).

and

$$c_5 = a_{11} + a_{21} + a_{13}a_{22} + a_{12}a_{23} + b_{11}\left(\xi - k_{11}\right) + b_{21}\left(\xi - k_{22}\right), \tag{6.26a}$$

$$c_4 = a_{23}\left[a_{11} + b_{11}\left(\xi - k_{11}\right)\right] + a_{13}\left[a_{21} + b_{21}\left(\xi - k_{22}\right)\right] + a_{10} + a_{20} + a_{12}a_{22}, \tag{6.26b}$$

$$c_3 = a_{22}\left[a_{11} + b_{11}\left(\xi - k_{11}\right)\right] + a_{12}\left[a_{21} + b_{21}\left(\xi - k_{22}\right)\right] + a_{13}a_{20} + a_{10}a_{23}, \tag{6.26c}$$

$$c_2 = b_{11}\left\{a_{21}\left(\xi - k_{11}\right) - b_{21}\left[k_{11}\xi + \left(\xi - k_{11}\right)k_{22}\right]\right\} + a_{11}\left[a_{21} + b_{21}\left(\xi - k_{22}\right)\right] + a_{12}a_{20} + a_{10}a_{22}, \tag{6.26d}$$

$$c_1 = a_{20}\left[a_{11} + b_{11}\left(\xi - k_{11}\right)\right] + a_{10}\left[a_{21} + b_{21}\left(\xi - k_{22}\right)\right]. \tag{6.26e}$$

Based on this, conditions to satisfy the necessary condition (H1) are derived by inserting $\lambda = \mathrm{i}\omega_\mathrm{C}$ with $\omega_\mathrm{C} > 0$, separating the real and imaginary part and substituting $\omega_\mathrm{C}^2 = z$. This results in

$$0 = z^4 - \left[a_{13} + a_{23}\right] z^3 + c_4 z^2 - c_2 z + c_1 \mathrm{i}\omega_\mathrm{C} + a_{10}a_{20}, \tag{6.27a}$$

$$0 = -\left[\left(a_{12} + a_{22} + a_{13}a_{23}\right) z^3 - c_5 z^2 + c_3 z - c_1\right]\omega_\mathrm{C}. \tag{6.27b}$$

To solve the system of equations (6.27), the coefficients (6.26) are inserted into (6.27a) and the result is solved for ξ to obtain the critical point

$$\begin{aligned}\xi_\mathrm{H} = \frac{1}{z\left(b_{21}\left(a_{13}z - a_{11} + b_{11}\left(k_{11} + k_{22}\right)\right) + a_{23}b_{11}z - a_{21}b_{11}\right)}\Big[&z^4 - \left(a_{22} + a_{12} + a_{13}a_{23}\right) z^3 \\ &- \left(a_{23}b_{11}k_{11} + b_{21}k_{22}a_{13} - a_{22}a_{12} - a_{20} - a_{13}a_{21} - a_{11}a_{23} - a_{10}\right) z^2 \\ &- \left(b_{21}k_{22}\left(b_{11}k_{11} - a_{11}\right) - a_{21}b_{11}k_{11} + a_{20}a_{12} + a_{11}a_{21} - a_{10}a_{22}\right) z + a_{10}a_{20}\Big].\end{aligned}$$

Employing the critical point on (6.27b), yields

$$P_{\omega_\mathrm{C}} = d_0 + d_1 z + d_2 z^2 + d_3 z^3 + d_4 z^4 + d_5 z^5 + d_6 z^6 \tag{6.28}$$

with

$$d_0 = -a_{10}a_{20}\left(a_{20}b_{11} + a_{10}b_{21}\right), \tag{6.29a}$$

$$d_1 = -a_{10}b_{11}\left(\left(a_{21} - b_{21}k_{22}\right)^2 - 2a_{20}a_{22}\right) - a_{20}b_{21}\left(a_{11} - b_{11}k_{11}\right)^2 + a_{22}a_{10}^2 b_{21} + a_{12}a_{20}\left(a_{20}b_{11} + 2a_{10}b_{21}\right), \tag{6.29b}$$

$$\begin{aligned}d_2 = &-a_{10}\left(a_{22}^2 b_{11} - 2a_{23}b_{11}\left(a_{21} - b_{21}k_{22}\right) + 2a_{12}a_{22}b_{21} + 2a_{20}\left(b_{11} + b_{21}\right)\right) \\ &- a_{20}\left(a_{12}^2 b_{21} - 2a_{13}b_{21}\left(a_{11} - b_{11}k_{11}\right) + 2a_{22}a_{12}b_{11}\right) + a_{11}^2 a_{22}b_{21} \\ &+ b_{11}\left(a_{12}\left(a_{21} - b_{21}k_{22}\right)^2 + a_{22}b_{21}k_{11}\left(b_{11}k_{11} - 2a_{11}\right)\right) - a_{10}^2 b_{21} - a_{20}^2 b_{11},\end{aligned} \tag{6.29c}$$

$$\begin{aligned}d_3 = &\,2a_{11}b_{11}b_{21}k_{11} + 2a_{13}a_{22}b_{11}b_{21}k_{11} + 2a_{21}b_{11}b_{21}k_{22} \\ &+ a_{12}\left(b_{11}\left(a_{22}^2 - 2a_{23}\left(a_{21} - b_{21}k_{22}\right)\right) + 2a_{10}b_{21} + 2a_{20}\left(b_{11} + b_{21}\right)\right) \\ &- a_{11}^2 b_{21} - 2a_{13}a_{22}a_{11}b_{21} - a_{21}^2 b_{11} - a_{10}a_{23}^2 b_{11} + 2a_{10}a_{22}b_{11} \\ &+ 2a_{20}a_{22}b_{11} - a_{13}^2 a_{20}b_{21} + a_{12}^2 a_{22}b_{21} + 2a_{10}a_{22}b_{21} - b_{11}^2 b_{21}k_{11}^2 - b_{11}b_{21}^2 k_{22}^2,\end{aligned} \tag{6.29d}$$

$$\begin{aligned}d_4 = &\,b_{11}\left(a_{23}^2 a_{12} - a_{22}^2 + 2\left(a_{21}a_{23} - a_{22}a_{12}\right)\right) + b_{21}\left(a_{13}^2 a_{22} - a_{12}^2 + 2\left(a_{11}a_{13} - a_{22}a_{12}\right)\right) \\ &- 2\left(a_{13}k_{11} + a_{23}k_{22}\right)b_{11}b_{21} - a_{20}\left(2b_{11} + b_{21}\right) - a_{10}\left(b_{11} + 2b_{21}\right),\end{aligned} \tag{6.29e}$$

$$d_5 = \left(-a_{23}^2 + a_{12} + 2a_{22}\right)b_{11} + \left(-a_{13}^2 + 2a_{12} + a_{22}\right)b_{21} \tag{6.29f}$$

$$d_6 = -b_{11} - b_{21} \tag{6.29g}$$

In particular, (6.28) is a polynomial of 6th order, so that its roots and thus the critical points cannot be solved analytically [10, 15].

Crossing Condition of the Hopf Theorem To analyze the crossing condition (H2), the sensitivity of the eigenvalues crossing the imaginary is evaluated by determining the real-part of the derivative of the eigenvalue at the critical point, i.e., $d_{\mathrm{H}} = \mathrm{Re}(\frac{\mathrm{d}\lambda}{\mathrm{d}\xi}|_{\lambda=\mathrm{i}\omega_{\mathrm{C}}})$. Taking the derivative of the characteristic polynomial and solving it for $\frac{\mathrm{d}\lambda}{\mathrm{d}\xi}$, yields

$$\frac{\mathrm{d}\lambda}{\mathrm{d}\xi} = -\lambda \left(\frac{\mathrm{d}P_{\mathrm{CF}}}{\mathrm{d}\lambda}\right)^{-1} (e_4\lambda^4 + e_3\lambda^3 + e_2\lambda^2 + e_1\lambda + e_0) \tag{6.30}$$

with the coefficients

$$\begin{aligned} e_4 =& b_{11} + b_{21}, Te_3 = Ta_{23}b_{11} + a_{13}b_{21}, \\ e_2 =& a_{11}b_{11} + a_{12}b_{21}, Te_0 = a_{20}b_{11} + a_{10}b_{21}, \\ e_1 =& \left[a_{21}b_{11} + a_{11}b_{21} - b_{11}b_{21}\,(k_{11} + k_{22})\right]. \end{aligned}$$

Inserting $\lambda = \mathrm{i}\omega_{\mathrm{C}}$, taking the real-part, and sorting terms, results in

$$\begin{aligned} d_{\mathrm{H}} = \omega_{\mathrm{C}}^2[&8e_4\omega_{\mathrm{C}}^{10} + (7c_7e_3 - 6c_6e_4 - 8e_2)\omega_{\mathrm{C}}^8 + (6c_6e_2 - 7c_7e_1 - 5c_5e_3 + 4c_4e_4 + 8e_0)\omega_{\mathrm{C}}^6 \\ &+ (5c_5e_1 - 6c_6e_0 - 4c_4e_2 + 3c_3e_3 - 2c_2e_4)\omega_{\mathrm{C}}^4 + (4c_4e_0 - 3c_3e_1 + 2c_2e_2 - c_1e_3)\omega_{\mathrm{C}}^2 \\ &+ (c_1e_1 - 2c_2e_0)]. \end{aligned} \tag{6.31}$$

After substituting $\omega_{\mathrm{C}}^2 = z$ in (6.31), a polynomial of 5th order in terms of z emerges. This implies that its roots (and thus ξ_{H}) cannot be computed analytically [10, 15].

Numeric Results

As the degree of (6.28) is 6, the number of positive zeros is subsequently computed numerically by employing Sturm's Theorem.

Theorem 6.3 (Sturm's Theorem [15]) *Let $P(x) = x^n + a_{n-1}x^{n-1} + \ldots + a_0$ be a real-valued polynomial of degree $n \in \mathbb{N}$, whose zeros are unique. In addition, denote the Sturm sequence by $s(x) = (P, \frac{\mathrm{d}P}{\mathrm{d}x}, P_1, P_2, \ldots, P_m)$ with $m \in \mathbb{N}$,*

$$P_i = \begin{cases} -\mathrm{rem}\left(P, \frac{\mathrm{d}P}{\mathrm{d}x}\right), & \text{if } i = 1 \\ -\mathrm{rem}\left(\frac{\mathrm{d}P}{\mathrm{d}x}, P_1\right), & \text{if } i = 2 \\ -\mathrm{rem}\left(P_{i-2}, P_{i-1}\right), & \text{if } i = 3, \ldots, m \end{cases}, \tag{6.32}$$

$P_m \in \mathbb{R}$, and the remainder $\mathrm{rem}(\tilde{P}_1, \tilde{P}_2)$ of the polynomial division of $\tilde{P}_1$ by $\tilde{P}_2$. Then the number of real-valued zeros in an interval $[a, b] \subseteq \mathbb{R}$ is given by

$$n = \alpha - \beta, \tag{6.33}$$

where α and β denote the number of sign changes in the Sturm sequences $s(\alpha)$ and $s(\beta)$.

For the numerical analysis, the parameters are given in the Table A.5 in Appendix A.

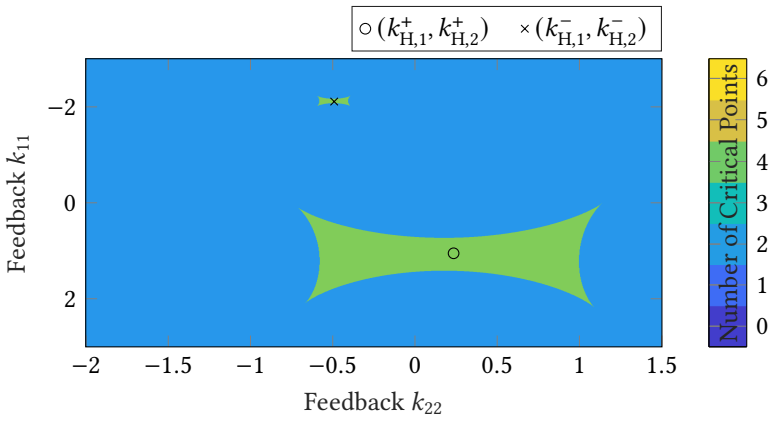

Figure 6.12.: Number of critical points (CPs) of two diffusively coupled oscillators of the form (6.1) in terms of the feedback k_{11} and k_{22}. For comparison, the critical points $(k^{\pm}_{\mathrm{H},1}, k^{\pm}_{\mathrm{H},2})$ of the uncoupled oscillators of the form (6.1) are given by the cross and circle.

Number of Critical Points The number of positive roots of P_{ω_C} is determined by applying Sturm's Theorem on (6.28) for the interval $[0, \infty)$. The result is depicted in Figure 6.12. It is demonstrated that the two diffusively oscillators of the form (6.1) have at least two critical points. Additionally, two regions with four critical points emerge around a neighborhood of the critical points (6.8a) from Theorem 6.1, i.e., the centers are given by $(k^{\pm}_{\mathrm{H},1}, k^{\pm}_{\mathrm{H},2})$. In particular, Proposition 3.5 implies that two diffusively coupled Andronov-Hopf oscillator have three critical points depending on the symmetric coupling strength, if their damping is close to zero. If the feedback strengths are in the neighborhood of the pairs $(k^{\pm}_{\mathrm{H},1}, k^{\pm}_{\mathrm{H},2})$, (6.24) will also satisfy this condition as the oscillators (6.1) will converge to a sub-manifold, which can be transformed by an isomorphism into the Andronov-Hopf oscillator. Hence, the bifurcations are subsequently divided into two groups by the bifurcations they are induced by. The first three critical points emerge around the pair $(k^{+}_{\mathrm{H},1}, k^{+}_{\mathrm{H},2})$ and the latter three critical points bifurcate from the pair $(k^{-}_{\mathrm{H},1}, k^{-}_{\mathrm{H},2})$.

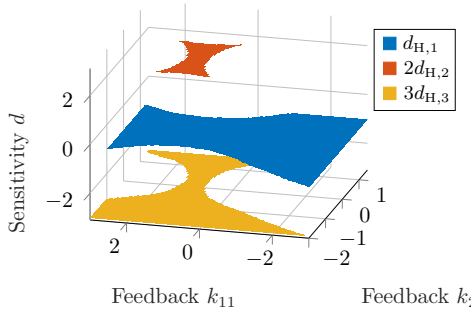

(a) Re-weighted sensitivities $d_{\mathrm{H},1}$, $2d_{\mathrm{H},2}$, and $3d_{\mathrm{H},3}$ of the critical points emerging from the pair $(k^{+}_{\mathrm{H},1}, k^{+}_{\mathrm{H},2})$.

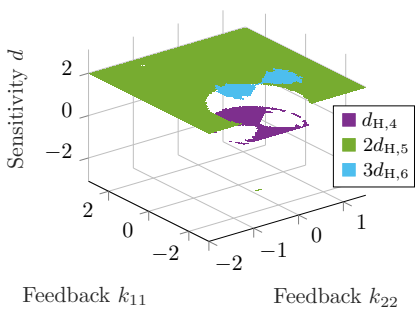

(b) Re-weighted sensitivities $d_{\mathrm{H},4}$, $2d_{\mathrm{H},5}$, and $3d_{\mathrm{H},6}$ of the critical points emerging from the pair $(k^{-}_{\mathrm{H},1}, k^{-}_{\mathrm{H},2})$.

Figure 6.13.: Re-weighted sensitivity of the eigenvalues on the imaginary axis.

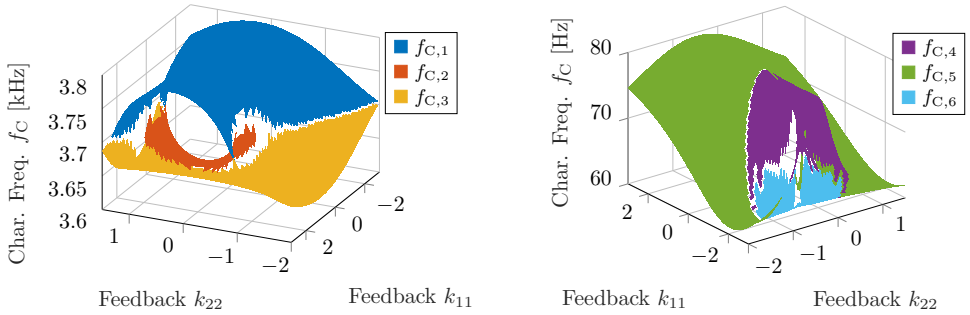

(a) Characteristic frequencies $f_{H,1}$, $f_{H,2}$, and $f_{H,6}$ of the critical points emerging from the pair $(k^+_{H,1}, k^+_{H,2})$.

(b) Characteristic frequencies $f_{H,4}$, $f_{H,5}$, and $f_{H,6}$ of the critical points emerging from the pair $(k^-_{H,1}, k^-_{H,2})$.

Figure 6.14.: Characteristic frequencies as a function of the feedback strengths k_{11} and k_{22} and the gain as a function of the external frequency f_{ex} and feedback strengths k_{11} and k_{22}. Here, the normalized frequency is given by $f = \omega/(2\pi)$.

Crossing Condition The crossing condition (H2) is evaluated by computing (6.31) numerically. The results of the (weighted) sensitivity are depicted in Figure 6.13. It is shown that the sensitivities d_H at all critical points are not vanishing. Thus, the crossing condition (H2) is satisfied for the critical points.

Frequency Tunability Close to the Critical Point Finally, the tunability enhancements imposed by diffusive coupling are investigated. For this, the characteristic frequency ω_C at the critical point in terms of the feedback strengths k_{11} and k_{22} is illustrated in Figures 6.14. Similar to two diffusively coupled Andronov-Hopf oscillators, the characteristic frequency $\omega_{H,i}$ can be tuned by varying the feedback strengths k_{11} and k_{22} and the frequency tunability is inhibited in the regions, where four critical points emerge.

6.3.3. Controller based on Delayed Feedback

Finally, the frequency tunability enhancements by introducing a controllable delayed feedback are investigated for the oscillator of the form (6.1). For this, let $\boldsymbol{x}_\tau(t) = \boldsymbol{x}(t-\tau)$ with a positive (and controllable) delay $\tau \geq 0$. Then the system is governed by

$$\dot{\boldsymbol{x}} = \boldsymbol{f}(\boldsymbol{x}, \boldsymbol{x}_\tau), \qquad t > 0, \tag{6.34a}$$

$$\boldsymbol{x}(\tau) = \boldsymbol{x}_0(\tau), \qquad \tau \in [-\theta, 0], \tag{6.34b}$$

$$y = x_4, \qquad t \geq 0 \tag{6.34c}$$

with

$$\boldsymbol{f}(\boldsymbol{x}, \boldsymbol{x}_\tau) = \begin{bmatrix} 1 \\ -c_{1,i}x_{1,i} - c_{3,i}x_{1,i}^3 - \mu_i x_{2,i} + \alpha_i x_{3,i} \\ -\beta x_3 + \zeta(k_1 x_4 + k_2 x_{4,\tau} + u_{DC})^2 \\ -\frac{1}{T}x_4 + \kappa x_2 \end{bmatrix}, \tag{6.34d}$$

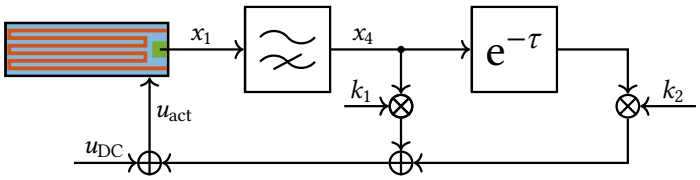

Figure 6.15.: Setup of the bio-inspired oscillator (6.1) with delayed feedback.

In addition, a sketch of the setup is illustrated in Figure 6.15. Subsequently, the frequency tunability is shown by analyzing the emergence of Andronov-Hopf bifurcations in (6.34). For this, analytical results are derived. It turns out that a quartic polynomial has to be solved to determine the critical points. Hence, the number of possible critical points (and thus the remaining bifurcation analysis) is evaluated numerically.

Analytical Results

To investigate the frequency tunability, the bifurcations of (6.34) are analyzed by employing the Hopf Theorem (see Theorem 2.9). For this, the linearization of the system is briefly summarized. Then analytical results for the necessary condition (H1) and the crossing condition (H2) are derived. Finally, the steepest change of the characteristic frequency at the critical point is determined to enhance the frequency tunability and to compare the emerging Andronov-Hopf bifurcations to the results of the Andronov-Hopf oscillator with delayed feedback.

Linearization As the equilibrium of the oscillator (6.1) is invariant to the delayed feedback of x_4, (6.34) can be linearized around the equilibrium (6.2), i.e.,

$$\boldsymbol{x}_{\mathrm{eq}} = \left[\sqrt{\tfrac{4p}{3}} \sinh\left(\tfrac{1}{3} \operatorname{arsinh}\left(\tfrac{q}{2} \sqrt{\tfrac{3}{p}}^{3} \right) \right) \quad 0 \quad \tfrac{\zeta}{\beta} u_{\mathrm{DC}}^2 \quad 0 \right]^{\mathrm{T}}.$$

Hence, the linearization of the oscillator (6.34) is given by

$$\Delta \dot{\boldsymbol{x}} = A_0 \Delta \boldsymbol{x} + A_1 \Delta \boldsymbol{x}_\tau \tag{6.35a}$$

with $\Delta \boldsymbol{x} = \boldsymbol{x} - \boldsymbol{x}_{\mathrm{eq}}$ and the system matrices

$$A_0 = \partial_{\boldsymbol{x}} \boldsymbol{f} = \begin{bmatrix} 0 & 1 & 0 & 0 \\ -\omega_0^2 & -\frac{\omega_0}{Q_0} & \alpha & 0 \\ 0 & 0 & -\beta & 2u_{\mathrm{DC}}\zeta k_1 \\ 0 & \kappa & 0 & -\frac{1}{T} \end{bmatrix}, \tag{6.36a}$$

$$A_1 = \partial_{\boldsymbol{x}_\tau} \boldsymbol{f} = \begin{bmatrix} 0 & 0 & 0 & 0 \\ 0 & 0 & 0 & 0 \\ 0 & 0 & 0 & 2u_{\mathrm{DC}}\zeta k_2 \\ 0 & 0 & 0 & 0 \end{bmatrix}. \tag{6.36b}$$

The local conditions (H1) and (H2) of the Andronov-Hopf bifurcations are investigated by analyzing the characteristic function

$$g_{\mathrm{CF}}(\lambda) = \det(A_0 + A_1 \mathrm{e}^{-\tau\lambda} - \lambda I_4) \tag{6.37}$$

with the identity matrix $I_4 \in \mathbb{R}^{4\times4}$ [95, 126, 114]. Inserting (6.36a) and (6.36b) in (6.37) yields

$$g_{\mathrm{CF}}(\lambda) = \lambda^4 + a_3\lambda^3 + a_2\lambda^2 + \left[a_1 - b_1\left(k_1 + k_2 e^{-\tau\lambda}\right)\right]\lambda + a_0 \tag{6.38}$$

with the parameters given by (6.7), i.e.,

$$\begin{aligned} a_0 &= \frac{\beta\Omega^2}{T}, & a_1 &= \beta\Omega^2 + \frac{\beta\mu}{T} + \frac{\Omega^2}{T}, \\ a_2 &= \frac{\beta}{T} + \beta\mu + \frac{\mu}{T} + \Omega^2, & a_3 &= \beta + \mu + \frac{1}{T}, \\ b_1 &= 2\alpha\kappa\zeta u_{\mathrm{DC}}. \end{aligned}$$

Necessary Condition of the Hopf Theorem Subsequently, the necessary condition (H1) of the Hopf Theorem is analyzed for the oscillator (6.34) in terms of the time delay τ. This is done by inserting $\tau = \tau_{\mathrm{H}}$ and $\lambda = \mathrm{i}\omega_{\mathrm{C}}$ into (6.38) with the characteristic frequency $\omega_{\mathrm{C}} > 0$ and the critical delay $\tau_{\mathrm{H}} > 0$, which results in

$$0 = \omega_{\mathrm{C}}^4 - \mathrm{i}a_3\omega_{\mathrm{C}}^3 - a_2\omega_{\mathrm{C}}^2 + \mathrm{i}\left[a_1 - b_1\left(k_1 + k_2 e^{-\mathrm{i}\tau_{\mathrm{H}}\omega_{\mathrm{C}}}\right)\right]\omega_{\mathrm{C}} + a_0. \tag{6.39}$$

Dividing (6.39) into real and imaginary part yields

$$0 = \omega_{\mathrm{C}}^4 - a_2\omega_{\mathrm{C}}^2 - k_2 b_1 \sin(\tau_{\mathrm{H}}\omega_{\mathrm{C}})\omega_{\mathrm{C}} + a_0, \tag{6.40a}$$

$$0 = -a_3\omega_{\mathrm{C}}^3 + \left[a_1 - b_1\left(k_1 + k_2\cos(\tau_{\mathrm{H}}\omega_{\mathrm{C}})\right)\right]\omega_{\mathrm{C}}. \tag{6.40b}$$

Solving (6.40a) for $\sin(\tau_{\mathrm{H}}\omega_{\mathrm{C}})$ results in

$$\sin(\tau_{\mathrm{H}}\omega_{\mathrm{C}}) = \frac{\omega_{\mathrm{C}}^4 - a_2\omega_{\mathrm{C}}^2 + a_0}{k_2 b_1 \omega_{\mathrm{C}}}. \tag{6.41}$$

Here, (6.41) is only real-valued for the critical delay τ_{C}, if $\left|\frac{\omega_{\mathrm{C}}^4 - a_2\omega_{\mathrm{C}}^2 + a_0}{k_2 b_1 \omega_{\mathrm{C}}}\right| \leq 1$. In addition, by inserting (6.41) into (6.40b) and employing $\sin^2(\tau_{\mathrm{H}}\omega_{\mathrm{C}}) + \cos^2(\tau_{\mathrm{H}}\omega_{\mathrm{C}}) = 1$, the equation

$$0 = (a_1 - k_1 b_1)\,\omega_{\mathrm{C}} - a_3\omega_{\mathrm{C}}^3 - \operatorname{sign}(k_2 b_1)\sqrt{k_2^2 b_1^2 \omega_{\mathrm{C}}^2 + \left(\omega_{\mathrm{C}}^4 - a_2\omega_{\mathrm{C}}^2 + a_0\right)^2}. \tag{6.42}$$

arises. Eq. (6.42) is simplified by adding the square root term, taking the square of the result and sorting the terms, which results in

$$\begin{aligned} 0 = a_0^2 - \left[2a_0a_2 - (a_1 - b_1k_1)^2 + b_1^2k_2^2\right]\omega_{\mathrm{C}}^2 \\ + \left[a_2^2 + 2a_0 - 2a_3(a_1 - b_1k_1)\right]\omega_{\mathrm{C}}^4 + \left(a_3^2 - 2a_2\right)\omega_{\mathrm{C}}^6 + \omega_{\mathrm{C}}^8. \end{aligned} \tag{6.43}$$

In particular, the zeros of (6.43) and (6.40) are identical, if

$$\left[k_2 b_1 > 0 \ \wedge \ (a_1 - k_1 b_1) - a_3 \omega_\mathrm{C}^2 > 0\right] \vee \left[k_2 b_1 < 0 \ \wedge \ (a_1 - k_1 b_1) - a_3 \omega_\mathrm{C}^2 < 0\right], \quad (6.44)$$

as (6.44) implies that the square root term in (6.42) is positive. Substituting $\omega_\mathrm{C}^2 = x$, a quartic polynomial with respect to x arises

$$0 = a_0^2 - \left[2a_0 a_2 - (a_1 - b_1 k_1)^2 + b_1^2 k_2^2\right] x + \left[a_2^2 + 2a_0 - 2a_3 (a_1 - b_1 k_1)\right] x^2 + \left(a_3^2 - 2a_2\right) x^3 + x^4. \quad (6.45)$$

Hence (6.43) can be solved analytically in principle. Subsequently, the number of real-valued zeros of (6.43) is investigated numerically.

Crossing Condition of the Hopf Theorem The crossing condition (H2) of the Hopf Theorem (see Theorem 2.9) is evaluated by determining (2.14). For (6.34), the crossing condition (H2) can be expressed by

$$d = \mathrm{num}\left(\mathrm{Re}\frac{\mathrm{d}\lambda}{\mathrm{d}\tau}\bigg|_{\lambda=\mathrm{i}\omega_\mathrm{C}}\right) \neq 0 \quad (6.46)$$

with the operator $\mathrm{num}(n(x)/d(x)) = n(x)$, which takes the numerator of a irreducible rational function $n(x)/d(x)$. By taking the derivative of (6.38) with respect to τ and solving the result for $\frac{\mathrm{d}\lambda}{\mathrm{d}\tau}$, the sensitivity reads

$$\frac{\mathrm{d}\lambda}{\mathrm{d}\tau} = -\frac{b_1 k_2 \lambda^2}{\mathrm{e}^{\tau\lambda}} \left(\frac{\mathrm{d}g_\mathrm{CF}}{\mathrm{d}\tau}\right)^{-1}. \quad (6.47)$$

with

$$\frac{\mathrm{d}g_\mathrm{CF}}{\mathrm{d}\tau} = \left[\lambda\left(3a_3\lambda + 2a_2 + 4\lambda^2\right) + a_1 - b_1 k_1\right] + b_1 k_2 (\tau\lambda - 1).$$

Inserting (6.47) into (6.46) and sorting terms, results in

$$d = -b_1 k_2 \omega_\mathrm{C}^2 \left[\left(b_1 k_1 - a_1 + 3a_3\omega_\mathrm{C}^2\right)\cos\left(\tau_\mathrm{H}\omega_\mathrm{C}\right) + \left(2a_2\omega_\mathrm{C} - 4\omega_\mathrm{C}^3\right)\sin\left(\tau_\mathrm{H}\omega_\mathrm{C}\right) + b_1 k_2\right]. \quad (6.48)$$

Eq. (6.48) can be transformed into a quartic polynomial by asserting $d = 0$, applying $\sin^2(\tau_\mathrm{H}\omega_\mathrm{C}) + \cos^2(\tau_\mathrm{H}\omega_\mathrm{C}) = 1$, inserting (6.41) into (6.48), and sorting terms. As the number and value of the roots of this quartic polynomial has to be investigated to analyze the crossing condition (H2), further analytic analysis of (6.48) is rather involved. Hence, the crossing condition (H2) is evaluated by determining (6.48) numerically.

Steepest Change of the Characteristic Frequency By controlling the Andronov-Hopf bifurcation with a time delay, the characteristic frequency becomes a nonlinear function of the feedback strengths k_1 and k_2, so that $\omega_C = \omega_C(k_1, k_2)$ holds true. To demonstrate the effects of the controllable time delay on the characteristic frequency, the steepest change of the characteristic frequency is considered. This is done by exploiting the normalized gradient, so that the optimal feedback $\boldsymbol{k}_o = [k_{1,o}, k_{2,o}]^T$ is determined by

$$\boldsymbol{k}_o[j+1] = \boldsymbol{k}_o[j] + (-1)^l \frac{\epsilon \nabla \omega_C(\boldsymbol{k}_o[j])}{\|\nabla \omega_C(\boldsymbol{k}_o[j])\|}, \qquad \boldsymbol{k}_o[0] = \boldsymbol{k}_0$$

with the gradient $\nabla\omega_C(\boldsymbol{k}_o[j]) \in \mathbb{R}^2$, the step size $\epsilon > 0$, and the initial conditions $\boldsymbol{k}_0 \in \mathbb{R}$ for all $l = 1, 2$. Here, the index l is utilized to assign the direction of the steepest change. If $l = 1$ holds true, the feedback $\boldsymbol{k}_o$ follows the steepest decent. In contrast, the direction of the feedback $\boldsymbol{k}_o$ follows the steepest ascend, if $l = 2$. In addition, the gradient reads

$$\nabla\omega_C = \begin{bmatrix} -\frac{b_1\omega_C}{C}\sqrt{b_1^2k_2^2\omega_C^2 - \left(\omega_C^4 - a_2\omega_C^2 + a_0\right)^2} \\ -\operatorname{sign}(b_1k_2)\frac{b_1^2k_2\omega_C^2}{C} \end{bmatrix}$$

with

$$C = 2\left(a_2 - 2\omega_C^2\right)\left(\omega_C^4 - a_2\omega_C^2 + a_0\right)\omega_C + b_1^2k_2^2\omega_C + \left[b_1k_1 + 3a_3\omega_C^2 - a_1\right]\sqrt{b_1^2k_2^2\omega_C^2 - \left(\omega_C^4 - a_2\omega_C^2 + a_0\right)^2}.$$

The conditions (6.44) and $|k_1 + k_2| < |k_H^{\pm}|$ can be imposed to keep the oscillator (6.34) in the sub-critical regime.

Numerical Results

Subsequently, the remainder of the bifurcation analysis is done numerically since the number of real-valued zeros of a quartic polynomial is difficult to evaluate analytically. For this, the parameters from Table A.6 in Appendix A are used and the critical points in the delay-free case read $k_H^+ = 1.0525$ and $k_H^- = -2.1101$. The analysis is done as follows: First, the zeros of (6.43) are localized by evaluating its discriminant and its auxiliary variables. The approach is summarized in the following theorem.

Theorem 6.4 ([111]) *Denote the quartic polynomial $P = x^4 + a_3x^3 + a_2x^2 + a_1x + a_0$ with the coefficients $a_i \in \mathbb{R}$ for all $i = 1, 2, 3, 4$ and let*

$$\begin{aligned} D = &-27a_1^4 - 4a_3^3a_1^3 + 18a_2a_3a_1^3 - 4a_2^3a_1^2 + a_2^2a_3^2a_1^2 - 6a_0a_3^2a_1^2 \\ &+ 144a_0a_2a_1^2 + 18a_0a_2a_3^3a_1 - 192a_0^2a_3a_1 - 80a_0a_2^2a_3a_1 + 16a_0a_2^4 \\ &- 27a_0^2a_3^4 + 256a_0^3 - 128a_0^2a_2^2 - 4a_0a_2^3a_3^2 + 144a_0^2a_2a_3^2 \end{aligned}$$

Then the zeros of P can be characterized as follows:

- *If $D < 0$, the zeros of P are distinct and there are two real-valued and a pair of complex-conjugated zeros.*
- *If $D > 0$, the zeros of P are distinct and there are either real-valued or complex valued. In addition,*
  - *if $a_3 < 0$ and $a_0 > \frac{a_3^2}{4}$ or $a_3 \geq 0$, all zeros of P are complex-valued,*
  - *if $a_3 < 0$ and $a_0 < \frac{a_3^2}{4}$, all zeros of P are real-valued.*

Second, the emergence of Andronov-Hopf bifurcations is investigated by computing the necessary condition (H1) and the crossing condition (H2) numerically in terms of the feedback strengths k_1 and k_2. Finally, the results of the bifurcation analysis are refined by determining the steepest change of the characteristic frequency ω_{H}.

Number of Critical Points The discriminant of (6.43) and its corresponding auxiliary variables are evaluated to determine the number of the real-valued zeros. Combing the real-valued zeros with (6.44) the positive zeros can be deduced. The results are shown in Figure 6.16. Here, it can be deduced by comparing Figure 6.16b and 6.16c that the real-valued zeros of (6.44) can be positive and negative. Hence, the constraint (6.44) is needed to determine the critical points. Thus, the number of critical points varies between 2 and 4.

Bifurcation Analysis To investigate the necessary condition (H1) and to show frequency tunability, (6.43) is solved for the characteristic frequency $\omega_{\mathrm{C},m}$ numerically and the critical delay is obtained by computing

$$\tau_{\mathrm{H},m}[l] = \frac{1}{\omega_{\mathrm{C},m}} \left[\arcsin\left(\frac{\omega_{\mathrm{H},m}^4 - a_2\omega_{\mathrm{H},m}^2 + a_0}{k_2 b_1 \omega_{\mathrm{H},m}} \right) + 2\pi l \right] \tag{6.49}$$

for $l \in \mathbb{Z}$ and $m = 1, 2, 3, 4$. Subsequently, only the critical points for $l = 0$ are considered. The results are depicted in Figure 6.17, so that the visualization is simplified. This can be done since the characteristic frequencies $f_{\mathrm{C},m}$ remain constant and the critical delays $\tau_{\mathrm{H},m}[l]$ are increased by the constant $2\pi l/f_{\mathrm{C},m}$. Here, the dynamic regimes of (6.34) are divided into the sub-critical regime (see Figure 6.17b, 6.17d, and 6.17f) and the complete dynamics (see Figure 6.17a, 6.17c, and 6.17e). In particular, the sub-critical regime can be determined by imposing $|k_1 + k_2| \leq |k_{\mathrm{H}}^{\pm}|$ with the critical feedback strength $k_{\mathrm{H}}^{\pm}$ from Theorem 6.1.

It is can be deduced from Figures 6.17a-6.17d that the bifurcations emerging from the controllable delay τ are related to the bifurcations emerging from the feedback strength $k_1 + k_2$ as $\tau_{\mathrm{H},1} = \tau_{\mathrm{H},2} = 0$ (or $\tau_{\mathrm{H},3} = \tau_{\mathrm{H},4} =$, respectively), if $k_1 + k_2 = k_{\mathrm{H}}^{+}$ (or $k_1 + k_2 = k_{\mathrm{H}}^{-}$, respectively) holds true. In addition, frequency tunability is demonstrated in Figures 6.17e and 6.17f. In comparison to the other methods, the characteristic frequency can be increased and decreased.

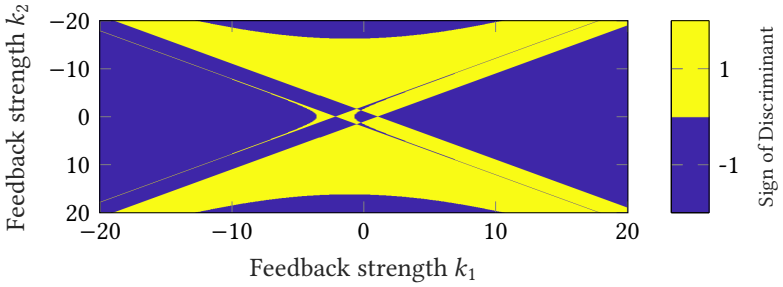

(a) Sign of the discriminant of the polynomial (6.45).

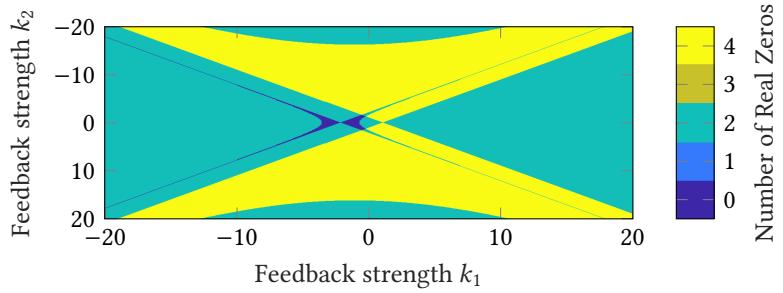

(b) Number of real-valued zeros of the polynomial (6.45).

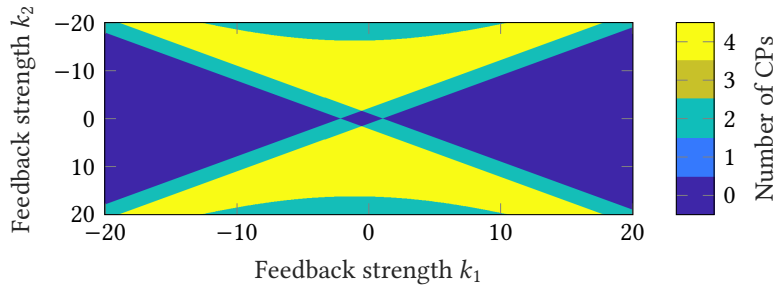

(c) Number of positive zeros of the polynomial (6.45) and the number of critical points (CPs) of (6.34).

Figure 6.16.: Color map of the discriminant, the number of real zeros, and the number of positive zeros of the polynomial (6.45).

Moreover, the crossing condition (H2) is evaluated by computing the sign of (6.48) in terms of the feedback strengths k_1 and k_2. The results are illustrated in Figure 6.18. Here, it is demonstrated that the sign of (6.48) remains constant for all feedback strengths k_1 and k_2. The direction in which a pair of complex conjugated eigenvalues travel is given as follows: A pair of eigenvalues travels from the complex right half-plane to the left half-plane, if the critical delays $\tau_{\mathrm{H},2}$ and τ_{H_4} are surpassed. In contrast, if the critical delays $\tau_{\mathrm{H},1}$ and τ_{H_3} are surpassed, a pair of eigenvalues travels from the complex left half-plane to the right half-plane. Hence, if

$$(\tau > \tau_{\mathrm{H},2}[l] \wedge \tau_{\mathrm{H},2}[l] < \tau_{\mathrm{H},2}[l]) \vee (\tau > \tau_{\mathrm{H},4}[l] \wedge \tau_{\mathrm{H},4}[l] < \tau_{\mathrm{H},3}[l]).$$

holds true for all $l \in \mathbb{Z}$, the characteristic frequency can be decreased.

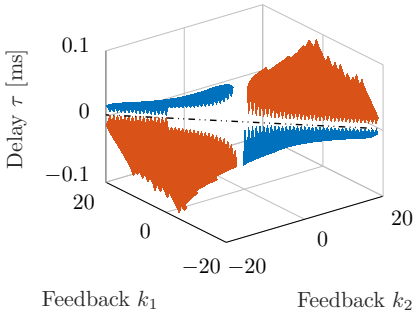

(a) Critical delays emerging from k_{H}^{+}.

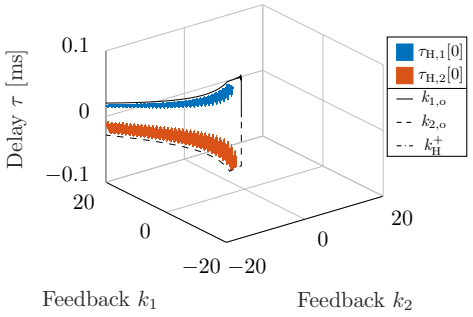

(b) Critical delays emerging from k_{H}^{+} in the sub-critical regime.

(c) Critical delays emerging from k_{H}^{-}.

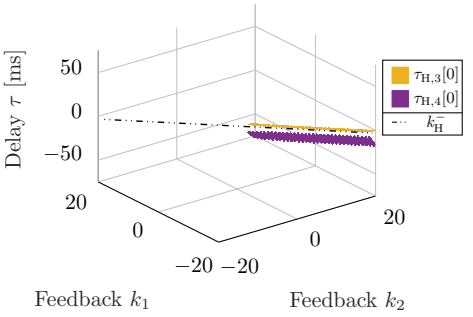

(d) Critical delays emerging from k_{H}^{-} in the sub-critical regime.

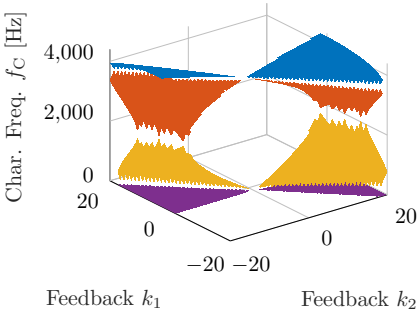

(e) Characteristic frequencies $f_{\mathrm{H},1}$, $f_{\mathrm{H},2}$, $f_{\mathrm{H},3}$, and $f_{\mathrm{H},4}$.

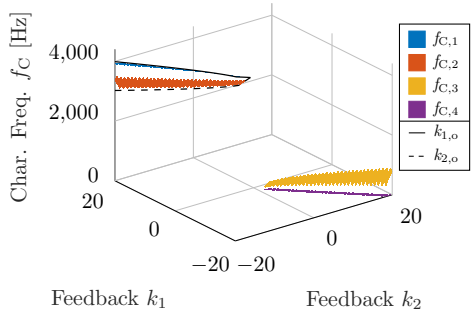

(f) Characteristic frequencies $f_{\mathrm{H},1}$, $f_{\mathrm{H},2}$, $f_{\mathrm{H},3}$, and $f_{\mathrm{H},4}$ in the sub-critical regime.

Figure 6.17.: Critical delays $\tau_{\mathrm{H},m}[0]$, critical feedback strengths $k_{\mathrm{H}}^{\pm}$, and characteristic frequencies $f_{\mathrm{H},m}$ at the critical point for all $m = 1, 2, 3, 4$ as a function of the feedback strengths k_1 and k_2. The critical delay and characteristic frequency in terms of the steepest change $\boldsymbol{k}_{\mathrm{o}}$ are visualized by the solid and dashed line.

Steepest Change To visualize the frequency tunability further, the characteristic frequencies $\omega_{\mathrm{H},1}$ and $\omega_{\mathrm{H},2}$ and positive critical delays $\tau_{\mathrm{H},1}$ and $\tau_{\mathrm{H},2}$ as a function of k_1 for the steepest change are computed numerically. For this, the numerical parameters are assumed to be he initial conditions $k_{1,0} = 1.001 \times k_{\mathrm{H}}^{+}$ and $k_{1,0} = -0.001 \times k_{\mathrm{H}}^{+}$ and the weight $\epsilon = 3.45 \times 10^{-3}$. On the one hand, the steepest change of the time delays $\tau_{\mathrm{H},1}$ and $\tau_{\mathrm{H},2}$ and characteristic frequencies $f_{\mathrm{H},1}$ $f_{\mathrm{H},2}$ in the sub-critical regime is depicted by the solid lines and dashed lines in Figures 6.17b and 6.17f depict. Here, it showcased that

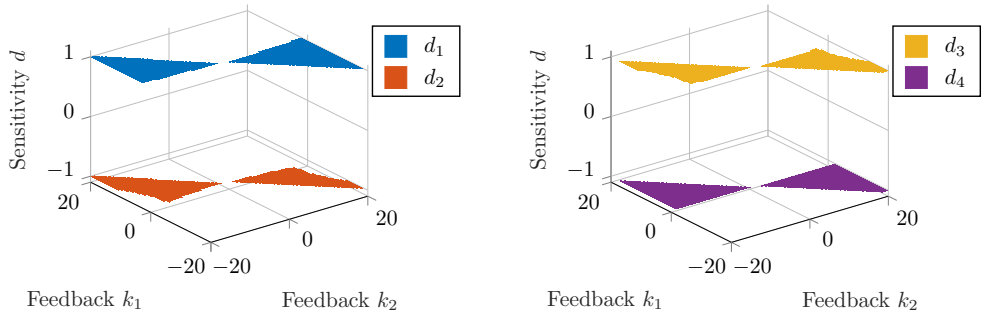

(a) Sign of the sensitivities d_1 and d_2.

(b) Sign of the sensitivities d_3 and d_4.

Figure 6.18.: Sign of the sensitivities d_1, d_2, d_3, and d_4 at their respective critical points.

the steepest change in the sub-critical regime either follows the conditions (6.44) or it is constrained by $|k_1 + k_2| < |k_{\mathrm{H}}^{\pm}|$. On the other hand, the characteristic frequencies $\omega_{\mathrm{H},1}$ and $\omega_{\mathrm{H},2}$ and positive critical delays $\tau_{\mathrm{H},1}$ and $\tau_{\mathrm{H},2}$ of the steepest change are illustrated Figure 6.19. By following the steepest change, the visualization is significantly simplified and the tunability is easier to analyze as the number of tunability parameters is reduced. With this reduction, it is demonstrated that the emerging Andronov-Hopf bifurcations are similar to the numerical results of Example 3.9. Hence, the characteristic frequency has a lower limit in the sub-critical regime, since a Hopf-Hopf bifurcation is induced. Finally, the eigenvalue, which is closest to the imaginary axis, is depicted in Figure 6.20. It is showcased that the characteristic frequency is also tunable in the sub-critical regime by assigning the feedback k_1 and k_2.

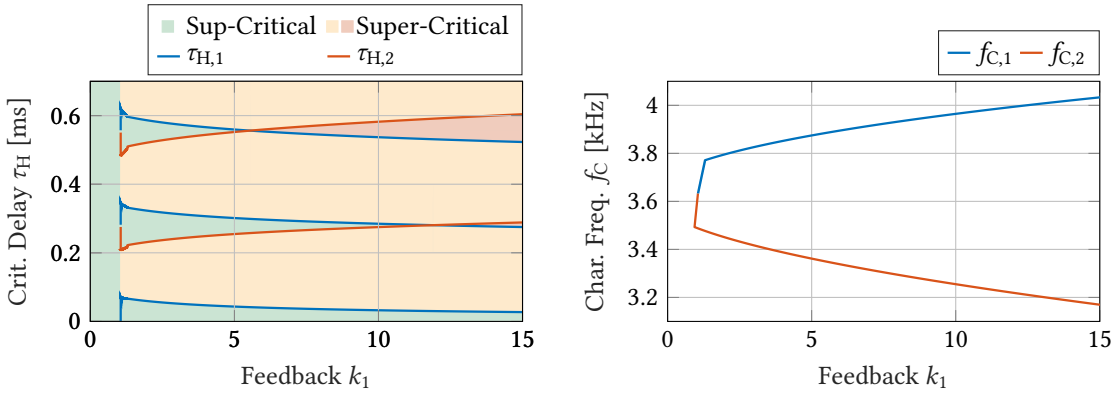

(a) Critical delays $\tau_{\mathrm{H},1}$ and $\tau_{\mathrm{H},2}$ following the steepest change of the characteristic frequency $\omega_{\mathrm{C},1}$ and $\omega_{\mathrm{C},2}$.

(b) Steepest change of the characteristic frequency $\omega_{\mathrm{C},1}$ and $\omega_{\mathrm{C},2}$.

Figure 6.19.: Dynamics of system (6.34) for the steepest change of the characteristic frequency. The normalized frequency given by $f_{\mathrm{H}} = \omega_{\mathrm{H}}/(2\pi)$.

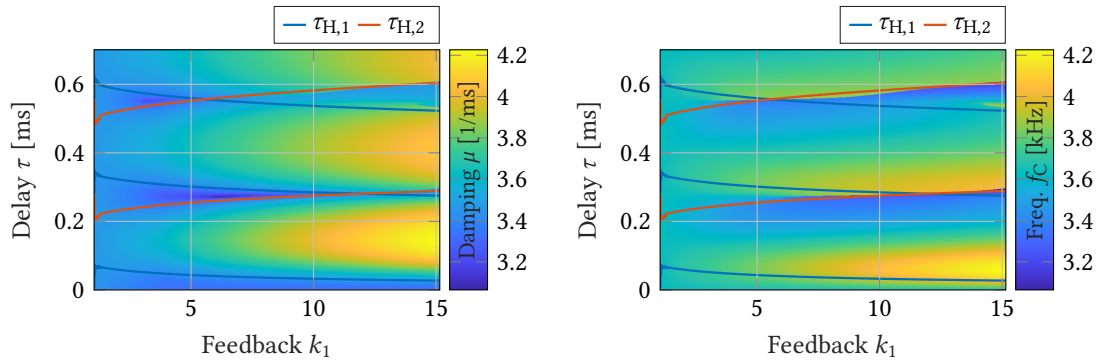

(a) Real part of the eigenvalue, which are closest to the imaginary axis.

(b) Imaginary part of the eigenvalue, which are closest to the imaginary axis.

Figure 6.20.: Eigenvalue, which are closest to the imaginary axis, as a function of the delay τ and the feedback strength k_1. The normalized frequency given by $f_H = \omega_H/(2\pi)$.

6.3.4. Consequences for the Controller Design based on Andronov-Hopf Oscillators

The controllers, which have been designed based on the Andronov-Hopf oscillator, have successfully enabled frequency tunability and controllable Andronov-Hopf bifurcations for the oscillator model (6.1). Hence, nonlinear controllers designed based on normal forms can be exploited to predict the local dynamics of (general) nonlinear systems. In addition, all emerging Andronov-Hopf bifurcations, which have been induced by diffusive coupling or a controllable delay, can be explained by the dynamics of the Andronov-Hopf oscillators with the same controller since the controllers operate the MEMS in a neighborhood of the critical points of the MEMS with proportional feedback. In contrast to diffusive coupling and a controllable delay, the emerging bifurcations induced by injective coupling cannot be completely predicted by the normal form based controller. This comes from the fact that non-local interactions between the oscillators emerged. These induce an additional Andronov-Hopf bifurcation, which inhibits the performance of the controller. In comparison to MEMS with geometric nonlinearities, these proposed controllers are a promising approach to enable frequency tunability since they are implementable on a FPGA. Hence, frequency tunability can even be induced in MEMS with simple geometry. In addition, it has been observed in [79, 155] that the external stimuli can tune the characteristic frequency in a MEMS with a geometric nonlinearity. This results in a frequency modulation of the external stimuli, so that the external signal cannot be recovered as the carrier frequency of the modulation is unknown. This effect cannot be observed in the oscillators with the controllers based on the normal form.

Part IV.

Summary and Outlook

7. Conclusions

In the following, a short summary of the presented results and an outlook to future research activities is provided.

7.1. Summary

In this work, the controller design to enable and exploit frequency tunability while maintaining a controllable Andronov-Hopf bifurcation is proposed for neuromorphic acoustic sensors. Here, it is assumed that neuromorphic acoustic sensors are based on oscillators, which exhibit at least one controllable Andronov-Hopf bifurcation. This comes from the fact that the response of these oscillators to an external stimuli is similar to the response of the cochlea, i.e., both systems have a frequency-selective and compressive response in the sub-critical regime when they are excited.

To enable frequency tunability in a nonlinear system, different controllers have been designed for the Andronov-Hopf oscillator. This oscillator model is given by the super-critical normal form of the Andronov-Hopf bifurcation and it can be viewed as a benchmark oscillator model for neuromorphic acoustic sensors. It is demonstrated that the controllers, which are based on coupling and a controllable time delay, can be utilized to enhance frequency tunability, while preserving the controllable Andronov-Hopf bifurcations in the oscillator. For injectively coupled oscillators, an optimal network topology has been proposed to control the maximum number of Andronov-Hopf bifurcations, which have a tunable characteristic frequency at their critical point. It is showcased that the characteristic frequency can be tuned in an interval, which is not directly restricted by the natural frequency of the individual oscillators. In contrast to this, the dynamics of diffusively coupled oscillators become more complicated, so that two diffusively coupled Andronov-Hopf oscillators have been investigated analytically. Frequency tunability has been demonstrated and depending on the bifurcation parameter, the number of critical points varies. For a controller based on a controllable time delay, the emerging Andronov-Hopf bifurcations can be separated into two classes, which are characterized by their characteristic frequency. This comes form the fact that the characteristic frequency at the critical point can be either increased or decreased.

To verify the controller design based on the benchmark oscillator,a MEMS is considered. This system is modeled by two coupled PDEs given by the mechanical and the thermodynamic subsystem of the MEMS. On the one hand, the mechanical subsystem is derived by applying the extended Hamiltonian principle on an Euler-Bernoulli beam. On the other

hand, the thermodynamic subsystem is the generalized heat conduction for thermoelastic systems. Moreover, both subsystems are coupled by the Duhamel-Neumann law. To simplify the bifurcation analysis of the MEMS model, the mechanical subsystem is approximated by the Rayleigh-Ritz method and the thermodynamic subsystem is approximated by the Galerkin method. With this, an a nonlinear finite-dimensional ODE representation is obtained that is used to show that the MEMS exhibits controllable Andronov-Hopf bifurcations by properly feeding back the measured deflection of the MEMS. Therefore, this oscillator model can be used to verify the performance of the controller, which is designed based on the benchmark oscillator model. It is demonstrated that the predicted frequency tunability is enabled by coupling the oscillators or delaying the feedback.

Moreover, superordinate controllers are proposed to enable an in-sensor Fourier transform by mimicking the frequency decomposition of the basilar membrane. It is shown that the in-sensor Fourier transform can achieved using an array of frequency-selective oscillators. This approach is investigated for Andronov-Hopf oscillators. If the characteristic frequency is untunable, the frequency spectrum can be sampled by exploiting many oscillators. By additionally asserting that the oscillators are frequency tunable, the number of oscillators can be decreased by different algorithms, such as sequential sampling, to sample the frequency domain. In particular, sequential sampling, which is motivated by sampling of a time series, is compared to a machine-learning based approach. It turns out that the latter approach is able to outperform sequential sampling in various examples.

7.2. Outlook

Finally, an outlook to future research activities is provided.

7.2.1. Emergence of Andronov-Hopf Bifurcations

The emergence of Andronov-Hopf bifurcations has to be analyzed further, since only the first order dominant mode model of the MEMS has been considered. Even though this model is validated in experiments as shown in [81, 136, 150], the influence of the higher modes should be investigated. For this, either the bifurcation of a higher order dominant mode model or the bifurcation of the PDE model of the MEMS should be analyzed. However, even the ODE of the second order dominant mode model has at least a dimension[1] of 6. For this 6th order ODE, it can be shown that the necessary condition is satisfied by solving the zeros of a quartic polynomial in terms of the feedback strength. Yet, the characterization of the locations of the zeros is rather involving, since the discriminant of this quartic polynomial and its auxiliary parameters are a highly nonlinear system of equations in

[1] To derive this model, the mechanical subsystem is approximated by the second order dominant mode model, while the thermodynamic subsystem is described by a first order model. This can be done since the higher modes of the thermodynamic subsystem are more difficult to be excited by acoustic stimuli, which is band limited from 20 Hz and 20 kHz [50, 121].

terms of the system parameter of the MEMS. Hence, numerical methods have to be applied to analyze the critical points of these bifurcations even for the second order dominant mode model.

7.2.2. Further Investigation of the Benchmark Oscillator Model and Tunability

The benchmark oscillator model and its results towards the tunability enhancement have to be investigated further in two way: First, the tunability of other properties of an oscillator, which exhibits a controllable Andronov-Hopf bifurcation, has to be characterized. For instance, the desired (linear) gain and the amplitude, where compression begins, can be tuned by adjusting the bifurcation parameter and the nonlinearity of the system. With this, the response of the oscillator can be optimally chosen for different environments. In particular, the compression can, e.g., be used to introduce redundancy in the measured signal, so that two different signals can be separated [70]. Second, the relationship between the dominant model of the MEMS and the normal form of the Andronov-Hopf bifurcation has to be established. For this different methods, e.g., the perturbation method, can be used to approximate this relationship [49, 51].

7.2.3. Alternative Sensor Designs and Actuations

The sensor design and actuation can be changed to improve the performance of the neuromorphic acoustic sensor. For instance, an additional layer of shape memory alloy might introduce additional nonlinearities, such the characteristic frequency can be tuned in a larger interval. In addition, the actuation can also be done with a piezo-electric layer or the MEMS could be actuated by impulses. For instance, the impulsive actuation can be investigated by assuming fixed and periodic impulses so that the Floquet Theory can be applied to investigate the so-called Floquet spectrum, which can be used to analyze the bifurcations of an impulsive ODE [22].

Part V.

Appendix

A. Parameters of the Numerical Evaluations

A.1. Parameters in Chapter 4

Subsequently, the numerical parameters in Section 4.3 are given in Table A.1 and Table A.2.

Table A.1.: Numerical parameters of the Sampler of the Frequency Domain.

Parameters			Value
Damping	μ	$[\frac{1}{s}]$	-800
Minimal Frequency	ω_{min}	$[\frac{1}{s}]$	$2\pi \cdot 2000$
Maximal Frequency	ω_{min}	$[\frac{1}{s}]$	$2\pi \cdot 3800$
Spacing	ω_{Δ}	$[\frac{1}{s}]$	$2\pi \cdot 200$
Number of Explorations	m_{ex}	/	9
Forgetting Rate	a	/	0.01

Table A.2.: Numerical parameters for the three different scenarios.

Parameters			Scenario 1	Scenario 2	Scenario 3
Amplitude	ρ_1	/	$5 \cdot 10^{-4}$	$2 \cdot 10^{-4}$	$2 \cdot 10^{-4}$
	ρ_2	/	$1 \cdot 10^{-4}$	$2 \cdot 10^{-4}$	$2 \cdot 10^{-4}$
Frequency	ω_1	$[\frac{1}{\mathrm{s}}]$	$2\pi \cdot 2600$	$2\pi \cdot 2600$	$2\pi \cdot 2600$
	ω_2	$[\frac{1}{\mathrm{s}}]$	$2\pi \cdot 3400$	$2\pi \cdot 3400$	$2\pi \cdot 4400$
Phase	φ_1	/	0	0	0
	φ_2	/	$\frac{\pi}{2}$	$\frac{\pi}{2}$	$\frac{\pi}{2}$
Convergence number	$m^{\mathrm{RF}}_{\mathrm{conv},1}$	/	4	4	4
	$m^{\mathrm{RF}}_{\mathrm{conv},2}$	/	3	3	3
	$m^{\mathrm{RF}}_{\mathrm{conv},3}$	/	2	2	2
	$m^{\mathrm{RF}}_{\mathrm{conv},4}$	/	1.5	2	2
Convergence Time	$T_{\mathrm{RF},1}$	[s]	$1 \cdot T_{\mathrm{seq}}$	$1 \cdot T_{\mathrm{seq}}$	$1 \cdot T_{\mathrm{seq}}$
	$T_{\mathrm{RF},2}$	[s]	$0.875 \cdot T_{\mathrm{seq}}$	$1 \cdot T_{\mathrm{seq}}$	$1 \cdot T_{\mathrm{seq}}$
	$T_{\mathrm{RF},3}$	[s]	$0.75 \cdot T_{\mathrm{seq}}$	$1 \cdot T_{\mathrm{seq}}$	$1 \cdot T_{\mathrm{seq}}$
	$T_{\mathrm{RF},4}$	[s]	$0.5 \cdot T_{\mathrm{seq}}$	$0.75 \cdot T_{\mathrm{seq}}$	$0.75 \cdot T_{\mathrm{seq}}$
Number of Maxima	$n_{\mathrm{max},1}$	/	1	2	1
	$n_{\mathrm{max},2}$	/	1	2	1
	$n_{\mathrm{max},3}$	/	1	2	2
	$n_{\mathrm{max},4}$	/	1	2	1

A.2. Clamped-Clamped MEMS

Subsequently, the numerical parameters of the clamped-clamped MEMS sensors are depicted in Table A.3.

Table A.3.: Parameters of the clamped-clamped MEMS sensor.

Parameter			MEMS Sensor
Natural Frequency	f_0	[Hz]	3630
Spring Constant	c_3	$[\frac{1}{\mathrm{m}^2 \cdot \mathrm{s}^2}]$	$36.38 \cdot 10^7$
Q-Factor	Q	/	80
Calibration factor	κ	$[\frac{\mathrm{V}}{\mathrm{m}}]$	$17.12 \cdot 10^5$
Resistance	R	$[\Omega]$	12.5
Transfer factor	α	$[\frac{\mathrm{m}^2}{\mathrm{K} \cdot \mathrm{s}^2}]$	19.2
	$\alpha\gamma$	$[\frac{\mathrm{K} \cdot \mathrm{m}^2}{\mathrm{A}^2 \cdot \mathrm{K}^2 \cdot \mathrm{s}^3}]$	$64.53 \cdot 10^6$
Time constant	β	$[\frac{1}{\mathrm{s}}]$	147.5
	T	[s]	$1 \cdot 10^{-3}$

A.3. Injectively Coupled MEMS

Subsequently, the numerical parameters of the injectively MEMS are given in Table A.4.

Table A.4.: Parameters of the injectively coupled MEMS.

Parameter			MEMS Sensor	
			1	2
Natural Frequency	f_0	[Hz]	3630	3790
Spring Constant	c_3	$[\frac{1}{\mathrm{m^2 s^2}}]$	0	
Q-Factor	Q	/	40, 80	
Calibration factor	κ	$[\frac{\mathrm{V}}{\mathrm{m}}]$	$17.12 \cdot 10^5$	
Resistance	R	$[\Omega]$	12.5	
Transfer factor	α	$[\frac{\mathrm{m^2}}{\mathrm{Ks^2}}]$	19.2	
	$\alpha\gamma$	$[\frac{\mathrm{Km^2}}{\mathrm{A^2 K^2 s^3}}]$	$64.53 \cdot 10^6$	
Time constant	β	$[\frac{1}{\mathrm{s}}]$	147.5	
	T	[s]	$1 \cdot 10^{-3}$	
DC-Voltage	u_{DC}	[mV]	200	

A.4. Two Diffusively Coupled MEMS

Subsequently, the numerical parameters of the two diffusively coupled MEMS are given in Table A.5.

Table A.5.: Parameters of the diffusively coupled MEMS.

Parameter			MEMS Sensor	
			1	2
Natural Frequency	f_0	[Hz]	3630	3790
Spring Constant	c_3	$[\frac{1}{\mathrm{m}^2 \cdot \mathrm{s}^2}]$	0	
Q-Factor	Q	/	40	
Calibration factor	κ	$[\frac{\mathrm{V}}{\mathrm{m}}]$	$17.12 \cdot 10^5$	
Resistance	R	$[\Omega]$	12.5	
Transfer factor	α	$[\frac{\mathrm{m}^2}{\mathrm{K}^{\ldots 2}}]$	19.2	
	$\alpha\gamma$	$[\frac{\mathrm{K} \cdot \mathrm{m}^2}{\mathrm{A}^2 \cdot \mathrm{K}^2 \cdot \mathrm{s}^3}]$	$64.53 \cdot 10^6$	
Time constant	β	$[\frac{1}{\mathrm{s}}]$	147.5	250
	T	[s]	$1 \cdot 10^{-3}$	
DC-Voltage	u_{DC}	[mV]	200	

A.5. MEMS with Controllable Delay

Subsequently, the numerical parameters of the MEMS with a controllable delay are given in Table A.6.

Table A.6.: Parameters of the MEMS with controllable delay.

Parameter			Value
Natural Frequency	f_0	[Hz]	3630
Spring Constant	c_3	$[\frac{1}{\mathrm{m}^2 \cdot \mathrm{s}^2}]$	0
Q-Factor	Q	/	40
Calibration factor	κ	$[\frac{\mathrm{V}}{\mathrm{m}}]$	$17.12 \cdot 10^5$
Resistance	R	$[\Omega]$	12.5
Transfer factor	α	$[\frac{\mathrm{m}^2}{\mathrm{K} \cdot \mathrm{s}^2}]$	19.2
	$\alpha\gamma$	$[\frac{\mathrm{K} \cdot \mathrm{m}^2}{\mathrm{A}^2 \cdot \mathrm{K}^2 \cdot \mathrm{s}^3}]$	$64.53 \cdot 10^6$
Time constant	β	$[\frac{1}{\mathrm{s}}]$	147.5
	T	[s]	$1 \cdot 10^{-3}$
DC-Voltage	u_{DC}	[mV]	200

B. Auxiliary Equations

Auxiliary equations for the bifurcation analysis of three coupled Andronov-Hopf oscillators and for the critical point of two coupled MEMS are subsequently summarized.

B.1. Three Coupled Andronov-Hopf Oscillators

The equations for the cubic polynomial to determine the critical point of three coupled Andronov-Hopf oscillators, and coefficients for polynomials to prove the emerging of Andronov-Hopf bifurcations are summarized.

B.1.1. Cubic Polynomial to Determine the Critical Points

$$
\begin{aligned}
P_{\mathrm{N}} = &\left[a_2^2 a_0\left(a_1^2 - 2b_2 b_0\right) + b_1^2\left(a_2 b_2 b_0 - a_0 c_1\right) + b_1\left(b_2 a_0\left(a_2 a_1 - a_0\right) + a_2 b_0\left(a_2 a_1 + 3a_0\right)\right)\right. \\
&\left. + a_2 a_0^2\left(b_2^2 + 2a_1\right) + a_2^3 b_0^2 - b_1^3 b_0 + a_0^3\right] + \left[a_0\left(b_1\left(a_2 b_2 - b_1\right) + 2a_1 a_2^2\right) + a_2^2 b_0 b_1\right. \\
&\left. + 2a_2 a_0^2\right] v_2(\mathbf{1}) + \left[2a_2^3 b_0 + a_2^2\left(a_1 b_1 - 2a_0 b_2\right) + a_2 b_1\left(3a_0 + b_1 b_2\right) - b_1^3\right] v_2(\boldsymbol{\omega}) \\
&+ \left[2a_0\left(b_2\left(a_2 b_2 - b_1\right) + 2a_1 a_2\right) + a_2 b_0\left(3b_1 - 2a_2 b_2\right) + a_1 b_1\left(a_2 b_2 - b_1\right) + 3a_0^2\right. \\
&\left. + a_1^2 a_2^2\right] v_2(\boldsymbol{\mu}) - \left[2a_0\left(b_2\left(a_2 b_2 - b_1\right) + 2a_1 a_2\right) + a_2 b_0\left(3b_1 - 2a_2 b_2\right) + a_1 b_1\left(a_2 b_2 - b_1\right)\right. \\
&\left. + 3a_0^2 + a_1^2 a_2^2\right] v_3 - a_2^3 v_2^2(\boldsymbol{\omega}) + a_2\left(2a_2 b_2 - 3b_1\right) v_2(\boldsymbol{\omega}) v_2(\boldsymbol{\mu}) - a_2^2 b_1 v_2(\mathbf{1}) v_2(\boldsymbol{\omega}) \\
&- \left[b_2\left(a_2 b_2 - b_1\right) + 3a_0 + 2a_1 a_2\right] v_2^2(\boldsymbol{\mu}) - \left[b_1\left(a_2 b_2 - b_1\right) + 2a_1 a_2^2 + 4a_0 a_2\right] v_2(\mathbf{1}) v_2(\boldsymbol{\mu}) \\
&- a_0 a_2^2 v_2^2(\mathbf{1}) + \left[a_2\left(3b_1 - 2a_2 b_2\right)\right] v_3 v_2(\boldsymbol{\omega}) + \left[2\left(b_2\left(a_2 b_2 - b_1\right) + 3a_0 + 2a_1 a_2\right)\right] v_3 v_2(\boldsymbol{\mu}) \\
&+ \left[b_1\left(a_2 b_2 - b_1\right) + 2a_1 a_2^2 + 4a_0 a_2\right] v_3 v_2(\mathbf{1}) - \left[b_2\left(a_2 b_2 - b_1\right) + 3a_0 + 2a_1 a_2\right] v_3^2 + v_2^3(\boldsymbol{\mu}) \\
&+ 2a_2 v_2^2(\mathbf{1}) v_2(\boldsymbol{\mu}) + a_2^2 v_2(\mathbf{1}) v_2^2(\boldsymbol{\mu}) - 3v_3 v_2^2(\boldsymbol{\mu}) - 4a_2 v_3 v_2(\mathbf{1}) v_2(\boldsymbol{\mu}) - a_2^2 v_3 v_2^2(\mathbf{1}) \\
&+ 3v_3^2 v_2(\boldsymbol{\mu}) + 2a_2 v_3^2 v_2(\mathbf{1}) - v_3^3. \qquad \text{(B.1)}
\end{aligned}
$$

B.1.2. Coefficients of the Function Determining the Number of Andronov-Hopf Bifurcations Induced by the Line Graph

$$
\begin{aligned}
d_{000} =& a_0^2 \left(b_1 \left(2\omega_3 \left(4a_2+3\mu_3\right)-2b_2\mu_3\right)+20a_2b_2\mu_3\omega_3+36a_2\mu_3\omega_3^2-12a_1\mu_3\left(a_2+\mu_3\right)\right.\\
&+8a_2^2\omega_3^2+18b_2\mu_3^2\omega_3-b_2^2\mu_3^2-b_1^2+27\mu_3^2\omega_3^2\left.\right)+2a_0\left(3a_1b_1\mu_3^2\omega_3-9a_1b_2\mu_3^3\omega_3\right.\\
&-2a_2^2\omega_3\left(\omega_3\left(\omega_3\left(3b_2\mu_3-2b_1\right)-5a_1\mu_3\right)+9b_0\mu_3\right)+a_2\left(a_1\mu_3\omega_3\left(\mu_3\left(9\omega_3-11b_2\right)\right.\right.\\
&\left.+b_1\right)+6a_1^2\mu_3^2-9b_0\mu_3\left(\mu_3\left(b_2+5\omega_3\right)+b_1\right)+\omega_3^2\left(b_1\mu_3\left(b_2+9\omega_3\right)+6b_2^2\mu_3^2+b_1^2\right)\left.\right)\\
&+a_1b_2^2\mu_3^3+2a_1b_1b_2\mu_3^2+a_1b_1^2\mu_3+6a_1^2\mu_3^3+2a_2^3\omega_3^4-9b_1b_2\mu_3^2\omega_3^2-3b_1^2\mu_3\omega_3^2-b_1^3\omega_3\\
&-2b_2^3\mu_3^3\omega_3-27b_0\mu_3^3\omega_3-5b_1b_2^2\mu_3^2\omega_3-4b_1^2b_2\mu_3\omega_3-9b_0b_2\mu_3^3-9b_0b_1\mu_3^2\left.\right)\\
&-\left(a_1\mu_3+b_1\omega_3\right)^2\left(2b_1\left(\omega_3\left(a_2+2\mu_3\right)+b_2\mu_3\right)+\left(b_2\mu_3-a_2\omega_3\right)^2+4a_1\mu_3\left(a_2+\mu_3\right)\right.\\
&\left.+b_1^2\right)+2b_0\mu_3\left(b_2\mu_3-a_2\omega_3+b_1\right)\left(b_1\left(\omega_3\left(5a_2+9\mu_3\right)+4b_2\mu_3\right)+2\left(b_2\mu_3-a_2\omega_3\right)^2\right.\\
&\left.+9a_1\mu_3\left(a_2+\mu_3\right)+2b_1^2\right)+27b_0^2\mu_3^2\left(a_2+\mu_3\right)^2+4a_0^3\left(a_2+\mu_3\right), \qquad \text{(B.2a)}\\
d_{100} =& 2\left(3a_1b_1\mu_3^2\omega_3-9a_1b_2\mu_3^3\omega_3-2a_2^2\omega_3\left(\omega_3\left(\omega_3\left(3b_2\mu_3-2b_1\right)-5a_1\mu_3\right)+9b_0\mu_3\right)\right.\\
&+a_0\left(b_1\left(2\omega_3\left(4a_2+3\mu_3\right)-2b_2\mu_3\right)+20a_2b_2\mu_3\omega_3+36a_2\mu_3\omega_3^2-12a_1\mu_3\left(a_2+\mu_3\right)\right.\\
&+8a_2^2\omega_3^2+18b_2\mu_3^2\omega_3-b_2^2\mu_3^2-b_1^2+27\mu_3^2\omega_3^2\left.\right)+a_2\left(a_1\mu_3\omega_3\left(\mu_3\left(9\omega_3-11b_2\right)+b_1\right)\right.\\
&\left.+6a_1^2\mu_3^2-9b_0\mu_3\left(\mu_3\left(b_2+5\omega_3\right)+b_1\right)+\omega_3^2\left(b_1\mu_3\left(b_2+9\omega_3\right)+6b_2^2\mu_3^2+b_1^2\right)\right)-3b_1^2\mu_3\omega_3^2\\
&+a_1b_2^2\mu_3^3+2a_1b_1b_2\mu_3^2+a_1b_1^2\mu_3+6a_1^2\mu_3^3+6a_0^2\left(a_2+\mu_3\right)+2a_2^3\omega_3^4-9b_1b_2\mu_3^2\omega_3^2-b_1^3\omega_3\\
&\left.-2b_2^3\mu_3^3\omega_3-27b_0\mu_3^3\omega_3-5b_1b_2^2\mu_3^2\omega_3-4b_1^2b_2\mu_3\omega_3-9b_0b_2\mu_3^3-9b_0b_1\mu_3^2\right), \qquad \text{(B.2b)}\\
d_{010} =& 2\left(6a_1^2\mu_3^4+a_1b_2^2\mu_3^4-9b_0b_2\mu_3^4-2b_2^3\omega_1\mu_3^4-27b_0\omega_1\mu_3^4-9a_1b_2\omega_1\mu_3^4-9b_0b_1\mu_3^3\right.\\
&+2a_1b_1b_2\mu_3^3-6a_1^2\mu_1\mu_3^3-a_1b_2^2\mu_1\mu_3^3+9b_0b_2\mu_1\mu_3^3-6b_1b_2^2\omega_1\mu_3^3-9a_1b_1\omega_1\mu_3^3\\
&+b_1b_2^2\omega_3\mu_3^3+12a_1b_1\omega_3\mu_3^3+2b_2^3\mu_1\omega_3\mu_3^3+27b_0\mu_1\omega_3\mu_3^3+9a_1b_2\mu_1\omega_3\mu_3^3\\
&-9b_1b_2\omega_1\omega_3\mu_3^3+a_1b_1^2\mu_3^2+6b_1^2\omega_3^2\mu_3^2+9b_1b_2\mu_1\omega_3^2\mu_3^2+9b_0b_1\mu_1\mu_3^2-2a_1b_1b_2\mu_1\mu_3^2\\
&-6b_1^2b_2\omega_1\mu_3^2+2b_1^2b_2\omega_3\mu_3^2+5b_1b_2^2\mu_1\omega_3\mu_3^2-3a_1b_1\mu_1\omega_3\mu_3^2-9b_1^2\omega_1\omega_3\mu_3^2+3b_1^2\mu_1\omega_3^2\mu_3\\
&-a_1b_1^2\mu_1\mu_3-2b_1^3\omega_1\mu_3+b_1^3\omega_3\mu_3+4b_1^2b_2\mu_1\omega_3\mu_3-6a_0^2\left(\mu_1-\mu_3\right)\left(a_2+\mu_3\right)+b_1^3\mu_1\omega_3\\
&+2a_2^3\omega_3^3\left(\mu_3\omega_1-\mu_1\omega_3\right)+a_0\left(9b_2\omega_1\mu_3^3-b_2^2\mu_3^3+9b_2\omega_3\mu_3^3+27\omega_1\omega_3\mu_3^3-9a_2\omega_3^2\mu_3^2\right.\\
&-27\mu_1\omega_3^2\mu_3^2+b_2^2\mu_1\mu_3^2+9a_2b_2\omega_1\mu_3^2+11a_2b_2\omega_3\mu_3^2-18b_2\mu_1\omega_3\mu_3^2+45a_2\omega_1\omega_3\mu_3^2\\
&-10a_2^2\omega_3^2\mu_3-36a_2\mu_1\omega_3^2\mu_3+12a_1\left(\mu_1-\mu_3\right)\left(a_2+\mu_3\right)\mu_3-20a_2b_2\mu_1\omega_3\mu_3-8a_2^2\mu_1\omega_3^2\\
&+18a_2^2\omega_1\omega_3\mu_3+b_1^2\left(\mu_1-\mu_3\right)+b_1\left(2b_2\left(\mu_1-\mu_3\right)\mu_3+3\left(\mu_3\left(3\omega_1-\omega_3\right)-2\mu_1\omega_3\right)\mu_3\right.\\
&\left.+a_2\left(\mu_3\left(9\omega_1-\omega_3\right)-8\mu_1\omega_3\right)\right)+a_2^2\left(9b_0\mu_3\left(2\mu_1\omega_3+\mu_3\left(\omega_3-3\omega_1\right)\right)+\omega_3\left(a_1\mu_3\left(\mu_3\right.\right.\right.\\
&\left.\left.\times\left(9\omega_1+\omega_3\right)-10\mu_1\omega_3\right)+\omega_3\left(6b_2\mu_3\left(\mu_1\omega_3-\mu_3\omega_1\right)+b_1\left(\mu_3\left(3\omega_1+\omega_3\right)\right.\right.\right.\\
&\left.\left.\left.-4\mu_1\omega_3\right)\right)\right)+a_2\left(6a_1^2\left(\mu_3-\mu_1\right)\mu_3^2+9b_0\left(b_1\left(\mu_1-\mu_3\right)+\mu_3\left(b_2\left(\mu_1-\mu_3\right)+5\mu_1\omega_3\right.\right.\right.\\
&\left.\left.\left.+\mu_3\left(\omega_3-6\omega_1\right)\right)\right)\mu_3-a_1\left(b_1\left(\mu_3\left(9\omega_1-10\omega_3\right)+\mu_1\omega_3\right)+\mu_3\left(9\omega_3\left(\mu_1\omega_3-\mu_3\omega_1\right)\right.\right.\right.\\
&\left.\left.\left.+b_2\left(\mu_3\left(9\omega_1+2\omega_3\right)-11\mu_1\omega_3\right)\right)\right)\mu_3-\omega_3\left(\left(\mu_3\left(3\omega_1-4\omega_3\right)+\mu_1\omega_3\right)b_1^2+\mu_3b_1\left(9\omega_3\right.\right.\right.\\
&\left.\left.\left.\times\left(\mu_1\omega_3-\mu_3\omega_1\right)+b_2\left(\mu_1\omega_3+\mu_3\left(2\omega_3-3\omega_1\right)\right)\right)+6b_2^2\mu_3^2\left(\mu_1\omega_3-\mu_3\omega_1\right)\right)\right)\right), \qquad \text{(B.2c)}
\end{aligned}
$$

$$
\begin{aligned}
d_{001} =& 2\left(6a_1^2\mu_3^4 - 9b_0b_2\mu_3^4 - 2b_2^3\omega_2\mu_3^4 - 27b_0\omega_2\mu_3^4 - 9a_1b_2\omega_2\mu_3^4 - 9b_0b_1\mu_3^3 + 2a_1b_1b_2\mu_3^3\right.\\
&+a_1b_2^2\mu_3^4 - 6a_1^2\mu_2\mu_3^3 - a_1b_2^2\mu_2\mu_3^3 + 9b_0b_2\mu_2\mu_3^3 - 6b_1b_2^2\omega_2\mu_3^3 - 9a_1b_1\omega_2\mu_3^3 + a_1b_1^2\mu_3^2\\
&+b_1b_2^2\omega_3\mu_3^3 + 12a_1b_1\omega_3\mu_3^3 + 2b_2^3\mu_2\omega_3\mu_3^3 + 27b_0\mu_2\omega_3\mu_3^3 + 9a_1b_2\mu_2\omega_3\mu_3^3 - 9b_1b_2\omega_2\omega_3\mu_3^3\\
&+6b_1^2\omega_3^2\mu_3^2 + 9b_1b_2\mu_2\omega_3^2\mu_3^2 + 9b_0b_1\mu_2\mu_3^2 - 2a_1b_1b_2\mu_2\mu_3^2 - 6b_1^2b_2\omega_2\mu_3^2 + 2b_1^2b_2\omega_3\mu_3^2\\
&+5b_1b_2^2\mu_2\omega_3\mu_3^2 - 3a_1b_1\mu_2\omega_3\mu_3^2 - 9b_1^2\omega_2\omega_3\mu_3^2 + 3b_1^2\mu_2\omega_3^2\mu_3 - a_1b_1^2\mu_2\mu_3 - 2b_1^3\omega_2\mu_3\\
&+b_1^3\omega_3\mu_3 + 4b_1^2b_2\mu_2\omega_3\mu_3 - 6a_0^2\left(\mu_2-\mu_3\right)\left(a_2+\mu_3\right) + b_1^3\mu_2\omega_3 + 2a_2^3\omega_3^3\left(\mu_3\omega_2 - \mu_2\omega_3\right)\\
&+a_0\left(+9b_2\omega_2\mu_3^3 - b_2^2\mu_3^3 + 9b_2\omega_3\mu_3^3 + 27\omega_2\omega_3\mu_3^3 - 9a_2\omega_3^2\mu_3^2 - 27\mu_2\omega_3^2\mu_3^2 + b_2^2\mu_2\mu_3^2\right.\\
&+9a_2b_2\omega_2\mu_3^2 + 11a_2b_2\omega_3\mu_3^2 - 18b_2\mu_2\omega_3\mu_3^2 + 45a_2\omega_2\omega_3\mu_3^2 - 10a_2^2\omega_3^2\mu_3 - 36a_2\mu_2\omega_3^2\mu_3\\
&+12a_1\left(\mu_2-\mu_3\right)\left(a_2+\mu_3\right)\mu_3 - 20a_2b_2\mu_2\omega_3\mu_3 + 18a_2^2\omega_2\omega_3\mu_3 - 8a_2^2\mu_2\omega_3^2 + \left(\mu_2-\mu_3\right)\\
&\times b_1^2 + b_1\left(2b_2\left(\mu_2-\mu_3\right)\mu_3 + 3\left(\mu_3\left(3\omega_2-\omega_3\right) - 2\mu_2\omega_3\right)\mu_3 + a_2\left(\mu_3\left(9\omega_2-\omega_3\right)\right.\right.\\
&\left.\left.-8\mu_2\omega_3\right)\right) + a_2^2\left(9b_0\mu_3\left(2\mu_2\omega_3 + \mu_3\left(\omega_3 - 3\omega_2\right)\right) + \omega_3\left(a_1\mu_3\left(\mu_3\left(9\omega_2+\omega_3\right)\right.\right.\right.\\
&\left.\left.\left.-10\mu_2\omega_3\right) + \omega_3\left(6b_2\mu_3\left(\mu_2\omega_3 - \mu_3\omega_2\right)\left(\mu_3\left(3\omega_2+\omega_3\right) - 4\mu_2\omega_3\right)\right)\right)\right) + b_1 + a_2\left(6a_1^2\mu_3^2\right.\\
&\times\left(\mu_3-\mu_2\right) + 9b_0\mu_3\left(b_1\left(\mu_2-\mu_3\right) + \mu_3\left(b_2\left(\mu_2-\mu_3\right) + 5\mu_2\omega_3 + \mu_3\left(\omega_3 - 6\omega_2\right)\right)\right)\\
&-a_1\left(b_1\left(\mu_3\left(9\omega_2 - 10\omega_3\right) + \mu_2\omega_3\right) + \mu_3\left(9\omega_3\left(\mu_2\omega_3 - \mu_3\omega_2\right) + b_2\left(\mu_3\left(9\omega_2+2\omega_3\right)\right.\right.\right.\\
&\left.\left.\left.-11\mu_2\omega_3\right)\right)\right)\mu_3 - \omega_3\left(\left(\mu_3\left(3\omega_2 - 4\omega_3\right) + \mu_2\omega_3\right)b_1^2 + \mu_3\left(9\omega_3\left(\mu_2\omega_3 - \mu_3\omega_2\right)\right.\right.\\
&\left.\left.\left.+b_2\left(\mu_2\omega_3 + \mu_3\left(2\omega_3 - 3\omega_2\right)\right)\right)b_1 + 6b_2^2\mu_3^2\left(\mu_2\omega_3 - \mu_3\omega_2\right)\right)\right), \qquad \text{(B.2d)}\\
d_{200} =& b_1\left(8a_2\omega_3 - 2b_2\mu_3 + 6\mu_3\omega_3\right) + 20a_2b_2\mu_3\omega_3 + 36a_2\mu_3\omega_3^2 - 12a_1\mu_3^2 - 12a_1a_2\mu_3\\
&+12a_0\left(a_2+\mu_3\right) + 8a_2^2\omega_3^2 + 18b_2\mu_3^2\omega_3 - b_2^2\mu_3^2 - b_1^2 + 27\mu_3^2\omega_3^2, \qquad \text{(B.2e)}\\
d_{020} =& 18a_2b_2\mu_3^3\omega_1 + 2a_2b_2\mu_3^3\omega_3 - 18a_2b_2\mu_1\mu_3^2\omega_1 - 22a_2b_2\mu_1\mu_3^2\omega_3 + 20a_2b_2\mu_1^2\mu_3\omega_3 - 2b_1\\
&\times\left(\mu_1-\mu_3\right)\left(a_2\left(\mu_3\left(9\omega_1 - 5\omega_3\right) - 4\mu_1\omega_3\right) + b_2\left(\mu_1-\mu_3\right)\mu_3 + 3\mu_3\left(\mu_3\left(3\omega_1 - 2\omega_3\right)\right.\right.\\
&\left.\left.-\mu_1\omega_3\right)\right) + 54a_2\mu_3^3\omega_1^2 - 18a_2\mu_3^3\omega_1\omega_3 + 27a_2^2\mu_3^2\omega_1^2 - a_2^2\mu_3^2\omega_3^2 + 18a_2\mu_1\mu_3^2\omega_3^2 - b_2^2\mu_3^4\\
&- 18a_2^2\mu_3^2\omega_1\omega_3 - 90a_2\mu_1\mu_3^2\omega_1\omega_3 + 36a_2\mu_1^2\mu_3\omega_3^2 + 20a_2^2\mu_1\mu_3\omega_3^2 - 36a_2^2\mu_1\mu_3\omega_1\omega_3\\
&+ 8a_2^2\mu_1^2\omega_3^2 - 12a_1\mu_3^4 - 12a_1a_2\mu_3^3 + 24a_1\mu_1\mu_3^3 - 12a_1\mu_1^2\mu_3^2 + 24a_1a_2\mu_1\mu_3^2 - 12a_1a_2\mu_1^2\mu_3\\
&+ 12a_0\left(\mu_1-\mu_3\right)^2\left(a_2+\mu_3\right) + 18b_2\mu_3^4\omega_1 - 18b_2\mu_1\mu_3^3\omega_1 - 18b_2\mu_1\mu_3^3\omega_3 + 18b_2\mu_1^2\mu_3^2\omega_3\\
&+ 2b_2^2\mu_1\mu_3^3 - b_2^2\mu_1^2\mu_3^2 - b_1^2\left(\mu_1-\mu_3\right)^2 + 27\mu_3^4\omega_1^2 - 54\mu_1\mu_3^3\omega_1\omega_3 + 27\mu_1^2\mu_3^2\omega_3^2, \qquad \text{(B.2f)}\\
d_{002} =& 18a_2b_2\mu_3^3\omega_2 + 2a_2b_2\mu_3^3\omega_3 - 18a_2b_2\mu_2\mu_3^2\omega_2 - 22a_2b_2\mu_2\mu_3^2\omega_3 + 20a_2b_2\mu_2^2\mu_3\omega_3 - 2b_1\\
&\times\left(\mu_2-\mu_3\right)\left(a_2\left(\mu_3\left(9\omega_2 - 5\omega_3\right) - 4\mu_2\omega_3\right) + b_2\left(\mu_2-\mu_3\right)\mu_3 + 3\mu_3\left(\mu_3\left(3\omega_2 - 2\omega_3\right)\right.\right.\\
&\left.\left.-\mu_2\omega_3\right)\right) + 54a_2\mu_3^3\omega_2^2 - 18a_2\mu_3^3\omega_2\omega_3 + 27a_2^2\mu_3^2\omega_2^2 - a_2^2\mu_3^2\omega_3^2 + 18a_2\mu_2\mu_3^2\omega_3^2 - b_2^2\mu_3^4\\
&- 18a_2^2\mu_3^2\omega_2\omega_3 - 90a_2\mu_2\mu_3^2\omega_2\omega_3 + 36a_2\mu_2^2\mu_3\omega_3^2 + 20a_2^2\mu_2\mu_3\omega_3^2 - 36a_2^2\mu_2\mu_3\omega_2\omega_3\\
&+ 8a_2^2\mu_2^2\omega_3^2 - 12a_1\mu_3^4 - 12a_1a_2\mu_3^3 + 24a_1\mu_2\mu_3^3 - 12a_1\mu_2^2\mu_3^2 + 24a_1a_2\mu_2\mu_3^2 + 18b_2\mu_3^4\omega_2\\
&- 12a_1a_2\mu_2^2\mu_3 + 12a_0\left(\mu_2-\mu_3\right)^2\left(a_2+\mu_3\right) - 18b_2\mu_2\mu_3^3\omega_2 - 18b_2\mu_2\mu_3^3\omega_3 + 18b_2\mu_2^2\mu_3^2\omega_3\\
&+ 2b_2^2\mu_2\mu_3^3 - b_2^2\mu_2^2\mu_3^2 - b_1^2\left(\mu_2-\mu_3\right)^2 + 27\mu_3^4\omega_2^2 - 54\mu_2\mu_3^3\omega_2\omega_3 + 27\mu_2^2\mu_3^2\omega_3^2, \qquad \text{(B.2g)}
\end{aligned}
$$

$$
\begin{aligned}
d_{110} =& -2\left(20a_2b_2\mu_1\mu_3\omega_3 - 9a_2b_2\mu_3^2\omega_1 + b_1\left(a_2\left(8\mu_1\omega_3 + \mu_3\left(\omega_3 - 9\omega_1\right)\right) + 2b_2\mu_3\left(\mu_3 - \mu_1\right)\right.\right.\\
&\left.\left.+3\mu_3\left(2\mu_1\omega_3 + \mu_3\left(\omega_3 - 3\omega_1\right)\right)\right) - 11a_2b_2\mu_3^2\omega_3 + 9a_2\mu_3^2\omega_3^2 - 45a_2\mu_3^2\omega_1\omega_3 + 12a_1\mu_3^3\\
&+10a_2^2\mu_3\omega_3^2 + 36a_2\mu_1\mu_3\omega_3^2 - 18a_2^2\mu_3\omega_1\omega_3 + 8a_2^2\mu_1\omega_3^2 + 12a_1a_2\mu_3^2 - 12a_1a_2\mu_1\mu_3\\
&-12a_1\mu_1\mu_3^2 + 12a_0\left(\mu_1 - \mu_3\right)\left(a_2 + \mu_3\right) - 9b_2\mu_3^3\omega_1 - 9b_2\mu_3^3\omega_3 + 18b_2\mu_1\mu_3^2\omega_3\\
&+b_2^2\mu_3^3 - b_2^2\mu_1\mu_3^2 + b_1^2\left(\mu_3 - \mu_1\right) - 27\mu_3^3\omega_1\omega_3 + 27\mu_1\mu_3^2\omega_3^2\Big), \qquad \text{(B.2h)}\\
d_{101} =& -2\left(20a_2b_2\mu_2\mu_3\omega_3 - 9a_2b_2\mu_3^2\omega_2 + b_1\left(a_2\left(8\mu_2\omega_3 + \mu_3\left(\omega_3 - 9\omega_2\right)\right) + 2b_2\mu_3\left(\mu_3 - \mu_2\right)\right.\right.\\
&\left.\left.+3\mu_3\left(2\mu_2\omega_3 + \mu_3\left(\omega_3 - 3\omega_2\right)\right)\right) - 11a_2b_2\mu_3^2\omega_3 + 9a_2\mu_3^2\omega_3^2 - 45a_2\mu_3^2\omega_2\omega_3 + 12a_1\mu_3^3\\
&+10a_2^2\mu_3\omega_3^2 + 36a_2\mu_2\mu_3\omega_3^2 - 18a_2^2\mu_3\omega_2\omega_3 + 8a_2^2\mu_2\omega_3^2 + 12a_1a_2\mu_3^2 - 12a_1\mu_2\mu_3^2\\
&-12a_1a_2\mu_2\mu_3 + 12a_0\left(\mu_2 - \mu_3\right)\left(a_2 + \mu_3\right) - 9b_2\mu_3^3\omega_2 - 9b_2\mu_3^3\omega_3 + 18b_2\mu_2\mu_3^2\omega_3\\
&+b_2^2\mu_3^3 - b_2^2\mu_2\mu_3^2 + b_1^2\left(\mu_3 - \mu_2\right) - 27\mu_3^3\omega_2\omega_3 + 27\mu_2\mu_3^2\omega_3^2\Big), \qquad \text{(B.2i)}\\
d_{011} =& 2\left(9b_2\omega_1\mu_3^4 - b_2^2\mu_3^4 - 12a_1\mu_3^4 + 9b_2\omega_2\mu_3^4 + 27\omega_1\omega_2\mu_3^4 - 12a_1a_2\mu_3^3 + b_2^2\mu_1\mu_3^3 + 12a_1\mu_1\mu_3^3\right.\\
&+b_2^2\mu_2\mu_3^3 + 12a_1\mu_2\mu_3^3 + 9a_2b_2\omega_1\mu_3^3 - 9b_2\mu_2\omega_1\mu_3^3 + 9a_2b_2\omega_2\mu_3^3 - 9b_2\mu_1\omega_2\mu_3^3 - a_2^2\omega_3^2\mu_3^2\\
&+54a_2\omega_1\omega_2\mu_3^3 + 2a_2b_2\omega_3\mu_3^3 - 9b_2\mu_1\omega_3\mu_3^3 - 9b_2\mu_2\omega_3\mu_3^3 - 9a_2\omega_1\omega_3\mu_3^3 - 27\mu_2\omega_1\omega_3\mu_3^3\\
&-9a_2\omega_2\omega_3\mu_3^3 - 27\mu_1\omega_2\omega_3\mu_3^3 + 9a_2\mu_1\omega_3^2\mu_3^2 + 9a_2\mu_2\omega_3^2\mu_3^2 + 27\mu_1\mu_2\omega_3^2\mu_3^2 + 12a_1a_2\mu_1\mu_3^2\\
&+12a_1a_2\mu_2\mu_3^2 - b_2^2\mu_1\mu_2\mu_3^2 - 12a_1\mu_1\mu_2\mu_3^2 - 9a_2b_2\mu_2\omega_1\mu_3^2 - 9a_2b_2\mu_1\omega_2\mu_3^2 + 27a_2^2\omega_1\omega_2\mu_3^2\\
&-11a_2b_2\mu_1\omega_3\mu_3^2 - 11a_2b_2\mu_2\omega_3\mu_3^2 + 18b_2\mu_1\mu_2\omega_3\mu_3^2 - 9a_2^2\omega_1\omega_3\mu_3^2 - 45a_2\mu_2\omega_1\omega_3\mu_3^2\\
&-9a_2^2\omega_2\omega_3\mu_3^2 - 45a_2\mu_1\omega_2\omega_3\mu_3^2 + 10a_2^2\mu_1\omega_3^2\mu_3 + 10a_2^2\mu_2\omega_3^2\mu_3 + 36a_2\mu_1\mu_2\omega_3^2\mu_3\\
&-12a_1a_2\mu_1\mu_2\mu_3 + 20a_2b_2\mu_1\mu_2\omega_3\mu_3 - 18a_2^2\mu_2\omega_1\omega_3\mu_3 - 18a_2^2\mu_1\omega_2\omega_3\mu_3 + 8a_2^2\mu_1\mu_2\omega_3^2\\
&+12a_0\left(\mu_1 - \mu_3\right)\left(\mu_2 - \mu_3\right)\left(a_2 + \mu_3\right) + b_1^2\left(\mu_1 - \mu_3\right)\left(\mu_3 - \mu_2\right) + b_1\mu_3\left(2b_2\left(\mu_1 - \mu_3\right)\right.\\
&\times\left(\mu_3 - \mu_2\right) + a_2\left(\mu_2\left(8\mu_1\omega_3 + \mu_3\left(\omega_3 - 9\omega_1\right)\right) + \mu_3\left(\mu_3\left(9\omega_1 + 9\omega_2 - 10\omega_3\right) + \mu_1\right.\right.\\
&\left.\left.\times\left(\omega_3 - 9\omega_2\right)\right)\right) + 3\mu_3\left(\mu_2\left(2\mu_1\omega_3 + \mu_3\left(\omega_3 - 3\omega_1\right)\right) + \mu_3\left(\mu_3\left(3\omega_1 + 3\omega_2 - 4\omega_3\right)\right.\right.\\
&\left.\left.\left.\left.+\mu_1\left(\omega_3 - 3\omega_2\right)\right)\right)\right)\Big), \qquad \text{(B.2j)}\\
d_{300} =& 4\left(a_2 + \mu_3\right), \qquad \text{(B.2k)}\\
d_{030} =& -4\left(\mu_1 - \mu_3\right)^3\left(a_2 + \mu_3\right), \qquad \text{(B.2l)}\\
d_{003} =& -4\left(\mu_2 - \mu_3\right)^3\left(a_2 + \mu_3\right), \qquad \text{(B.2m)}\\
d_{210} =& -12\left(\mu_1 - \mu_3\right)\left(a_2 + \mu_3\right), \qquad \text{(B.2n)}\\
d_{201} =& -12\left(\mu_2 - \mu_3\right)\left(a_2 + \mu_3\right), \qquad \text{(B.2o)}\\
d_{021} =& 12\left(\mu_1 - \mu_3\right)^2\left(\mu_3 - \mu_2\right)\left(a_2 + \mu_3\right), \qquad \text{(B.2p)}\\
d_{012} =& -12\left(\mu_1 - \mu_3\right)\left(\mu_2 - \mu_3\right)^2\left(a_2 + \mu_3\right), \qquad \text{(B.2q)}\\
d_{120} =& 12\left(\mu_1 - \mu_3\right)^2\left(a_2 + \mu_3\right), \qquad \text{(B.2r)}\\
d_{102} =& 12\left(\mu_2 - \mu_3\right)^2\left(a_2 + \mu_3\right), \qquad \text{(B.2s)}\\
d_{111} =& 24\left(\mu_1 - \mu_3\right)\left(\mu_2 - \mu_3\right)\left(a_2 + \mu_3\right). \qquad \text{(B.2t)}
\end{aligned}
$$

B.1.3. Coefficients of the Linear Functions of the Proof of Theorem 3.3

$$c_{\mathrm{I},v_3,1,00} = \omega_3\left(\omega_3\left(b_2+\omega_3\right)-a_1\right)+b_0, \tag{B.3a}$$

$$c_{\mathrm{I},v_3,1,10} = \omega_3-\omega_1, \tag{B.3b}$$

$$c_{\mathrm{I},v_3,1,01} = \omega_3-\omega_2, \tag{B.3c}$$

$$\begin{aligned} c_{\mathrm{I},v_3,2,00} =& 3b_1^2\left(2a_2\omega_3+\mu_3\left(b_2+3\omega_3\right)\right)+3b_1\left(2a_2\omega_3+\mu_3\left(b_2+3\omega_3\right)\right)^2+\mu_3^3\left(9\omega_3\left(3a_1+b_2^2\right)\right.\\ &\left.+b_2^3-27b_0\right)+3a_2^2\mu_3\left(9a_1\omega_3-5b_2\omega_3^2-9b_0+3\omega_3^3\right)+8a_2^3\omega_3^3+b_1^3\\ &+6a_2\mu_3^2\left(\omega_3\left(9a_1-3b_2\omega_3+b_2^2\right)-9b_0\right), \end{aligned} \tag{B.3d}$$

$$c_{\mathrm{I},v_3,2,10} = 27\mu_3\left(\omega_1-\omega_3\right)\left(a_2+\mu_3\right)^2, \tag{B.3e}$$

$$c_{\mathrm{I},v_3,2,01} = 27\mu_3\left(\omega_2-\omega_3\right)\left(a_2+\mu_3\right)^2, \tag{B.3f}$$

$$\begin{aligned} c_{\mathrm{I},\xi_2,1,00} =& \left(\left(\mu_3\omega_1-\mu_1\omega_3\right)\left(\omega_1\left(a_2+\mu_3\right)-\omega_3\left(a_2+\mu_1\right)+b_2\left(\mu_3-\mu_1\right)\right)\right.\\ &\left.-a_1\left(\mu_1-\mu_3\right)^2-b_1\left(\mu_1-\mu_3\right)\left(\mu_3\omega_1-\mu_1\omega_3\right)\left(\omega_1-\omega_3\right)\right)\\ &+a_0\left(\mu_1-\mu_3\right)^2\left(\omega_1-\omega_3\right)-b_0\left(\mu_1-\mu_3\right)^3, \end{aligned} \tag{B.3g}$$

$$c_{\mathrm{I},\xi_2,1,10} = \left(\mu_1-\mu_3\right)^2\left(\omega_1-\omega_3\right), \tag{B.3h}$$

$$c_{\mathrm{I},\xi_2,1,01} = \left(\mu_1-\mu_3\right)^2\left(\mu_3\left(\omega_1-\omega_2\right)+\mu_1\left(\omega_2-\omega_3\right)+\mu_2\left(\omega_3-\omega_1\right)\right), \tag{B.3i}$$

$$\begin{aligned} c_{\mathrm{I},\xi_2,2,00} =& 3b_1^2\left(\mu_3\left(b_2\left(\mu_1-\mu_3\right)-3\omega_1\left(a_2+\mu_3\right)\right)+\omega_3\left(a_2\left(2\mu_1+\mu_3\right)+3\mu_1\mu_3\right)\right)+3b_1\left(\mu_3\omega_3\right.\\ &\times\left(2b_2\left(a_2\left(2\mu_1+\mu_3\right)+3\mu_1\mu_3\right)-3\omega_1\left(a_2+\mu_3\right)\left(a_2+3\mu_3\right)\right)+\omega_3^2\left(a_2^2\left(4\mu_1-\mu_3\right)\right.\\ &\left.+12a_2\mu_1\mu_3+9\mu_1\mu_3^2\right)-b_2\mu_3^2\left(6\omega_1\left(a_2+\mu_3\right)+b_2\left(\mu_3-\mu_1\right)\right)\Big)-3a_2\mu_3\omega_3^2\left(b_2\left(a_2\right.\right.\\ &\left.\times\left(5\mu_1+\mu_3\right)+6\mu_1\mu_3\right)+3a_2\omega_1\left(a_2+\mu_3\right)\Big)+\mu_3\left(\left(\mu_3-\mu_1\right)\left(54a_2b_0\mu_3+27a_2^2b_0\right.\right.\\ &\left.\left.+\left(27b_0-b_2^3\right)\mu_3^2\right)-9\omega_1\left(a_2+\mu_3\right)\left(\mu_3\left(3a_1\left(a_2+\mu_3\right)+b_2^2\mu_3\right)-3a_0\left(a_2+\mu_3\right)\right)\right)\\ &+3\mu_3\omega_3\left(b_2\mu_3\left(b_2\left(2a_2\mu_1+\mu_3\left(a_2+3\mu_1\right)\right)+6a_2\omega_1\left(a_2+\mu_3\right)\right)-9a_0\left(a_2+\mu_3\right)^2\right.\\ &\left.+9a_1\mu_1\left(a_2+\mu_3\right)^2\right)+a_2^2\omega_3^3\left(a_2\left(8\mu_1+\mu_3\right)+9\mu_1\mu_3\right)+b_1^3\left(\mu_1-\mu_3\right), \end{aligned} \tag{B.3j}$$

$$c_{\mathrm{I},\xi_2,2,10} = 27\mu_3\left(\omega_1-\omega_3\right)\left(a_2+\mu_3\right)^2, \tag{B.3k}$$

$$c_{\mathrm{I},\xi_2,2,01} = 27\mu_3\left(\mu_3\left(\omega_1-\omega_2\right)+\mu_1\left(\omega_2-\omega_3\right)+\mu_2\left(\omega_3-\omega_1\right)\right)\left(a_2+\mu_3\right)^2 \tag{B.3l}$$

B.2. Critical Point of Two Injectively Coupled Groups of MEMS Sensors

The equations for the matrix Q and the characteristic frequency are summarized. For this, let $i = 1, 2, 3$. Then the bifurcation point of a network consisting of two different groups of MEMS sensors is given by

$$\omega_{\mathrm{C}}^2 = \frac{a_{11}b_{21}-a_{21}b_{11}-b_{11}b_{21}(k_{11}-k_{22}+2q_{21})}{a_{13}b_{21}-a_{23}b_{11}}, \tag{B.4a}$$

$$q_{11} = \frac{a_{13}[a_{21}+b_{21}(q_{21}-k_{22})]-a_{23}[a_{11}-b_{11}(k_{11}+q_{21})]}{a_{13}b_{21}-a_{23}b_{11}}, \tag{B.4b}$$

$$
\begin{aligned}
q_{12} =& \frac{1}{2b_{11}b_{21}(a_{13}b_{21}-a_{23}b_{11})^{3/2}\sqrt{a_{11}b_{21}-b_{11}[a_{21}+b_{21}(k_{11}-k_{22}+2q_{21})]}} \\
&\times [a_{21}b_{11}(b_{21}(2a_{11}(b_{11}-b_{21})+a_{12}(a_{13}b_{21}-a_{23}b_{11})-2b_{11}(k_{11}-k_{22}+2q_{21})) \\
&\quad\times(b_{11}-b_{21})+a_{22}b_{11}(a_{23}b_{11}-a_{13}b_{21}))+b_{21}(a_{11}(b_{21}(a_{12}(a_{23}b_{11}-a_{13}b_{21}) \\
&\quad+2b_{11}(b_{11}-b_{21})(k_{11}-k_{22}+2q_{21}))+a_{22}b_{11}(a_{13}b_{21}-a_{23}b_{11}))+(k_{11}-k_{22}+2q_{21}) \\
&\quad\times b_{11}(b_{21}(a_{12}(a_{13}b_{21}-a_{23}b_{11})-b_{11}(b_{11}-b_{21})(k_{11}-k_{22}+2q_{21}))+a_{22}b_{11} \\
&\quad\times(a_{23}b_{11}-a_{13}b_{21}))+a_{11}^2b_{21}(b_{21}-b_{11})+a_{10}(a_{23}b_{11}-a_{13}b_{21})^2) \\
&\quad+(b_{21}-b_{11})a_{21}^2b_{11}^2-a_{20}b_{11}(a_{23}b_{11}-a_{13}b_{21})^2], \qquad \text{(B.4c)}
\end{aligned}
$$

$$
q_{21} = \frac{c_2}{3c_3}-\frac{2}{3|c_3|}\sqrt{c_2^2+c_1c_3}\cos\left[\frac{2\pi i}{3}+\frac{1}{3}\arccos\left(\frac{c_3}{|c_3|}\frac{9c_1c_2c_3-2c_2^2-27c_0c_3^2}{2|c_2^2+c_1c_3|^{\frac{3}{2}}}\right)\right], \qquad \text{(B.4d)}
$$

$$
\begin{aligned}
q_{22} =& \frac{1}{2b_{11}b_{21}(a_{13}b_{21}-a_{23}b_{11})^{3/2}\sqrt{a_{11}b_{21}-b_{11}[a_{21}+b_{21}(k_{11}-k_{22}+2q_{21})]}} \\
&\times [a_{21}b_{11}(b_{21}(a_{12}(a_{13}b_{21}-a_{23}b_{11})-2a_{11}(b_{11}+b_{21})+2b_{11}(b_{11}+b_{21}) \\
&\quad\times(k_{11}-k_{22}+2q_{21}))+a_{22}b_{11}(a_{13}b_{21}-a_{23}b_{11}))+(k_{11}-k_{22}+2q_{21})) \\
&\quad\times b_{21}(a_{11}(b_{21}(a_{12}(a_{23}b_{11}-a_{13}b_{21})-2b_{11}(b_{11}+b_{21})+(a_{23}b_{11}-a_{13}b_{21})) \\
&\quad\times a_{22}b_{11}+b_{11}(k_{11}-k_{22}+2q_{21})(b_{21}(a_{12}(a_{13}b_{21}-a_{23}b_{11})+(b_{11}+b_{21}) \\
&\quad\times b_{11}(k_{11}-k_{22}+2q_{21}))+a_{22}b_{11}(a_{13}b_{21}-a_{23}b_{11}))+a_{11}^2b_{21}(b_{11}+b_{21}) \\
&\quad+a_{10}(a_{23}b_{11}-a_{13}b_{21})^2)+a_{21}^2(b_{11}+b_{21})b_{11}^2+a_{20}b_{11}(a_{23}b_{11}-a_{13}b_{21})^2], \qquad \text{(B.4e)}
\end{aligned}
$$

with the auxiliary constants

$$
\begin{aligned}
c_0 =& [-a_{21}b_{11}(b_{21}(2a_{11}(b_{11}+b_{21})+a_{12}(a_{23}b_{11}-a_{13}b_{21})-2b_{11}(b_{11}+b_{21})(k_{11}-k_{22})) \\
&+a_{22}b_{11}(a_{23}b_{11}-a_{13}b_{21}))+b_{21}(a_{11}(b_{21}(a_{12}(a_{23}b_{11}-a_{13}b_{21})-2b_{11}(b_{11}+b_{21}) \\
&\times(k_{11}-k_{22}))+a_{22}b_{11}(a_{23}b_{11}-a_{13}b_{21}))+b_{11}(k_{11}-k_{22})(b_{21}(a_{12}(a_{13}b_{21}-a_{23}b_{11}) \\
&+b_{11}(b_{11}+b_{21})(k_{11}-k_{22}))+a_{22}b_{11}(a_{13}b_{21}-a_{23}b_{11}))+a_{11}^2b_{21}(b_{11}+b_{21})+a_{10}(a_{23}b_{11} \\
&-a_{13}b_{21})^2)+a_{21}^2(b_{11}+b_{21})b_{11}^2+a_{20}b_{11}(a_{23}b_{11}-a_{13}b_{21})^2][a_{23}(b_{11}k_{11}-a_{11}) \\
&+a_{13}(a_{21}-b_{21}k_{22})], \\
c_1 =& 2b_{11}b_{21}(a_{13}^2b_{21}(b_{21}(a_{22}b_{11}(k_{11}-2k_{22})-a_{12}b_{21}k_{22}-a_{11}a_{22}+a_{10}a_{23})-2a_{20}a_{23}b_{11} \\
&+a_{21}(2a_{22}b_{11}+a_{12}b_{21}))+a_{13}(-2a_{21}(b_{21}((2b_{11}+b_{21})(a_{11}-b_{11}k_{11})+a_{22}a_{23}b_{11}^2 \\
&+b_{11}k_{22}(3b_{11}+2b_{21})))+b_{21}(b_{21}(a_{11}-b_{11}k_{11})(a_{11}-2a_{12}a_{23}-b_{11}k_{11})-2a_{10}a_{23}^2b_{11} \\
&+2k_{22}(b_{21}(2b_{11}+b_{21})(a_{11}-b_{11}k_{11})+a_{22}a_{23}b_{11}^2)+b_{11}b_{21}(3b_{11}+2b_{21})k_{22}^2) \\
&+a_{21}^2b_{11}(3b_{11}+2b_{21})+a_{20}a_{23}^2b_{11}^2)+a_{23}(a_{11}b_{11}(2b_{21}(a_{12}a_{23}-(2b_{11}+3b_{21})k_{11} \\
&+(b_{11}+2b_{21})k_{22})+a_{22}a_{23}b_{11}-2a_{21}(b_{11}+2b_{21}))+b_{11}^2(a_{21}(2(b_{11}+2b_{21})k_{11}-a_{12}a_{23} \\
&-2b_{21}k_{22})+k_{11}(b_{21}k_{11}(2b_{11}+3b_{21})-a_{23}(a_{22}b_{11}+2a_{12}b_{21}))+b_{21}k_{22}(a_{12}a_{23} \\
&-2(b_{11}+2b_{21})k_{11})+a_{21}^2+a_{10}a_{23}^2+b_{21}^2k_{22}^2)+a_{11}^2b_{21}(2b_{11}+3b_{21}))+a_{20}a_{13}^3b_{21}^2),
\end{aligned}
$$

$$
\begin{aligned}
c_2 =& -4b_{11}^2 b_{21}^2 (a_{13}(b_{21}(2a_{11} - a_{12}a_{23} - 2b_{11}k_{11} + (3b_{11} + b_{21})k_{22}) + a_{22}a_{23}b_{11} \\
& - a_{21}(3b_{11} + b_{21})) + a_{23}(b_{11}(a_{12}a_{23} - 2a_{21} - (b_{11} + 3b_{21})k_{11} + 2b_{21}k_{22}) \\
& + a_{11}(b_{11} + 3b_{21})) - a_{22}a_{13}^2 b_{21}), \\
c_3 =& 8(a_{13} + a_{23})b_{11}^3 b_{21}^3.
\end{aligned}
$$

List of Figures

List of Tables

References

[1] J. Abeßer. “A review of deep learning based methods for acoustic scene classification”. In: *Applied Sciences* 10.6 (2020), p. 2020.

[2] F. Abreu Araujo, M. Riou, J. Torrejon, S. Tsunegi, D. Querlioz, K. Yakushiji, A. Fukushima, H. Kubota, S. Yuasa, M. D. Stiles, and J. Grollier. “Role of non-linear data processing on speech recognition task in the framework of reservoir computing”. In: *Scientific Reports* 10.1 (2020), p. 328.

[3] S. G. Adams, F. Bertsch, and N. C. MacDonald. “Independent tuning of the linear and nonlinear stiffness coefficients of a micromechanical device”. In: *Proceedings of Ninth International Workshop on Micro Electromechanical Systems*. 1996, pp. 32–37.

[4] M. Albach. *Elektrotechnik*. Pearson Deutschland GmbH, 2011.

[5] M. H. D. A. Alsakkal and J. H. B. Wijekoon. “An Active Hopf-based Digital Hardware Cochlea Implementation”. In: *2022 IEEE Symposium Series on Computational Intelligence (SSCI)*. IEEE. 2022, pp. 664–671.

[6] H. Ammari and B. Davies. “Mimicking the active cochlea with a fluid-coupled array of subwavelength Hopf resonators”. In: *Proceedings of the Royal Society A* 476.2234 (2020), p. 20190870. ISSN: 1364-5021, 1471-2946.

[7] D. G. Aronson, G. B. Ermentrout, and N. Kopell. “Amplitude response of coupled oscillators”. In: *Physica D: Nonlinear Phenomena* 41.3 (1990), pp. 403–449. ISSN: 01672789.

[8] J. Ashmore, P. Avan, W. E. Brownell, P. Dallos, K. Dierkes, R. Fettiplace, K. Grosh, C. M. Hackney, A. J. Hudspeth, F. Jülicher, B. Lindner, P. Martin, J. Meaud, C. Petit, J. R. Santos Sacchi, and B. Canlon. “The remarkable cochlear amplifier”. In: *Hearing Research*. Special Issue: Annual Reviews 2010 266.1 (2010), pp. 1–17.

[9] P. Ashwin and J. W. Swift. “The dynamics of n weakly coupled identical oscillators”. In: *Journal of Nonlinear Science* 2 (1992), pp. 69–108.

[10] R. G. Ayoub. “Paolo Ruffini’s contributions to the quintic”. In: *Archive for History of Exact Sciences* 23.3 (1980), pp. 253–277. ISSN: 1432-0657.

[11] H. D. Baehr and S. Kabelac. *Thermodynamik: Grundlagen und technische Anwendungen*. 13., neu bearb. und erw. Aufl. Springer-Lehrbuch. Berlin Heidelberg: Springer, 2006. ISBN: 978-3-540-32513-0.

[12] K.-H. Best. “Gesetzmäßigkeiten Der Lautdauer”. In: *Glottotheory* 1.1 (2008), pp. 1–9. ISSN: 2196-6907, 1337-7892.

[13] J. Bewersdorff. *Galois Theory for Beginners: A Historical Perspective, Second Edition*. American Mathematical Society, 2021. ISBN: 978-1-4704-6658-9.

[14] A. W. Bronkhorst. "The cocktail party phenomenon: A review of research on speech intelligibility in multiple-talker conditions". In: *Acta Acustica united with Acustica* 86.1 (2000), pp. 117–128.

[15] I. N. Bronstein, J. Hromkovic, B. Luderer, H.-R. Schwarz, J. Blath, A. Schied, S. Dempe, G. Wanka, and S. Gottwald. *Taschenbuch der Mathematik*. Verlag Europa-Lehrmittel, 2016, pp. 671, 712–713.

[16] W. E. Brownell. "Outer hair cell electromotility and otoacoustic emissions". In: *Ear and Hearing* 11.2 (1990), p. 82.

[17] V. A. Caliskan, O. C. Verghese, and A. M. Stankovic. "Multifrequency averaging of DC/DC converters". In: *IEEE Transactions on Power Electronics* 14.1 (1999), pp. 124–133. ISSN: 1941-0107.

[18] S. Camalet, T. D., F. Julicher, and J. Prost. "Auditory sensitivity provided by self-tuned critical oscillations of hair cells". In: *Proceedings of the National Academy of Sciences* 97.7 (2000), pp. 3183–3188. ISSN: 0027-8424, 1091-6490.

[19] L. H. Carney, M. J. McDuffy, and I. Shekhter. "Frequency glides in the impulse responses of auditory-nerve fibers". In: *The Journal of the Acoustical Society of America* 105.4 (1999), pp. 2384–2391. ISSN: 0001-4966, 1520-8524.

[20] E. C. Cherry. "Some experiments on the recognition of speech, with one and with two ears". In: *The Journal of the acoustical society of America* 25.5 (1953), pp. 975–979.

[21] M. Chinmulgund, R. B. Inturi, and J. A. Barnard. "Effect of Ar gas pressure on growth, structure, and mechanical properties of sputtered Ti, Al, TiAl, and Ti3Al films". In: *Thin solid films* 270.1-2 (1995), pp. 260–263.

[22] K. E. M. Church and X. Liu. *Bifurcation Theory of Impulsive Dynamical Systems*. Vol. 34. IFSR International Series in Systems Science and Systems Engineering. Springer International Publishing, 2021. ISBN: 978-3-030-64533-5.

[23] J. J. Collins and I. Stewart. "A group-theoretic approach to rings of coupled biological oscillators". In: *Biological Cybernetics* 71.2 (1994), pp. 95–103.

[24] J. J. Collins and I. N. Stewart. "Coupled nonlinear oscillators and the symmetries of animal gaits". In: *Journal of Nonlinear Science* 3.1 (1993), pp. 349–392. ISSN: 0938-8974, 1432-1467.

[25] V. F. Dal Poggetto, F. Bosia, D. Urban, P. H. Beoletto, J. Torgersen, N. M. Pugno, and A. S. Gliozzi. "Cochlea-inspired tonotopic resonators". In: *Materials & Design* 227 (2023), p. 111712. ISSN: 02641275.

[26] P. Dallos. "The active cochlea". In: *The Journal of Neuroscience* 12.12 (1992), pp. 4575–4585.

[27] H. Davis. "An active process in cochlear mechanics". In: *Hearing Research* 9.1 (1983), pp. 79–90.

[28] S. Davis and P. Mermelstein. "Comparison of parametric representations for monosyllabic word recognition in continuously spoken sentences". In: *IEEE Transactions on Acoustics, Speech, and Signal Processing* 28.4 (1980), pp. 357–366. ISSN: 0096-3518.

[29] E. De Boer and A. L. Nuttall. "The mechanical waveform of the basilar membrane. I. Frequency modulations ("glides") in impulse responses and cross-correlation functions". In: *The Journal of the Acoustical Society of America* 101.6 (1997), pp. 3583–3592. ISSN: 0001-4966, 1520-8524.

[30] H. Ding, L. Fu, Y. Wang, and J. Xie. "Resonant frequency tunable silicon fishbone-shaped MEMS double ended tuning fork". In: *2016 IEEE 11th Annual International Conference on Nano/Micro Engineered and Molecular Systems (NEMS)*. 2016, pp. 233–236.

[31] T. A. J. Duke and F. Jülicher. "Critical Oscillators as Active Elements in Hearing". In: *Active Processes and Otoacoustic Emissions in Hearing*. Ed. by G. A. Manley, R. R. Fay, and A. N. Popper. Vol. 30. Series Title: Springer Handbook of Auditory Research. New York, NY: Springer New York, 2007, pp. 63–92.

[32] M. Egretzberger and A. Kugi. "A dynamical envelope model for vibratory gyroscopes". In: *Microsystem Technologies* 16.5 (2010), pp. 777–786. ISSN: 1432-1858.

[33] M. Egretzberger, F. Mair, and A. Kugi. "Model-based control concepts for vibratory MEMS gyroscopes". In: *Mechatronics* 22.3 (2012), pp. 241–250. ISSN: 09574158.

[34] V. M. Eguíluz, M. Ospeck, Y. Choe, A. J. Hudspeth, and M. O. Magnasco. "Essential Nonlinearities in Hearing". In: *Physical Review Letters* 84.22 (2000). Publisher: American Physical Society, pp. 5232–5235.

[35] B. Ermentrout, Y. Park, and D. Wilson. "Recent advances in coupled oscillator theory". In: *Philosophical Transactions of the Royal Society A: Mathematical, Physical and Engineering Sciences* 377.2160 (2019), p. 20190092.

[36] G. B. Ermentrout and N. Kopell. "Frequency Plateaus in a Chain of Weakly Coupled Oscillators, I." In: *SIAM Journal on Mathematical Analysis* 15.2 (1984), pp. 215–237. ISSN: 0036-1410, 1095-7154.

[37] A. Erturk and D. J. Inman. *Piezoelectric energy harvesting*. John Wiley & Sons, 2011.

[38] J. G. F. Francis. "The QR transformation a unitary analogue to the LR transformation—Part 1". In: *The Computer Journal* 4.3 (1961), pp. 265–271.

[39] S. Geršić and G. Altmann. "Ein Modell für die Variabilität der Vokaldau- er". In: *Glottometrika* 9 (1988), pp. 49–58.

[40] T. Gold and J. Gray. "Hearing. II. The physical basis of the action of the cochlea". In: *Proceedings of the Royal Society B: Biological Sciences* 135.881 (1948), pp. 492–498.

[41] T. Gold, R. J. Pumphrey, and J. Gray. "Hearing. I. The cochlea as a frequency analyzer". In: *Proceedings of the Royal Society B: Biological Sciences* 135.881 (1948), pp. 462–491.

[42] M. Golubitsky and I. Stewart. *The symmetry perspective: from equilibrium to chaos in phase space and physical space*. Vol. 200. Springer Science & Business Media, 2003.

[43] F. Gomez, T. Lorimer, and R. Stoop. "Signal-Coupled Subthreshold Hopf-Type Systems Show a Sharpened Collective Response". In: *Physical Review Letters* 116.10 (2016), p. 108101. ISSN: 0031-9007, 1079-7114.

[44] V. K. Goyal and V. K. Goyal. *Energy and Variational Principles in Applied Mechanics*. Mayagüez Press, 2011.

[45] E. I. Green. "The story of Q". In: *American Scientist* 43.4 (1955), pp. 584–594.

[46] D. Gross, W. Hauger, J. Schröder, and W. A. Wall. *Technische Mechanik 2: Elastostatik*. 2021.

[47] V. Gubbi, T. Ivanov, K. Ved, C. Lenk, and M. Ziegler. "Bio-inspired acoustic MEMS sensor with tunable resonance frequency". In: *Sensors and Actuators A: Physical* 387 (2025), p. 116369.

[48] J. Guckenheimer and P. Holmes. *Nonlinear oscillations, dynamical systems, and bifurcations of vector fields*. Vol. 42. Springer Science & Business Media, 2013.

[49] S. Guo and J. Wu. *Bifurcation Theory of Functional Differential Equations*. Vol. 184. Applied Mathematical Sciences. New York, NY: Springer New York, 2013.

[50] J. E. Hall and M. E. Hall. *Guyton and Hall textbook of medical physiology e-Book*. Elsevier Health Sciences, 2020.

[51] M. Han and P. Yu. *Normal Forms, Melnikov Functions and Bifurcations of Limit Cycles*. Vol. 181. Applied Mathematical Sciences. Springer London, 2012. ISBN: 978-1-4471-2918-9.

[52] E. Hering, R. Martin, and M. Stohrer. *Physik für Ingenieure*. Springer-Verlag, 2007.

[53] R. B. Hetnarski, M. R. Eslami, and G. M. L. Gladwell. *Thermal stresses: advanced theory and applications*. Vol. 41. Springer, 2009.

[54] P. Hidnert and H. S. Krider. "Thermal expansion of aluminum and some aluminum". In: (1952).

[55] G. Hinton, L. Deng, D. Yu, G. Dahl, A.-r. Mohamed, N. Jaitly, A. Senior, V. Vanhoucke, P. Nguyen, T. Sainath, and B. Kingsbury. "Deep Neural Networks for Acoustic Modeling in Speech Recognition: The Shared Views of Four Research Groups". In: *IEEE Signal Processing Magazine* 29.6 (2012), pp. 82–97. ISSN: 1053-5888.

[56] J. Holdsworth, I. Nimmo-Smith, R. Patterson, and P. Rice. "Implementing a gammatone filter bank". In: *Annex C of the SVOS Final Report: Part A: The Auditory Filterbank* 1 (1988), pp. 1–5.

[57] G. C. Holmes. "The use of hyperbolic cosines in solving cubic polynomials". In: *The Mathematical Gazette* 86.507 (2002), pp. 473–477. ISSN: 0025-5572, 2056-6328.

[58] M. A. Hopcroft, W. D. Nix, and T. W. Kenny. "What is the Young's Modulus of Silicon?" In: *Journal of Microelectromechanical Systems* 19.2 (2010), pp. 229–238.

[59] F. C. Hoppensteadt and E. M. Izhikevich. *Weakly connected neural networks*. Vol. 126. Springer Science & Business Media, 1997.

[60] A. J. Hudspeth. “Making an effort to listen: mechanical amplification in the ear”. In: *Neuron* 59.4 (2008), pp. 530–545.

[61] A. J. Hudspeth, F. Jülicher, and P. Martin. “A critique of the critical cochlea: Hopf—a bifurcation—is better than none”. In: *Journal of neurophysiology* 104.3 (2010), pp. 1219–1229.

[62] T. Ivanov. “Piezoresistive cantilevers with an integrated bimorph actuator”. PhD thesis. Citeseer, 2004.

[63] P. L. M. Johannesma. “The pre-response stimulus ensemble of neurons in the cochlear nucleus”. In: *Symposium on Hearing Theory, 1972*. IPO. 1972.

[64] F. Jülicher and J. Prost. “Spontaneous Oscillations of Collective Molecular Motors”. In: *Physical Review Letters* 78.23 (1997), pp. 4510–4513.

[65] B. El-Kareh and L. N. Hutter. *Fundamentals of semiconductor processing technology*. Springer Science & Business Media, 2012.

[66] S. T. Karris. *Signals and systems with Matlab applications*. Orchard Publications, 2003.

[67] D. T. Kemp. “Otoacoustic emissions, travelling waves and cochlear mechanisms”. In: *Hearing Research* 22.1-3 (1986), pp. 95–104.

[68] D. T. Kemp. “Stimulated acoustic emissions from within the human auditory system”. In: *The Journal of the Acoustical Society of America* 64.5 (1978), pp. 1386–1391.

[69] A. Kern and R. Stoop. “Essential Role of Couplings between Hearing Nonlinearities”. In: *Physical Review Letters* 91.12 (2003), p. 128101.

[70] A. Kern and R. Stoop. “Principles and Typical Computational Limitations of Sparse Speaker Separation Based on Deterministic Speech Features”. In: *Neural Computation* 23.9 (2011), pp. 2358–2389. ISSN: 0899-7667, 1530-888X.

[71] H. K. Khalil. *Nonlinear Systems*. Pearson Education. Prentice Hall, 2002. ISBN: 9780130673893.

[72] C. Köppl and G. A. Manley. “Spontaneous otoacoustic emissions in the bobtail lizard. I: General characteristics”. In: *Hearing research* 71.1-2 (1993), pp. 157–169.

[73] V. Kuleshov and D. Precup. “Algorithms for multi-armed bandit problems”. In: *arXiv preprint arXiv:1402.6028* (2014).

[74] Y. Kuramoto. “Rhythms and turbulence in populations of chemical oscillators”. In: *Physica A: Statistical Mechanics and its Applications* 106.1-2 (1981), pp. 128–143. ISSN: 03784371.

[75] K. Kuttler. “An Introduction to Linear Algebra”. In: *Brigham Young University: Provo, UT, USA* (2010).

[76] Y. A. Kuznetsov, I. A. Kuznetsov, and Y. Kuznetsov. *Elements of applied bifurcation theory*. Vol. 112. Springer, 1998.

[77] K. B. Lee and Y.-H. Cho. “A triangular electrostatic comb array for micromechanical resonant frequency tuning”. In: *Sensors and Actuators A: Physical* 70.1 (1998), pp. 112–117.

[78] K. B. Lee, L. Lin, and Y.-H. Cho. “A frequency-tunable microactuator with a varied comb-width profile”. In: *17th IEEE International Conference on Micro Electro Mechanical Systems. Maastricht MEMS 2004 Technical Digest.* 2004, pp. 257–260.

[79] Y.-C. Lee, L.-K. Wang, Y.-C. Chuang, H.-C. Hong, and Y. Chiu. “Electrothermal Tunable MEMS Oscillators for MEMS-Based Reservoir Computing”. In: *IEEE Sensors Letters* 8.7 (2024), pp. 1–4.

[80] C. Lenk, A. Ekinci, I. W. Rangelow, and S. Gutschmidt. “Active, artificial hair cells for biomimetic sound detection based on active cantilever technology”. In: *40th Annual International Conference of the IEEE Engineering in Medicine and Biology Society (EMBC).* 2018, pp. 4488–4491.

[81] C. Lenk, P. Hövel, K. Ved, S. Durstewitz, T. Meurer, T. Fritsch, A. Männchen, J. Küller, D. Beer, T. Ivanov, and M. Ziegler. “Neuromorphic acoustic sensing using an adaptive microelectromechanical cochlea with integrated feedback”. In: *Nature Electronics* (2023). Publisher: Nature Publishing Group, pp. 1–11. ISSN: 2520-1131.

[82] C. Lenk, L. Seeber, M. Ziegler, P. Hövel, and S. Gutschmidt. “Enabling Adaptive and Enhanced Acoustic Sensing using Nonlinear Dynamics”. In: *2020 IEEE International Symposium on Circuits and Systems (ISCAS).* IEEE. 2020, pp. 1–4.

[83] K. D. Lerud, J. C. Kim, F. V. Almonte, L. H. Carney, and E. W. Large. “A canonical oscillator model of cochlear dynamics”. In: *Hearing Research* 380 (2019), pp. 100–107.

[84] E. A. Lopez-Poveda and R. Meddis. “A human nonlinear cochlear filterbank”. In: *The Journal of the Acoustical Society of America* 110.6 (2001), pp. 3107–3118.

[85] J. Lunze. *Regelungstechnik 1.* Vol. 10. Springer, 2013.

[86] R. F. Lyon. “Automatic Gain Control in Cochlear Mechanics”. In: *The Mechanics and Biophysics of Hearing.* Vol. 87. Series Title: Lecture Notes in Biomathematics. New York, NY: Springer New York, 1990, pp. 395–402.

[87] R. F. Lyon. “Using a cascade of asymmetric resonators with fast-acting compression as a cochlear model for machine-hearing applications”. In: *Autumn meeting of the acoustical society of japan.* 2011, pp. 509–512.

[88] A. Mahajan and D. Teneketzis. “Multi-armed bandit problems”. In: *Foundations and applications of sensor management.* Springer, 2008, pp. 121–151.

[89] G. A. Manley, L. Gallo, and C. Köppl. “Spontaneous otoacoustic emissions in two gecko species, Gekko gecko and Eublepharis macularius”. In: *The Journal of the Acoustical Society of America* 99.3 (1996), pp. 1588–1603.

[90] D. G. Manolakis and V. K. Ingle. *Applied digital signal processing: theory and practice.* Cambridge University Press, 2011.

[91] J. E. Marsden and M. McCracken. *The Hopf bifurcation and its applications*. Applied mathematical sciences v. 19. New York: Springer-Verlag, 1976. ISBN: 978-0-387-90200-5.

[92] P. Martin and A. J. Hudspeth. "Active hair-bundle movements can amplify a hair cell's response to oscillatory mechanical stimuli". In: *Proceedings of the National Academy of Sciences* 96.25 (1999). Publisher: National Academy of Sciences Section: Biological Sciences, pp. 14306–14311. ISSN: 0027-8424, 1091-6490.

[93] A. Mauroy and I. Mezić. "On the use of Fourier averages to compute the global isochrons of (quasi)periodic dynamics". In: *Chaos: An Interdisciplinary Journal of Nonlinear Science* 22.3 (2012), p. 033112. ISSN: 1054-1500, 1089-7682.

[94] L. Meirovitch. *Fundamentals of vibrations*. Waveland Press, 2010.

[95] W. Michiels and S.-I. Niculescu. *Stability and Stabilization of Time-Delay Systems*. Society for Industrial and Applied Mathematics, 2007.

[96] T. Middelmann, A. Walkov, G. Bartl, and R. Schödel. "Thermal expansion coefficient of single-crystal silicon from 7 K to 293 K". en. In: *Physical Review B* 92.17 (2015), p. 174113. ISSN: 1098-0121, 1550-235X.

[97] A. R. Møller and H. G. Nilsson. "Inner Ear Impulse Response and Basilar Membrane Modelling". In: *Acta Acustica united with Acustica* 41 (1979).

[98] G. Nellis and S. Klein. *Heat transfer*. Cambridge university press, 2008.

[99] J. C. Neu. "Coupled Chemical Oscillators". In: *SIAM Journal on Applied Mathematics* 37.2 (1979), pp. 307–315. ISSN: 0036-1399, 1095-712X.

[100] R. W. D. Nickalls. "A new approach to solving the cubic: Cardan's solution revealed". In: *The Mathematical Gazette* 77.480 (1993), pp. 354–359. ISSN: 0025-5572, 2056-6328.

[101] W. Nowacki. *Dynamic problems of thermoelasticity*. Springer Science & Business Media, 1975.

[102] D. O'Shaughnessy. "Review of analysis methods for speech applications". In: *Speech Communication* (2023).

[103] M. Ospeck, V. M. Eguíluz, and M. O. Magnasco. "Evidence of a Hopf Bifurcation in Frog Hair Cells". In: *Biophysical Journal* 80.6 (2001), pp. 2597–2607.

[104] W. Pabst and E. Gregorová. "Elastic properties of silica polymorphs–a review". In: *Ceramics-Silikaty* 57.3 (2013), pp. 167–184.

[105] C. J. Plack and A. J. Oxenham. "Basilar-membrane nonlinearity estimated by pulsation threshold". In: *The Journal of the Acoustical Society of America* 107.1 (2000), pp. 501–507.

[106] D. Premraj, K. Manoj, S. A. Pawar, and R. I. Sujith. "Effect of amplitude and frequency of limit cycle oscillators on their coupled and forced dynamics". In: *Nonlinear Dynamics* 103.2 (2021), pp. 1439–1452. ISSN: 0924-090X, 1573-269X.

[107] D. V. Ramana Reddy, A. Sen, and G.L. Johnston. "Time delay effects on coupled limit cycle oscillators at Hopf bifurcation". In: *Physica D: Nonlinear Phenomena* 129.1-2 (1999), pp. 15–34. ISSN: 01672789.

[108] I. W. Rangelow, T. Ivanov, A. Ahmad, M. Kaestner, C. Lenk, I. S. Bozchalooi, F. Xia, K. Youcef-Toumi, M. Holz, and A. Reum. "Active scanning probes: A versatile toolkit for fast imaging and emerging nanofabrication". In: *Journal of Vacuum Science & Technology B* 35.6 (2017).

[109] A. Recio, N. C. Rich, S. S. Narayan, and M. A. Ruggero. "Basilar-membrane responses to clicks at the base of the chinchilla cochlea". In: *The Journal of the Acoustical Society of America* 103.4 (1998), pp. 1972–1989. ISSN: 0001-4966.

[110] J. N. Reddy. *Energy principles and variational methods in applied mechanics*. John Wiley & Sons, 2017.

[111] E. L. Rees. "Graphical Discussion of the Roots of a Quartic Equation". In: *The American Mathematical Monthly* 29.2 (1922), pp. 51–55.

[112] W. S. Rhode. "Observations of the vibration of the basilar membrane in squirrel monkeys using the Mössbauer technique". In: *The Journal of the Acoustical Society of America* 49.4B (1971), pp. 1218–1231.

[113] W. S. Rhode and A. Recio. "Study of mechanical motions in the basal region of the chinchilla cochlea". In: *The Journal of the Acoustical Society of America* 107.6 (2000), pp. 3317–3332.

[114] J.-P. Richard. "Some trends and tools for the study of time-delay systems". In: *CESA'98, 2nd Conf. IMACS-IEEE conference on Computational Engineering in Systems Applications*. 1998, pp. 27–43.

[115] H. Robbins. "Some aspects of the sequential design of experiments". In: (1952).

[116] D. Roeser, S. Gutschmidt, T. Sattel, and I. W. Rangelow. "Tip Motion—Sensor Signal Relation for a Composite SPM/SPL Cantilever". In: *Journal of Microelectromechanical Systems* 25.1 (2016), pp. 78–90. ISSN: 1941-0158.

[117] S. Rosen and A. Fourcin. "Frequency selectivity and the perception of speech". In: *Frequency selectivity in hearing* (1986).

[118] E. J. Routh. *A treatise on the stability of a given state of motion, particularly steady motion*. Macmillan and Company, 1877.

[119] M. A. Ruggero, N. C. Rich, A. Recio, S. S. Narayan, and L. Robles. "Basilar-membrane responses to tones at the base of the chinchilla cochlea". In: *The Journal of the Acoustical Society of America* 101.4 (1997), pp. 2151–2163.

[120] M. Rupin, G. Lerosey, J. De Rosny, and F. Lemoult. "Mimicking the cochlea with an active acoustic metamaterial". In: *New Journal of Physics* 21.9 (2019), p. 093012. ISSN: 1367-2630.

[121] K. S. Saladin and L. Miller. *Anatomy & physiology*. WCB/McGraw-Hill New York, 1998.

[122] G. Schöner, W.Y. Jiang, and S. Kelso. "A synergetic theory of quadrupe- dal gaits and gait transitions *". In: *Journal of Theoretical Biology* 142 (1990), pp. 359–91.

[123] C. A. Shera. "Frequency glides in click responses of the basilar membrane and auditory nerve: Their scaling behavior and origin in traveling-wave dispersion". In: *The Journal of the Acoustical Society of America* 109.5 (2001), pp. 2023–2034. ISSN: 0001-4966, 1520-8524.

[124] J. R. Silvester. "Determinants of block matrices". In: *The Mathematical Gazette* 84.501 (2000), pp. 460–467. ISSN: 0025-5572, 2056-6328.

[125] M. Slaney. "An efficient implementation of the Patterson-Holdsworth auditory filter bank". In: *Apple Computer, Perception Group, Tech. Rep* 35.8 (1993).

[126] H. Smith. *An Introduction to Delay Differential Equations with Applications to the Life Sciences*. Vol. 57. Texts in Applied Mathematics. New York, NY: Springer New York, 2011.

[127] G.-B. Stan and R. Sepulchre. "Analysis of Interconnected Oscillators by Dissipativity Theory". In: *IEEE Transactions on Automatic Control* 52.2 (2007), pp. 256–270.

[128] P. Stephan, S. Kabelac, M. Kind, D. Mewes, K. Schaber, and T. Wetzel, eds. *VDI-Wärmeatlas: Fachlicher Träger VDI-Gesellschaft Verfahrenstechnik und Chemieingenieurwesen*. Springer Reference Technik. Berlin, Heidelberg: Springer Berlin Heidelberg, 2019. ISBN: 978-3-662-52988-1 978-3-662-52989-8.

[129] R. Stoop. "Why Hearing Aids Fail and How to Solve This". In: *Frontiers in Network Physiology* 2 (2022). Publisher: Frontiers. ISSN: 2674-0109.

[130] R. Stoop and F. Gomez. "Desired sounds from tuning a complex network of nonlinear Hopf nodes". In: *IFAC Proceedings Volumes* 45.12 (2012), pp. 70–74. ISSN: 14746670.

[131] R. Stoop, J.-J. V. D. Vyver, and A. Kern. "Limit cycles, noise, and chaos in hearing". In: *Microscopy Research and Technique* 63.6 (2004), pp. 400–412.

[132] S. H. Strogatz. *Nonlinear dynamics and chaos with student solutions manual: With applications to physics, biology, chemistry, and engineering*. CRC Press, 2018.

[133] R. R. A. Syms. "Electrothermal frequency tuning of folded and coupled vibrating micromechanical resonators". In: *Journal of Microelectromechanical Systems* 7.2 (1998), pp. 164–171.

[134] K. Tanaka, Y. Mochida, M. Sugimoto, K. Moriya, T. Hasegawa, K. Atsuchi, and K. Ohwada. "A micromachined vibrating gyroscope". In: *Sensors and Actuators A: Physical* 50.1 (1995), pp. 111–115.

[135] J. Timcheck et al. "The Intel neuromorphic DNS challenge". In: *Neuromorphic Computing and Engineering* 3.3 (2023), p. 034005. ISSN: 2634-4386.

[136] K. Ved, C. Lenk, T. Ivanov, P. Hövel, and M. Ziegler. "Bio-inspired, adaptive acoustic sensor: Sensing properties in dependence of feedback parameters". In: *AIP Conference Proceedings*. Vol. 3062. 1. AIP Publishing. 2024.

[137] D. Verstraeten, B. Schrauwen, and D. Stroobandt. "Isolated word recognition using a Liquid State Machine". In: *EuroSpeech'2005, European Conference on Speech Communication*. 2005.

[138] A. Vilfan and T. Duke. “Frequency clustering in spontaneous otoacoustic emissions from a lizard’s ear”. In: *Biophysical journal* 95.10 (2008), pp. 4622–4630.

[139] X. Wang. “A Simple Proof of Descartes’s Rule of Signs”. In: *The American Mathematical Monthly* 111.6 (2004), pp. 525–526.

[140] H. Watanabe, N. Yamada, and M. Okaji. “Linear Thermal Expansion Coefficient of Silicon from 293 to 1000 K”. en. In: *International Journal of Thermophysics* 25.1 (2004), pp. 221–236. ISSN: 0195-928X.

[141] J. Wei and C. Zhang. “Stability analysis in a first-order complex differential equations with delay”. In: *Nonlinear Analysis: Theory, Methods & Applications* 59.5 (2004), pp. 657–671. ISSN: 0362546X.

[142] B. Wen and K. Boahen. “A Silicon Cochlea With Active Coupling”. In: *IEEE Transactions on Biomedical Circuits and Systems* 3.6 (2009), pp. 444–455.

[143] J. J. Yao and N. C. MacDonald. “A micromachined, single-crystal silicon, tunable resonator”. en. In: *Journal of Micromechanics and Microengineering* 5.3 (1995), pp. 257–264.

[144] S. A. Zawawi, A. A. Hamzah, B. Y. Majlis, and F. Mohd-Yasin. “A review of MEMS capacitive microphones”. In: *Micromachines* 11.5 (2020), p. 484.

[145] L. Zhao and S. Zhou. “Compact Acoustic Rainbow Trapping in a Bioinspired Spiral Array of Graded Locally Resonant Metamaterials”. In: *Sensors* 19.4 (2019), p. 788. ISSN: 1424-8220.

[146] M. Zolfagharinejad, J. Büchel, L. Cassola, S. Kinge, G. S. Syed, A. Sebastian, and W. G. van der Wiel. “In-Materia Speech Recognition”. In: *arXiv preprint arXiv:2410.10434* (2024).

Own Publications

Journal Publications

[147] H. F. J. Rolf, P. Feketa, and T. Meurer. "Delay-Controlled Frequency Tuning of a MEMS Sensor for Neuromorphic Acoustic Sensing". In: *IEEE Access* 13 (2025), pp. 38940–38951. ISSN: 2169-3536. DOI: 10.1109/ACCESS.2025.3546435.

[148] H. F. J. Rolf, P. Feketa, A. Schaum, and T. Meurer. "Implementing the Fourier Transform in a Sensor: A Benchmark Application for Neuromorphic Acoustic Sensing". In: *Neuromorphic Computing and Engineering* 5.3 (2025). ISSN: 26344386. DOI: 10.1088/2634-4386/ade7ac.

[149] H. F. J. Rolf and T. Meurer. "On coupled oscillators modeling bio-inspired acoustic sensors: Bifurcation analysis toward tunability enhancement". In: *Chaos: An Interdisciplinary Journal of Nonlinear Science* 34.10 (2024), pp. 103–135. ISSN: 1054-1500, 1089-7682. DOI: 10.1063/5.0217847.

[150] K. Ved, H. F. J. Rolf, T. Ivanov, T. Meurer, M. Ziegler, and C. Lenk. "Coupling-induced tunability of characteristic frequency, bandwidth and gain of artificial hair cells". In: *Hearing Research* 462 (2025), p. 109260. ISSN: 03785955. DOI: 10.1016/j.heares.2025.109260.

[151] K. Ved, H. F. J. Rolf, T. Ivanov, T. Meurer, M. Ziegler, and C. Lenk. "Mimicking Cochlear Pre-Processing using Critically Coupled MEMS Sensors". In: *Neuromorphic Computing and Engineering* (2026). ISSN: 26344386. DOI: 10.1088/2634-4386/ae45c9.

Conference Publications

[152] H. F. J. Rolf, R. Kumar, and T. Meurer. "Effects of Time Delay on the Resonance Frequency of Andronov-Hopf Bifurcations in Neuromorphic Devices". In: *IFAC-PapersOnLine*. 26th International Symposium on Mathematical Theory of Networks and Systems (MTNS 2024) 58.17 (2024), pp. 13–18. ISSN: 24058963. DOI: 10.1016/j.ifacol.2024.10.106.

[153] H. F. J. Rolf and T. Meurer. "Amplitude control for an artificial hair cell undergoing an Andronov-Hopf bifurcation". In: *IFAC-PapersOnLine*. 12th IFAC Symposium on Nonlinear Control Systems (NOLCOS 2022) 56.1 (2023), pp. 181–186. ISSN: 24058963. DOI: 10.1016/j.ifacol.2023.02.031.

[154] H. F. J. Rolf and T. Meurer. "Bifurcation analysis of coupled Andronov-Hopf oscillators: A geometric approach". In: *IFAC-PapersOnLine*. 25th International Symposium on Mathematical Theory of Networks and Systems (MTNS 2022) 55.30 (2022), pp. 504–509. ISSN: 24058963. DOI: 10.1016/j.ifacol.2022.11.103.

[155] H. F. J. Rolf and T. Meurer. “Enabling Tunability of a MEMS Sensor with a Geometric Nonlinearity”. In: *IFAC-PapersOnLine*. 7th IFAC Conference on Analysis and Control of Nonlinear Dynamics and Chaos (ACNDC 2024) 58.5 (2024), pp. 66–71. ISSN: 2405-8963. DOI: 10.1016/j.ifacol.2024.07.065.

[156] H. F. J. Rolf and T. Meurer. “Exploiting Asymmetries in Diffusively Coupled Oscillators to Enable Frequency Tunability in Neuromorphic Devices”. In: *IFAC-PapersOnLine*. 11th Vienna International Conference on Mathematical Modelling (MATHMOD 2025) 59.1 (2025), pp. 217–222. ISSN: 24058963. DOI: 10.1016/j.ifacol.2025.03.038.